Topology optimization in interfacial flows using the pseudopotential model

Graham Danny Koyeerath

THESE DE DOCTORAT

NANTES UNIVERSITE

ECOLE DOCTORALE N° 602
Sciences de l'Ingénierie et des Systèmes
Spécialité : « *Energétique-Thermique-Combustion* »

Par
Graham Danny KOYEERATH

Topology optimization in interfacial flows using the pseudopotential model.

Thèse présentée et soutenue à Nantes, le 21 Juin 2024
Unité de recherche : UMR6607

Composition du Jury :

Président :	François DUBOIS	Professeur, CNAM, Paris.
Rapporteurs :	Aimy BAZYLAK	Professeur, University of Toronto.
	Frederic TOPIN	Maitre de conférences-HDR, IUSTI, Aix-Marseille Université.
Examinateurs :	François DUBOIS	Professeur, CNAM, Paris.
	Volker P. SCHULZ	Professeur, Dir. STCIT, DHBW Mannheim.
Invité :	Florian DUGAST	École Centrale de Nantes & Naval Group, France.
Dir. de thèse :	Bruno AUVITY	Professeur, LTEN, Nantes Université.
Co-dir. de thèse :	Christophe JOSSET	Maitre de conférences, LTEN, Nantes Université.
	Yann FAVENNEC	Maitre de conférences-HDR, LTEN, Nantes Université.

Acknowledgments

The completion of this doctorate would have not been possible without the people listed subsequently:

Christophe Josset, whose continued motivation and guidance were indispensable. Yann Favennec, who apart from his motivation, imparted skills and insights in the field of topology optimization. Bruno Auvity (Director of the thesis), who provided valuable insights and also aided in the bureaucratic aspects of the thesis. Florian Dugast (my predecessor whose topic was: Topology optimization for convective heat transfer), who helped with countless doubt solving sessions. Jad Houssien, who completed an internship using an open source LBM solver (OpenLB) for validation of the in-house CUDA LBM code.

Volker Schulz (also a jury member) and Jérôme Bellettre for their constructive comments during the annual CSI. Aimy Bazylak and Frederic Topin for reviewing my thesis are providing their insights. François Dubois for agreeing to be a part of the jury.

Steven Le Corre and Cathy Castelain (the current and the previous Director of LTeN) along with the team of LTeN, for their cooperation and goodwill. Centre de Calcul Intensif des Pays de la Loire (CCIPL), for their provision of GPU super-computing facility. To the Ecolé doctoral for providing necessary assistance and smoothening my doctoral journey.

The One, who is *steady* in the *transient* state of my life. Family and friends, for their prayers and motivation. And last but not the least my colleagues at LTeN, for the time well spend in group lunches, various discussions (scientific and otherwise) and after-work sports (Fuse-ball and Tennis, both of which I picked up during my stay in Nantes).

Table of contents

List of Figures

List of Tables

Nomenclature

Abbreviation

ACE	Allen-Cahn equation
BB	Bounceback boundary condition
BC	Boundary condition
CHE	Cahn-Hillard equation
CO	Convective outlet
CS	Carnahan-Starling
EDM	Exact difference forcing scheme
EOS	Equation of state
GA	Genetic algorithm
GDL	Gas diffusion layer
LB	Lattice Boltzmann
LBE	Lattice Boltzmann equation
LBM	Lattice Boltzmann method
MCMP-FE	multicomponent multiphase –Free energy method
MCMP-SC	multicomponent multiphase –Shan and Chen method
MD	Molecular Dynamics
NO	Neumann outlet
NS	Navier Stokes
NWF	Non-wetting fluid
PEMFC	Proton/Polymer exchange membrane fuel cell
PF	Phase field
PI	Pressure inlet
PO	Pressure outlet
PR	Peng Robinson
PSO	Particle swarm optimization
SCMP-FE	Single component multiphase –Free energy method

SCMP-SC Single component multiphase –Shan and Chen method

TOSFP topology optimization for steady-state forward problem

TOTFP topology optimization for transient-state forward problem

VI Velocity inlet

VO Velocity outlet

WF Wetting fluid

WGS Wettability Gradient Surface

Operator

$\langle \boldsymbol{a}, \boldsymbol{b} \rangle$ Inner product between vectors $\boldsymbol{a}$ and $\boldsymbol{b}$

$\|\boldsymbol{a}\|_1$ The L1 norm of $\boldsymbol{a}$

$\|\boldsymbol{a}\|_2$ The L2 norm of $\boldsymbol{a}$

$\mathbb{1}_{\{i<0\}}$ Indicator function whose value is unity when the underlying condition is satisfied, for e.g. $i < 0$

Symbols

α Nature of a computational node: fluid ($\alpha = 1$) or solid ($\alpha = 0$)

α_v Constant of proportionality in the theoretical relation for migration velocity

χ A function to designated any quantities of interest, used for BC nomenclature exclusively

Λ Collision operator

$\mathring{\mathbf{f}}$ $\mathring{\mathbf{f}} = \{\mathring{f}_0, \mathring{f}_1, \mathring{f}_2, \mathring{f}_3, \mathring{f}_4, \mathring{f}_5, \mathring{f}_6, \mathring{f}_7, \mathring{f}_8\}$, collectively represents the adjoint-state (corresponding to LBM) variables

$\mathbf{f}$ $\mathbf{f} = \{f_0, f_1, f_2, f_3, f_4, f_5, f_6, f_7, f_8\}$, collectively represents the LBM state variable for D2Q9

$\mathcal{F}$ Entirety of the LBM problem along with the boundary conditions

$\mathcal{C}_{\text{drop}}$ Center of gravity of the droplet (in the context of the droplet motion on a WGS)

$\mathcal{D}$ $\mathcal{D}_{\text{s}} \cup \mathcal{D}_{\text{f}}$; The entire domain

$\mathcal{D}_{\text{f}}$ Solid domain

$\mathcal{D}_{\text{s}}$ Fluid domain

$\mathcal{J}$ The cost function for the optimisation problem

$\mathcal{L}$ The Lagrange function

$\mathcal{P}$ Residue of the boundaries in the LBM problem

$\mathcal{R}$ Residue of the LBM problem

$\mathring{f}$ Probability distribution function for the adjoint-state model

$\mathscr{F}$ Force term which could be incorporated using multiple strategies

$\mathscr{H}$ Notation for different LBM models used.

$\mathscr{I}_{\text{lbm}}$ Iteration number for LBM, also it indicates LBM time as $\Delta t = 1$ t.s.

$\mathscr{I}_{\text{opt}}$	Iteration number for optimization solvers
$\mathscr{S}$	Saturation in the fluid domain $\mathcal{D}_{\text{f}}$
$\mathscr{X}$	Cost function along the boundaries
$\mathscr{Y}$	Cost function along the domain
ν	Kinematic viscosity of the fluid
$\mathscr{N}_x$	Total number of nodes or length of domain in x-direction
$\mathscr{N}_y$	Total number of nodes or length of domain in y-direction
ω	$(\Delta t)\tau^{-1}$
ϕ	The porosity of the domain; used only in the topology optimization context
Ψ	Level-set variable; used for describing the solid using 'α'
ψ	Pseduopotential function, which is function of density of fluid
ρ	Density of fluid
ρ_{w}	Fictitious solid wall density, also known as pseudo-density
τ	The relaxation time: $\tau = 3\nu + 0.5$
Bo	Bond number
Ca	Capillary number
θ_{dy}	Dynamic contact angle
θ_{stat}	Static contact angle, also represented by θ if the context is clear
Re	Reynolds number
Υ	Represents the wettability profile of a surface
$\boldsymbol{e}$	Particle velocity in LBM
$\boldsymbol{F}_{\text{p}}$	Interparticular force for the pseudopotential model
$\boldsymbol{r}$	Location vector: $r_x\hat{i} + r_y\hat{j}$ for a two dimensional domain in Cartesian co-ordinates
$\boldsymbol{u}_{\text{mig}}$	Analytically obtained migration velocity
$\boldsymbol{V}_{\text{mig}}$	Numerically obtained migration velocity
e_s	Speed of sound in LBM framework
f	Probability distribution function used in LBM
G	Interaction strength; used for calculation of interparticular force
M	$\frac{\mu_{\text{NWF}}}{\mu_{\text{WF}}}$, Dynamic viscosity ratio; where μ is the dynamic viscosity
p	Pressure of the fluid
T_c	Critical temperature, corresponds to critical point (with pressure p_c)

Résumé

L'origine de cette thèse est liée à la problématique de la gestion thermofluidique des piles à combustible à membrane d'échange de protons. Cette problématique est étudiée au sein du LTeN à Nantes Université depuis de nombreuses années. Ce type de pile à combustible est considéré comme une technologie prometteuse dans le cadre de la décarbonation, notamment pour des application de mobilité, mais plusieurs verrous scientifiques restent à lever pour fiabiliser et améliorer ses performances, et donc contribuer à son essor. L'un des défis est de parvenir à un équilibre hydrique dans les couches de diffusion de gaz de la pile à combustible. L'eau libérée après la réaction de l'H_2 contribue à hydrater la membrane (en maintenant sa résistivité protonique au minimum), mais si l'eau excédentaire n'est pas évacuée, celle-ci empêche l'approvisionnement en gaz réactifs (H_2 et O_2) des couches catalytiques, interrompant ainsi la réaction de la pile à combustible. Il s'agit donc de gérer efficacement l'apport de gaz d'une part, et l'évacuation de l'eau liquide d'autre part, tout en assurant la continuité électrique. Actuellement, cette problématique est gérée par l'utilisation d'un milieu poreux généralement non structuré – appelé couche de diffusion des gaz ou *gaz diffusion layer* (GDL). Le poreux est le plus souvent un feutre ou un tissu de carbone dont les caractéristiques classiques sont les suivantes : une épaisseur de l'ordre de plusieurs centaines de micromètre, une porosité supérieur à 80 %, une répartition de taille de pores allant du micron à quelques dizaines de microns et des diamètres de brin de l'ordre du micron. Un traitement hydrophobe est souvent utilisé afin d'éviter l'imbibition totale de la GDL, la phase liquide circulant ainsi à travers les zones moins hydrophobes ou à pores plus larges. Une manière originale de tenter une réponse à cette problématique de gestion fluidique consiste à poser la question de la définition de la structure poreuse permettant un écoulement optimal de ces fluides. Il s'agit donc d'un problème d'allocation optimale de la matière (structure de la GDL) afin d'optimiser un écoulement diphasique (réactifs gazeux et eau liquide) pour des conditions aux limites particulières (entrées fluidiques opposées) et sous contraintes (porosité et continuité de la phase solide). Ce type de problème d'optimisation topologique structurel est très complexe ; il n'a, à notre connaissance, jamais été traité dans la littérature et nécessite le développement de nouveaux outils de modélisation et d'optimisation. Le développement d'une telle méthode d'optimisation topologique appliquée aux écoulements diphasiques en milieu poreux est donc un objectif à long terme et les différents travaux développés au cours de cette thèse y contribuent.

Toute résolution d'un problème optimisation nécessite de choisir en premier lieu le modèle (en l'occurence ici un modèle physique) pour simuler les phénomènes physique en question. Dans notre cas, la simulation numérique des écoulements multiphasiques et interfaciaux peut être divisée en deux catégories : les modèles d'approche de "haut en bas" '*top to bottom*) et ceux de "bas en haut" (*bottom up*). Dans la première catégorie, nous avons les modèles macroscopiques qui couplent généralement les équations de Navier–Stokes avec les méthodes de suivi des interfaces. Les méthodes les plus utilisés parmi celles-ci sont les VOF (*volume of fluid*) et le suivi de lignes de niveaux (*level-set*). Dans la seconde catégorie, les forces d'interaction sont prescrites, permettant de dériver les paramètres macroscopiques. La dynamique moléculaire et les méthodes mésoscopiques comme le modèle de Van der Waal et la méthode de lattice Boltzmann (LBM) font partie de cette seconde catégorie.

Le modèle LBM multiphasique le plus utilisé, à savoir le modèle pseudopotentiel, présente une interface diffuse ne nécessitant pas la résolution d'une équation de suivi de l'interface. L'interface

de ce modèle est le résultat des forces interparticulaires, c'est-à-dire mésoscopiques. Le modèle pseudopotentiel est connu pour sa simplicité de mise en œuvre et son efficacité car il ne nécessite pas la résolution de l'équation de continuité comme dans le cas des équations de Navier–Stokes. Ainsi, les données des nœuds voisins ne sont nécessaires que pour le calcul des forces interparticulaires. Cela nous permet de tirer parti de l'algorithme par ailleurs hautement parallélisable, en exécutant les codes sur des cartes GPU à l'aide de l'interface `CUDA`, le problème de transport résolu étant non-linéaire uniquement à l'échelle locale. En fonction du problème à résoudre, il est ainsi possible d'accélérer la résoluton jusqu'à 50 fois par rapport à un programme en langage `C` exécuté sur un seul processeur. La LBM est donc très adaptée à la parallélisation de type GPU, c'est-à-dire à l'exécution simultanée d'un grand nombre de *threads*. Bien que le manuscrit n'aborde pas l'aspect du codage, il joue un rôle important dans le choix du modèle LBM approprié pour l'optimisation. En résumé, nous avons choisi le modèle pseudopotentiel multiphase à composante unique (single component multiphase – SCMP-SC) développé initiallement Par Shan and Chen pour modéliser la physique. Ce modèle et le solveur rapide associé contituent la première "brique" de l'algorithme d'optimisation.

Dans le chapitre 2, diverses extensions ou modifications du modèle SCMP-SC (telles que le modèle *multi-range*, les différents schémas de forçage, l'intégration d'une équation d'état réaliste (*equation of state* – EOS), la discrétisation d'ordre supérieur du pseudopotentiel, etc.) ont été présentées et testées. Au final, nous avons choisi d'utiliser l'EOS de Carnahan-Starling (CS-EOS) ainsi que le schéma de forçage de la méthode des différences exactes (*exact difference method* – EDM) pour une plus grande stabilité du solveur et des vitesses parasites (*spurious currents*) plus faibles. Les valeurs des paramètres fixés à la fois *a priori* et *a posteriori*, les simulations physiques aident à comparer les performances des différentes modifications/extensions. En résumé, le modèle à plages multiples associé au schéma de forçage CS-EOS–EDM donne les meilleurs résultats, avec des courants parasites relativement faibles, ce qui se reflète dans la stabilité du problème direct. Les résultats concernant la loi de Laplace, les courbes de co-existance liquide-vapeur et la corrélation entre l'angle de contact statique (θ_{stat}) et la pseudo-densité (ρ_{w}) pour le mur sont cohérents et permettent ainsi de valider notre modèle direct. Ces valeurs de paramètres sont ensuite utilisées pour modéliser des phénomènes plus complexes.

Le problème de l'ascension capillaire, tant en instationnaire (loi de Washburn) qu'en stationnaire (loi de Jurin) est ainsi résolu (par rapport à une hauteur capillaire air-eau réelle, *via* les similitudes des nombres sans dimension). Nous observons par ailleurs l'effet de la compressibilité de la phase vapeur pour le SCMP-SC qui a été atténué en augmentant la viscosité cinématique de la vapeur de 40 %. Nous observons également des oscillations capillaires dans le comportement dynamique de la colonne de liquide, comme précédemment rapporté dans la littérature. Ces oscillations (avec l'augmentation du diamètre du tube) augmentent à la fois en amplitude (par rapport à la hauteur de Jurin) et en fréquence, ce qui constitue un indicateur de la présence d'effets inertiels.

La dynamique d'une gouttelette sur une surface horizontale idéale à gradient de mouillabilité a aussi été testée (*wettability gradient surface* – WGS). Dans le cas d'un faible gradient, il est fait état dans la littérature d'une vitesse asymptotique constante atteinte par la goutte. Ici, avec de très petits gradients de mouillabilité, nous obtenons une corrélation linéaire entre la vitesse de migration à l'asymptote et le gradient du cosinus de l'angle de contact statique, et, de plus, la constante de proportionnalité résultante est en bonne adéquation avec la valeur théorique $\alpha_v = 0.33$ obtenue dans [1].

Ces différents résultats montrent ainsi la capacité du solveur développé à capturer des phénomènes non linéaires et dynamiques et valident par la même l'outil numérique développé.

Ces résultats ayant été obtenus dans le cadre de conditions aux limites "simples" (périodiques ou murs imperméables – *bounce-back*), la suite des travaux a concerné l'implémentation des conditions aux limites en pression et en vitesse pour des géométries ouvertes. Alors que ces conditions aux limites sont bien définies pour les modèles macroscopiques, et relativement uniques – exception faites de leur discrétisation –, leurs déclinaisons à l'échelle mésoscopiques sont beaucoup plus nombreuses, et leur stabilité peu documentée. Les principaux cas d'étude ont été le tube droit (pour le drainage et l'imbibition), la goutte dans un écoulement vapeur en canal, le tube en escalier et

le tube à trajectoire privilégiée. Les conditions de Neumann et convective ont été testées pour les sorties et celles de Zou and He et Ladd pour les entrées. Les résultats obtenus pour les simulations susmentionnés ne sont plus fiables quand l'interface atteint la frontière en sortie. En fait, une pluralité d'artefacts numériques a été observée, et ce, principalement lorsque l'interface a atteint le voisinage de la frontière, ou l'a traversée. De plus, une évaporation de la phase liquide a été observée au niveau des fronts interfaciaux exposés aux sorties (uniquement dans la phase initiale de la simulation). Des comparaisons ont été menées avec le logiciel libre OpenLB, sans plus de succès. Malgré la simplicité apparente de l'implémentation de ces conditions aux limites, au moment de la rédaction de cette thèse, nous n'avons toujours pas réussi à reproduire les résultats de [2] et [3].

L'outil développé a par la suite été utilisé pour des simulations d'écoulements en milieux poreux plus réalistes. Les résultats s'avèrent fiables et stables pour des structures poreuses simples et pour des écoulements à nombre capillaire élevés. Dans le cas du drainage – pour lequel un débit est imposé – nous avons observé une évolution linéaire de la saturation, à l'exception de phénomènes transitoires tels que les sauts de Haines. Pour des nombres capillaires plus faibles ($\mathrm{Ca} \leq 10^{-3}$), nous observons le phénomène de condensation en sortie, l'effondrement des bulles de vapeur, et l'instabilité du schéma numérique. Conscients des limites du schéma SCMP-SC actuel, nous avons répété le même cas de test en utilisant le schéma MCMP-SC (*multi-component multi-phase*) pour $\log|\mathrm{Ca}| = -4.25$, et avons finalement obtenu le résultat souhaité, similaire aux résultats publiés. Ces limitations du schéma SCMP-SC ont modifié l'objectif initial d'optimisation de la GDL, fonctionnant dans le régime de digitations capillaires avec des conditions aux limites en pression et débit, pour se recentrer sur un cas plus académique : un milieu poreux avec des conditions aux limites périodiques et de non glissement.

Le chapitre 3 est dédié à l'optimisation topologique en monophasique. Le modèle du chapitre précédent, c'est-à-dire le modèle SCMP, est utilisé en tant que modèle direct. Le modèle monophasique est obtenu à partir du modèle diphasique en annulant quelques termes bien choisis, la structure du modèle direct monophasique étant exactement celle du modèle diphasique du chapitre précédent. La fonction courbe de niveau (*level-set*) est utilisée pour la ségrégation entre la phase solide et la phase fluide. À l'interface entre ces deux phases, la condition de rebond (*bounce-back*) est appliquée. Dans les problèmes d'optimisation traités, il s'agit de minimiser une fonctionnelle en jouant sur la topologie du milieu, c'est-à-dire, *in fine*, sur la courbe de niveau. L'espace paramétrique de contrôle de la courbe de niveau étant bâtie sur la discrétisation du modèle direct, sa dimension ne permet pas l'utilisation de la méthode des différences finies pour le calcul du gradient de la fonction de coût. En revanche, la méthode de l'état adjoint permet le calcul du gradient à l'unique condition de résoudre un unique problème additionnel : le problème de l'état adjoint. Cet état adjoint est obtenu en cherchant le point selle du Lagrangien, cette fonctionnelle augmentée comprenant la fonctionnelle de coût à laquelle sont rajoutées les contraintes : toutes les équations du modèle d'état, les conditions aux limites, les conditions initiales, etc. Une difficulté relative aux schémas LBM est le grand nombre d'équations de transport couplées (par ex. pour le schéma D2Q9, neuf équations de transports sont couplées en plus desquelles il convient d'ajouter trois équations sur chaque nœud frontière). Le calcul des états adjoints sur un modèle LBM est loin d'être trivial, l'une des difficultés étant le calcul des dérivées de la fonction à l'équilibre, une autre difficulté étant le calcul des états adjoints aux frontières. L'actualisation de la fonction courbe de niveaux est faite selon un algorithme de descente à gradient de type plus grande pente, suivant les travaux antérieurs de **??**, en ne suivant pas la méthodologie plus classique pour laquelle la courbe de niveau est elle-même advectée. Deux cas tests sont mis en œuvre pour tester la méthodologie déployée. Le premier est un distributeur pour lequel il s'agit d'obtenir une topologie telle que les débits en sorties soient aussi proches que possible les unes des autres, une contrainte de porosité étant de plus appliquée. Le second cas est un coude pour lequel il s'agit d'obtenir une topologie telle que la perte de charge soit minimale. Ces deux cas tests réalisés avec succès ont permis de valider l'ensemble de l'approche : l'algorithme itératif global, le modèle LBM direct, le modèle LBM adjoint, la stratégie de réactualisation de la fonction courbe de niveau, etc.

Le chapitre 4 traite de l'optimisation de la distribution spatiale de mouillabilité. Les cas pra-

tiques où l'on souhaite déplacer des gouttes sont relativement nombreux, allant de l'amélioration de la condensation à la micro-fluidique. Comme évoqué au chapitre 2, une distribution non homogène de mouillabilité peut induire le déplacement d'une goutte de liquide sur une paroi plane sous l'effet du déséquilibre des forces capillaires, de la partie la plus hydrophobe vers la partie la plus hydrophile de la plaque. La question posée est ainsi la suivante : pour un fluide donné (propriétés thermophysiques, taille de goutte) et des conditions opératoires fixées (longueur du déplacement, plage de mouillabilité), quelle est la distribution spatiale optimale de la mouillabilité permettant à la goutte de se déplacer le plus rapidement, sachant que, tant théoriquement qu'expérimentalement, les surfaces dites à gradient de mouillabilité sont plus précisément à gradient constant ? Le modèle SCMP-SC présenté et développé précédemment est ainsi utilisé pour simuler le déplacement de la goutte liquide. Le paramètre de contrôle permettant de faire varier la mouillabilité est la densité du solide, propriété fictive qui permet – théoriquement – de varier continûment, de superhydrophobe ($\theta_{\text{contact}} = 180$ avec $\rho_{\text{solide}} = \rho_{\text{vapeur}}$) à superhydrophile ($\theta_{\text{contact}} = 0$ avec $\rho_{\text{solide}} = \rho_{\text{liquide}}$). La fonction de coût à minimiser est le temps final nécessaire pour que le centre de gravité de la goutte atteigne l'emplacement cible ; minimiser celle-ci revient à maximiser la vitesse moyenne. Pour plus de simplicité, le gradient de la fonction de coût par rapport à la variable de contrôle a été évalué par différences finies. Afin d'éviter au maximum les problèmes de minima locaux, une stratégie d'approche multi-échelle a été utilisée : le profil initial de mouillabilité est initialement discrétisé en 2 segments ($i = 1$; 3 degrés de liberté). Une fois le profil optimal à l'itération i identifié (2^i+1 degrés de liberté) celui-ci est discrétisé plus finement (itération i+1, $2^{i+1}+1$) et le processus d'optimisation est alors relancé, jusqu'à convergence spatiale. Concernant le pas de descente pour l'actualisation de la variable de contrôle, une méthode simple de recherche linéaire par dichotomie est utilisée. Au préalable, plusieurs profils analytiques de mouillabilité ont été testés (linéaire, quadratique, cubique) et la conclusion globale est que le profil quadratique convexe Υ_{qcv} est le plus performant ; le profil linéaire ayant été retenu comme profil initial pour l'optimisation. Les principaux résultats sont les suivants. Pour les rapports de déplacement faibles, $L/D = 3,2$, le profil optimal n'est pas monotone en espace, ce qui est relativement contre intuitif. En effet, une rediminution subite de la mouillabité devrait freiner voire stopper la goutte, ce qui n'est pas le cas ici. La vitesse moyenne de la goutte est ainsi augmentée de 69 % par rapport au profil linéaire. Par ailleurs, afin de maximiser l'effet du gradient de mouillabilité et donc les effets capillaires, la zone de variation de la mouillabilité se retrouve diminuée jusqu'à être nulle sous les positions initiale et finale. De plus, afin de contrer l'étalement de la goutte sur la partie hydrophile, et donc l'augmentation de la friction, le gradient est plus important dans la partie hydrophile, expliquant ainsi les performances du profil quadratique convexe. Finalement pour les plus grandes plaques ($L/D >= 6.4$) la solution optimale se rapproche du profil quadratique. Ainsi, d'un point de vue pratique, ce dernier semble être un profil générique acceptable, même si, pour chaque configuration, l'optimisation a permis une amélioration par rapport à celui-ci. L'ensemble de ces résultats a été publié dans le journal *Physics of fluids*.

Le chapitre 5 est une extension du chapitre 3 en ce sens qu'il traite de l'optimisation topologique en multiphasique plutôt qu'en monophasique. La plupart des outils numériques déployés dans le chapitre 3 peuvent être repris, mais le modèle direct étant celui du chapitre 2, l'état adjoint associé doit, lui aussi, être calculé formellement. Dans le calcul de l'état adjoint, il s'agit de calculer les dérivées de multiples fonctions composées. Par exemple, la fonction à l'équilibre prend maintenant en compte les forces inter-particulaires, localement mais aussi dans l'entourage direct, ces forces étant elle-mêmes fonctions de la pression, celle-ci étant définie à l'aide de l'équation d'état réaliste de Carnahan-Starling. Le développement formel de l'état adjoint a été effectué ; ce travail ardu n'a, selon notre connaissance, jamais été publié. Le calcul du gradient a été effectué pour deux situations distinctes : en premier lieu dans le cadre de l'optimisation topologique de la structure du milieu poreux (allocation optimale de la matière) ; en second lieu dans le cadre de l'optimisation de la mouillabilité du milieu (allocation optimale d'une propriété spatiale). L'implémentation des états adjoints et des gradients a débuté dans le cadre de cette thèse mais, à l'heure où nous écrivons ces lignes, les gradients n'ont pu être validés par comparaison avec les différences finies, même si les ordres de grandeur sont similaires. Il est difficile de dire si l'erreur – puisque visiblement il y en a

une – vient du travail formel du calcul analytique des dérivées, ou si elle vient de l'implémentation numérique. Les développements mathématiques donnés dans ce chapitre et les développements numériques associés appellent donc un nouveau travail de lecture approfondie, tant sur le plan mathématique que numérique. Nous considérons ainsi ce chapitre comme une ouverture et un appel à de nouveaux travaux.

Chapter 1

The big picture

The optimization of systems and processes is an exercise that is carried out by an expert taking into account ones experience and domain knowledge. This process is manual, tedious and the results are subjective i.e. even though the improvements registered in the processes/systems are objective, it becomes difficult to ascertain/replicate an objective manner to obtain the optimized results. Here we explore a mathematical approach to different physical problems by utilizing optimization algorithms. The physical problems under consideration belongs to a sub-class of multiphase flows specifically the interfacial flows. These flows involve fluids (liquid and its vapor or gas) that are immiscible and compressible. With the advent of computers and exponential increase of disposable computation power, both the numerical modeling (of the physical problem) and its associated optimization studies have become feasible. Modeling the physical problem is an important process, which has led to the reduction in cost of research while drastically increasing the amount of data generated. This data obtained can now be fed into an optimization algorithm for performing an optimization study.

How are interfacial flows/fluids modeled?

Interfacial flow is a generic term which include a wide spectrum of flows consisting of two or more phases and/or components. Such flows most notably includes immiscible liquids flows, liquid-gas flows among others. Each of these flows have a variety of applications for example oil-water emulsions, atomization process and so on. Interfacial flow through porous media is also one important field of research with application in the field of petroleum extraction, gas-diffusion layer in fuel cells, diffusion of reactants in porous catalyst and so on. It has thus become important to model/replicate these flows and understand their behavior. This is accomplished by models/methods which are based on the governing equation (GE) used for describing the flows. Hence these models are crudely classified by the scale at which the GE describes the flows: microscopic, mesoscopic and macroscopic methods.

Conventionally the macroscopic hydrodynamic models are the most extensively utilized. This is because different macroscopic quantities of systems are of interest. This simulations are generally performed by iteratively solving the discretized form of the Navier-Stokes (NS) equations which are

given as:

$$\frac{\partial \rho}{\partial t} + \nabla \cdot (\rho \boldsymbol{U}) = 0 \tag{1.1}$$

$$\frac{\partial \rho u}{\partial t} + \nabla \cdot (\rho u \boldsymbol{U}) = -\frac{\partial p}{\partial x} + \nabla \cdot (\mu \nabla u) + S_{Mx} \tag{1.2}$$

$$\frac{\partial \rho v}{\partial t} + \nabla \cdot (\rho v \boldsymbol{U}) = -\frac{\partial p}{\partial y} + \nabla \cdot (\mu \nabla v) + S_{My} \tag{1.3}$$

$$\frac{\partial \rho w}{\partial t} + \nabla \cdot (\rho w \boldsymbol{U}) = -\frac{\partial p}{\partial z} + \nabla \cdot (\mu \nabla w) + S_{Mz} \tag{1.4}$$

$$\frac{\partial \rho i}{\partial t} + \nabla \cdot (\rho i \boldsymbol{U}) = -p \nabla \cdot (\boldsymbol{U}) + \nabla \cdot (k \nabla T) + \Phi + S_i \tag{1.5}$$

where u, v, w are the velocity components, i is the total energy, S_{Mx}, S_{My}, S_{Mz} are the momentum source terms, S_i is an energy source term, $\boldsymbol{U}$ is the velocity vector, k is thermal conductivity, p is pressure, Φ is the dissipation function and μ is the dynamic viscosity. The above set of partial differential equations (PDE) is for a compressible Newtonian fluid. And it can be observed that the number of unknowns are greater than the number of equations. This is also known as the closure problem, which necessitates the use of additional equations of state or hypothesis/postulation regarding the state for obtaining a solution. Also the presence of non-linear terms in the momentum and energy conservation equations makes obtaining analytical solutions only possible for certain initial and boundary conditions along with certain assumptions (required for simplifying the initial set of equation). The popular methods/models for interfacial flows/fluids simulations are level-set (LS) [4–7] and volume of fluid (VOF) [8, 9] based on NS equation which require interface tracking, It is observed that these methods are complicated and resource intensive in nature as they require separate interface tracking/construction calculations, apart form solving different set of equations for each individual phase in the flow. This methods describe the dynamic evolutions of few large interface, while the information of numerous tiny-dispersive interfaces is often missed. Some other methods do not require interface tracking/capturing, examples of these methods are the discrete element method [10], algebraic slip model [11] and the Eulerian-Eulerian multiphase model [12]. Now a for porous media simulation the pore network model (PNM) [13, 14] is popular (both for single and multiple phases). Here we simplify the pore structure and thus we have a computationally cheap method. The accuracy of the method depends on the extend of geometry simplification including the exclusion of the smaller pores. Another interesting family of upcoming models for multiphase simulations is the smoothed particle hydrodynamics (SPH) [15–17], while this group of models are computationally expensive they are known for their accuracy.

Conversely, we have molecular dynamics (MD) methods where location and velocities of each microscopic particle is of interest to reproduce the behavior of a particular system. At that scale the macroscopic properties like temperature, viscosity, pressure are not defined. The interactions i.e. collisions between particles are considered to be perfectly elastic, i.e., reversible in nature and the equations describing them are simple to implement. The disadvantage of this method is that it could be used for only understanding phenomena at small scales as it is very resource intensive, also extraordinary amount detail/resolution is not necessary for capturing a macroscopic phenomenon. Ref.[18] is an example of using MD along with multiphase Monte Carlo simulation to simulate CO_2 intercalations in different clay structures. In between the macro and the micro we have the mesoscopic scale, where models like dissipative particle dynamics (DPD) [19] and lattice Boltzmann method (LBM) borrows the advantages from methods of both micro and macroscale. These models accounts for microscopic interactions between particles in a statistical manner, thereby intrinsically generating fluid-fluid and fluid-solid interfaces. The LB equation i.e. Eq.(2.12) is linear in nature because of which the implementation becomes easier. As in MD simulations the microscopic systems are assumed to be reversible in nature but it successfully reproduces the non-linearity and or irreversibility of the macroscopic system. This method is inherently parallel, as during the computationally intensive part of the iteration (collision process) no data transfer is required, thereby

allowing for a speed-up. This makes lattice Boltzmann method a favorable choice for a multiphase simulation and especially for topology optimization, where the physical simulation has to be performed repeatedly. Further detail regarding the various multiphase models in LBM is found in chapter 2. Now while we delineate different methods, we have outliers, like blend of methods i.e. they use some aspects from the other models/methods for e.g. LBM-VOF [20, 21] or LS-VOF [22], also multi-scale simulations [23, 24] both categories of hybrid models will not further elaborated as this is beyond the scope of the thesis. Next, we discuss the various processes/systems where we intend to utilize optimization.

What are the different problems of interest?

The context for the selection of the topic of the thesis was a research interest (of the local team at LTEN, Nantes Université) in proton exchange membrane fuel cell (PEMFC). The PEMFC owing to zero emission, high efficiency and power density is a potential alternative for conventional engines. Though feasible, the technology has issues with respect to cost and durability, thus making its commercialization difficult. Some of the major hurdles in the way are due to lack of choice/cheap catalysts allowing the PEMFC to operate at room temperature, durability and the water management in the fuel cell. This work was initially focused on the water management aspect of the fuel cell. The PEMFC as depicted in Fig.(1.1) has a membrane sandwiched between two catalytic layers which are in turn connected (on the either side) to the corresponding electrodes and gas channels via the Gas Diffusion Layer (GDL). The functions of a GDL are to allow for: diffusion of gas and drainage of product water, along with electrical and thermal conductivity. Liquid water is formed in the catalyst layer (on the oxygen side) and it flows toward the gas flow channels being driven by capillary pressure in opposition to gas diffusion. To prevent choking the gas supply to the catalyst, excess water need to be drained out. At the same time care should be taken to avoid the dehydration of the membrane, as this causes increase in proton resistance, thereby increasing also the heat loss. Thus maximum power output can only be achieved if the necessary balance is maintained.

Generally, the strategy is for the GDL to be coated with hydrophobic material (for e.g. PTFE) either fully or partially to prevent excessive water logging [25]. Though making the surface hydrophobic decreases the water accumulation in the GDL, it does not always corresponds to low impact on the gas diffusion/supply. This is because both the amount and the distribution of water in the porous structure are important [26]. One other strategy is to define the water removal pathways in a GDL, thus ensuring a steady gas supply. In general, hybrid (hydrophilic and hydrophobic) arrangements were shown to have better performance [26]. Similarly [27] performs a review on the scientific strategies for the GDL. Though both these and other strategies are in part effective (as they are undertaken by experts with an engineering and subjective approach), more needs to be understood so as to predict an optimum topology (including the structure of the porous media itself) or an optimum distribution of surface properties for a given topology. This requires an objective mathematical approach which is applicable to the fluid problem at hand.

The optimization algorithm intended to be used is a general method and hence is not limited to the fuel cell, but can be used in similar systems. Another utilization case is to optimize energy systems, especially those having a phase change during the heat transfer like for e.g. a vapor chambers (VC; the VC is a planar heat pipe) and heat pipes [30–32]. These are efficient cooling devices used in HVAC systems and also in consumer electronics. Their efficiency depend on the performance of the internal wicking structure which regulates the flow of the coolant towards the hot region. It is here, where the heat is absorbed during the phase change of the coolant and the evaporated coolant is convected towards the cold region. Here again the wick structure and its wettability profile are good candidates for optimization. Figure 1.2 shows the schematic visualizations for both vapor chambers and heat pipes. Another field of interest is the wettability gradient surface (WGS) which in turn could be used in micro-systems like the lab-on-chip (LOC) and other heat exchanging surfaces like the condenser and the evaporator. A detailed commentary on its importance along with its subsequent optimization can be found in chapter 4.

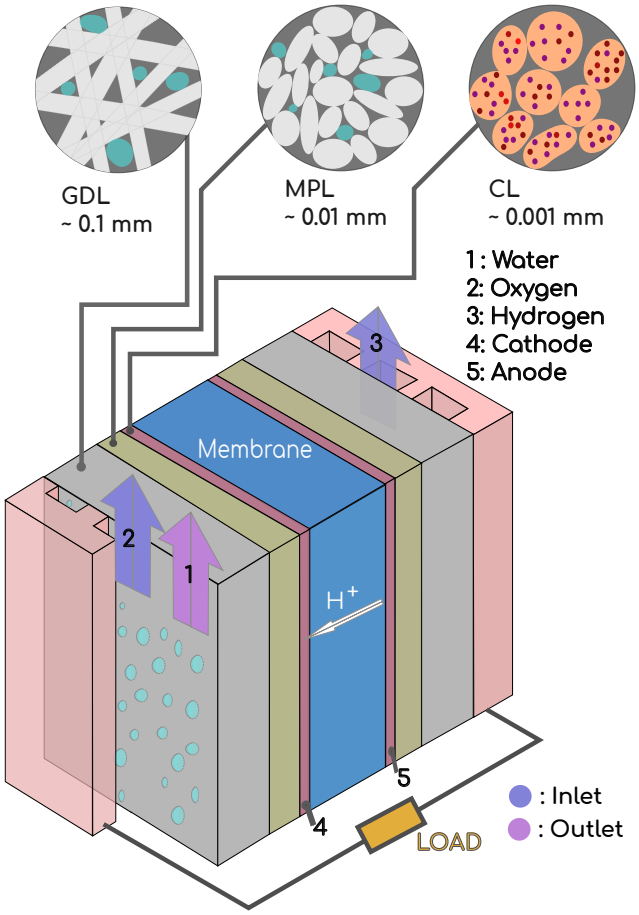

Figure 1.1: Axis-symmetric schematic view of a PEMFC

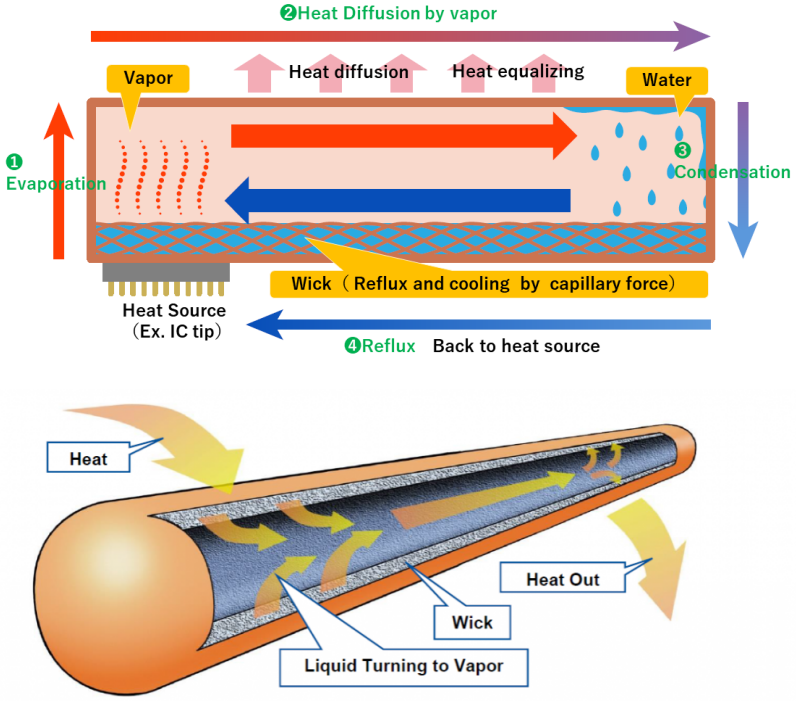

Figure 1.2: Schematic diagrams of vapour chamber (from [28]) and heat pipe (from [29])

What are optimization algorithms?

An optimization algorithm refers to the mathematical procedure/treatment which reflects certain strategies to arrive towards an ideal/optimal system or an efficient process. Optimization or mathematical programming is a broad subject engulfing a variety of applications from logistics to machine learning and numerical simulation. The optimization algorithms can be categorized in two ways: the former is the gradient free optimization methods and later is the gradient based optimization. The gradient free optimization also known as zero-order optimization consists of deterministic methods like simplex [33, 34] or stochastic methods like particle swarm optimization (PSO) [35] and genetic algorithm (GA) [36]. A recent example of genetic algorithm [37] was utilized for performing the topology optimization. These methods are put to use when the cost function gradients are difficult to compute or does not exists [38]. Conversely the gradient optimization requires the cost function gradient which is further classified into first, intermediate (between 1^{st} and 2^{nd}) and second order methods. We utilize only the first order gradient methods in the thesis. Further information regarding the different gradient optimizers i.e. methods or algorithm is detailed in chapter 3.

When optimization is applied to obtain change in the geometric aspect of the system depending on the parameter set (after the geometry is parameterized) it becomes possible for categorizing optimization into three groups: size optimization, shape optimization and topology optimization [39, 40]. Figure 1.3 visualizes the parameter set (in orange) for each kind of optimization. In size optimization [41] the parameter set has usually a single variable which if optimized gives us the minimum of the cost function. In shape optimization [42] the parameter set is the topology of the surface which could be modified to minimize the cost function. The topology optimization on the other hand has the most extensive parameter-set i.e. equivalent of the number of the individual nodes/elements of the mesh (used for modeling the physical problem) in the region of interest. This provides it with sufficient degree of freedom to create holes, structures (when starting from no initial solid structures). Essentially it becomes a material allocation problem [40]. We discuss a brief history of topology optimization in chapter 3, after which we perform a state of the art for topology optimization in interfacial flows in chapter 5.

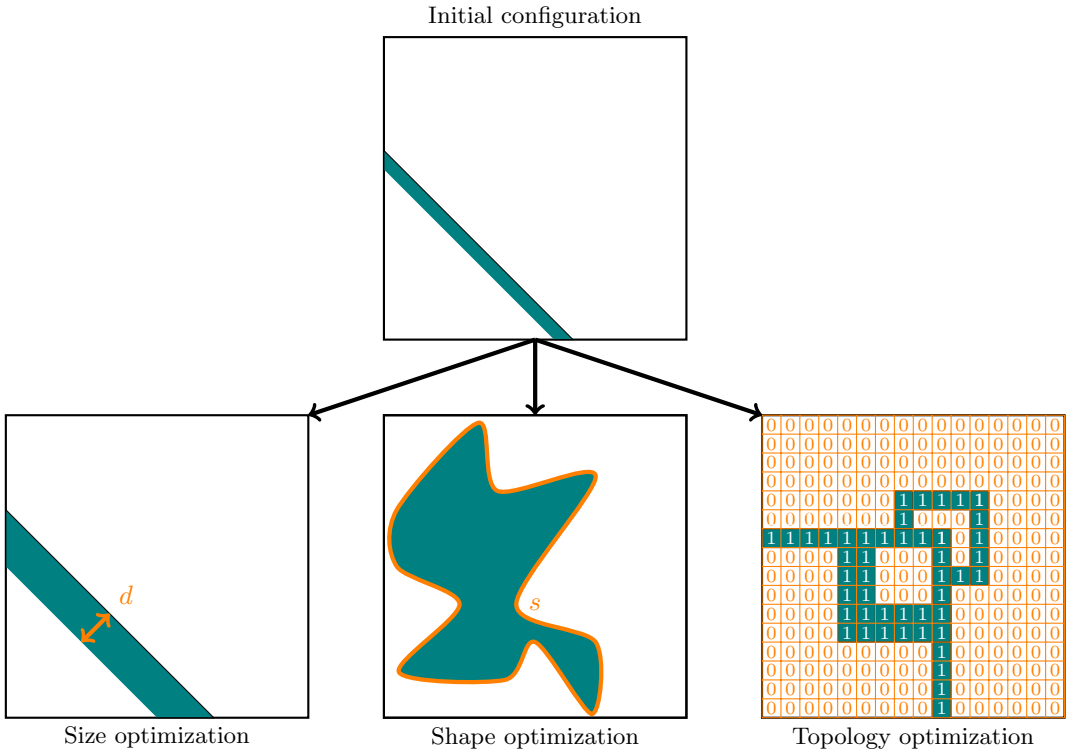

Figure 1.3: The different types of optimization (from [40])

Objectives and contribution of this thesis

Here the primary objective is to modify the flow characteristics by adjusting/ tweaking the capillary forces. This necessitates the development an optimization tool for topology optimization in interfacial flows such that we are:

1. Finding an optimum porous media or wick structure (which has a homogeneous wettability profile) such that the relevant cost function is minimized.
2. Finding an optimum wettability profile for a particular topology (porous media or wick structure) such that the objective function is minimized.

Briefly, the contributions of this thesis are:

1. Using multiscale optimizer for discovering optimized wettability profiles of a horizontal plate (for droplet motion on the plate) i.e. a WGS.
2. Developing wettability optimizer, using adjoint-state model for SCMP-SC.
3. Developing topology optimizer, using adjoint-state model for SCMP-SC.

Overview of the thesis

In chapter 2, we began by discussing the different facets of LBM methods (including the boundary conditions). Next we explore different multiphase LBM models families. After which we provide a detailed description of the SCMP-SC model used along with its modifications and extension. This discussion is completed by detailing the parameters used in the SCMP-SC model. The proposed model undergoes the process of validation before it could be deemed fit for use in an optimization algorithm. Multiple test/benchmark simulations are attempted such as the: Laplace rule, droplet moving on a flat plate, capillary simulation, simulations with open boundaries (normal tube, stepped tube, droplet flowing through a channel, preferential pathways and finally the porous media simulations). The results of each tests are discussed and conclusions (pertaining to the competence of the LBM model, the nature of the optimization problem feasible for SCMP-SC and etc...) are drawn.

Chapter 3 is commenced by a brief introduction to topology optimization history, followed by a discussion regarding different components (i.e. adjoint-state, level-set, gradient descent optimizer and etc...) used in the gradient based topology optimization. Next we present the LBM governing equation and derive the adjoint-state governing equation, initial conditions and later also the boundary conditions (from the LBM boundary conditions). Finally we demonstrate topology optimization for single phase flow problem by applying it to a 90° pipe bend. After discussing the results we conclude this chapter. This chapter is only a prelude for chapter 5.

In chapter 4 we diverge from the topology optimization narrative and only focus on optimization of wettability profiles for droplet motion on WGS. After describing the problem and commenting on the state of the art for efforts in optimization of a WGS, we describe our optimization strategy i.e. the multiscale method, the definition of the objective function and etc.... Next we set constraint values using the pre-optimization study. This aids in reducing the search area for the minimum cost function. Next we perform the multiscale optimization and retrieve some optimized profiles. This result are further discussed and analyzed using the post-optimization studies. Finally various implications of this study are discussed and then we draw a few conclusions.

In chapter 5 we return back to the topology optimization narrative. Here after discussing the state of the art for topology optimization in interfacial flows, we derive the adjoint-state model for the SCMP-SC (for topology optimization). Next we develop an adjoint-state model for wettability profile optimization. Finally, we draw our conclusion.

Ultimately, we reiterate the relevant bits of the narrative and highlight our conclusions of the thesis.

Chapter 2

Interfacial flows with LBM

Lattice Boltzmann Method (LBM) is amongst the recent advances in CFD with successful implementation in disciplines requiring simulation of multiphase flows [43] (for e.g. biology[44], pharmacy, oil and gas industry[45]), reacting flows (chemical industry) and flows around complex geometry like porous media[46, 47]. LBM tries to reproduce a particular phenomenon at a macroscopic scale by considering particles interactions at mesoscopic scale, rather than solving the relevant (macroscopic) governing partial differential equations. The mesoscopic particle interaction is governed by the Boltzmann equation. The Chapmann-Enskog theory/analysis [48] demonstrates that under certain assumptions one recovers the Navier-Stokes equations which implies that the lattice Boltzmann method is competent in replicating/modeling real world fluid/flow systems.

Lattice Boltzmann method first appeared in the 80's as the successor of Lattice Gas Automata (LGA) method. LGA could also be used for hydrodynamic simulations, but this method generated a lot of numerical noise. This meant that large amounts of time and space averaging was required for obtaining a proper macroscopic flow field [49]. This was one of the major factors leading to the loss of interest in further development of LGA after LBM was proposed and implemented successfully. Nevertheless, LBM and LGA have a similar hydrodynamic behavior. So, LBM is noise free apart from being inherently parallel in nature, easy to numerically implement also the scheme generally used is an explicit one (having a decent accuracy) which makes it a strong contender for multiphase simulation. The lattice Boltzmann method operates in a mesoscopic realm and hence we would utilize different frameworks for units, as is detailed in appendix C.

2.1. Boltzmann equation

The Boltzmann equation describes the evolution of a single particle distribution function as a gas relaxes towards an equilibrium state from an initial perturbation. The single particle (probability) distribution function is denoted as $f(\boldsymbol{r},\boldsymbol{e},t)$ and is defined such that $f(\boldsymbol{r},\boldsymbol{e},t)\,\mathrm{d}^3\boldsymbol{r}\,\mathrm{d}^3\boldsymbol{e}$ is the probability to find a particle which at time t are located in the phase space control element $\mathrm{d}^3\boldsymbol{r}\,\mathrm{d}^3\boldsymbol{e}$ about a location $\boldsymbol{r}$ (here the location is defined by using a vector $\boldsymbol{r} = r_x\hat{i}+r_y\hat{j}+r_z\hat{k}$) and having a velocity $\boldsymbol{e}$ [50]. The distribution function f has 6 DOF (i.e. the Cartesian co-ordinates x,y,z with the corresponding velocity components u,v,w) and also varies with time. Thus total/absolute change in time of this function can be expressed as:

$$\frac{\mathrm{d}f}{\mathrm{d}t} = \boldsymbol{e}\frac{\partial f}{\partial \boldsymbol{r}} + \boldsymbol{a}\frac{\partial f}{\partial \boldsymbol{e}} + \frac{\partial f}{\partial t} \tag{2.1}$$

where $\boldsymbol{a}$ is acceleration of the fluid. This change corresponds to the collisions (and hence the exchange of momentum) between the constituent particles of the gas amongst themselves and also with its surrounding. This change represented by Boltzmann in the form of a collision operator (Λ).

Hence the Boltzmann equation can be written in a general form as:

$$\boldsymbol{e}\frac{\partial f}{\partial \boldsymbol{r}} + \boldsymbol{a}\frac{\partial f}{\partial \boldsymbol{e}} + \frac{\partial f}{\partial t} = \Lambda \tag{2.2}$$

2.1.1. Discretization for obtaining LBM

The lattice Boltzmann equation (LBE) is obtained by discretizing the Boltzmann equation in space and in velocity (both direction and magnitude). The velocity discretization is such that individual particle site is connected to its neighboring particle sites, in a manner ensuring isotropy of moments. The nomenclature to specify a particular velocity discretization is DxQy where x is the spatial dimension (1, 2, 3) of the problem and y is the number of velocity directions considered including the zero velocity. Generally used two dimensional velocity discretizations are D2Q4, D2Q5 and D2Q9. The most popular stencil for realizing advection problems in 2D is the D2Q9 stencil, due to higher degree of isotropy as compared to D2Q4 and D2Q5.

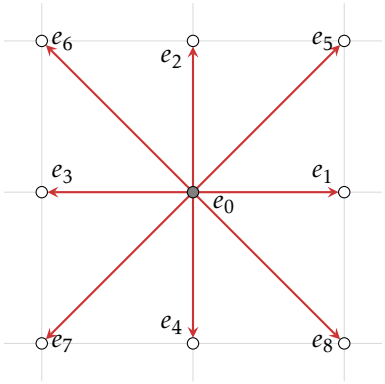

Figure 2.1: D2Q9 stencil

After discretizing eq. (2.2), LBE can be given in a general form for the i^{th} direction as:

$$f_i(\boldsymbol{r} + \Delta\boldsymbol{r}, t + \Delta t) - f_i(\boldsymbol{r}, t) = \Lambda_i + \mathscr{F}_i \tag{2.3}$$

where $\mathscr{F}_i$ is an external force term acting on the fluid. Since the distribution function is now only dependent on $\boldsymbol{r}$ and t for a particular velocity direction, therefore it is known as velocity distribution function denoted as $f(\boldsymbol{r}, t)$. Also LBE is the discretized form of the Boltzmann equation and hence the macroscopic values can now be retrieved as:

Definition 2.1.1.

$$\rho = \sum_i f_i \tag{2.4}$$

$$\rho\boldsymbol{u} = \sum_i \boldsymbol{e}_i f_i \tag{2.5}$$

Please note that these macroscopic quantities are recovered in the mesoscopic realm and hence are quantified in lattice Boltzmann units (as discussed in appendix C).

The D2Q9 stencil was used for all the simulations. Generally for LBM a structured grid is used along with finite difference method (FDM) for mesh discretization. Note that there is an additional velocity discretization. In other words the total computational mesh is the number of velocity directions (i.e. 9) times the actual geometry mesh. For simplicity, consider the lattice spacing $\Delta r_x = 1$ l.u. (lattice unit), $\Delta r_y = 1$ l.u. and time stepping(Δt) to be 1 t.s. (lattice Boltzmann time). Thus the lattice speed e is 1 l.u./t.s. and the velocity of sound (e_s) for D2Q9 is given as:

$$e_s = \frac{\|\boldsymbol{e}_1\|}{\sqrt{3}} = \frac{1}{\sqrt{3}} = 0.577 \text{ l.u./t.s.} \tag{2.6}$$

The location/distance vector for the D2Q9 stencil is given as:

$$|\boldsymbol{r}_i| = \begin{cases} 0 \text{ l.u.} & \forall\ i\ \in [0] \\ 1 \text{ l.u.} & \forall\ i\ \in [1,2,3,4] \\ \sqrt{2} \text{ l.u.} & \forall\ i\ \in [5,6,7,8] \end{cases} \tag{2.7}$$

The lattice Boltzmann method is implemented in steps sequentially starting from collision, where we solve for an i^{th} direction:

$$f_i^{\text{pc}}(\boldsymbol{r},t) = f_i^{(k)}(\boldsymbol{r},t) + \Lambda_i^{(k)} + \mathscr{F}_i^{(k)} \tag{2.8}$$

where k represents the current LBM iteration and 'pc' represents intermediary time which (has no physical sense but rather) indicates that the computational process of an iteration has not been completed. After this we stream the data to the new location $(\boldsymbol{r}+\Delta\boldsymbol{r})$ for the new time $(t+\Delta t)$ which represented by next iteration $k+1$. This is represented by (for an i^{th} direction):

$$f_i^{(k+1)}(\boldsymbol{r}+\Delta\boldsymbol{r}, t+\Delta t) = f_i^{\text{pc}}(\boldsymbol{r},t) \tag{2.9}$$

Later the iteration is completed by implementing the boundary conditions applicable and ultimately by computing macroscopic variables by using eq. (2.4) and eq. (2.5). In the following subsections, we discuss regarding these components of the LBM implementation and later provide an algorithm algorithm 1 for a multiphase LBM code of our choice.

2.1.2. Collision operator

For defining the manner of change in distribution function with respect to (w.r.t) time due to collision it is worth noting that:

- Boltzmann only took into account binary collisions, since for a dilute gas the probability of ternary or higher order collision occurring is negligible.
- Velocity of the particles was assumed not dependent on its position.

Thus the R.H.S. of eq. (2.2) is expressed as a binary collision operator which is given as[50]:

$$\Lambda = \left(\frac{\partial f}{\partial t}\right)_{\text{coll}} = \int d\Omega_o \int d\boldsymbol{e}_2\ \sigma_h(\Omega_o)|\boldsymbol{e}_1 - \boldsymbol{e}_2|(\check{f}_1\check{f}_2 - f_1 f_2) \tag{2.10}$$

where 1 and 2 represents interacting particles in no particular order, Ω_o is the scattering angle of the binary collision, σ_h is the differential cross-section of this collision, while $\check{f}$ and f are distribution function after and before collision and are numbered w.r.t the corresponding velocities. Here the collision operator is integrated for all possible values of $\boldsymbol{e}_2$ for a fixed value of $\boldsymbol{e}_1$. Thus the Boltzmann equation essentially became an integro-differential equation which was non-linear in nature. This complicates the process to numerically solve the equation. Hence it is approximated using different collision operators like the BGK/SRT [51], MRT [52, 53] and TRT [54] amongst others. Also entropic lattice Boltzmann models [55] provides an alternative paradigm which reorganizes the relaxation collision operator. These models are used sparingly due to their complexity. Further we only elaborate on the approximations used for simulations referred to in the thesis.

2.1.2.a. Single relaxation time (SRT) model

This scheme employs a linear term to approximate the collision operator. It was proposed by [51] and has thereafter been popular for simulations due to its simplicity as it uses a single relaxation time (τ) parameter. The collision operator is given as:

$$\Lambda_{\text{BGK}} = -\frac{f - f^{\text{eq}}}{\tau} \tag{2.11}$$

where f^{eq} denotes the equilibrium distribution function. Substituting Λ_{BGK} and $\omega = (\Delta t)\tau^{-1}$ in eq. (2.3) and rearranging the equation yields:

$$f_i(\boldsymbol{r} + \Delta\boldsymbol{r}, t + \Delta t) = \omega f_i^{\mathrm{eq}}(\boldsymbol{r}, t) + (1 - \omega) f_i(\boldsymbol{r}, t) + \mathscr{F}_i \tag{2.12}$$

which is the standard equation for the SRT model also known as the LBGK model.

Meanwhile, for a two dimensional advection-diffusion problem it can be derived that:

$$f_i^{\mathrm{eq}} = w_i \rho \left(1 + \frac{\boldsymbol{e}_i \cdot \boldsymbol{u}}{e_s^2} + \frac{(\boldsymbol{e}_i \cdot \boldsymbol{u})^2}{2e_s^4} - \frac{(\boldsymbol{u})^2}{2e_s^2}\right) \tag{2.13}$$

where the weight function (w_i) is dependent on $\boldsymbol{e}_i$ and can be given as:

$$w_i = \begin{cases} 4/9 & \forall\ i\ \in [0] \\ 1/9 & \forall\ i\ \in [1,2,3,4] \\ 1/36 & \forall\ i\ \in [5,6,7,8] \end{cases} \tag{2.14}$$

The equilibrium distribution function is essentially a truncated Hermite expansion of the Maxwellian equilibrium distribution [56].

Also for hydrodynamic simulations on D2Q9, the relation between the kinematic viscosity (ν) and the relaxation time can be given as:

$$\nu = \frac{\Delta x^2}{3\Delta t}(\tau - 0.5) \tag{2.15}$$

As previous mentioned $\Delta r_x = \Delta r_y = \Delta t = 1$ and $\omega = \dfrac{\Delta t}{\tau}$. Thus, we can rephrase the same equation as shown below:

$$\tau = 3\nu + 0.5 \tag{2.16}$$

It is worth noting that the scheme loses stability, when $\tau \to 0.5$. The relaxation time is the numerical equivalent of any diffusivity coefficient for the corresponding transport equation for example: heat diffusivity coefficient and viscosity for heat conduction and fluid flow respectively. For the errors to be negligible while using the formulation of LBM with BGK approximation, the macroscopic velocity $\boldsymbol{u}$ defined for the simulation should very small as compared to the lattice speed of sound e_s. The macroscopic velocity should be chosen such that for a particular geometric configuration the velocity at all points in the domain is well below e_s.

2.1.2.b. Multiple relaxation time (MRT) model

Here collision occurs in the moment space and not in the distribution function space. The uses of this model increases stability and can be tuned also for greater accuracy. This collision operator allows for independent adjustment of bulk and kinematic viscosity [57]. This model slightly slower than BGK but is more accurate. The collision operator is given by:

$$\Lambda_{\mathrm{MRT}} = -\mathbf{M}^{-1}\mathbf{S}(\mathbf{m} - \mathbf{m}^{\mathrm{eq}}) \tag{2.17}$$

where $\mathbf{m} = \mathbf{M} \cdot f$, $\mathbf{m}^{\mathrm{eq}} = \mathbf{M} \cdot f^{\mathrm{eq}}$ and for D2Q9

$$\mathbf{M} = \begin{bmatrix} 1 & 1 & 1 & 1 & 1 & 1 & 1 & 1 & 1 \\ -4 & -1 & -1 & -1 & -1 & 2 & 2 & 2 & 2 \\ 4 & -2 & -2 & -2 & -2 & 1 & 1 & 1 & 1 \\ 0 & 1 & 0 & -1 & 0 & 1 & -1 & -1 & 1 \\ 0 & -2 & 0 & 2 & 0 & 1 & -1 & -1 & 1 \\ 0 & 0 & 1 & 0 & -1 & 1 & 1 & -1 & -1 \\ 0 & 0 & -2 & 0 & 2 & 1 & 1 & -1 & -1 \\ 0 & 1 & -1 & 1 & -1 & 0 & 0 & 0 & 0 \\ 0 & 0 & 0 & 0 & 0 & 1 & -1 & 1 & -1 \end{bmatrix} \quad \text{and}$$

$$\mathbf{S} = \mathrm{diag}\begin{bmatrix} \omega_1 & \omega_2 & \omega_3 & \omega_4 & \omega_5 & \omega_6 & \omega_7 & \omega_8 & \omega_9 \end{bmatrix}$$

The matrix $\mathbf{S}$ in this case is a 9×9 diagonal relaxation matrix in which ω_8 and ω_9 are related to the kinematic viscosity as shown in eq. (2.15), while ω_2 is related to the bulk viscosity of the fluid. It is also required that $\omega_1 = \omega_4 = \omega_6$ and $\omega_5 = \omega_7$. Hence we can tune ω_1, ω_2, ω_3, ω_5 and ω_8 for greater accuracy and stability. For all the simulations using this collision operator we specify $\mathbf{S}$ as:

$$\mathbf{S} = \mathrm{diag}\begin{bmatrix} 1.0 & 0.7 & 0.7 & 1.0 & 1.7 & 1.0 & 1.7 & 1.0 & 1.0 \end{bmatrix}$$

This values were determined by trail and error such minimum spurious currents were generated in the droplet simulation. Also, the f^{eq} term in eq. (2.17) is described by eq. (2.13). Substituting Λ_{MRT} and rearranging the equation yields:

$$f_i(\boldsymbol{r} + \Delta\boldsymbol{r}, t + \Delta t) = f_i(\boldsymbol{r}, t) - \mathbf{M}^{-1}\mathbf{S}(\mathbf{m} - \mathbf{m}^{\mathrm{eq}}) + \mathscr{F}_i \tag{2.18}$$

It is to be noted that the use of Λ_{MRT} might modify the structure/formulation of $\mathscr{F}$ depending on the force incorporation method used.

2.1.3. Streaming

This step of the LBM algorithm involves purely the transfer of data. In an otherwise inherently parallel calculation or code especially for single phase LBM, this step creates bottlenecks and is hence often decoupled from the computationally intensive collision step. As we perform this step/process after the collision but the time-step calculation remains (i.e. the current streaming step and the application of the boundary conditions), it is a common practice to refer to this processes/steps as happening in post-collision time. These processes are tagged as 'pc' i.e. post-collision. Here the post-collision values/data are rearranged/streamed to the neighboring nodes in the direction of the particle velocity components. The implementation (in two dimensions) differs depending on whether one is finding the correct location i.e. the destination to write data, where $(\boldsymbol{r} + \Delta\boldsymbol{r})$ for the i^{th} velocity component is given as:

$$(r_x + \Delta r_{i,x})\big|_{t=z+\Delta t} = (r_x\big|_{t=z} + \boldsymbol{e}_{i,x} + \mathscr{N}_x) \bmod (\mathscr{N}_x) \tag{2.19}$$

$$(r_y + \Delta r_{i,y})\big|_{t=z+\Delta t} = (r_y\big|_{t=z} + \boldsymbol{e}_{i,y} + \mathscr{N}_y) \bmod (\mathscr{N}_y) \tag{2.20}$$

(at time $t = z$), OR, whether one is finding the source location to read from the data, where $(\boldsymbol{r} + \Delta\boldsymbol{r})$ for the i^{th} velocity component is given as:

$$(r_x + \Delta r_{i,x})\big|_{t=z} = (r_x\big|_{t=z+\Delta t} - \boldsymbol{e}_{i,x} + \mathscr{N}_x) \bmod (\mathscr{N}_x) \tag{2.21}$$

$$(r_y + \Delta r_{i,y})\big|_{t=z} = (r_y\big|_{t=z+\Delta t} - \boldsymbol{e}_{i,y} + \mathscr{N}_y) \bmod (\mathscr{N}_y) \tag{2.22}$$

where $\boldsymbol{e}_{i,x}$ and $\boldsymbol{e}_{i,y}$ are the x and y components of the i^{th} particle velocity, $\Delta r_{i,x}$ and $\Delta r_{i,y}$ are the corresponding changes to the location vector (for the i^{th} direction) and where the domain length along the x and y direction are the $\mathscr{N}_x$ and $\mathscr{N}_y$ and the domain size is given as $\mathscr{N}_x \times \mathscr{N}_y$. The difference between the two implementations of streaming (as shown schematically in fig. 2.2) is that writing data at one location is computationally cheaper even though the same process is accomplished. By default both these implementation enforces periodicity in the domain, more about which is discussed later in section 2.1.4.a.

2.1.4. Boundary conditions (BC)

The boundary conditions for LBM are generally simple for numerical implementations but are at the same time not straight forward, as the implementation focuses on the mesoscopic scale details. The goal of a boundary condition is to find the unknown distribution function along the directions which are extending inward into the fluid region form the domain or solid boundaries.

There are various different methods for applying each type of boundary condition and hence an exhaustive listing is not possible. Comparative studies [58, 59] have been performed for outlet

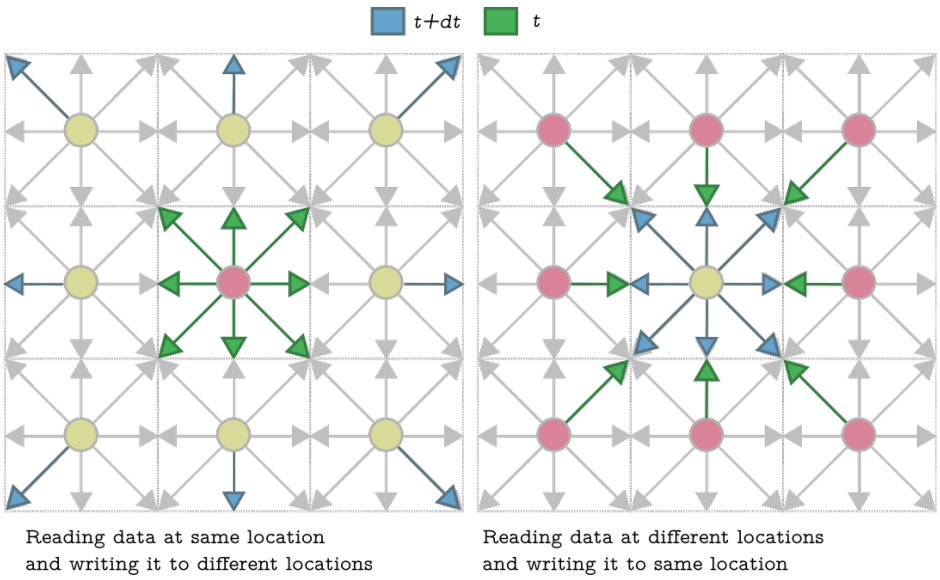

Figure 2.2: Implementation difference in the streaming process for LBM

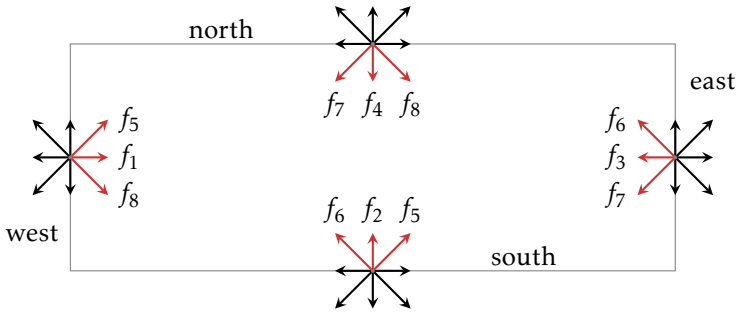

Figure 2.3: Unknown distribution functions at boundaries

boundary conditions for multiphase flows, which is the primary focus of this work. In all the boundary conditions that were employed for simulations were wall (bounceback), velocity inlet, pressure outlet, Neumann conditions and periodic boundary conditions. It is to be noted that while using any of the open boundary conditions like extrapolation boundary conditions (EBC), Neumann boundary condition (NBC), convective boundary condition (CBC) or Zou and He (ZH) for pseudopotential model we require ghost nodes for finding $\nabla\psi$ in the interparticle force formulation i.e. eq. (2.65).

2.1.4.a. Periodic BC

The implementation of this boundary condition requires that the distribution functions exiting from one boundary be fed as an input on the opposite boundary. Thus for a 2D domain if we have only periodic boundaries, then the domain would be interconnected like a torus. The periodic boundary conditions on the western and eastern boundaries (refer fig. 2.3) are given as:

$$f_i(r_x = 1, r_y, t + \Delta t) = f_i^{\text{pc}}(r_x = \mathcal{N}_x, r_y, t) \quad \forall\ i \in [1, 5, 8] \tag{2.23}$$

and

$$f_i(r_x = \mathcal{N}_x, r_y, t + \Delta t) = f_i^{\text{pc}}(r_x = 1, r_y, t) \quad \forall\ i \in [3, 6, 7] \tag{2.24}$$

Thus the fluid exiting form east would enter through the west and vice-versa. Hence mass and momentum is always conserved.

2.1.4.b. *Ghost nodes*

This are special set of nodes required in the Shan and Chen multiphase paradigm (this model is described later in section 2.2.3) for satisfying the requirement of neighboring nodes. These neighboring nodes are used for constructing a gradient of pseudopotential ($\nabla_r \psi$). Generally one ghost node layer is sufficient until and unless the multirange model is used. This has an effect of breaking the *periodicity* of the domain. Hence it is useful for implementing open boundary conditions amongst other things. For Shan and Chen multiphase model is sufficient to only copy the density of the adjacent layer i.e. no collision or streaming steps are required for these nodes. If we had ghost nodes present on the east boundary (refer fig. 2.3) then, we could write:

$$\rho(r_x = \mathcal{N}_x, r_y) = \rho(r_x = \mathcal{N}_x - 1, r_y) \tag{2.25}$$

Ghost node is also used amongst other multiphase LBM models. Some methods require streaming of probability distribution function also. For SCMP-SC model this streaming is not required. Also when used in tandem with open boundary a force imbalance (normal to the boundary) at the boundary by using information from the penultimate layer rather than the ultimate layer (which is adjacent to the Ghost nodes/layer). Thus for the eastern boundary (refer fig. 2.3) we write:

$$\rho(r_x = \mathcal{N}_x, r_y) = \rho(r_x = \mathcal{N}_x - 2, r_y) \tag{2.26}$$

Generally though, this force imbalance is negligible unless the interface touches the boundary. The literature [3, 58], also suggests ghost node (for those adjacent to the outflow boundary) treatment which is dependent on the outflow boundary formulation, where the data is streamed into the ghost node.

2.1.4.c. *Wall BC*

Here, the wall boundary condition for LBM is categorized on the basis of the mesh type on which the boundary condition is applied i.e. using Lagrangian or Eulerian mesh [48]. One can specify conditions for curved wall [60], moving wall [61] and deformable/soft wall [62, 63] (for e.g. Immersed boundary condition). Here we only detail about fullway and halfway bounceback BC.

2.1.4.c.1. *Simple Bounceback (BB)*

The BB is the simplest implementation of a no-slip wall. Two different variants of the BB conditions have been utilized for the simulations i.e. the fullway BB and the halfway BB (refer fig. 2.4). It is to be noted that the position of the wall for both this variants are approximately midway between the solid and the fluid node. The exact location of the wall depends on relaxation time in the case of Λ_{BGK} and this limitation could be circumvented by the use of Λ_{MRT} or Λ_{TRT} [48]. The bounceback is second order accurate for the straight boundaries and at low Reynolds number. For both variants used here the staircase effect is observed for the inclined and the curved boundaries.

The fullway BB allows for information to be streamed into the solid nodes where BB is applied for all the velocity direction. Hence this can be used for walls of any orientation and the BB is implemented as (on solid nodes) and for new time step ($t + \Delta t$):

$$f_i(r_x, r_y, t + \Delta t) = f_{\bar{i}}(r_x, r_y, t + \Delta t) \quad \forall\ i \in [0, 1, 2, 3, 4, 5, 6, 7, 8] \tag{2.27}$$

where $\bar{i} = [\bar{0}, \bar{1}, \bar{2}, \bar{3}, \bar{4}, \bar{5}, \bar{6}, \bar{7}, \bar{8}] = [0, 3, 4, 1, 2, 7, 8, 5, 6]$. And this data is then streamed to the fluid domain at the next iteration.

The halfway BB on the other hand allows no information to be streamed into the solid nodes, performing BB only for the velocity directions from the solid. This allows BB to be applied to very thin or a zero node thick solid wall. This is a direction based boundary condition but can be implemented in the streaming step in a general fashion using if statements to check whether

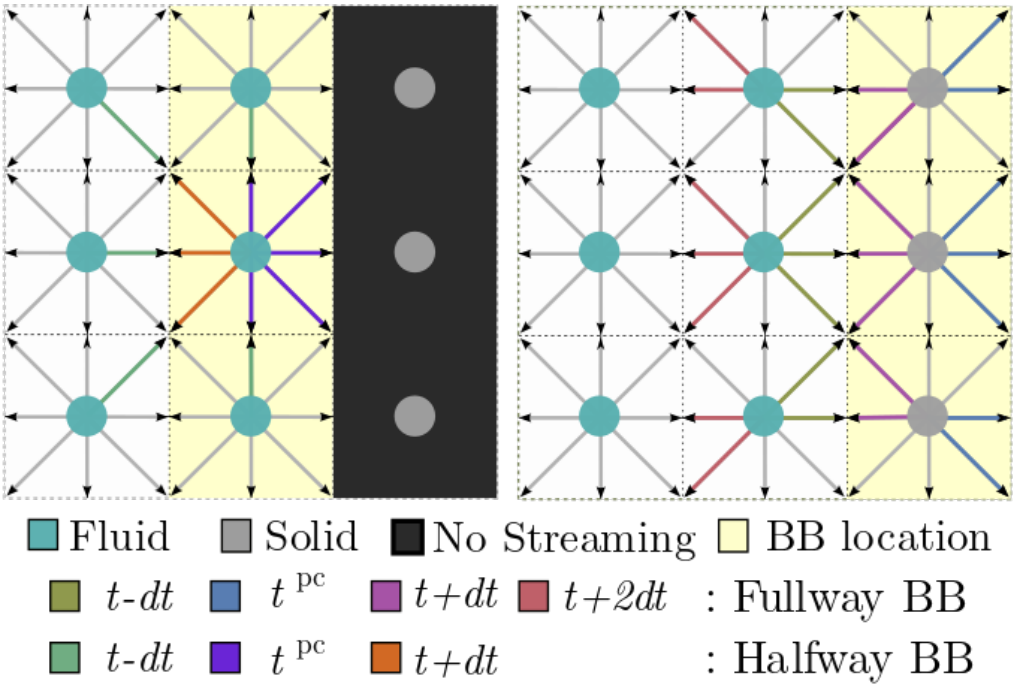

Figure 2.4: Data streaming for halfway and fullway BB. (Schematic diagram)

each link ends up on solid or fluid nodes [48], which is used in the code. The more traditional implementation for a wall on the east (on fluid nodes) and for new time step $(t + \Delta t)$:

$$f_i(r_x, r_y, t + \Delta t) = f_{\bar{i}}^{\text{pc}}(r_x, r_y, t) \quad \forall\ i \in [3, 6, 7] \tag{2.28}$$

where f_i^{pc} is the distribution function post collision (but before streaming). Thus we can notice that time it takes for particle information to return to bulk is Δt and $2\Delta t$ for halfway and fullway BB respectively. Hence halfway BB is said to have higher temporal accuracy.

2.1.4.d. Open BC

Many different schemes have been proposed for the closure of equations in LBM. The list mentioned here is by no means extensive. Only a fraction of this proposed solutions are applicable and for a multiphase simulation. For multiphase LBM models generally, ghost node layers are required in tandem with open boundaries.

2.1.4.d.1. Ladd velocity BC

The Ladd velocity [64] boundary condition is a simple modification to the standard BB boundary condition. For this boundary condition, the density and the velocity of the fluid at the boundary is required. The modification or rather a correction term accounts for the momentum gained by the fluid in the vicinity of the boundary. For a velocity inlet at the north (refer fig. 2.3), on the top-most layer of fluid nodes:

$$f_i(r_x, r_y, t + \Delta t) = f_{\bar{i}}^{\text{pc}}(r_x, r_y, t) - 2w_{\bar{i}}\rho(r_x, r_y, t)\frac{\boldsymbol{u}(r_x, r_y, t) \cdot \boldsymbol{e}_{\bar{i}}}{e_s^2} \quad \forall\ i \in [4, 8, 7] \tag{2.29}$$

2.1.4.d.2. Zou and He (ZH)

This boundary condition was proposed by [65] and has been thereafter used widely. Here, the equality of the non-equilibrium part of the distribution functions normal to the boundary is as-

sumed while solving for the unknown distribution functions apart from eq. (2.4) and eq. (2.5). The final set of equations is arrived upon by algebraic manipulation. Thus for the velocity inlet at the north (refer fig. 2.3) we specify u_x, u_y and find ρ and other unknown distribution functions as:

$$\rho = \frac{f_0 + f_1 + f_3 + 2(f_2 + f_5 + f_6)}{1 + u_y} \tag{2.30}$$

$$f_4 = f_2 - \frac{2}{3}\rho u_y \tag{2.31}$$

$$f_8 = f_6 - \frac{1}{2}(f_1 - f_3) - \frac{1}{6}\rho u_y + \frac{1}{2}\rho u_x \tag{2.32}$$

$$f_7 = f_5 + \frac{1}{2}(f_1 - f_3) - \frac{1}{6}\rho u_y - \frac{1}{2}\rho u_x \tag{2.33}$$

Similarly for the pressure inlet at north we would specify $u_x = 0$ (if value is unknown), ρ and later use eq. (2.30) for finding u_y. It is to be noted that the values to be specified in either case are constants. This may make it unfavorable for use when mass flux across the boundary is multiphase in nature especially for single component multiphase flows defined by a single distribution function.

Due to the above mentioned limitation, generally this boundary condition is not used as a pressure outlet when multiphase flow exit is expected.

2.1.4.d.3. Extrapolation scheme (EBC)

This method of specifying the boundary condition is dependent on the boundary normal. Here the unknown distribution functions at the outlet boundary is given by performing extrapolation upstream. Hence an outlet to the south (refer fig. 2.3) is given as:

$$f_i(r_x, r_y = 1) = 2f_i(r_x, r_y = 2) - f_i(r_x, r_y = 3) \quad \forall\ i \in [2, 5, 6] \tag{2.34}$$

This method was observed to least accurately simulate the exit for the droplet in a channel [58] and a stable result has not been yet obtained for our study.

2.1.4.d.4. Neumann boundary condition (NBC)

This boundary condition requires that no change should be observed in the quantities of interest as mass flux occurs across the boundary. In other words no significant effects in the domain should occur due to the presence of the boundary itself. This in mathematical form is given by:

$$\frac{\partial \chi}{\partial \boldsymbol{n}} = 0 \tag{2.35}$$

where χ represents the relevant quantity; in our case mostly (but not solely) f, $\boldsymbol{n}$ is the normal to the boundary. This equation is simply discretized (for the southern outlet refer fig. 2.3) and the distribution function values at the new time step $(t + \Delta t)$ are given by:

$$f_i(r_x, r_y = 1, t + \Delta t) = f_i(r_x, r_y = 2, t + \Delta t) \quad \forall\ i \in [0, 1, 2, 3, 4, 5, 6, 7, 8] \tag{2.36}$$

2.1.4.d.5. Convective boundary condition (CBC)

Here we utilize a convective equation to approximate the quantities of interest, rather than simply setting the directional derivatives to be zero as in eq. (2.35). This makes it computationally expensive as compared to the NBC but overall produces better results [58, 59]. In mathematical form this is given by:

$$\frac{\partial \chi}{\partial t} + \boldsymbol{U} \cdot \frac{\partial \chi}{\partial \boldsymbol{n}} = 0 \tag{2.37}$$

where $\boldsymbol{U}$ is the velocity of fluid. For a southern boundary (refer fig. 2.3) for all quantities of interest the above equation can be discretized as follows:

$$f_i(r_x, r_y = 1, t + \Delta t) = \frac{f_i(r_x, r_y = 1, t) + \lambda f_i(r_x, r_y = 2, t + \Delta t)}{1 + \lambda} \quad \forall\ i \in [0, 1, 2, 3, 4, 5, 6, 7, 8] \tag{2.38}$$

where $\lambda = U(t + \Delta t) \cdot \Delta t / \Delta x$. The CBC has there variants depending on how the value for U is considered. For the southern boundary we can specify these choices for velocity as:

$$U = u_{\text{avg}} = \frac{\sum_{r_x} u_y(r_x, r_y = 2)}{N} \tag{2.39}$$

$$U = u_{\text{local}} = u_y(r_x, r_y = 2) \tag{2.40}$$

$$U = u_{\text{max}} = \max_{r_x}[u_y(r_x, r_y = 2)] \tag{2.41}$$

where N is number of fluid nodes considered. Thus, we will used CBC-A, CBC-L and CBC-M to indicate each variant. The advection term can also been discretized according to second-order implicit finite difference [3]. The same discretization is also applicable for Neumann BC.

2.2. Multiphase LBM models

Multiphase models based on LBM can be in general categorized into four major groups: color-gradient models, free energy models, phase field LB models and pseudo-potential models [66]. Few models exists which does not fit into the classification of the four model families in multiphase LBM like for example free surface [67] model and others. Here rather than an exhaustive analysis, we describe in brief one example model for three multiphase LBM model families. Few detailed references for multiphase LBM models are [48, 67–71]. By default, we assume the D2Q9 schema.

2.2.1. Color gradient model

The Colour-Gradient model uses a two component which was proposed by Rothmann and Keller [72], and it was 1st introduced by Gunstensen et al.[73] for simulation of immiscible binary fluids based on a 2d hexagonal lattice. Later modification allow for variation of density and viscosity. The two immiscible fluids are labeled as *red* and *blue*, where each is assigned a distribution function i.e. f_i^{red} and f_i^{blue}. The total distribution function is given as $f_i = f_i^{\text{red}} + f_i^{\text{blue}}$, where both sets of distribution functions are updated using the solver. The process for the sake of algorithm is sub-divided into two steps i.e. collision and streaming. The equation for collision is given as:

$$f_i^{\kappa,\text{pc}}(\boldsymbol{r}, t) = f_i^{\kappa}(\boldsymbol{r}, t) + \Lambda_i^{\kappa} \quad \forall\ \kappa \in [\text{red, blue}] \tag{2.42}$$

Now, for the streaming step the equation is given as:

$$f_i^{\kappa}(\boldsymbol{r} + \Delta\boldsymbol{r}, t + \Delta t) = f_i^{\kappa,\dagger}(\boldsymbol{r}, t) \tag{2.43}$$

where $f_i^{\kappa,\dagger}$ is obtained in an intermediate step known as the recoloring step. This recoloring operator for the κ^{th} component is given as:

$$f_i^{\kappa,\dagger} = \frac{\rho^{\kappa}}{\rho} f_i^{\text{pc}} + \beta \frac{\rho^{\text{red}} \rho^{\text{blue}}}{\rho^2} f_i^{\text{eq}}(\rho, \boldsymbol{u} = 0) \cos(\lambda_i) \tag{2.44}$$

where $f_i^{\text{pc}} = \sum_{\kappa} f_i^{\kappa,\text{pc}}$, β is a constant (which is used for adjusting the interface thickness) whose value lies between 0 and 1, the total density is $\rho = \sum_{\kappa} \rho^{\kappa}$ and the total momentum is $\rho\boldsymbol{u} = \sum_{\kappa} \sum_i f_i^{\kappa} \boldsymbol{e}_i$. For this model, the collision operator is constructed from two sub-operators such that:

$$\Lambda_i^{\kappa} = \Lambda_i^{\kappa,1} + \Lambda_i^{\kappa,2} \tag{2.45}$$

where $\Lambda_i^{\kappa,1}$ is the standard collision operator like for e.g. BGK (as defined previously in section 2.1.2). The equilibrium distribution function of $f_i^{\kappa,\mathrm{eq}}$ is given as:

$$f_i^{\kappa,\mathrm{eq}} = \rho^\kappa \left(C_i + w_i \left(\frac{\boldsymbol{e}_i \cdot \boldsymbol{u}}{e_s^2} + \frac{(\boldsymbol{e}_i \cdot \boldsymbol{u})^2}{2e_s^4} - \frac{\boldsymbol{u}^2}{2e_s^2} \right) \right) \tag{2.46}$$

where density definition for each component remains unchanged and the coefficients (C_i) are provided as [74] (for components with identical densities we can substitute $C_i = w_i$). If the relaxation time (τ) of each component is different, then the τ at the interface is determined using an interpolation scheme as mentioned in [74]. The second collision sub-operator is more complex with different suggestions existing in the literature. An example formulation is [73]:

$$\Lambda_i^{\kappa,2} = \frac{A^\kappa}{2} |\boldsymbol{o}| (2 \cdot \cos^2(\lambda_i) - 1) \tag{2.47}$$

where A^κ effects the interfacial tension and λ_i is the angle between the color gradient $\boldsymbol{o}(\boldsymbol{r}, t)$ and the velocity direction $\boldsymbol{e}_i$. Also we have $\cos(\lambda_i) = \dfrac{\boldsymbol{e}_i \cdot \boldsymbol{o}}{|\boldsymbol{e}_i| \cdot |\boldsymbol{o}|}$ where the color gradient is calculated as:

$$\boldsymbol{o}(\boldsymbol{r}, t) = \sum_i \boldsymbol{e}_i \sum_j [f_j^{\mathrm{red}}(\boldsymbol{r} + \boldsymbol{e}_i \Delta t, t) - f_j^{\mathrm{blue}}(\boldsymbol{r} + \boldsymbol{e}_i \Delta t, t)] \tag{2.48}$$

Another formulation [75] for $\Lambda_i^{\kappa,2}$ is suggested as the correct collision operator and is given as:

$$\Lambda_i^{\kappa,2} = \frac{A^\kappa}{2} |\boldsymbol{o}| \left[w_i \frac{(\boldsymbol{e}_i \cdot \boldsymbol{o})^2}{|\boldsymbol{o}|^2} - B_i \right] \tag{2.49}$$

where the B_i is constant and is given as:

$$B_i = \begin{cases} -\frac{4}{27} & \forall\ i \in [0] \\ \frac{2}{27} & \forall\ i \in [1,2,3,4] \\ \frac{5}{108} & \forall\ i \in [5,6,7,8] \end{cases} \tag{2.50}$$

This formulation allows for correct reproduction of terms corresponding to the interfacial tension in the NS equations.

2.2.2. Phase field model

The phase field (PF) model utilizes an additional parameter for recognition of different phases and to capture the interface dynamics via the use of Cahn-Hillard equation (CHE) or Allen-Cahn equation (ACE) (local and non-local) [76]. With CHE one obtains a sharp interface while with ACE a diffused interface is observed. For the thesis, instead of a detailed description of all various PF models, we elaborate on the model where ACE is used [77]. This model is intended to be used for immiscible and incompressible fluids. As mentioned previously, apart from the NS equations the model additionally utilizes the AC equation. This equation provides us with the evolution of the interface and is given as:

$$\frac{\partial \varphi}{\partial t} + \nabla \cdot (\varphi \boldsymbol{u}) = \nabla \cdot M \left(\nabla \varphi - \frac{1 - 4(\varphi - \varphi_0)^2}{\xi} \boldsymbol{n} \right) \tag{2.51}$$

where φ is the phase field, M is the mobility, ξ is the interfacial width, μ is the dynamic viscosity, φ_0 represents the location of the interface and $\boldsymbol{n} = \nabla\varphi / |\nabla\varphi|$ is the unit normal vector. Here after discretization according to LBM (i.e. finite difference discretization + velocity direction discretization), the ACE is given as:

$$h_i(\boldsymbol{r} + \boldsymbol{e}_i \Delta t, t + \Delta t) = h_i(\boldsymbol{r}, t) + \frac{\widetilde{h}_i^{\mathrm{eq}}(\boldsymbol{r}, t) - h_i(\boldsymbol{r}, t)}{\tau_\varphi + 1/2} + F_{\varphi,i}(\boldsymbol{r}, t) \tag{2.52}$$

where the force is formulated as:

$$F_{\varphi,i} = \Delta t \frac{[1-4(\varphi-\varphi_0)^2]}{\xi} w_i \boldsymbol{e}_i \cdot \boldsymbol{n} \tag{2.53}$$

and h is the phase field distribution function, τ_φ is the corresponding relaxation time (which in turn is related to the mobility ,M, as $M = \tau_\varphi e_s^2 \Delta t$) and the modified equilibrium distribution function is given as:

$$\widetilde{h}_i^{\mathrm{eq}} = h_i^{\mathrm{eq}} - \frac{F_{\varphi,i}}{2} \tag{2.54}$$

where we could write the equilibrium phase-field distribution function (h_i^{eq}) as:

$$h_i^{\mathrm{eq}} = w_i \varphi \left[1 + \frac{\boldsymbol{e}_i \cdot \boldsymbol{u}}{\boldsymbol{e}_s^2} + \frac{(\boldsymbol{e} \cdot \boldsymbol{u})^2}{2\boldsymbol{e}_s^4} - \frac{\boldsymbol{u}^2}{2\boldsymbol{e}_s^2} \right] \tag{2.55}$$

The phase field is thus obtained as:

$$\varphi = \sum_i h_i \tag{2.56}$$

after which the density at fluid node η is calculated using the interpolation :

$$\rho(\eta) = \rho_{\mathrm{L}} + \frac{\varphi(\eta) - \varphi_{\mathrm{L}}}{\rho_{\mathrm{H}} - \rho_{\mathrm{L}}} \tag{2.57}$$

where H and L represents the heavy and light phases. While the first probability distribution function (PDF) was used for modeling the phases, the second PDF is used for modeling the hydrodynamics. The second PDF is given as:

$$g_i(\boldsymbol{r} + \boldsymbol{e}_i \Delta t, t + \Delta t) = g_i(\boldsymbol{r}, t) + \Lambda_i + \mathscr{F}_i \tag{2.58}$$

where Λ, as before is the collision operator utilizing the relaxation time (related to kinematic viscosity of fluid i.e. $\nu = \tau e_s^2 \Delta t$). Here it also possible to vary τ for the heavy and light fluids based on interpolation between the relaxation times of each fluid or alternatively between the viscosities of each fluid. The formulation for the BGK and MRT collision operators are given as:

$$\Lambda_{\mathrm{BGK},i} = \frac{g_i - \widetilde{g}_i^{\mathrm{eq}}}{\tau + 0.5} \tag{2.59}$$

and

$$\Lambda_{\mathrm{MRT},i} = \mathbf{M}^{-1}\mathbf{S}\mathbf{M}(g_i - \widetilde{g}_i^{\mathrm{eq}}) \tag{2.60}$$

where the modified equilibrium distribution is given as:

$$\widetilde{g}_i^{\mathrm{eq}} = g_i^{\mathrm{eq}} - \frac{\mathscr{F}_i}{2} \tag{2.61}$$

The equilibrium distribution for the PDF modeling the hydrodynamics is given as:

$$g_i^{\mathrm{eq}} = w_i \left[\frac{p}{\rho e_s^2} + \frac{\boldsymbol{e}_i \cdot \boldsymbol{u}}{e_s^2} + \frac{(\boldsymbol{e}_i \cdot \boldsymbol{u})^2}{2e_s^4} - \frac{\boldsymbol{u}^2}{2e_s^2} \right] \tag{2.62}$$

Also the hydrodynamic forcing term is given as:

$$\mathscr{F}_i = w_i \frac{\boldsymbol{e}_i \cdot \boldsymbol{F}_{\mathrm{T}}}{\rho e_s^2} \Delta t \tag{2.63}$$

where the total force for this model is given as:

$$\boldsymbol{F}_{\mathrm{T}} = \boldsymbol{F}_\sigma + \boldsymbol{F}_{\mathrm{body}} + \boldsymbol{F}_{\mathrm{pr}} + \boldsymbol{F}_\mu \tag{2.64}$$

Here in the above equation $\boldsymbol{F}_\sigma$ represents the surface tension force, $\boldsymbol{F}_{\mathrm{body}}$ represents the body forces in the simulation, $\boldsymbol{F}_{\mathrm{pr}}$ represents the pressure force and $\boldsymbol{F}_\mu$ represents the viscous force in the simulation. The formulation for these forces are detailed in [77].

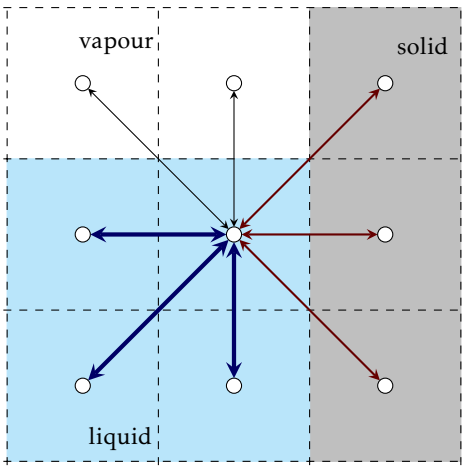

Figure 2.5: Interparticular forces between adjacent nodes.

2.2.3. Pseudopotential model

The pseudopotential LB method uses interparticle potential to mimic fluid particle interactions. This leads to a spontaneous separation of fluid phases or components, without resorting to any techniques to track or capture interfaces. The interparticle potential formulation will result to a non-ideal pressure tensor, which is different from that in the free-energy LB method [66]. Also for this method, momentum at a point/node is modified to account for the effect of the interparticular force. Thus, local momentum is not conserved but the global momentum always remains conserved. The pseudopotential model due to its simplicity, is amongst the popular LBM based multiphase method.

2.2.3.a. Single component model (SCMP-SC)

The pseudopotential/Shan and Chen model [78] introduces phase separation intrinsically by using interparticular forces which is modeled on pseudopotential or effective mass (ψ). The pseudopotential function at a point is in turn dependent on the local density. Due to this, high density fluid at a site/node would translate into a stronger attractive force (assuming $G < 0$) on all adjacent nodes. Thus the mutual interaction force between a pair of two adjacent nodes each having higher density fluid would be greater than if one of those nodes had lower density fluid (as indicated in fig. 2.5), where thickness of line is used to depict the force intensity). The least interaction force would be observed if both nodes had lower density fluid. As a result, the regions of higher densities would be strongly attracted to each other as compared to regions of lower density which leads into segregation or phase separation. Thus no additional function is required for plotting/capturing or tracking the interface, which can be directly visualized by plotting density field during the post-processing.

The downside of the progressive nature of intensity of force would be that, the interface is observed to be diffused rather than being sharp. Thus, if exact location of the interface is required, then additional computation would be required. Also, the local scope of the interparticular force means that momentum is not conserved locally though it is conserved globally.

The continuous form of the interparticular force at a location/node η is given as [79–81]:

$$\boldsymbol{F}_{\mathrm{p}} = -\mathcal{G}\psi\nabla_{\boldsymbol{r}}\psi = -\mathcal{G}\frac{\nabla_{\boldsymbol{r}}\psi^2}{2} \tag{2.65}$$

where $\mathcal{G}$ is a constant and ψ is the pseudopotential. The discretized version of the eq. (2.65) for the

fluid-fluid interactions is given by:

$$\boldsymbol{F}_{\mathrm{p}}(\eta) = -G\psi(\eta) \sum_{\substack{i \\ \vartheta_i=\eta+\Delta t\boldsymbol{e}_i\in\mathcal{D}_{\mathrm{f}} \\ |\vartheta_i-\eta|\leq\sqrt{2}}} w_{\mathrm{fr},i}\psi(\vartheta_i)\boldsymbol{e}_i \tag{2.66}$$

where $w_{\mathrm{fr},i}$ is the forcing weight function depended on $\boldsymbol{e}_i$. and is equal to the initial weight function (w_i), G is a numerical quantity called interaction strength which is defined as $T = -1/G$, where T is numerical temperature. The standard equation for describing the relation between density based pseudopotential and pressure corresponding to eq. (2.65) is given by:

$$p = \rho e_s^2 + \frac{Gc_0\psi^2}{2} \tag{2.67}$$

There have been other works for e.g. [81, 82] discussing different interparticle force formulations and their performances. For this work we use a slightly modified version of pressure equation given as:

$$p = \rho e_s^2 + \frac{Ge_s^2\psi^2}{2} \tag{2.68}$$

This change in equation merely alters the location of the critical point, but the nature of the equation remains the same. Rewriting this equation we obtain:

$$\psi = \sqrt{\frac{2(p-\rho e_s^2)}{Ge_s^2}} \tag{2.69}$$

In the original SC model, the formulation of the pseudopotential function is defined as:

$$\psi = \rho_0\left(1-\exp\left(\frac{-\rho}{\rho_0}\right)\right) \tag{2.70}$$

from which the value for pressure is later obtained by using eq. (2.67). Other common forms of the pseudopotential function are:

$$\psi = \rho \tag{2.71}$$

and

$$\psi = \psi_0\exp\left(\frac{-\rho_0}{\rho}\right) \tag{2.72}$$

The original Shan and Chen model [78] used what is known as the velocity shift force scheme. Here instead of treating the interparticle force as an external force it is indirectly incorporated by the modifying/shifting the velocity as given by eq. (2.5). Thus forming what is known as the equilibrium velocity. For a local fluid node η it is formulated as:

$$\boldsymbol{u}^{\mathrm{eq}} = \boldsymbol{u} + \frac{\boldsymbol{F}_{\mathrm{T}}(\eta)}{\omega\rho} \tag{2.73}$$

where $\omega = (\Delta t)\tau^{-1}$ is the relaxation frequency, $\boldsymbol{F}_{\mathrm{T}}$ is the total force which is elaborated in section 2.3.6. The physical velocity u_p is obtained as:

$$\boldsymbol{u}_p = \boldsymbol{u} + \frac{\boldsymbol{F}_{\mathrm{T}}(\eta)}{2\rho} \tag{2.74}$$

Now, the equilibrium velocity is to be substituted in the distribution function given by eq. (2.13). Thus for Λ_{BGK} we obtain eq. (2.12) with $\mathscr{F}_i = 0$ in the final equation.

2.2.3.b. *Multi-component model (MCMP-SC)*

The Shan and Chen LB model could also be used for simulating multi-components flows [79]. The original model has a density ratio of order 1. Each component has its own viscosity and hence relaxation time i.e. τ_1 and τ_2. The formulation is the interparticular force remains the same (as compared to SCMP-SC) for each component, with the only exception that the other component influence is also considered. The total interparticular force for a component at η is:

$$\boldsymbol{F}_{p,\kappa}(\eta) = -\psi_\kappa(\eta) \sum_{\substack{i \\ \vartheta_i=\eta+\Delta t\boldsymbol{e}_i\in\mathcal{D}_\mathrm{f} \\ |\vartheta_i-\eta|\leq\sqrt{2}}} w_{\mathrm{fr},i}\left[G_{\kappa\kappa}\psi_\kappa(\vartheta_i) + G_{\kappa\bar{\kappa}}\psi_{\bar{\kappa}}(\vartheta_i)\right]\boldsymbol{e}_i \quad \forall\ \kappa\in[1,2],\ \forall\ \bar{\kappa}\in[2,1] \tag{2.75}$$

where $G_{\kappa,\bar{\kappa}}$ and $G_{\kappa,\kappa}$ represent the interaction strength for between different components and interaction strength for the same component. Here a positive value of interaction strength models repulsive forces and the conversely a negative value represents attractive forces. Now for the κ^{th} component, the pseudopotential ψ_κ was originally defined by eq. (2.70), the equilibrium distribution function $f_{i,\kappa}^{\mathrm{eq}}$ is given by eq. (2.13). The velocity remains common for both the components and thus becomes another coupling point between the two components after the interaction force:

$$\boldsymbol{u} = \frac{\sum_\kappa(\sum_i e_i f_{i,\kappa})}{\sum_\kappa \rho_\kappa} \tag{2.76}$$

where equilibrium velocity is defined as:

$$\boldsymbol{u}^{\mathrm{eq}} = \boldsymbol{u} + \frac{\sum_\kappa \boldsymbol{F}_{T,\kappa}\tau_\kappa}{\sum_\kappa \rho_\kappa} \tag{2.77}$$

and meanwhile the physical velocity is defined as:

$$\boldsymbol{u}_p = \boldsymbol{u} + \frac{\sum_\kappa \boldsymbol{F}_{T,\kappa}/2}{\sum_\kappa \rho_\kappa} \tag{2.78}$$

Thus we have the similar LBM equations for both components which is given as:

$$f_i^\kappa(\boldsymbol{r}+\boldsymbol{e}_i\Delta t, \Delta t) = f_i^\kappa(\boldsymbol{r}, t) + \Lambda_i^\kappa \quad \forall\ \kappa\in[1,2] \tag{2.79}$$

here $\mathscr{F}_{i,\kappa} = 0$ for the velocity shift scheme. Finally, the relation between the pressure and the pseudopotential is given as:

$$p = \sum_{\kappa\in[1,2]}\left(\frac{\rho_\kappa}{3} + \frac{G_{\kappa\kappa}\psi_\kappa^2}{6} + \frac{G_{\kappa\bar{\kappa}}\psi_\kappa\psi_{\bar{\kappa}}}{6}\right) \tag{2.80}$$

The following section 2.3 discusses the improvements which are applicable to the SCMP-SC and by extension these could also be utilized for an MCMP-SC. Multi-component multiphase (MCMP-SC) model suggested by [83] using PR EOS with the velocity shift forcing scheme was able to obtain a high density ratio by controlling the force ratio $\frac{|\boldsymbol{F}_{1,1\ \max}|}{|\boldsymbol{F}_{1,2\ \max}|}$, where 1 represents the heavier phase. It was observed that as the ratio increased the density ratio also increased up to the order of 10^3. The MCMP model suggested by [84] for simulating realistic flows, incorporated certain modifications to improve the method like use of PR EOS with modified Guo formulation as given by [85], to increase the density ratio and improve thermodynamic consistency. They achieved a density ratio of about 1000 and viscosity ratio of about 16.15, which corresponds to the air-water system in real life.

Multiphase LBM generally exhibits a diffused interface being devoid of the interface tracking equations. In the case of the pseudopotential method [86], this interface is directly a result of the interparticle forces. These forces are present both between each fluid particles and between fluid and solid particles. Among all the major multiphase LBM models (color gradient, phase field, free energy and pseudopotential), the pseudopotential method is used the most commonly [48]. It is

known for its efficiency and simplicity, as it generally does not employ the Poisson equation for pressure. These factors play a significant role in the our selection of this method. We choose the SCMP-SC with intent of utilizing it for modeling physics which would later be fed as an input to a optimization algorithm. The optimizer, requires multiple reruns of the physical simulation (hereafter also referred to as the forward problem) which all the more underlines the requirement of a lightweight solver.

2.3. Modification/Extension for the SCMP-SC

The original Shan and Chan model, suffers from some deficiencies in modeling two-phase fluid flow such as the relatively large spurious current, low density and kinematic viscosity ratios, thermodynamic inconsistency, coupling effect between the EOS and surface tension, and dependence of surface tension and density ratio on the viscosity [84].These limitations may have insignificant effect on the two-phase flow inside porous media due to the dominate role of surface tension. A number of improvements to the model have been proposed and can be divided into two categories: those that modify the force calculation, such as increasing the order of isotropy or modifying the equation of state , and those that improve the incorporation of the force term into the equilibrium distribution functions [85].

The former modification includes the multirange models, models using different equation of state. The multirange model considers the nearest and the next nearest layer of nodes for proper resolution of force (with the appropriate weight function) and results into decoupling the equation of state and the surface tension [87]. Similar method was proposed by [88], wherein just as before two layer of nodes was used for forcing with different values of interaction strength for each layer (G_1 and G_2). This method seems to provide flexibility for adjusting the values of interaction potential i.e. density ratio and surface tension independently. Also this model has lower spurious current. Shan and Chen models were tested by [80] by using different equation of state. The equation of state was used to define the value for pressure which later on defined the value of the pseudopotential function. The Peng-Robinson EOS was found to have the least spurious current and the maximum density ratio of the order of 10^3.

The latter modifications include the use of forcing schemes Guo forcing scheme, the exact difference method (EDM) and so on. The original forcing scheme (velocity shift scheme) causes the surface tension to be dependent on kinematic viscosity. It has been shown recently that while the Guo forcing scheme recovers the Navier-Stokes equations correctly, while the EDM introduces an error into the pressure tensor, proportional to the square of the forcing term [85]. Also in paper [85] they perform a third order analysis on the pressure tensor in the Pseudopotential method, thereby arriving upon an improved Guo force scheme. Only relevant modifications (i.e. those that have used or is proposed to be used) are elaborated below.

2.3.1. Different equation of states (EOS)

The models employing the standard equation of state are stable only for low density ratios of the $O(10^2)$. To obtain higher density ratio and lower spurious current the use of realistic equation of state for e.g. Van der Waal, CS and PR and others was suggested by ref.[80, 89]. As mentioned previously in the original Shan and Chen formulation the pressure is obtained from the pseudopotential which is described as a function of density of the fluid. Conversely, for the realistic equation of state the pseudopotential function is obtained from pressure of the fluid which is described by an equation of state (i.e. a function of density). *One additional thing to note here is that use of equation of states breaks the previous linkage $T = -1/G$. Generally, this changes the meaning and significance of temperature (T) as it would now arise from EOS itself, while G now becomes an independently tuned parameter.*

2.3.1.a. *Peng-Robinson (PR) EOS*

Here, a realistic equation of state is used for defining pressure and then eq. (2.69) is used for obtaining pseudopotential. PR EOS enables parameters (for e.g. pressure and temperature) to be defined in terms of critical properties and acentric factor of the fluids. Pressure is given as:

$$p = \frac{\rho RT}{1-b\rho} - \frac{a\rho^2\alpha}{1+2b\rho-b^2\rho^2} \tag{2.81}$$

where $\alpha = \left(1+(0.37464+1.54226\zeta-0.26992\zeta^2)\left(1-\sqrt{\frac{T}{T_c}}\right)\right)^2$, $a = \frac{0.45724R^2T_c^2}{p_c}$, $b = \frac{0.0778RT_c}{p_c}$ and ζ = Pitzer's acentric factor.

2.3.1.b. *Carnahan-Starling (CS) EOS*

Here the pressure is defined using CS formulation, and pseudopotential function can be obtained as previously using eq. (2.69). Pressure is given as:

$$p = \rho RT\frac{1+b\rho/4+(b\rho/4)^2-(b\rho/4)^3}{(1-b\rho/4)^3} - a\rho^2 \tag{2.82}$$

where $a = \frac{0.4963R^2T_c^2}{p_c}$ and $b = \frac{0.18727RT_c}{p_c}$. It is to be noted that for a particular value of b the diffused interface thickness can be controlled by value of a as demonstrated by [90]. Also that sharper interface would decrease the stability.

2.3.2. Different forcing schemes

The standard forcing scheme for the Shan and Chen model is known as the velocity shift scheme as the velocity used for the equilibrium particle distribution function is *shifted* by adding the impact of the interparticular force. Popular forcing schemes like Guo, EDM amongst others have been compared with the original force scheme in studies such as [91] and found to have lower spurious current and better overall performance. The only drawback of these forcing schemes (as compared to the original) is that these exhibit a lower stability for lower temperatures.

2.3.2.a. *Guo forcing scheme*

This forcing scheme was proposed by [92]. Here the velocity/momentum is modified to account for the effects of the interparticle forces. For this scheme we modify the velocity recovered from eq. (2.5). The physical velocity would still be given by eq. (2.74). The velocity $\boldsymbol{u}_p$ is then used for computing the equilibrium distribution function by using the eq. (2.13), which would then in turn be used for solving the lattice Boltzmann equation. This formulation requires an explicit addition of force in the LBE and hence for Λ_{BGK} we obtain eq. (2.12) as the final equation. Here, $\mathscr{F}_i$ is the interaction force term distributed along the nine directions by the formulation given by Guo[93, 94]:

$$\mathscr{F}_i = \mathscr{F}_{\text{guo},i} = \left(1-\frac{1}{2\tau}\right)\left(\frac{\boldsymbol{e_i}-\boldsymbol{u_p}}{e_s^2}+\frac{\boldsymbol{e_i}\cdot\boldsymbol{u_p}}{e_s^4}\boldsymbol{e_i}\right)w_i\boldsymbol{F}_{\text{T}}\Delta t \tag{2.83}$$

Now for Λ_{MRT} the final equation is given by eq. (2.18) where $\mathscr{F}_i$ is given as [94]:

$$\mathscr{F}_i = \Omega_i - \frac{1}{2}\mathbf{M}^{-1}\mathbf{S}\mathbf{M}(\Omega_i) \tag{2.84}$$

where $\Omega_i = \left(\frac{\boldsymbol{e_i}-\boldsymbol{u_p}}{e_s^2}+\frac{\boldsymbol{e_i}\cdot\boldsymbol{u_p}}{e_s^4}\boldsymbol{e_i}\right)w_i\boldsymbol{F}_{\text{T}}\Delta t$.

2.3.2.b. *Exact difference method (EDM) forcing scheme*

This forcing scheme was introduced by [89] to properly represent the affect of the body forces of any nature. This forcing scheme is simple to implement with different Λ, such that the final equations with Λ_{BGK} and Λ_{MRT} are eq. (2.12) and eq. (2.18) respectively where:

$$\mathscr{F}_i = \mathscr{F}_{\mathrm{edm},i} = \Delta f_i = f_i^{\mathrm{eq}}(\rho, \boldsymbol{u} + \Delta\boldsymbol{u}) - f_i^{\mathrm{eq}}(\rho, \boldsymbol{u}) \tag{2.85}$$

with $\Delta\boldsymbol{u} = F_{\mathrm{T}}\Delta t/\rho$. Here the physical velocity is again described by eq. (2.74). This forcing scheme has been observed to remove relaxation time (τ) dependence of surface tension (σ) for the SRT model [91]. Also in this study it was observed to have a smaller density ratio limit as compared to Shan and Chen forcing scheme along with CS EOS. Finally we conclude this subsection with a nifty little table (table 2.1) detailing the different types of velocities used in the LBM algorithm along with the relevant forcing terms for each of the forcing scheme discussed in this thesis.

Forcing scheme	f^{eq} velocity ($\boldsymbol{u}^{\mathrm{eq}}$)	Real velocity ($\boldsymbol{u}_p$)	Forcing term ($\mathscr{F}_i$)
Velocity shift	$\frac{\sum_i f_i \boldsymbol{e}_i}{\rho} + \frac{\boldsymbol{F}_{\mathrm{T}}\tau}{\rho}$	$\frac{\sum_i f_i \boldsymbol{e}_i}{\rho} + \frac{\boldsymbol{F}_{\mathrm{T}}\Delta t}{2\rho}$	0
EDM	$\frac{\sum_i f_i \boldsymbol{e}_i}{\rho}$	$\frac{\sum_i f_i \boldsymbol{e}_i}{\rho} + \frac{\boldsymbol{F}_{\mathrm{T}}\Delta t}{2\rho}$	$f_i^{\mathrm{eq}}(\rho, \boldsymbol{u} + \Delta\boldsymbol{u}) - f_i^{\mathrm{eq}}(\rho, \boldsymbol{u})$
Guo	$\frac{\sum_i f_i \boldsymbol{e}_i}{\rho} + \frac{\boldsymbol{F}_{\mathrm{T}}\Delta t}{2\rho}$	$\frac{\sum_i f_i \boldsymbol{e}_i}{\rho} + \frac{\boldsymbol{F}_{\mathrm{T}}\Delta t}{2\rho}$	$\left(1 - \frac{1}{2\tau}\right)\left(\frac{\boldsymbol{e}_i - \boldsymbol{u}_p}{e_s^2} + \frac{\boldsymbol{e}_i \cdot \boldsymbol{u}_p}{e_s^4}\boldsymbol{e}_i\right) w_i \boldsymbol{F}_{\mathrm{T}}\Delta t$

Table 2.1: Corresponding velocities (equilibrium and physical) and force terms (for SRT collision operator) for each of the forcing schemes (from [91])

2.3.3. Multirange model

In nature it is common to observe both a strong and weak force in fluid particle interactions. The original SCMP-SC model only takes into account the attractive forces. While this allows for the separations of the two phases and formation of the interface, the model faces significant challenges for simulating multi-droplet scenarios [95]. This problem is specific to SCMP-SC as for MCMP-SC no unphysical mass transfer was reported. This problem can be addressed by adding a repulsive force. Sbragaglia's work [88] is one of the defining papers regarding this topic but this deals primarily with spatial discretization of the interparticular force. A few studies [96, 97] succeeded in modeling multi-droplet simulations using multirange model with SCMP-SC featuring attractive and repulsive forces. Thus using the latter formulation we obtain that the total fluid-fluid interparticle force can be sub-divided as follows:

$$\boldsymbol{F}_{\mathrm{p}} = \boldsymbol{F}_{\mathrm{p,attract}} + \boldsymbol{F}_{\mathrm{p,repel}} \tag{2.86}$$

where the attractive force ($G_1 < 0$) at location η is given as:

$$\boldsymbol{F}_{\mathrm{p,attract}}(\eta) = -G_1\psi(\eta) \sum_{\substack{i \\ \vartheta_i = \eta + \Delta t \boldsymbol{e}_i \in \mathcal{D}_{\mathrm{f}} \\ |\vartheta_i - \eta| \leq \sqrt{2}}} w_{1,i}\psi(\vartheta_i)\boldsymbol{e}_i \tag{2.87}$$

and the repulsive force ($G_2 > 0$) at location η is obtained as:

$$\boldsymbol{F}_{\mathrm{p,repel}}(\eta) = -G_2\psi(\eta) \sum_{\substack{i \\ \vartheta_i = \eta + \Delta t \boldsymbol{e}_i \in \mathcal{D}_{\mathrm{f}} \\ |\vartheta_i - \eta| \leq 2\sqrt{2}}} w_{2,i}\psi(\vartheta_i)\boldsymbol{e}_i \tag{2.88}$$

where G_1 and G_2 are the corresponding interaction strengths for each of the force components. The corresponding forcing weight functions for the attractive component:

$$w_{1,i} = \begin{cases} 1/9 & \forall\ i\ \in [1,2,3,4] \\ 1/36 & \forall\ i\ \in [5,6,7,8] \end{cases} \tag{2.89}$$

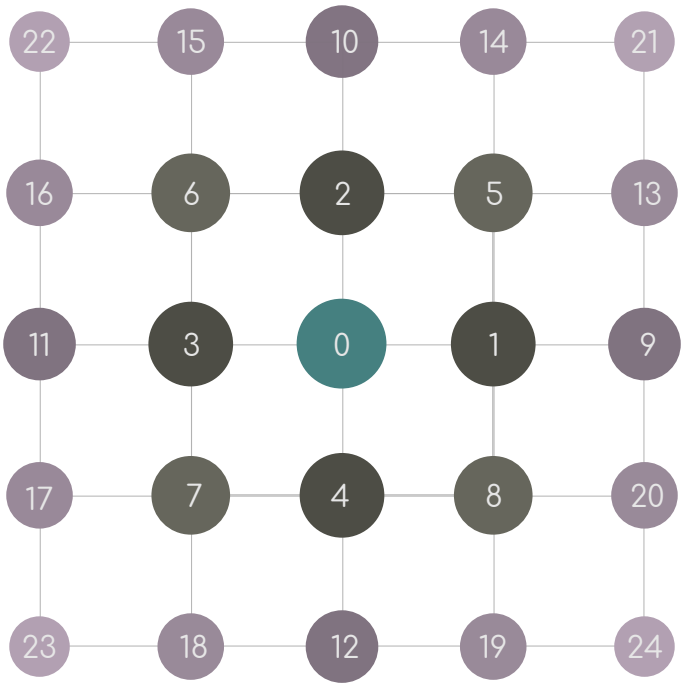

Figure 2.6: Adjacent nodes for multirange model

Finally the weight function for the repulsive component of force:

$$w_{2,i} = \begin{cases} 4/63 & \forall\ i\ \in [1,2,3,4] \\ 4/135 & \forall\ i\ \in [5,6,7,8] \\ 1/180 & \forall\ i\ \in [9,10,11,12] \\ 2/945 & \forall\ i\ \in [13,14,15,16,17,18,19,20] \\ 1/15120 & \forall\ i\ \in [21,22,23,24] \end{cases} \tag{2.90}$$

The fig. 2.6 displays the numbering, and the relative impact (by size and darkness of circular glyphs) in a two layered neighborhood of the location denoted by '0' i.e. the location η.

2.3.4. Dependency of relaxation time (τ) w.r.t fluid density

It is common practice to use the same relaxation time i.e. kinematic viscosity while modeling flows of compressible and multiphasic nature. It is only in LBM turbulence models that we computed the final relaxation time locally. For multiphasic flows, this would mean that the dynamic viscosity ratio (M) equals the density ratio. The results obtained from this arrangement is satisfactory for flows where viscous effects are negligible. To capture viscous effects it is helpful to have a kinematic viscosity ratio for vapor and liquid. If the liquid is more viscous (kinematically) than vapor, then this echos the natural phenomenon. Conversely, from the stability viewpoint it better to keep vapor kinematic viscosity (ν_{vap}) greater than the liquid viscosity (ν_{liq}). The latter viewpoint is applicable only in scenarios where viscous effects are negligible. At any rate, we will end up with two relaxation times τ_{liq} and τ_{vap} for liquid and vapor respectively. Now due to diffused interface we have a continuum of densities and hence the final relaxation time at η is interpolated as:

$$\tau(\eta) = \tau_{\text{liq}} + (\tau_{\text{vap}} - \tau_{\text{liq}})\frac{\rho(\eta) - \rho_{\text{liq}}}{\rho_{\text{vap}} - \rho_{\text{liq}}} \tag{2.91}$$

2.3.5. Higher order discretization of pseudopotential (ψ)

An alternative method [98], suggests a modification of the pseudopotential such that the new continuous form of the interparticular force is given as:

$$\boldsymbol{F}_p = -\beta\mathcal{G}\psi\nabla_{\boldsymbol{r}}\psi - \frac{1-\beta}{2}\mathcal{G}\nabla_{\boldsymbol{r}}\psi^2 \tag{2.92}$$

where β is a weighting factor as selected in [81]. Hence the modified interparticular force in the discretized form is given as:

$$\boldsymbol{F}_{\mathrm{p}}(\eta) = -G \sum_{\substack{i \\ \vartheta_i=\eta+\Delta t\boldsymbol{e}_i\in\mathcal{D}_{\mathrm{f}} \\ |\vartheta_i-\eta|\leq\sqrt{2}}} w_{\mathrm{fr},i}\left[\beta\psi(\eta)\psi(\vartheta_i) + \frac{1-\beta}{2}\psi^2(\vartheta_i)\right]\boldsymbol{e}_i \tag{2.93}$$

The higher order discretization increases overall the stability of the simulation by reducing the spurious current. Thus allows for operating over a wider temperature range. Section 2.4.2.a gives us insight of the relative performance of multirange and higher-order-discretization-of-pseudopotential models.

2.3.6. Total force

In the context of this thesis, the effective force or the external force ($\boldsymbol{F}_{\mathrm{T}}$) is the amalgamation of body forces ($\boldsymbol{F}_{\mathrm{body}}$), fluid-fluid interaction forces ($\boldsymbol{F}_{\mathrm{p}}$) and fluid-solid interaction forces ($\boldsymbol{F}_{\mathrm{s}}$). Thus, the total force on a node (as shown in fig. 2.5) can be given as:

$$\boldsymbol{F}_{\mathrm{T}} = \boldsymbol{F}_{\mathrm{body}} + \boldsymbol{F}_{\mathrm{p}} + \boldsymbol{F}_{\mathrm{s}} \tag{2.94}$$

It is this effective force which is later incorporated into the LBM formulation via forcing schemes (as previously mentioned in section 2.3.2).

2.3.6.a. Gravitational forces

Body forces (like gravity) on the fluid node are also considered while finding the total force acting on the fluid. Gravitational force is defined as:

$$\boldsymbol{F}_{\mathrm{gr}} = g_{\mathrm{gr}}\rho \tag{2.95}$$

To amplify the buoyant forces, one could imagine that the gravitational pull would be negligible for the lighter/vapor phase. This is accomplished by using the formulation

$$\boldsymbol{F}_{\mathrm{gr}} = g_{\mathrm{gr}}(\rho - \rho_{\mathrm{vap}}) \tag{2.96}$$

for gravitational force.

2.3.6.b. Wettability for SCMP-SC

Similarly, the formulation used for simulating fluid-solid interaction, i.e., adhesion for the i^{th} direction is given by:

$$\boldsymbol{F}_{\mathrm{s},i}(\eta) = -w_{\mathrm{fr},i}G_{\mathrm{ad}}\psi(\eta)\boldsymbol{e}_i \tag{2.97}$$

where $w_{\mathrm{fr},i}$ is the same weight function as in eq. (2.66), and G_{ad} is the numerical parameter controlling adhesion. A different suggestion [99] is that we substitute $G_{\mathrm{ad}} = G\psi$ such that the fluid-solid interaction force on a fluid node η could be given as:

$$\boldsymbol{F}_{\mathrm{s}}(\eta) = -G\psi(\eta) \sum_{\substack{i \\ \vartheta_i=\eta+\Delta t\boldsymbol{e}_i\in\mathcal{D}_{\mathrm{s}} \\ |\vartheta_i-\eta|\leq\sqrt{2}}} w_{\mathrm{fr},i}\psi(\vartheta_i)\boldsymbol{e}_i \tag{2.98}$$

where $\mathcal{D}_s$ is node in the solid domain. Here the pseudopotential at ϑ_i at the fluid-solid boundary (Γ_{sf}) is a function of a fictitious density ρ_w. Hereafter ρ_w would also be referred to as pseudo-density. The advantage of this substitution is that we adjust the contact angle between 0° and 180° by varying the pseudo-density form ρ_{liq} and ρ_{vap}. This causes the process to be intuitive rather than varying arbitrarily the value of G_{ad}.

2.4. Setting up of simulation model

Here we detail the process of choosing different parameter values which are a required for different simulation cases. Currently the parameter values can be segregated into two groups: values which are evident before any simulation i.e. a priori and values which are post-processed after benchmark simulations i.e. a posteriori. This benchmark simulation include the simulation for Laplace law (to obtain surface tension), contact angle simulation on a flat plate for satisfying the Young equation. This physical quantities aid in the non-dimensionalization process.

2.4.1. Parameter values fixed a priori

Performance of both the CS and the PR EOS used along with EDM forcing using both Λ_{BGK} and Λ_{MRT} was compared in [100]. This study concluded that spurious current is generally lower for CS EOS, though greater density ratio was obtained for PR EOS. Thus we chose to utilize CS EOS, EDM forcing and Λ_{MRT}. The parameters for Λ_{MRT} remains the same unless specified otherwise.

- $\mathscr{H}_1 \rightarrow$ This SCMP-SC models [91] uses Carnahan-Starling (CS) EOS where we assign the constant values as $G = -1$, $a = 1$, $b = 4$ and $R = 1$. Therefore, the critical temperature (T_c) is 0.09433 units and the critical pressure (p_c) is 0.004416295 units. Also, the EDM forcing scheme is used along with Λ_{MRT}. *Please note that the idea here is not to model a specific fluid based on the value of constants for CS EOS, rather to model a similar system based on equating the relevant non-dimensional numbers from the real world and the LBM system.*
- $\mathscr{H}_2 \rightarrow$ Here in addition to $\mathscr{H}_1$, we utilize multirange model for improved spatial discretization of force with constants $g_1 = -1.4$ and $g_2 = 0.7$.
- $\mathscr{H}_3 \rightarrow$ In addition to $\mathscr{H}_1$, here we utilize higher order discretization for $\nabla_{\boldsymbol{r}}\psi$ with a constant $\beta = 1.2$.
- $\mathscr{H}_4 \rightarrow$ This model [78, 99] of SCMP-SC is a open source LBM solver (OpenLB) model which uses eq. (2.72) for pressure, and eq. (2.68) for pseudopotential along with Guo forcing scheme. Here the value of the constants are $\psi_0 = 4$ and $\rho_0 = 200$ m.u./l.u.^{2}. Now, the densities are $\rho_{liq} = 524$ m.u./l.u.^{2} and $\rho_{vap} = 85$ m.u./l.u.^{2} (obtained a posteriori). Here we use the interaction potential $G = -120$ and the critical point is represented by an interaction strength of $G_c = -92.5$. Also the surface tension for this model is $\sigma = 14.3$ units (obtained a posteriori).
- $\mathscr{H}_5 \rightarrow$ Again this model [79, 92] of MCMP-SC is an OpenLB model. Here the Guo forcing scheme is used with the pseudopotential given by $\psi_\kappa = \rho_\kappa$. For simulating two immiscible fluids, we fix $G_{\kappa\bar{\kappa}} > 0$ and $G_{\kappa\kappa} = 0$. Here the density ratio for the standard model is nearly unity. For OpenLB solid-fluid interaction is controlled by using $G_{adh,\kappa}$.
- $\mathscr{H}_6 \rightarrow$ This model is a clone of $\mathscr{H}_4$, with the only differences being that it uses the EDM forcing scheme and that it was coded in-house.

2.4.2. Parameter values obtained a posteriori

The modeling of the benchmark test are instrumental in defining parameter values which are the byproduct of the force balance at the mesoscopic scale. This would be evident only after benchmark simulations, in other words, we obtain this results/parameter values after simulations. Later

Nomenclature	Model description	Source
$\mathscr{H}_1$	CS EOS + EDM forcing – [91]	In-house
$\mathscr{H}_2$	$\mathscr{H}_1$ + Multirange model	In-house
$\mathscr{H}_3$	$\mathscr{H}_1$ + Higher order $\nabla_{\boldsymbol{r}}\psi$ discretization	In-house
$\mathscr{H}_4$	OpenLB SCMP-SC – [78, 99] + Guo forcing	OpenLB
$\mathscr{H}_5$	OpenLB MCMP-SC – [79] + Guo forcing	OpenLB
$\mathscr{H}_6$	[99] + EDM forcing	In-house

Table 2.2: Scheme nomenclature for different models

Algorithm 1: General flow of a SCMP-SC algorithm

Input: Physical state: $\rho^{(0)}$ & $\boldsymbol{u}^{(0)}$, fluid-fluid interface along with geometry: $\mathcal{D} \in \mathcal{D}_\mathrm{f} \bigcup \mathcal{D}_\mathrm{s}$ and wettability: $\rho_\mathrm{w} \in \mathcal{D}_\mathrm{s}$

Initialize $f_i^{(0)} = f_i^{\mathrm{eq}}\ \forall\ i$ and compute for the fluid domain ($\mathcal{D}_\mathrm{f}$).

while *($\|\rho^{(z)} - \rho^{(z-1)}\|_1 \geq \gamma_\mathrm{c}$* **AND** *$k \leq k^{\max}$; where γ_c is a constant.)* **do**

- Compute pressure ($p^{(k)}$), pseudopotential ($\psi^{(k)}$) and forces ($\boldsymbol{F}_\mathrm{p}^{(k)}$, $\boldsymbol{F}_\mathrm{s}^{(k)}$, $\boldsymbol{F}_\mathrm{body}^{(k)}$) using eq. (2.82), eq. (2.69), eq. (2.66), eq. (2.98) and eq. (2.96) respectively
- Compute the equilibrium distribution function f^{eq} and perform collision i.e. to solve the RHS of eq. (2.18)
- Perform streaming i.e. the RHS of eq. (2.18) is copied at the LHS of the same equation.
- Perform bounceback for walls
- Compute for open boundaries and later for ghost nodes.
- Update the macroscopic variables like density ($\rho^{(k+1)}$) and velocity ($\boldsymbol{u}^{(k+1)}$)
- **if** *(k mod $\varsigma = 0$; where ς is an constant.)* **then**
  - Writing data to files
  - Storing density at z i.e. $\rho^{(z)}$
  - Increment z by 1 i.e. $z \leftarrow z + 1$.
- $k \leftarrow k + 1$

return *Macroscopic parameters like $\rho^{(\dagger)}$, $p^{(\dagger)}$ and $\boldsymbol{u}^{(\dagger)}$*

these parameter values are used for comparing LBM simulation with the real world. Some of the benchmark simulations are:

2.4.2.a. Coexistence curve

The coexistence curve are obtained from Maxwell's equations which provides theoretical densities (stable/equilibrium) densities for liquid and its vapor such that the overall pressure remains consistent across the fluids. The Maxwell's construction/equation can be stated as [99]:

$$\int_{V_{m,\mathrm{liq}}}^{V_{m,\mathrm{vap}}} p\ \mathrm{d}V_m = p_0(V_{m,\mathrm{vap}} - V_{m,\mathrm{liq}}) \tag{2.99}$$

where V_m is the molar volumes, p_0 is a constant pressure and p is the pressure defined by the equation of state. Thus here we find the pressure of the fluids (at one particular temperature) such that the above eq. (2.99) is validated i.e. the area under the p-V curve is equal to the rectangular area (as defined by the RHS), hence this is also known as the *equal area rule*. Thus we recover from the molar volumes the theoretical densities for one temperature. By repeating this process for different temperature one recovers the coexistence curve.

Now after obtaining the analytical curve, we utilize this result to validate our model. For the simulation, a straight/flat vapor-liquid interface with the domain saturation being 50% is modeled. The domain size here is $\mathscr{N}_x \times \mathscr{N}_y = 201 \times 201$ and all the boundaries are periodic in nature. For the reduction of the computational time, we initiate the simulation with theoretical/analytical density

values and a sharp interface. The density is referred from [91]. As the computation progresses, the diffused interface formation is completed. This is also accompanied by minor fluctuations of density value (adhering to conservation of mass) until equilibrium values are attained for the particular configuration. It is these values of densities at $t = t_f$ which are then plotted along with the analytical values. Figure 2.7 (a-b) shows the comparison for between the analytical and numerical density values for CS EOS for models $\mathscr{H}_1$, $\mathscr{H}_2$ and $\mathscr{H}_3$. It is also observed from these two figures that the vapor density (ρ_{vap}) is sensitive to changes in the model parameters for $\mathscr{H}_2$ and $\mathscr{H}_3$.

For all for the six sub-figures the curves colored *blue* represent the results of the model $\mathscr{H}_1$. For model $\mathscr{H}_2$ a near fit is observed for $g_2 = 0.7$ and an almost perfect match/fit is observed for $\mathscr{H}_3$ where $\beta = 1.2$. Another minor observation is that unlike $\mathscr{H}_3$, the curves retrieved for $\mathscr{H}_2$ exhibit a deviation in the shape of the curve at lower temperatures. Now, concerning fig. 2.7(c,d) which plot the spurious currents (which exists primarily in the vicinity of the interface) across different temperatures, we observe that for the current setup that, $\mathscr{H}_2$ performs consistently better having lower spurious current as compared to $\mathscr{H}_1$. On the other hand, $\mathscr{H}_3$ registers higher spurious currents with only few exceptions as compared to $\mathscr{H}_1$. This also reflects in the stability of the algorithm as the maximum density ratio for $\mathscr{H}_3$ is just shy of 200, against a maximum density ratio of above 600 for $\mathscr{H}_2$. So overall it becomes a practical decision to adopt model $\mathscr{H}_2$ for most of the simulations.

2.4.2.b. Surface tension/Laplace law

The simulation consists of a liquid droplet having a fixed radius suspended (i.e. without considering the gravitational forces) in the vapor or lighter fluid. For a stationary case the surface tension would balance with the pressure difference between the inside and the outside of the droplet. The relation between surface tension and pressure difference is provided by Laplace law. This law states that the pressure difference is inversely proportional to the radius of the droplet (in two dimensions) with the constant of proportionality being the surface tension itself.

The fig. 2.8.a and the fig. 2.8.b are the simulation results for the case where the liquid droplet with radius 22 l.u. is placed in domain of size 201×201. The domain is periodic on all sides. The first figure is the velocity profile exhibiting the direction and magnitude of spurious current. For any multiphase solver we observe the spurious currents primarily at the fluid-fluid interface. These current have a tendency to influence/adulterate the velocity field and hence care should be taken to minimize these currents such that its order of magnitude is lower than the fluid flow velocity. The second figure is a pressure profile through the centerline of the domain, the wild fluctuation as seen in the profile corresponds to the diffused interface which is not a physical result. Similar results have been obtained by [93] and is to be the feature of the model. This . The pressure difference (Δp) is calculated by considering the pressures at the midpoint of the centerline and at a point in the bulk of the surrounding phase. fig. 2.8.c depicts that the surface tension can be found by obtaining the slope for a plot of Δp values against the inverse of the corresponding droplet radius value. The surface tension (σ) for this scheme is 5.59×10^{-3} units.

2.4.2.c. Contact angle simulations for SCMP-SC

Here the case to be simulated is a liquid drop over a surface. the wettability of a surface depends upon the balance of the adhesive forces (between the solid and liquid particles) and the cohesive forces (in the liquid particles itself). the wetting of the surface can be measured in terms of the contact angle (θ) formed by the liquid droplet on the surface at the vapor-liquid-solid interface. when cohesive force decreases and is less than adhesive force the contact angle is less 90° and it tends to 0° and such a surface (w.r.t water) is known as hydrophilic surface. the vice-versa is also true, thus as the adhesion force decreases contact angle goes above 90° and tends to 180° and such a surface (w.r.t water) is known as hydrophobic surface.

Figure 2.9 depicts eight cases of observed contact angle of simulation with halfway BB (HBB). The domain sizes for these simulations were $\mathscr{N}_x \times \mathscr{N}_y = 301 \times 101$. For this simulations the domain is periodic on the east and the west boundaries but having wall on the top and the bottom. The

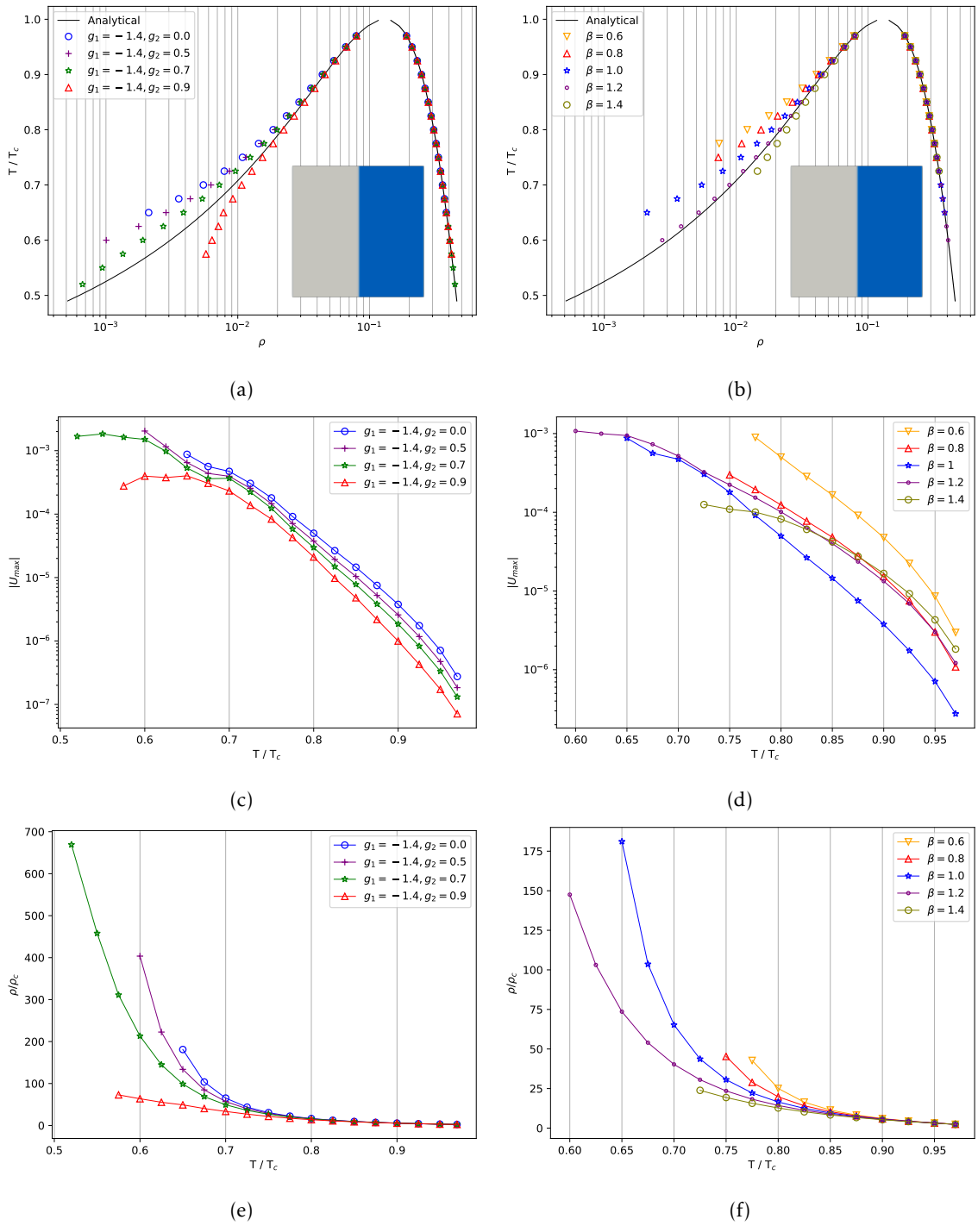

Figure 2.7: Coexistence curve for Carnahan-Starling EOS – simulating flat interface. (a), (c) and (d) are the coexistence curve, maximum absolute spurious current and density ratio respectively for Multirange model ($\mathscr{H}_2$). Similarly (b), (d) and (f) are the coexistence curve, maximum absolute spurious current and density ratio respectively for higher order ψ discretization ($\mathscr{H}_3$)

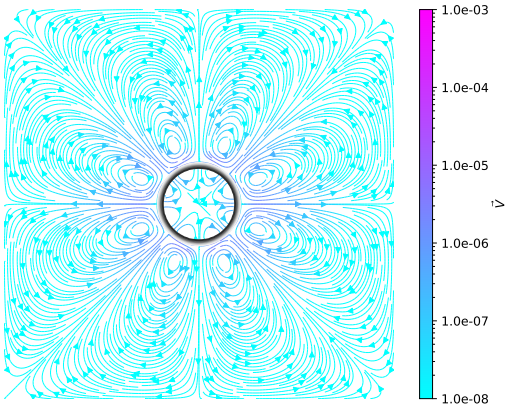

(a) Spurious currents (direction and magnitude)

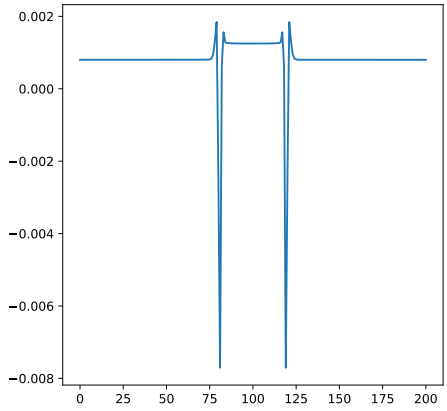

(b) Centerline pressure

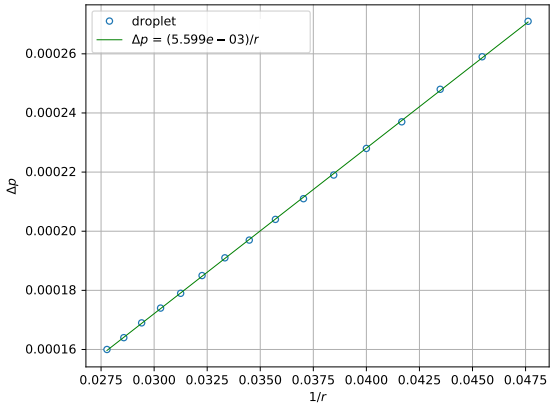

(c) Surface tension (σ) for a temperature

Figure 2.8: Suspended Droplet for Laplace law ($T/T_c = 0.825$, $\mathscr{H}_1$)

initialization of liquid as a semicircle is on the bottom wall at the center of the domain. The effect of gravity is minimal for this simulations with $g_{gr} = 10^{-7}$. As mentioned before, ρ_w is adjusted between ρ_{vap} (i.e. 180°) and ρ_{liq} (i.e. 0°) to achieve required contact angle. The contact angles were measured using the contact angle plugin of ImageJ software. Figure 2.10 plots the variation of θ versus normalized density $\left(\rho_w^* = \dfrac{\rho_w - \rho_{vap}}{\rho_{liq} - \rho_{vap}}\right)$. The nature of this model is such that studying the behavior of a liquid droplet on a surface with varying adhesion strength is possible with relative ease. Figure 2.10 shows the correlation between the static contact angle and pseudo-density of the wall. A linear correlation is observed across models ($\mathscr{H}_1$, $\mathscr{H}_2$ and $\mathscr{H}_3$) and across different temperatures with a deviation in slope observed for $T/T_c = 0.95$.

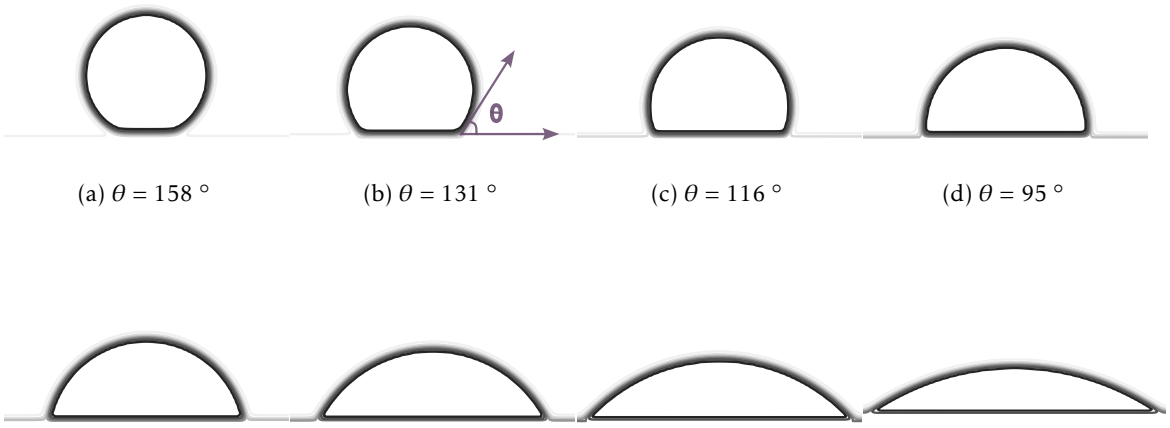

(a) $\theta = 158\,^\circ$ (b) $\theta = 131\,^\circ$ (c) $\theta = 116\,^\circ$ (d) $\theta = 95\,^\circ$

(e) $\theta = 78\,^\circ$ (f) $\theta = 63\,^\circ$ (g) $\theta = 48\,^\circ$ (h) $\theta = 33\,^\circ$

Figure 2.9: Contact angles for $T/T_c = 0.825$. ($\mathscr{H}_2$)

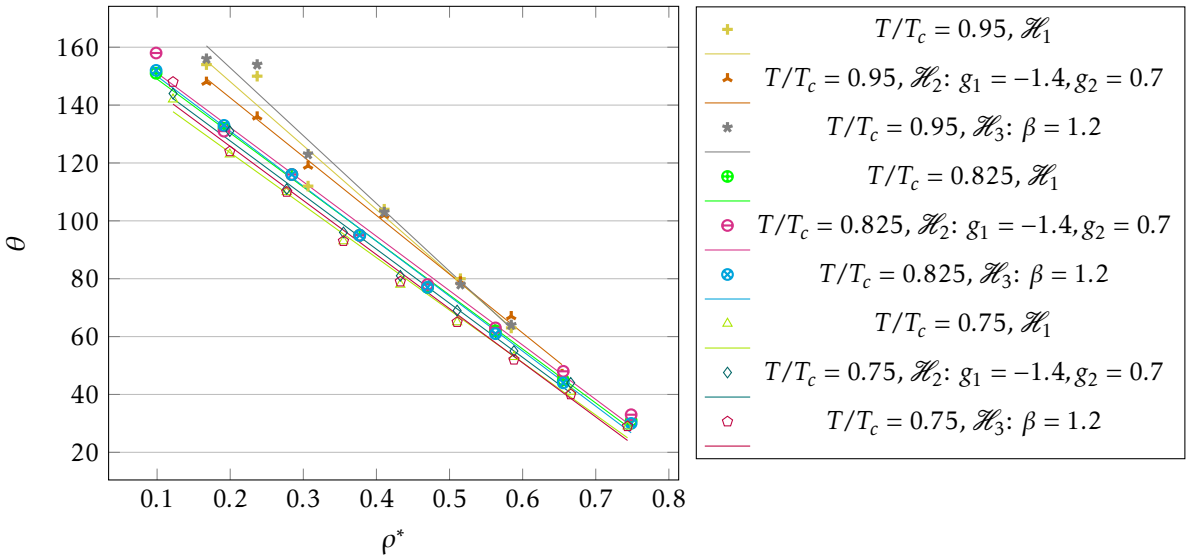

Figure 2.10: Contact angle ($\theta = \theta_{\text{stat}}$) for different ρ^*_{w} values at different temperatures.

From the next section onward, we perform validation studies for the SCMP-SC LBM solver so as to strengthen our case for utilization later in the optimization model/algorithm.

2.5. Wettability gradient surface (WGS)

A surface with variable wettability has been observed to propel/deform a droplet. Such surfaces are also known as wettability gradient surfaces (WGS). Figure 2.11 depicts the motion of a droplet under the influence of the linear wettability gradient. The streamlines are colored according to velocity intensity. Since the domain is periodic with a layer of solid nodes for modeling a flat surface/plate; the vapor is observed forming a boundary layer on both sides of the plate. Also at $\mathscr{T}_{\text{lbm}} = 46000$ t.s., we observe vortices in the droplet which are spurious currents in the proximity of an interface. These numerical artifacts seldom affect the phenomenon under consideration. Figure 2.13 illustrates motion of droplets on plates having wettability gradients of different form. Here is domain size is $\mathscr{N}_x \times \mathscr{N}_y = 601 \times 101$ with a plate length (L) of 580 l.u. and L/D ratio of 7.25. The gradient of

wettability only spans half the length of this plate. This section is a precursor for the chapter 4, which deals with the question of the optimum form i.e. distribution of the wettability gradient. A detailed discussion on the topic is availed therein. The following section 2.5.1, is used for validation of LBM for modeling droplet motion on a horizontal surface.

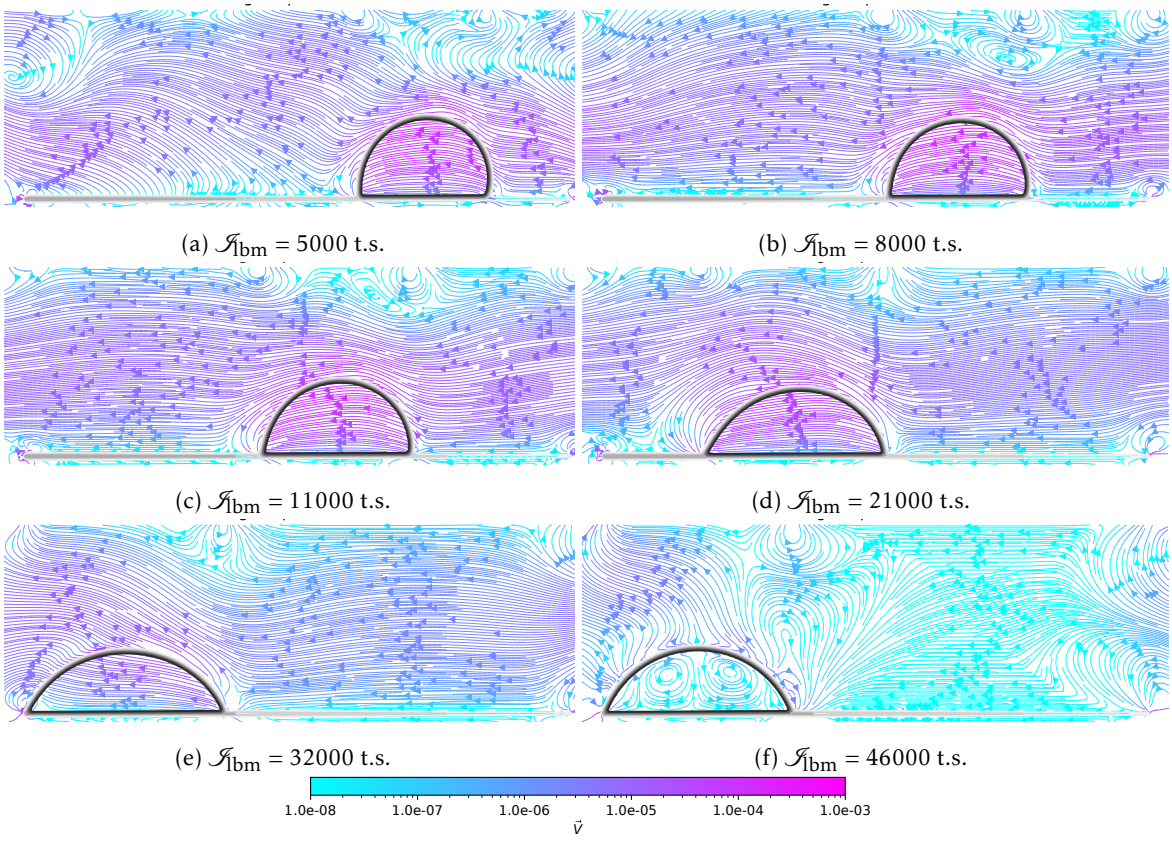

(a) $\mathscr{T}_{\text{lbm}}$ = 5000 t.s. (b) $\mathscr{T}_{\text{lbm}}$ = 8000 t.s.

(c) $\mathscr{T}_{\text{lbm}}$ = 11000 t.s. (d) $\mathscr{T}_{\text{lbm}}$ = 21000 t.s.

(e) $\mathscr{T}_{\text{lbm}}$ = 32000 t.s. (f) $\mathscr{T}_{\text{lbm}}$ = 46000 t.s.

Figure 2.11: Droplet movement due to linear density gradient for $T/T_c = 0.825$. ($\mathscr{H}_2$)

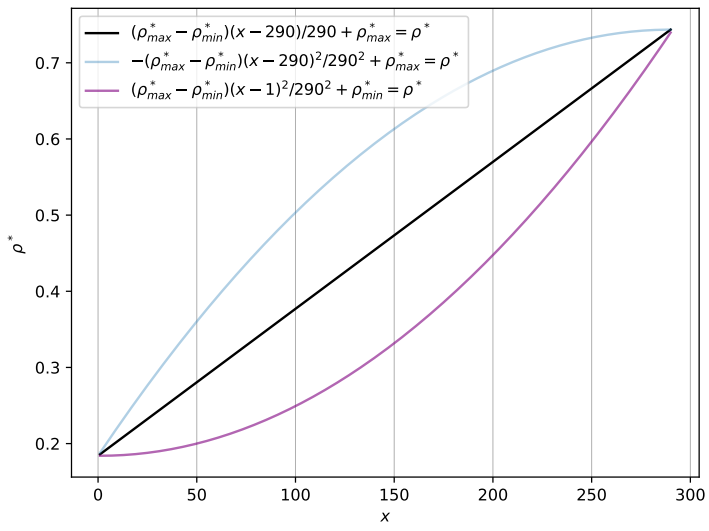

Figure 2.12: Rate of change of wettability for droplet movement (fig. 2.13) for $T/T_c = 0.75$

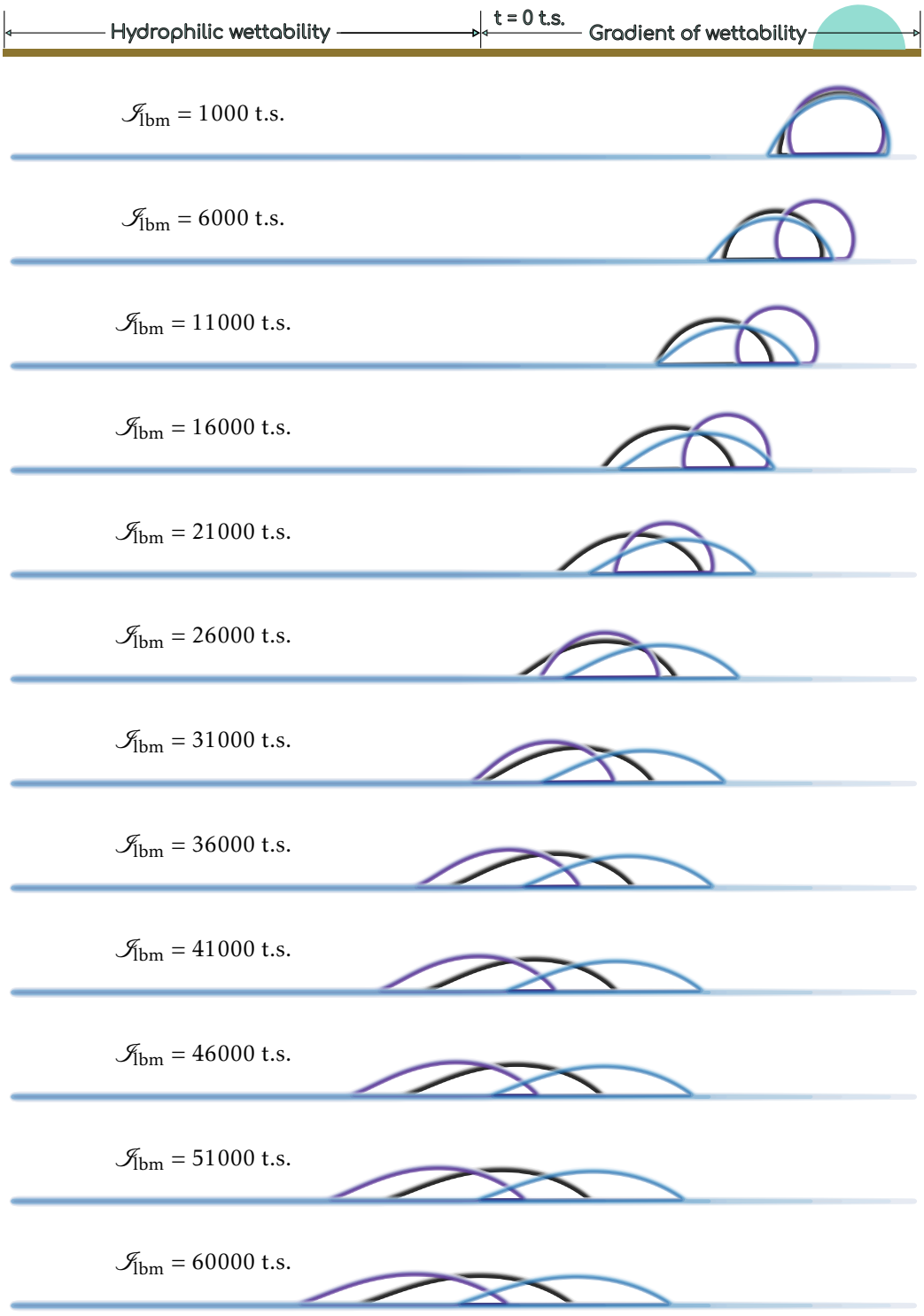

Figure 2.13: Comparative droplet movement for linear and quadratic (convex and concave) wettability gradient for $T/T_c = 0.75$. ($\mathscr{H}_2$). Refer fig. 2.12.

2.5.1. Asymptotic velocity of droplet

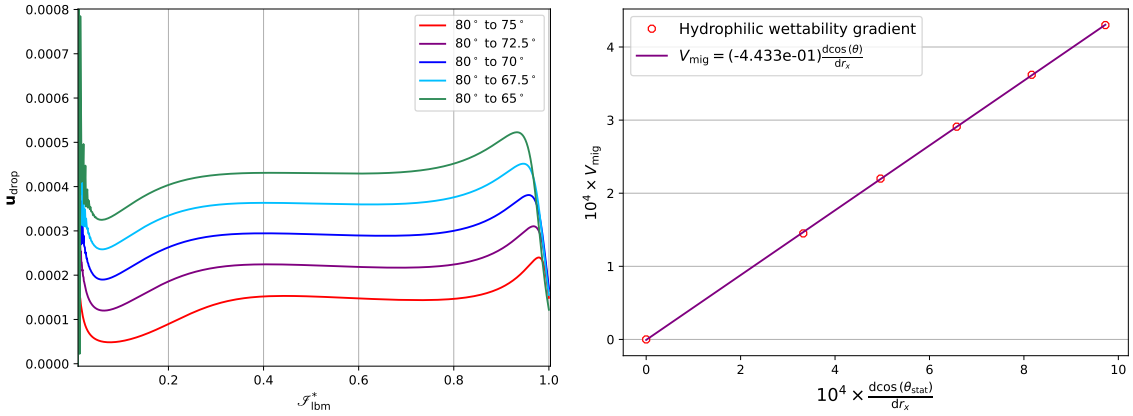

(a) (b)

Figure 2.14: (a)Velocity approaches asymptotic values for low intensity gradients. (b)Correlation between asymptotic velocity i.e. migration velocity ($\boldsymbol{V}_{\text{mig}}$) and intensity of the wettability gradient on a WGS (at $T/T_c = 0.875$). Using model $\mathscr{H}_1$

Generally, as a droplet is propelled on a WGS, its velocity ($\boldsymbol{u}_{\text{drop}}$) varies in accordance with the local gradient of wettability (under the belly of the droplet). For wettability gradient of low intensity, $\boldsymbol{u}_{\text{drop}}$ approaches an asymptotic value, i.e. a constant droplet velocity is observed for significant duration of the droplet journey. This is also known as migration velocity ($\boldsymbol{u}_{\text{mig}}$) of the droplet and is expressed as [1, 101]:

$$\boldsymbol{u}_{\text{mig}} = \alpha_v \frac{\sigma h_0}{\nu_{\text{liq}} \rho_{\text{liq}}} \left(\frac{\mathrm{d}\cos(\theta_{\text{stat}})}{\mathrm{d}r_x} \right) \tag{2.100}$$

where h_0 is the initial height of the droplet and α_v is the constant of proportionality. Figure 2.14a depicts the velocity of the droplet for low intensity gradients, after the initial fluctuation the velocity reaches an asymptotic value before peaking finally as the leading edge of the droplet touches the edge of the plate. Now it is observed [101] that the numerically obtained migration velocity ($\boldsymbol{V}_{\text{mig}}$) is linearly proportional to the intensity of the wettability gradient. *Please note the difference between two quantities $\boldsymbol{V}_{mig}$ and $\boldsymbol{u}_{mig}$; where the former quantity is numerically obtained the later quantity is analytically defined.* For a simulation on the small plate (i.e. domain size is $\mathscr{N}_x \times \mathscr{N}_y = 276 \times 101$ and length of plate (L) is 256 l.u.), the droplet size is such that $L/D = 4.51$, while the surface tension of the liquid is $\sigma = 0.003$. The Bond number of the simulation is Bo$= 2g_{\text{gr}}D^2\Delta\rho/(4\sigma) = 0.018294$ with the corresponding density ratio being $\rho_{\text{liq}}/\rho_{\text{vap}} = 7.35$ at temperature $T/T_c = 0.875$, the forward problem successfully reproduces the linearity for hydrophilic wettability distributions, as shown in fig. 2.14b (all values in fig. 2.14 are mentioned in LBM units). Also the constant of proportionality $\alpha_v = 0.28$ was recovered for hydrophilic wettability distributions against an $\alpha_v = 0.33$ obtained in [1]. As mentioned before we will utilize the wettability gradient surface as subject of our optimization studies.

2.6. Capillary tube

The capillary tube simulations can be considered to be an important precursor to simulating flow in an unsaturated porous media. This is because similar mechanisms are at work dictating the steady and dynamic behavior of fluids for both these systems. When modeling a real world case using LBM, the parameters are selected such that relevant non-dimensional numbers (like for e.g. Reynolds number, Bond number, capillary number, Weber number and etc.) of both the real world and LBM flow systems are the same. Thus rather than simulating/modeling a real world fluids like

air, water an equivalent flow is modeled. For this simulation, if the effect of gravity is required to be incorporated its strength can be determined by using the Bond number correlation. In other words this correlation is utilized for determining the appropriate gravitational strength/constant for a particular set of magnitudes of radius (R), contact angle (θ) and surface tension (σ) such that a similar system is obtained. The Bond number (Bo) is given as:

$$\mathrm{Bo} = \frac{2(\rho_{\mathrm{liq}} - \rho_{\mathrm{vap}})R^2 g_{\mathrm{gr}}}{\sigma \cos\theta^2} \tag{2.101}$$

Now the Laplace law can be given as: $\Delta p = \sigma\cos\theta/R$ and the hydrostatic pressure difference between top and bottom of a column of incompressible liquid is given as: $\Delta p = \Delta\rho h g$. Equating both relations we obtain:

$$h = \frac{\sigma\cos\theta}{(\rho_{\mathrm{liq}} - \rho_{\mathrm{vap}})R g_{\mathrm{gr}}} \tag{2.102}$$

From eq. (2.101) and eq. (2.102), it follows that the bond number for this case can be given as

$$\mathrm{Bo} = 2\frac{R}{h\cos\theta} \tag{2.103}$$

For e.g. a water-air system having a slit/capillary of radius 0.001 m, also for the tube we have a wetting surface with a contact angle $\theta_{\mathrm{real}} = 0°$, we know that $\rho_{\mathrm{liq}} = 10^3$ kg/m^3, $\rho_{\mathrm{vap}} \approx 1$ kg/m^3, with a surface tension of $\sigma = 0.07213$ N/m. Using eq. (2.102) and eq. (2.103), the height of capillary rise for the real world is calculated to be 0.00736 m, and the corresponding Bond number is Bo = 2/7.36. Similarly for (the LBM system) a capillary radius of 20 l.u., the gravity constant is estimated to be 3.16×10^{-6} units. *It is to be noted that unlike the real world simulation where we have a superhydrophilic capillary tube surfaces (i.e. completely wetting surface), for the LBM simulation the inner surfaces of the capillary are partially wetting (where $\theta = 48°$), this detail is captured by taking into account the contact angle for the Bond number formulation. This would also mean that the shape of the meniscus (in the LBM simulation) would differ from the real world.* Now for $\theta = 48°$ at $T/T_c = 0.825$ (where $\rho_{\mathrm{liq}} = 0.293$ units, $\rho_{\mathrm{vap}} = 0.02343$ units and surface tension is $\sigma = 0.0056$ units), we estimate the capillary height (h) to be 221 l.u..

For $\mathscr{H}_2$, the domain size for simulation is $\mathscr{N}_x \times \mathscr{N}_y = 1001 \times 500$, with periodic and wall BC. Due to the periodic boundary condition, if the wettability of the capillary tube is the same on the outer and inner sides of the tube or rather slit (due to the 2D nature of the simulation), then the simulation is equivalent of having two capillary tubes/slits (one having actual tube diameter and the other having a very large diameter being bounded by the outer sides of the tube/slit). Thus, we have contributions of competing capillary tube as illustrated by fig. 2.15a. To reduce the influence of the outer tube, we fix the wettability of the outermost layer of the tube to be almost 90° but slight leaning on the hydrophilic side. Also here the kinematic viscosities are the same for both the phase i.e. $\nu_{\mathrm{liq}} = \nu_{\mathrm{vap}} = 0.1666$ units, in other words the dynamic viscosity ratio here would equal the density ratio. After simulation we obtain the height of the column to be 255 l.u., where a 15% error is obtained due to the compressibility of the vapor phase [68]. As compression of a viscous fluid is more tedious, to test the hypothesis (of the compressibility of the vapor) we increase the viscosity of the vapor such that $\nu_{\mathrm{vap}} = \frac{140}{100}\nu_{\mathrm{liq}} = 0.23324$ units. Here eq. (2.91) is used for defining the local relaxation time. The column height obtained after simulation is 232 l.u., which represents a 5% error. The model also captures the dynamics of the rise of the capillary column. As the capillary tube is placed in a wetting fluid (i.e. the liquid) it is propelled to rise by the capillary forces of the tube. As the height of the column increases the gravity provides the resistance to the increase in the column height. The column height is stabilized when both the driving and resisting force are balanced. We divulge into the details later in the following subsections.

2.6.1. Washburn without gravity

In August 1920, Edward W. Washburn, submits a seminal paper [102] discussing the liquid penetration in capillaries and porous media. The Washburn equation describes the dynamics at the

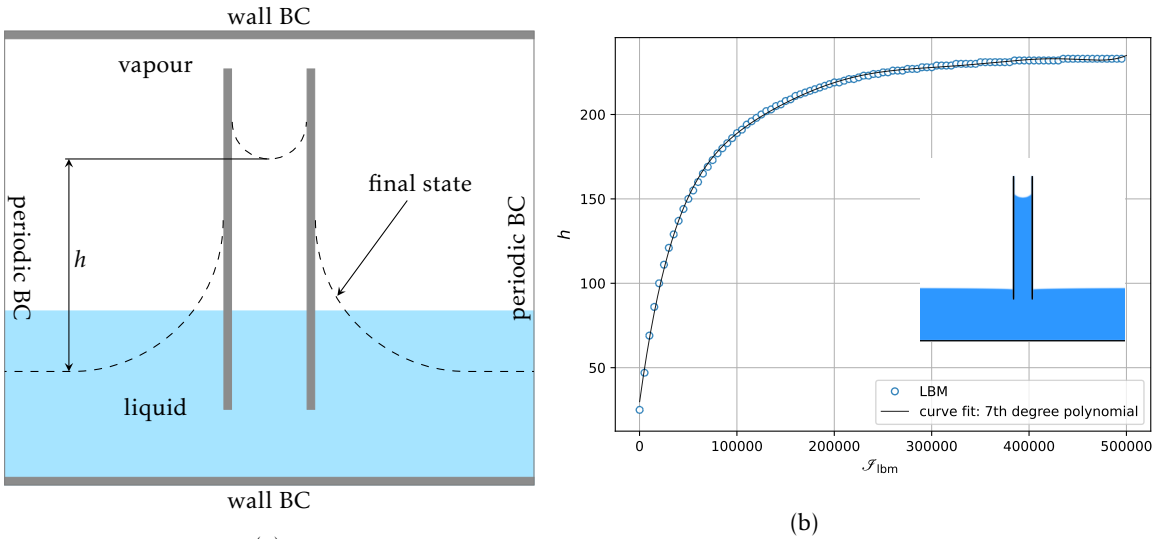

Figure 2.15: (a)Capillary simulation domain, final interface with the influence of two capillary; (b) Height of the column, after adjusting vapor viscosity. ($T/T_c = 0.825$, $\mathscr{H}_2$)

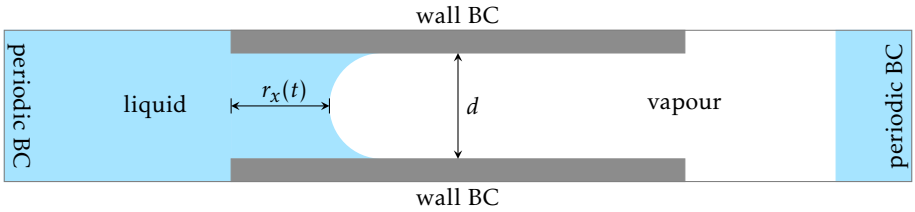

Figure 2.16: Simulation domain for Washburn validation

capillary interface/front. Here, after gravity is neglected [103], the equation is written as:

$$\frac{\mathrm{d}}{\mathrm{d}t}\left[r_x\frac{\mathrm{d}r_x}{\mathrm{d}t}\right] = \frac{2\sigma\cos\theta}{\rho_{\mathrm{liq}}d} - \frac{12\nu_{\mathrm{liq}}r_x}{d^2}\left[\frac{\mathrm{d}r_x}{\mathrm{d}t}\right] \tag{2.104}$$

where d is distance between the two plates, L is the maximum length of travel possible in the capillary i.e. the length/height of the capillary tube. For a system where the density ratio is not huge, the influence of the lighter phase cannot be neglected and Washburn equation can be solved to obtain [103]:

$$(\rho_{\mathrm{vap}}(L-r_x)+\rho_{\mathrm{liq}}r_x)\ddot{r_x} + (\rho_{\mathrm{liq}}-\rho_{\mathrm{vap}})(\dot{r_x})^2 = \frac{2\sigma\cos\theta}{d} - \frac{12\dot{r_x}}{d^2}(r_x\mu_{\mathrm{liq}}+\mu_{\mathrm{vap}}(L-r_x)) \tag{2.105}$$

If we neglect gravity, inertial forces and vapor viscosity then: [2, 103]:

$$d\sigma\cos(\theta) = 6r_x\nu\rho\frac{\mathrm{d}r_x}{\mathrm{d}t} \tag{2.106}$$

After integration we obtain:

$$\frac{d\sigma\cos(\theta)}{3\nu\rho}(t-0) = r_x^2(t) - r_x^2(0) \tag{2.107}$$

Thus rearranging eq. (2.107) we obtain $r_x(t)$ as:

$$r_x(t) = \sqrt{\frac{d\sigma\cos(\theta)}{3\nu\rho}t + r_x^2(0)} \tag{2.108}$$

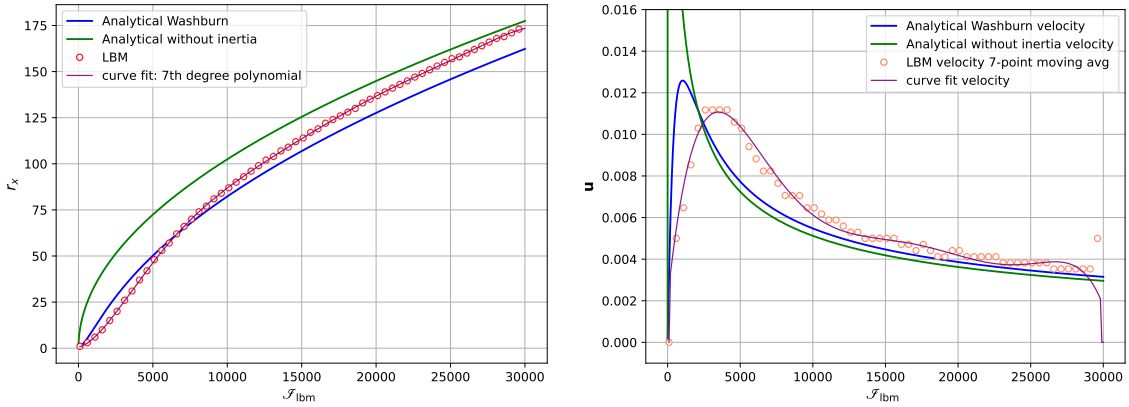

(a) Interface propagation

(b) Interface velocity

Figure 2.17: Front evolution for Washburn test case when $\rho_{liq}/\rho_{vap} = 12$ and $\nu_{vap}/\nu_{liq} = 1.4$ ($T/T_c = 0.825$)($\mathscr{H}_2$)

For $\mathscr{H}_2$, the simulation domain is illustrated by fig. 2.16, with a domain size of $\mathscr{N}_x \times \mathscr{N}_y = 401 \times 51$, having a distance between parallel plates of ($d = 41$ l.u.). Both the analytical equation i.e. eq. (2.105) and eq. (2.108) are used for comparison with the numerical results as shown in fig. 2.17. Here the gravitational constant is $g_{gr} = 0$, the liquid kinematic viscosity $\nu_{liq} = 0.1666$ units, while again the vapor viscosity is given as $\nu_{vap} = \frac{140}{100}\nu_{liq}$. For $T/T_c = 0.825$, the surface tension is $\sigma = 5.6 \times 10^{-3}$. Now eq. (2.108), predicts a sudden propagation of the interface as it comes under the influence of the capillary forces of the tube. On the other hand, eq. (2.105) predicts a latency and hence a smaller velocity of the interface/front. As the density ratio is of the order of $O(10^1)$, the viscous terms of the vapor when taken into account predicts a lower velocity. The progression of front in the simulation is delayed as an interface along with meniscus is formed. After which the front marches faster than eq. (2.105) (i.e. curve labeled as *analytical washburn*) to catch on to eq. (2.108) (i.e. curve labeled as *analytical without inertia*). This explanation is also supported by the graph indicating the interface velocity. For the numerical velocity, due to discretization sharp fluctuations are observed, two attempts have been made to mitigate an eyesore: the former consists of smoothing the numerical data using a moving point average and the latter consists of fitting a curve which could be latter used for velocity calculation. And we observe a reasonable convergence among these curves.

2.6.2. Inertial capillarity

Another interesting phenomenon observed by Washburn was that (as seen in fig. 2.17b), the velocity peaks when liquid is introduced to the capillary tube (especially with thin edges) even under the influence of gravity. This inertial component would dissipate during the initial rise of the column. It is possible to observe this inertial motion (in form of capillary oscillations) of the liquid column as shown by Quéré [104], if the viscosity of the liquid is low and the final column height is sufficiently small. More specifically, this behavior is predicted to occur when [104]:

$$\mu_{liq} << \frac{g_{gr}\rho_{liq}^{3/2}R^{5/2}}{\sigma^{1/2}} \tag{2.109}$$

For $\mathscr{H}_3$, we utilize the same parameters as the normal capillary tube i.e. $\mathscr{N}_x \times \mathscr{N}_y = 1001 \times 500$, $g_{gr} = 3.16 \times 10^{-6}$ units, $\theta_{stat} = 48°$, $\rho_{liq} = 0.293$ units and $\rho_{liq} = 0.02343$ units. Here the kinematic viscosity of the liquid is decreased where $\nu_{liq} = 0.0555$ units and the vapor viscosity is given as $\nu_{vap} = \frac{140}{100}\nu_{liq}$. Only the tube diameter or slit width (d) is varied from 80 l.u. to 200 l.u.. Figure 2.18 depicts interfacial position evolution corresponding to tube diameter, where height (h^*) is normalized w.r.t Jurin height (i.e. final height of liquid in a capillary column as $t \to \infty$). As is evident from fig. 2.18, with increase in the radius of the capillary tube one observes an increase in the number of

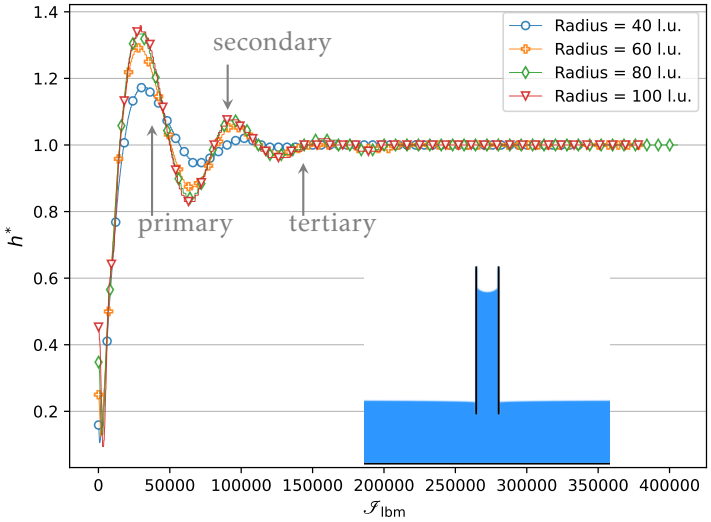

Figure 2.18: Non-linear fluctuations in the height of the liquid column in capillary tube due to inertia($T/T_c = 0.825$, model $\mathscr{H}_3$)

peaks (primary, secondary, tertiary and so on) with a simultaneous increase in the amplitude of the oscillations. Also as explained before the initial decrease in the column height is due to simultaneous interface and meniscus formation. This simulation is only possible due to the transient nature of the LBM solver.

2.7. Open boundaries

When we apply the open boundaries for the multiphase simulation the primary challenge lies in the boundary permitting the passage of the interface. The following simulations reveal the difficulties of incorporating open boundaries for SCMP-SC. Generally the inlet only injects fluid of a single phase, thereby making its implementation easy. Conversely, the outlet will during the course of the simulation encounter an interface and this causes unphysical results (Here *unphysical effects/results* refers to the deviation of the model results apart from the natural physical phenomenon. This might be caused due to the limitation of the model/algorithms, errors in code implementation and otherwise). Recently, at least two study [3] and [2] has been successful in incorporating these boundaries (the former velocity inlet and convective outlet and the latter uses Neumann outlet) for SCMP-SC which was coupled to thermal equations for studying phase change (i.e. boiling). Unfortunately, this success could not be replicated as of writing this thesis. To verify our results we also cross check our results using an open source lattice Boltzmann software (OpenLB) [105, 106]. It is a C++ program/library which for modeling LBM model for different case like: interfacial flows, heat transfer, turbulence, particle transport and so no. Later we encapsulate the comparisons of the results (i.e. those from OpenLB and the code developed in-house) in tables.

2.7.1. Normal tube

The normal tube simulation consists of a thin vertical tube with the inlet at top (north) and the outlet at the bottom (south). Flow through a tube can be categorized into two types which are drainage and imbibition. For drainage the non-wetting fluid (NWF) is invading (or is being injected into) a domain saturated by a wetting fluid (WF). Conversely, for imbibition the wetting fluid is invading a domain saturated by a non-wetting fluid. Unless specified otherwise the velocity and the pressure BC employs the ZH BC. Also no gravitational forces are applied for this study.

2.7.1.a. Velocity inlet - Neumann outlet (VI-BB-NO)

For $\mathscr{H}_1$, we simulate on a domain size of $\mathscr{N}_x \times \mathscr{N}_y = 90 \times 301$ and the tube radius is 30 l.u.. The initial length of the liquid column is 30 l.u. (starting from the velocity inlet (VI) to the liquid-vapor interface). It is to be noted that at time $t = 0$, we only initialize the VI with the constant inlet velocity. Simultaneously the velocity of all fluids farther in the domain are initialized to null velocity (this manner of initialization has been employed by default for simulations with velocity inlets, unless otherwise specified). This means that (in this case) the liquid injected will push the rest of the available liquid column. For a wide range of input velocities ($u_{y,\text{in}}$) ranging from 10^{-1} to 10^{-7}l.u./t.s., we obtain the corresponding saturation ($\mathscr{S}$) profiles. The saturation profiles are then plotted against normalized time. These saturation profiles are linear, as can be deciphered from table 2.4 and fig. 2.19a. Here non-dimensional or normalized time is defined as $t/\tilde{t}$, which is similar to $\mathscr{S}^*_{\text{lbm}}$. The normalization is done using theoretical time which is defined as $\tilde{t} = \dfrac{\Delta(r_y)}{u_{y,\text{in}}}$. For liquid velocities such that, $u_{y,\text{in}} \leq 10^{-4}$ l.u./t.s., stalling is observed in the latter part of the simulation, as the liquid interface reaches the vicinity of Neumann outlet.

To elaborate we plot fig. 2.19b which depicts the velocity field for $u_y = 10^{-6}$l.u./t.s. and the fig. 2.19c which is the corresponding centerline velocity at $\mathscr{S}_{\text{lbm}} = 2 \times 10^7$t.s.. The velocity field is analyzed by dividing it into four regions. The region I includes the velocity inlet and up to 20 nodes below, where acceleration of the liquid (up to 10^{-4}l.u./t.s.) from the corners of the VI is observed. Also in this region the liquid dissipates this additional energy as the liquid proceeds into the next region. The region II is the core of the liquid body and it moves with the velocity of 1.35×10^{-6}l.u./t.s.. This slight increase in velocity can be attributed to the development of the boundary layer. Also, we observe that region III the order of magnitude of spurious current is 10^{-5} l.u./t.s.. Though this is an order of magnitude greater than the inlet velocity it has practically no influence as observed previously in fig. 2.19a. In the region IV, non-physical vapor velocity predominately observed adjacent to the interfacial region and nearly null velocity ($\approx 10^{-10}$) at the outlet. The few irregularities observed are summarized as:

1. Initial reverse flow or rather *evaporation* (numerical artifact) is observed (especially $< 10^{-3}$ l.u./t.s.) and this has been linked to the presence of the outlet.

2. Compressibility of liquid is though to be dominant for lower velocities ($< 10^{-3}$ l.u./t.s.) hence the liquid interface is halted ahead of the outlet.

3. Effect of the boundary conditions on the interface shape and hence the saturation profile (as the interface touches the boundary).

Conversely, for the same configuration, when vapor is pushing/invading liquid being the non-wetting phase i.e. draining the liquid, the initial vapor domain/column collapses. Now for imbibition in tube we require the pressure inlet, currently this lies beyond the scope of the thesis. At any rate this configuration i.e. velocity inlet-bounceback-Neumann outlet (VI-BB-NO), allows for injection of liquid i.e. drainage, for injection of vapor, the vapor column collapses, refer table 2.6. Now to compare this result with OpenLB library is not possible as the Neumann BC is not presently available in OpenLB.

2.7.1.b. Velocity inlet - pressure outlet (VI-BB-PO)

The major issue with having a pressure boundary as an outlet boundary, is that for LBM the pressure of the fluid is linked invariably to its density. Thus a prescription of pressure at the outlet boundary will inadvertently arrest the flow of fluids without the prescribed density (in the multiphase scenario). For $\mathscr{H}_4$, while modeling the drainage test case, the domain size is given as $\mathscr{N}_x \times \mathscr{N}_y = 32 \times 300$, where the tube radius is 30 l.u.. Running the simulation for different input velocity ($u_{y,\text{in}}$) ranging from 10^{-1} l.u./t.s. to 10^{-5} l.u./t.s. the meniscus displacement and thereby the liquid saturation, also

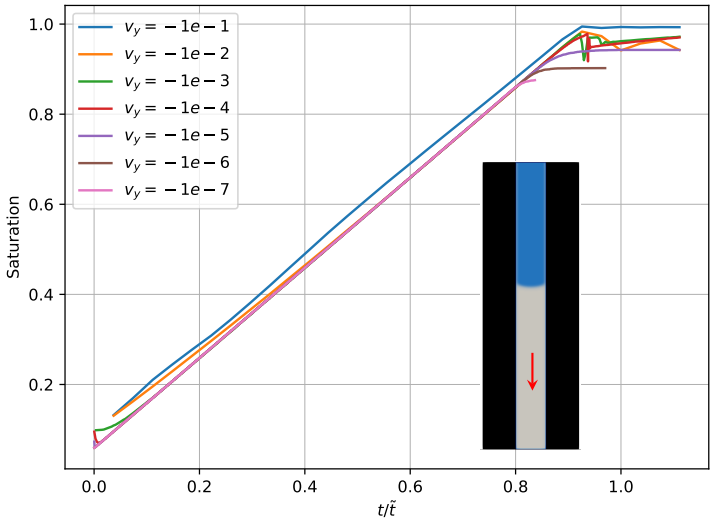

(a) Normalized saturation profile

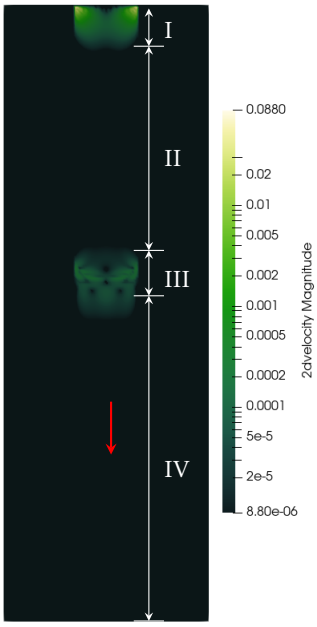

(b) Velocity magnitude for $u_{y,\text{in}} = 10^{-6}$l.u./t.s. at $\mathscr{T}_{\text{lbm}} = 2 \times 10^7$t.s..

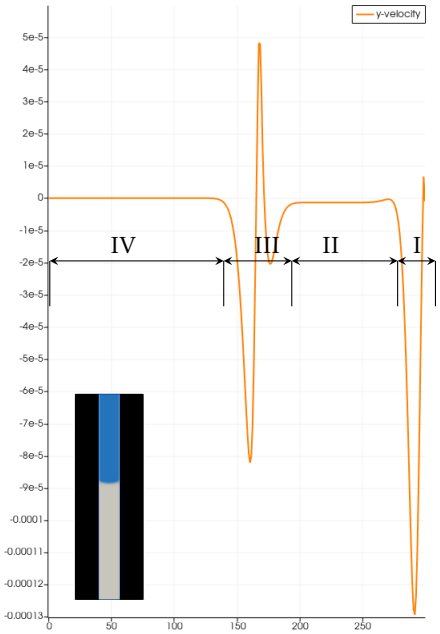

(c) Centerline velocity for $u_{y,\text{in}} = 10^{-6}$l.u./t.s. at $\mathscr{T}_{\text{lbm}} = 2 \times 10^7$t.s..

Figure 2.19: Drainage in normal tube; VI-BB-NO configuration ($\mathscr{H}_1$)

$\lvert u_y \rvert$	$(\tilde{t} = \Delta r_y / \lvert u_y \rvert)$(t.s.)	Actual time(t.s.)
10^{-1}	2.7×10^{3}	2.4×10^{-3}
10^{-2}	2.7×10^{4}	2.5×10^{4}
10^{-3}	2.7×10^{5}	2.65×10^{-5}
10^{-4}	2.7×10^{6}	–
10^{-5}	2.7×10^{7}	–

Table 2.3: LBM time for complete saturation (where $\tilde{t}$ is theoretical time)– Drainage in the normal tube (VI-BB-PO). ($\mathscr{H}_4$)

$\lvert u_y \rvert$	$(\tilde{t} = \Delta r_y / \lvert u_y \rvert)$(t.s.)	Actual time(t.s.)
10^{-1}	2.7×10^{-3}	2.4×10^{-3}
10^{-2}	2.7×10^{-4}	2.5×10^{-4}
10^{-3}	2.7×10^{-5}	2.5×10^{-5}
10^{-4}	2.7×10^{-6}	2.52×10^{-6}
10^{-5}	2.7×10^{-7}	–
10^{-6}	2.7×10^{-8}	–
10^{-7}	2.7×10^{-9}	–

Table 2.4: LBM time for complete saturation – Drainage in the normal tube (VI-BB-NO). ($\mathscr{H}_1$)

the mass conservation are obtained during drainage. Figure 2.21 indicates the conservation of mass for case with $u_{y,\text{in}} = 10^{-3}$ l.u./t.s.. The conservation of mass is defined as difference in flux (ΔQ) equals the change in mass of a system over time ($\sum_{\mathcal{D}} \frac{\Delta \rho}{\Delta t}$). From the graph it is evident that mass is not conserved at the initial phase of the simulation and also finally when the interface reaches the outlet boundary. Figure 2.20 shows the evolution of liquid saturation (non-wetting fluid). It can be seen that for velocities higher than 10^{-4} l.u./t.s. the liquid will completely fill the tube, but as the inlet velocity decrease the liquid movement will get slower so that for an inlet velocity of 10^{-4} l.u./t.s. the liquid saturation will only reach 40 %.

Now, we notice especially for the inlet velocity of 10^{-5} l.u./t.s. the initial liquid domain will collapse although at the beginning of the simulation the pressure at the inlet is higher than the outlet pressure. For $u_{y,\text{in}} = 10^{-1}$ l.u./t.s., the saturation curve is not linear. In fact for this case we observe a strong fluctuation of the inlet pressure, which is not the case for lower velocities where it remains constant at $P_{\text{in}} = 25.6$ units. As for the previous configuration, we compare the actual time (t) to reach complete tube saturation with the theoretical time to form non-dimensional time, (see table 2.3). Here the meniscus movement is slightly faster than the theoretical speed. It is observed that the that the liquid velocity is slightly higher than the input velocity. Also the vapor and liquid phase are not moving at the same velocity. On the other hand, when we perform the drainage test case with vapor pushing liquid (vapor is the non-wetting phase) the initial vapor domain/column will collapse.

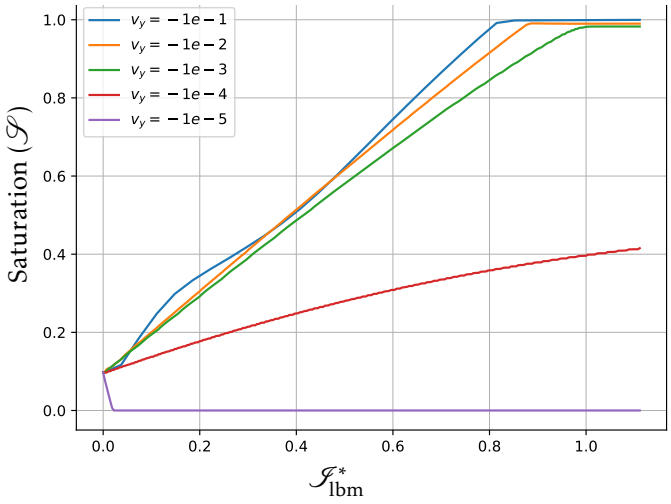

Figure 2.20: Normalized saturation profile – Drainage in the normal tube (VI-BB-PO). ($\mathscr{H}_4$)

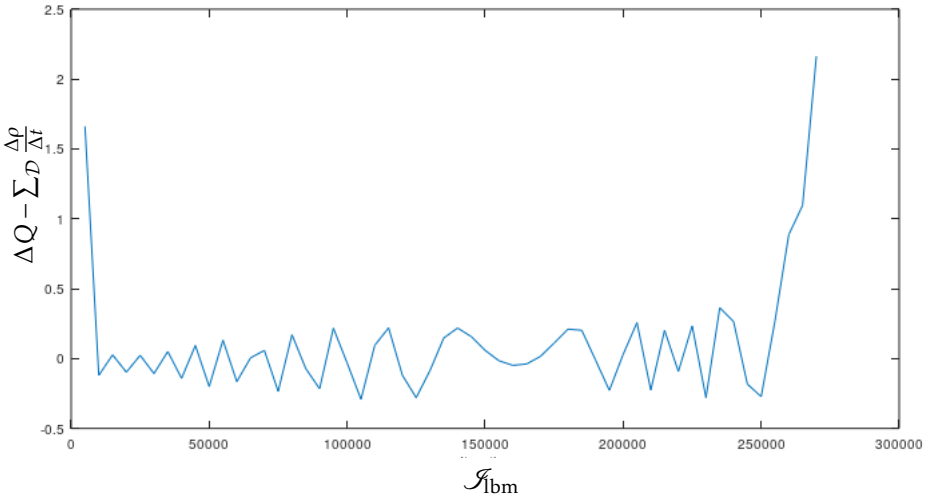

Figure 2.21: Mass conservation for normal tube (mass conservation(%) v/s $\mathscr{T}_{\text{lbm}}$); $u_{y,\text{in}} = 10^{-3}$ l.u./t.s.. (VI-BB-PO) ($\mathscr{H}_4$)

2.7.1.c. Pressure inlet - pressure outlet (PI-BB-PO)

For $\mathscr{H}_4$, and the same geometry as in section 2.7.1.b with different boundary conditions. Here we have pressure boundaries at the north and the south. The pressure boundary in LBM is implemented by fixing the density at the boundary. Discretionary values are attributed as the density at the inlet/outlet nodes, and by tuning the value of this density we control the value of the pressure and possibly the flow direction. Two cases are deliberated on:

1. When liquid pushes vapor: The liquid is present at the inlet where the pressure is fixed by setting $p_{\text{in}} = p(\rho_{\text{liq}})$ and the outlet pressure (vapor outlet) will be modified i.e. $p_{\text{out}} = p(\rho_{\text{vap}} + \daleth)$. Here, the liquid is the NWF. Thus if $\daleth = 0$, then both the liquid and the vapor pressure satisfies the Young-Laplace rule, in other words, the interface would proceed to south in the direction of the outlet. The tube will be completely filled as the interface reaches the outlet at $\mathscr{T}_{\text{lbm}} = 21 \times 10^3$ t.s.. If $\daleth = \frac{6.6}{100}\rho_{\text{avg}}$, (where $\rho_{\text{avg}} = 0.5(\rho_{\text{vap}} + \rho_{\text{liq}})$), such that $p_{\text{in}} < p_{\text{out}}$, then the interface would still proceed towards southern outlet. The tube would be saturated within $\mathscr{T}_{\text{lbm}} = 14 \times 10^3$ t.s., which was unexpected. Now if $\daleth = -\frac{6.6}{100}\rho_{\text{avg}}$, such that $p_{\text{in}} > p_{\text{out}}$, then the interface would proceed towards southwards as excepted. Only exception being that here

OpenLB				
LBM boundaries	Drainage in tube		Imbibition in tube	
	$\aleph > 1$	$\aleph < 1$	$\aleph < 1$	$\aleph > 1$
VI-BB-NO	–	–	–	–
VI-BB-PO	Pass. Good saturation but high vapour velocity	Fail. Vapour column collapse	Pass. Not of interest	Fail. Not of interest
PI-BB-PO	Pass. Liquid invades by default $[P_{in}(\rho_{liq}) > P_{out}(\rho_{vap})]$. For $P_{in}(\rho_{liq} + \beth) > P_{out}$ this behavior is reproduced.	Fail. Vapor front withdraws by default$[P_{in}(\rho_{vap}) < P_{out}(\rho_{liq})]$. For $[P_{in}(\rho_{vap} + \beth) > P_{out}]$ this behavior is reproduced. For $[P_{in}(\rho_{vap} - \beth) < P_{out}]$ the vapor invades.	Pass. (similar to Capillary)	Pass? For $[P_{in}(\rho_{liq} - \beth) < P_{out}]$ the liquid front withdraws.
Periodic-BB	Not possible	Not possible	Pass. (Capillary)	Pass

Here, $\aleph = \frac{\rho_{nwet}}{\rho_{wet}}$ and $\beth > 0$ such that $\beth$ causes significant change in pressure value.
VI : velocity inlet (Zou and He) PI/PO : pressure inlet/outlet (Zou and He)
BB : bounceback for walls NO : Neumann outlet CO : convective outlet

Table 2.5: Possibilities with OpenLB SCMP-SC– $\mathscr{H}_4$

the interface velocity is the smallest with a stall, preventing complete filling of the tube.The evolution of the saturation curve for these three $\beth$ values is shown on fig. 2.22a.

2. When vapor pushes liquid: Now the pressure of the vapor boundary will be fixed as $p_{in} = p(\rho_{vap})$ and the liquid boundary pressure will be modified i.e. $p_{out} = p(\rho_{liq} + \beth)$. Here the liquid is the WF. Now if $\beth = 0$, then both the liquid and the vapor pressures satisfies the Young-Laplace rule, however the initial vapor column collapses very quickly i.e. the vapor front withdraws back to the PI. When $\beth = \frac{6.6}{100}\rho_{avg}$, then $p_{in} < p_{out}$ i.e. again the vapor domain will quickly collapse. Figure 2.22b shows that at the beginning of the simulation the mass is not conserved so this configuration cannot be adopted later for our study. Now if $\beth = -\frac{6.6}{100}\rho_{avg}$, such that $p_{in} > p_{out}$ then the vapor front moves in the direction of the southern PO. The velocity of the vapor front increases as it transverses towards the PO. A complete drainage is achieved at $\mathscr{I}_{lbm} = 34 \times 10^3$ t.s..The corresponding mass conservation plot fig. 2.22c.

As these numerical experiments had shown, SCMP-SC is not the best tool to study imbibition. The code is very sensitive to the WF/NWF configuration and for the pressure condition at the boundaries. For liquid pushing vapor the meniscus seems to move in the expected direction, but when vapor pushes liquid or when modifying pressure at the boundaries, we retrieve unexpected results. A possible explanation could be the *phase change* phenomenon observed at the interface (without thermal excitation, other words this is a numerical artifact). Please note that it is possible to have a change in phase in the pseudopotential model, but this is the case only when non-equilibrium values are proposed for either or all of the phases/components/fluids. This *readjusting* of the density values is usually accomplished only in the beginning of the simulation. For our case we already fed the code the equilibrium values of the density and also the *phase change* we talk of only happens in the presence of an outlet. Meanwhile, an explanation for vapor column collapsing would be that the vapor isn't developing enough momentum to push liquid (due to compressibility). Thus, now we have a better idea of what can be expected with SCMP-SC for drainage and also when simulating imbibition in a porous media with open boundaries.

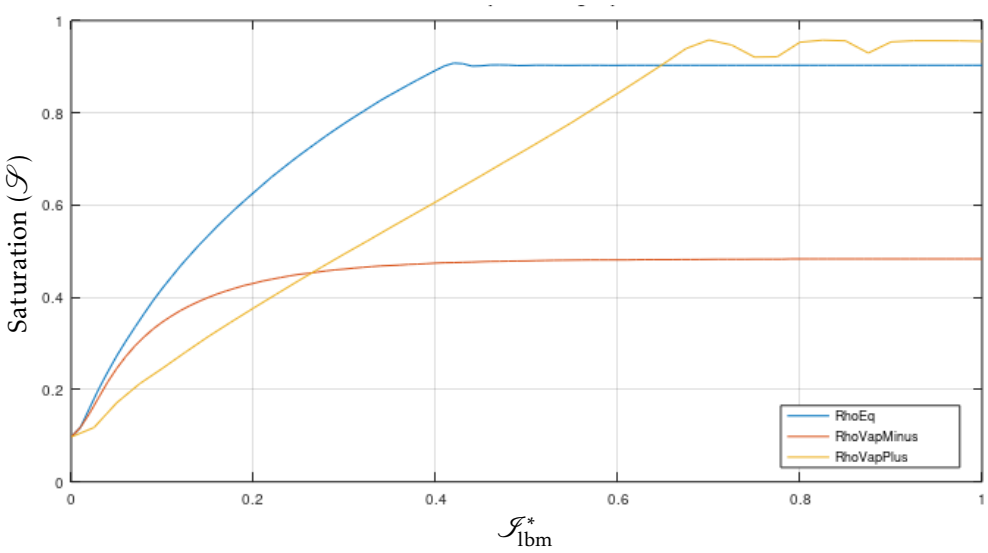

(a)

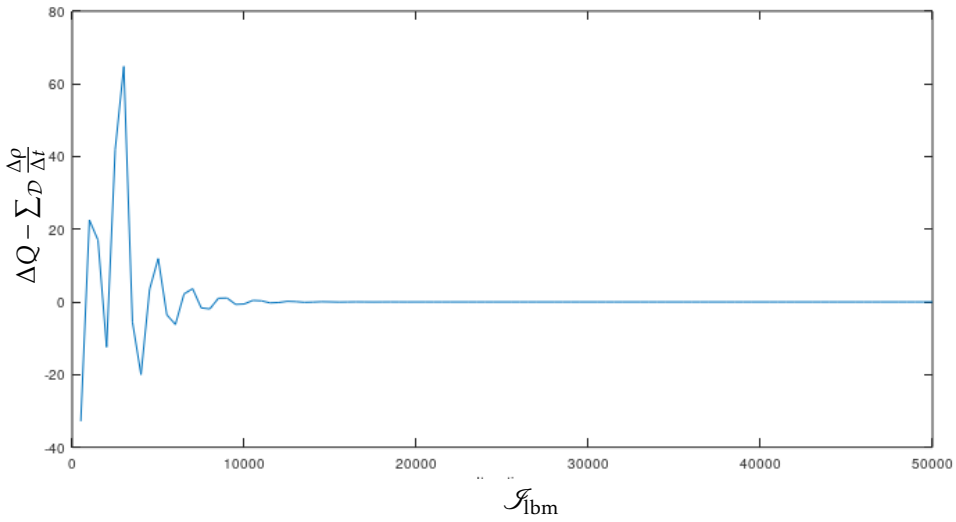

(b)

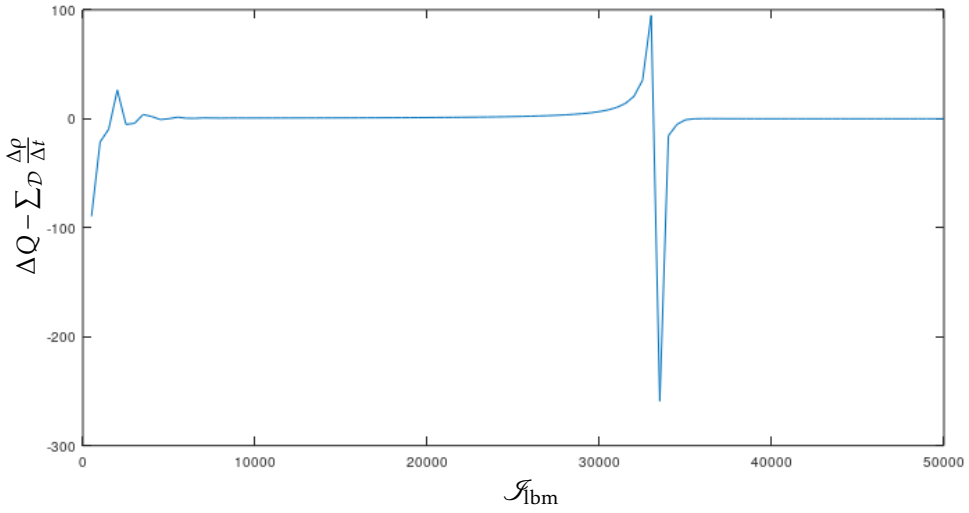

(c)

Figure 2.22: (a) Normalized saturation profile; (b) Mass conservation for vapor pushing liquid–$P_{\text{liq}} > P_{\text{vap}}$; (c) Mass conservation for vapor pushing liquid–$P_{\text{liq}} < P_{\text{vap}}$ (PI-BB-PO configuration and $\mathscr{H}_4$ model)

In-house CUDA code				
LBM boundaries	Drainage in tube		Imbibition in tube	
	$\aleph > 1$	$\aleph < 1$	$\aleph < 1$	$\aleph > 1$
VI-BB-NO	Pass. Good saturation but high vapour velocity	Fail. Vapour column collapses	Pass. Not of interest	Fail. Not of interest
VI-BB-PO	Pass. Good saturation but high vapour velocity	Fail	Pass. Not of interest	Fail. Not of interest
PI-BB-PO	Work in progress	Work in progress	Work in progress	Work in progress
Periodic-BB	Not possible	Not possible	Pass. (Capillary)	Pass

Here, $\aleph = \frac{\rho_{nw}}{\rho_w}$ and $\daleth > 0$ such that $\daleth$ causes significant change in pressure value.
VI : velocity inlet (Zou and He) PI/PO : pressure inlet/outlet (Zou and He)
BB : bounceback for walls NO : Neumann outlet CO : convective outlet

Table 2.6: Possibilities with in-house SCMP LBM solver – $\mathscr{H}_1$

2.7.2. Drop channel flow

Here we take a closer look at the effects of the Neumann outlet boundary on the interface (in a multiphase simulation). Hereafter unless specified otherwise the second order discretization is used for Neumann outlet. In this simulation we push a droplet towards the outlet. This is also a benchmark case used for testing different multiphase outlet behaviors [58]. For $\mathscr{H}_2$, the domain size is $\mathscr{N}_x \times \mathscr{N}_y = 91 \times 301$, where the tube diameter is 81 l.u.. The (Ladd's) VI lies in the north and the NO lies in the south. The initial droplet position was at the one third of the total length from the south. With an inlet velocity of 10^{-2} l.u./t.s., the vapor is injected pushing the droplet. Certain abnormalities are observed during the course of the simulation fig. 2.23:

1. A larger velocity is observed in the vapor ahead of droplet (i.e. towards the outlet) rather than in the rear. This could be partly due to initial pressure waves (which is commonly observed) which could influence the NO.

2. As soon as the droplet partially crosses the outlet boundary, this creates pressure waves (i.e. density fluctuations) also the droplet cannot fully travel through the outlet.

3. Reverse flow/filling is obtained at the outlet with an increase in saturation in spite of the vapor flux into the domain. This again hints to the compressibility of the vapor phase.

2.7.3. Stepped tube

During an liquid injection into an unsaturated porous media, the liquid and its interface can encounter a gradient in the pore diameter either smooth or sudden/sharp. Here we stack pores of different diameter on top of each other and pass a flow through this circuit. This simulation attempts to capture/understand the pressure fluctuations (at the inlet) when the interface moves to a larger pore and then a smaller pore. This simple test is interesting as we are able to distinguish what is the impact of discovering pores of different sizes. Usually in any normal porous media we observed a cumulative efforts as multiple pore discoveries are made as the liquid front is simultaneously introduced to these pores. Here for $\mathscr{H}_2$ the domain size is $\mathscr{N}_x \times \mathscr{N}_y = 91 \times 300$ and also having open boundaries i.e. (Ladd's) VI and NO boundary conditions. The inlet velocity is 10^{-4} l.u./t.s. i.e. $\mathfrak{Re}_{\text{inlet}} = 2.4 \times 10^{-3}$ and $\log|\mathfrak{Ca}| = -4.0$. Also the viscosity ratio is $\log|M| = 1.1$. We observe from the fig. 2.24c that as the interface moves into the larger pore initially there is a minor increase (in pressure) which is followed by a decrease of pressure as the liquid eases into the larger pore. Also, it can be seen that pinning of liquid to the sides of the tube reduces pressure instantly (which is observed three times as the interface transverses the larger tube). As the interface moves to the smaller

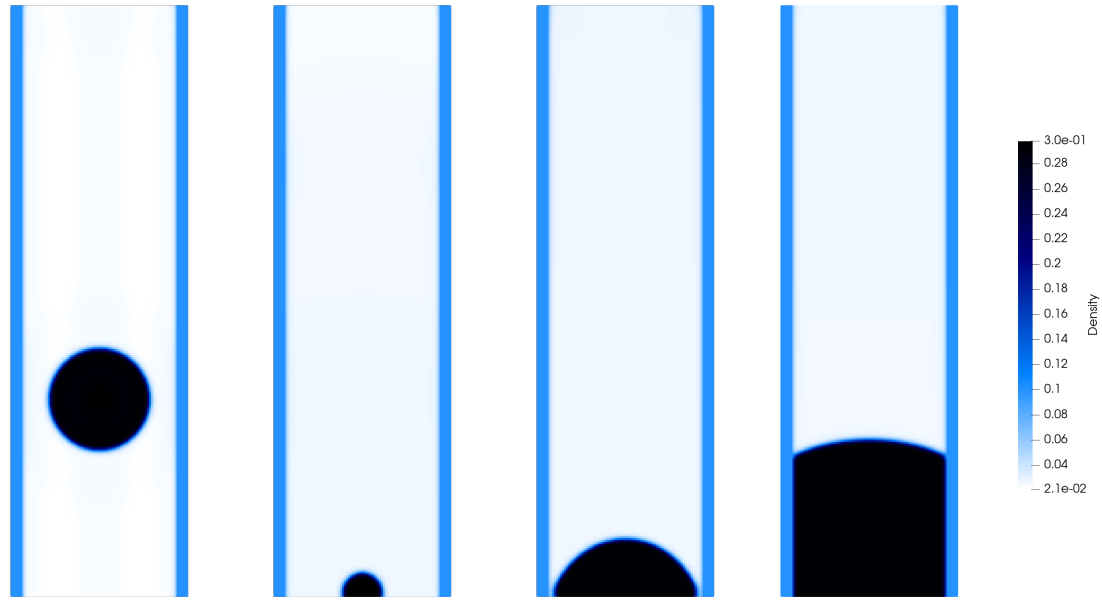

(a) $\mathscr{T}_{\text{lbm}} = 100$ t.s. (b) $\mathscr{T}_{\text{lbm}} = 7500$ t.s. (c) $\mathscr{T}_{\text{lbm}} = 34300$ t.s. (d) $\mathscr{T}_{\text{lbm}} = 60000$ t.s.

Figure 2.23: Droplet in a channel, model $\mathscr{H}_2$ and $T/T_c = 0.825$

pore the pressure spikes until sufficient pressure is buildup for pore invasion/breakthrough. The ratio of the diameters from the inlet to the outlet is $2:4:1$. The mass conservation curve for the stepped tube is depicted in fig. 2.24a. We observe reserve flow or more appropriately *evaporation* due to the outlet presence. Also the unphysical effects, as discussed previously are observed as the liquid interface comes into contact with the Neumann outlet. Thus we ignore the simulation results before the interface reaches the vicinity of the outlet.

2.7.4. Preferred path

For the previous stepped tube simulation we have looked at the behavior of the liquid as it goes sequentially through larger and smaller pores. Liquid invading a porous media uses the least resistant path. Often the liquid comes across a better route simultaneously and hence liquid flow direction/path in a porous media can change real time. This simulation is a proof of this concept. If we use the pore network model for this simulation then (as explained before), we would only observe the final steady path but not the transient change. For $\mathscr{H}_2$, the domain size is given by $\mathscr{N}_x \times \mathscr{N}_y = 201 \times 301$, the ratio of the inlet, channel, larger and smaller pore radii are $4:2:8:1$. Here the model has (Ladd's) VI and NO boundary conditions. The inlet velocity is 10^{-5} l.u./t.s. i.e. $\text{Re}_{\text{inlet}} = 2.4 \times 10^{-3}$ and $\log|\text{Ca}| = -4.0$. Also the viscosity ratio is $\log|M| = 1.1$. Here the liquid interface comes simultaneously in contact with the larger and shorter pores. After the initial *evaporation*, the interface is such that the channel towards the smaller pore is partially invaded while the opposing channel (towards the larger pore) is mostly emptied. This is reflected by an initial decrease in saturation and also a deviation from mass conservation. As we proceed further the interface reaches the smallest pore first (being pinned on to the smaller pore interface) and later as the interface passes through the top corner of the channel (i.e. a small increase of cross-section of the pipe) we observe a minor Haines jump. The liquid front again achieves pinning at the smallest pore entry. As the breakthrough pressure is significant the liquid further invades towards the larger pore. When the liquid flows into the larger pore, this also cause backflow (i.e. Haines jump) in the channels. Now the flow is solely towards the larger pore. As discussed previously we again observe the second minor bump as the liquid enters the larger pore and this can be attributed to the change of radius of curvature of the interface. We observe reverse flow or more appropriately *evaporation*

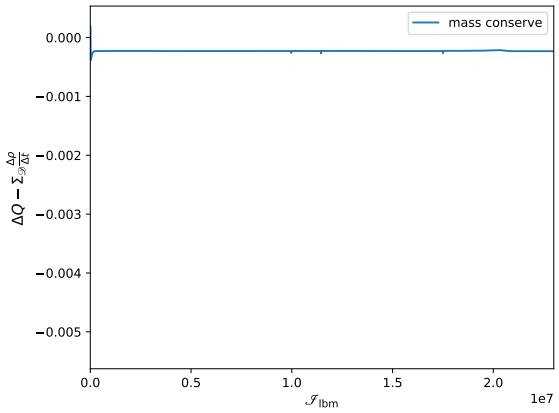

(a) Mass conservation for stepped tube.

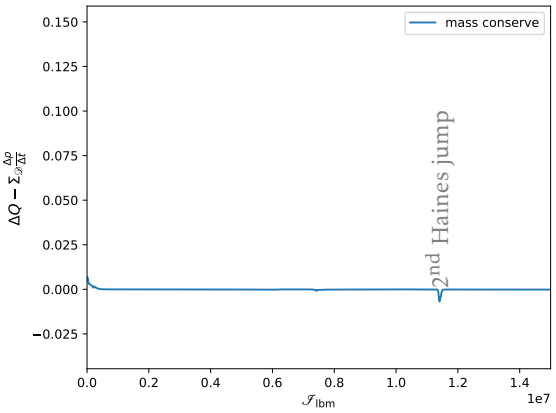

(b) Mass conservation for preferential pathway.

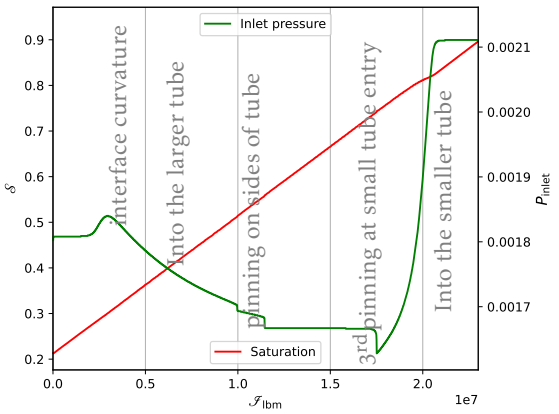

(c) Inlet pressure (at centerline) and saturation ($\mathcal{S}$) for stepped tube.

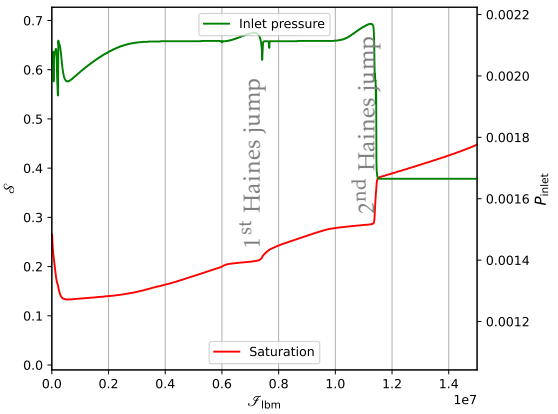

(d) Inlet pressure (at centerline) and saturation ($\mathcal{S}$) for preferential pathway.

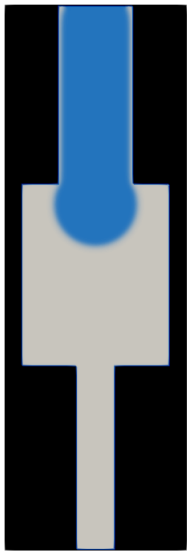

(e) Density field for stepped tube.

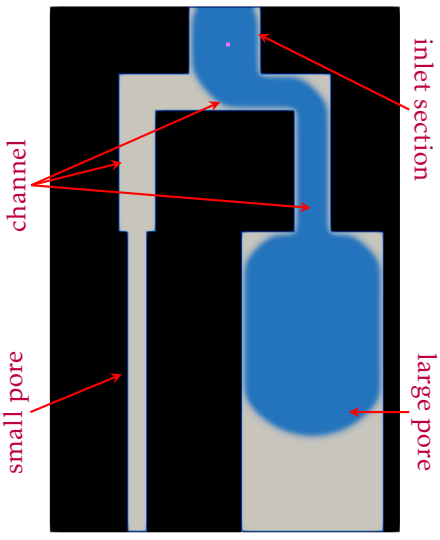

(f) Density field for preferential pathway.

Figure 2.24: Stepped tube and preferential pathway simulations, $\mathscr{H}_2$ model and $T/T_c = 0.825$

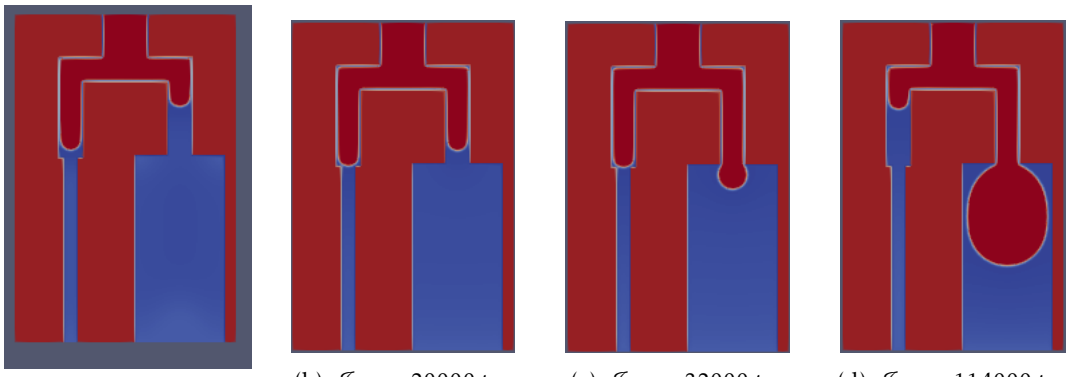

(a) $\mathscr{T}_{\text{lbm}}$ = 2000 t.s. (b) $\mathscr{T}_{\text{lbm}}$ = 20000 t.s. (c) $\mathscr{T}_{\text{lbm}}$ = 32000 t.s. (d) $\mathscr{T}_{\text{lbm}}$ = 114000 t.s.

Figure 2.25: Preferred path – $\mathscr{H}_5$

due to the outlet presence. This is also observed in the mass conservation fig. 2.24b where there is a rapid initial decrease of mass. Also we observe a small fluctuation corresponding to the change of flow pattern. Later as the interface reaches the Neumann outlet we observe unphysical effects, hence thereafter the simulation results are ignored.

Here for $\mathscr{H}_5$, the NWF is the heavier one (i.e. the liquid), with a static contact angle of $\theta_{\text{stat}} = 180°$, and open boundary conditions used are ZH VI and PO. At the initial time $t = 0$ the NWF and WF are at the same height, after which evaporation due to the influence of the outlet boundary is observed in the initial phase of the simulation. This relation was discovered when (to satisfy curiosity) the simulation was attempted without an outlet, no *evaporation* was observed (all this while keeping other parameters untouched). Thus the *evaporation* pushes back the NWF in the the channel towards the large tube (i.e. it remains partially invaded, see fig. 2.25a). After the initial deviation the NWF starts pushing the WF. As the NWF in the channel towards the small pore did not experience a significant *evaporation*, it will reach the smallest pore first (fig. 2.25b). Given that the liquid pressure is less than the smallest pore breakthrough pressure, the NWF cannot penetrate the smaller tube (pore) and the pressure will increase (A to B fig. 2.26). Once the NWF reaches the largest pore on the right side, and knowing that the liquid pressure is higher than the right side breakthrough pressure, the NWF will exit the channel towards the small pore and be redirected to enter inside the larger diameter pore/tube and forms a drop (fig. 2.25c). As the diameter of this drop increase, the pressure will decrease (B to C to D fig. 2.26), until it reaches the corresponding capillary pressure when the diameter of the drop is equal to the tube diameter(fig. 2.25d).

2.8. Porous medium

Porous media simulations have played an important role in understanding the behavior of different fluids in wetting and non-wetting pores (having possibly variable cross-section). Also depending on a few simulation parameters phenomenon such capillary and viscous fingering, Haines jump amongst others could be explored. Few example of porous media are sponge, GDL, soil, rock amongst others. Such cases have be modeled for different scenarios, for example: different LBM models have been used for GDL simulation [107], modeling flow in porous asphalt [2] and carbon dioxide storage in/of rocks [108]. Now the flow patterns observed when a non-wetting fluid invades a porous media saturated by wetting fluid can be differentiated into different flows regimes (as shown in fig. 2.27) based on the capillary number and viscosity ratio [109]. The capillary number (Ca) can be given as:

$$\text{Ca} = \frac{u_{\text{NWF}} \nu_{\text{NWF}} \rho_{\text{NWF}}}{\sigma \cos(\theta_{\text{stat}})} \tag{2.110}$$

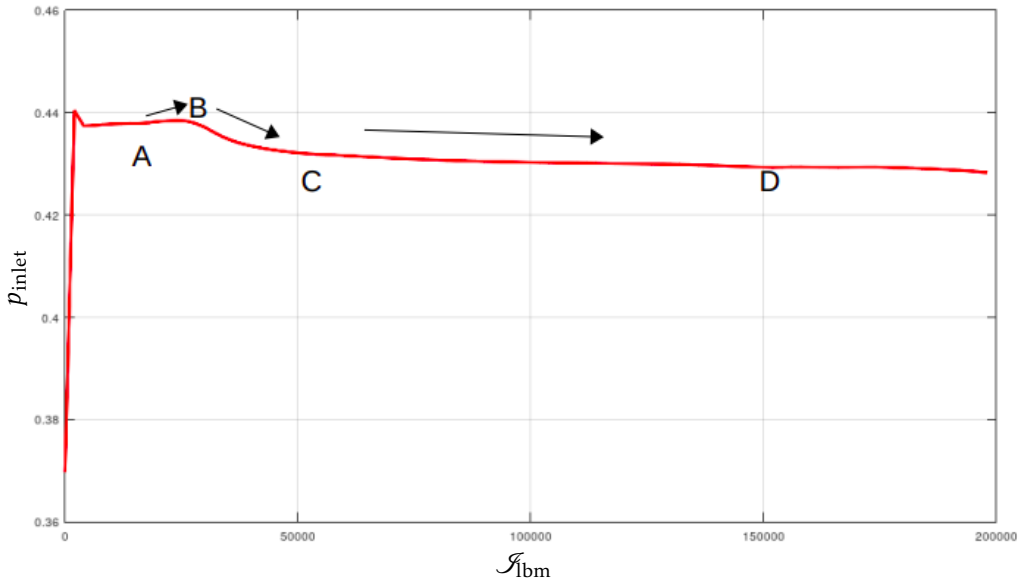

Figure 2.26: Preferred path : Pressure variation measured at a point on the centerline and in proximity to the VI – $\mathscr{H}_5$

where u_{NWF} and ν_{NWF} are mean velocity and kinematic viscosity of the non-wetting invading fluid. Now, the viscosity ratio (M) is given as:

$$M = \frac{\mu_{\text{NWF}}}{\mu_{\text{WF}}} = \frac{\nu_{\text{NWF}}\rho_{\text{NWF}}}{\nu_{\text{WF}}\rho_{\text{WF}}} \tag{2.111}$$

where μ_{WF} is the dynamic viscosity of the wetting fluid.

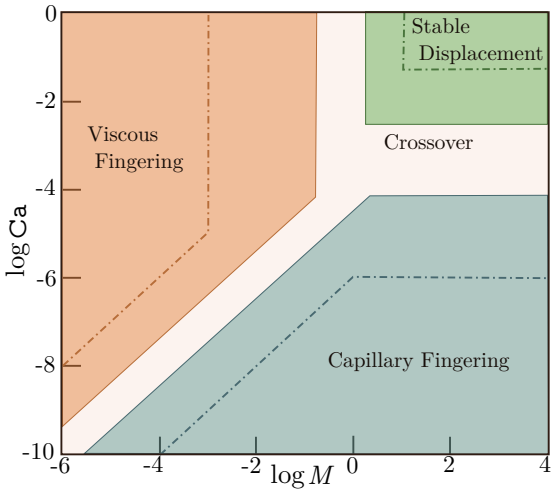

Figure 2.27: Unsaturated porous media flow regimes [110] as discovered by Lenormand

Now for the porous media simulation, we use the homogeneous porous media domain from [110] as shown in fig. 2.31. Here the domain size is $\mathscr{N}_x \times \mathscr{N}_y = 1853 \times 1045$, we have zero gravity, inlet on the west and the outlet on the east. Here for modeling and comparing answers we use two of our models $\mathscr{H}_1$ and $\mathscr{H}_2$, where for the latter model the vapor kinematic viscosity is 40% greater than the liquid viscosity. Thus the (logarithm of the) dynamic viscosity ratio for $\mathscr{H}_1$ is $\log|M| = 1.1$, while for $\mathscr{H}_2$ the value is $\log|M|$=0.9545. The simulation occurs at temperature $T/T_c = 0.825$ and pore wall density is $\rho_w = 0.05$ units, i.e. the non-dimensional density is $\rho_w^* = 0.1$. For the inlet velocity (of the non-wetting liquid phase) $u_x = 10^{-3}$ l.u./t.s., we observe the stable displacement regime for

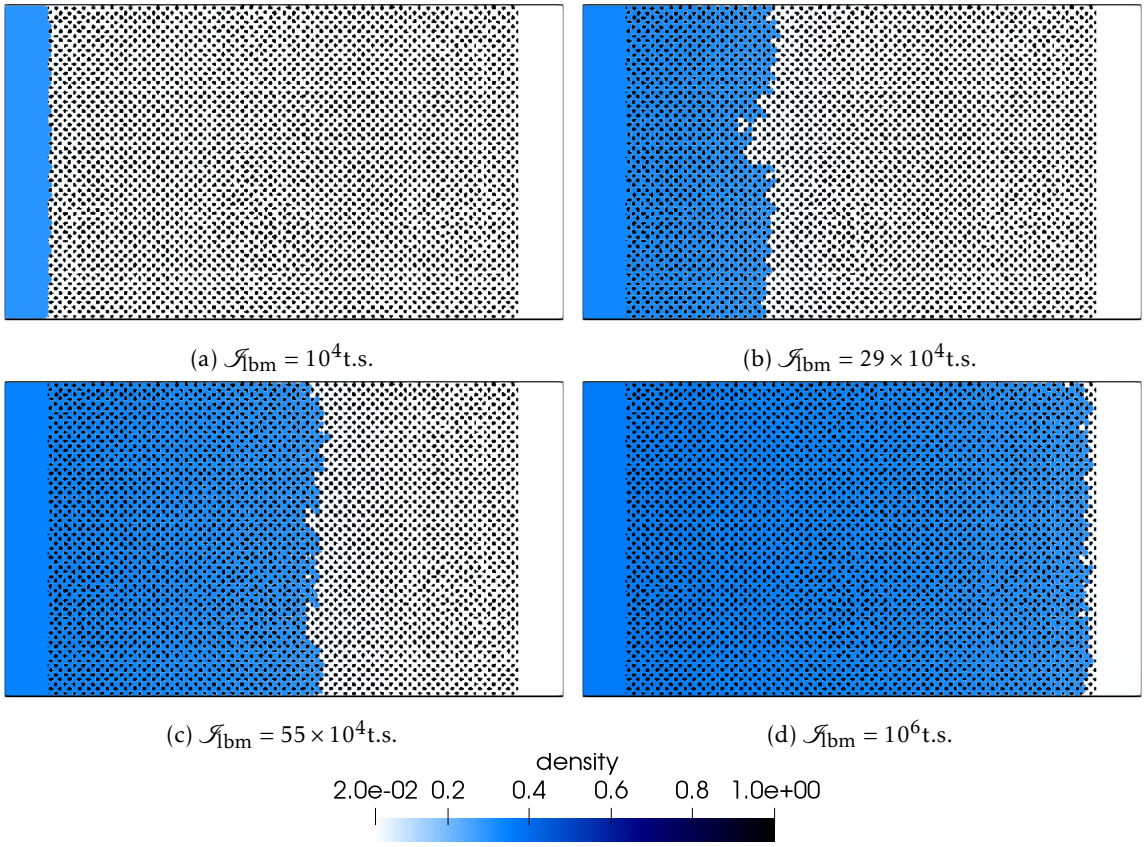

(a) $\mathscr{T}_{\text{lbm}} = 10^4$t.s. (b) $\mathscr{T}_{\text{lbm}} = 29 \times 10^4$t.s.

(c) $\mathscr{T}_{\text{lbm}} = 55 \times 10^4$t.s. (d) $\mathscr{T}_{\text{lbm}} = 10^6$t.s.

Figure 2.28: Homogeneous porous media simulation($\log|\text{Ca}| = -2$, $\log(M) = 0.9$ and $\mathscr{H}_2$).

both the models $\mathscr{H}_1$ and $\mathscr{H}_2$. Figure 2.28 depicts results for model $\mathscr{H}_2$, this is similar to $\mathscr{H}_1$ results and fig. 2.30a plots the inlet pressure at the centerline and the saturation profile. The saturation profile is linear as expected, the only minor deviation is noticed as the liquid front almost reaches the end of the porous medium. We also notice a spike in p_{inlet} after 40% of the simulation time has elapsed, followed by a steeper rate of increase in the pressure. Now when the inlet velocity is $u_x = 10^{-4}$ l.u./t.s., we have results for model $\mathscr{H}_2$. Figure 2.29 depicts the various stages of saturation for $\mathscr{H}_2$ simulation. Also the fig. 2.30b, likewise plots the saturation curve and the inlet pressure at the centerline. Like before we observe a linear saturation profile except at the final phase of the simulation. Again we also observe a spike in inlet pressure after 40% of simulation time has elapsed and this is followed by a steeper rate of increase in the pressure. At this Ca number ($\log|\text{Ca}| = -3$) we are in the crossover region (see fig. 2.27) and further decreasing the velocity would push us into the capillary fingering region. We began observing capillary fingers for this simulations, though at the later stage (of the simulation) the liquid front is more or less stably displaced. Also we observe collapsing of bubbles, when its resolution decreases below a particular value. Comparatively, the $\mathscr{H}_1$ model performs poorly. Up unto this point of writing the thesis, there are certain issues with the simulation results of $\mathscr{H}_1$ using the NBC, which are:

1. Random density fluctuations or rather pressure waves are observed in the region adjacent to the outlet as highlighted in the fig. 2.31. This fluctuations seem to *resonate* till liquid is condensed near the outlet.

2. Initial *evaporation*/phase change as observed in other open boundary simulation i.e. some of the liquid is sucked out by the outlet, but a small quantity remains before the inlet injects additional liquid. The reason for this phenomenon is unknown.

3. Another interesting point observed in most of our porous media simulations, is a strange/unphysical

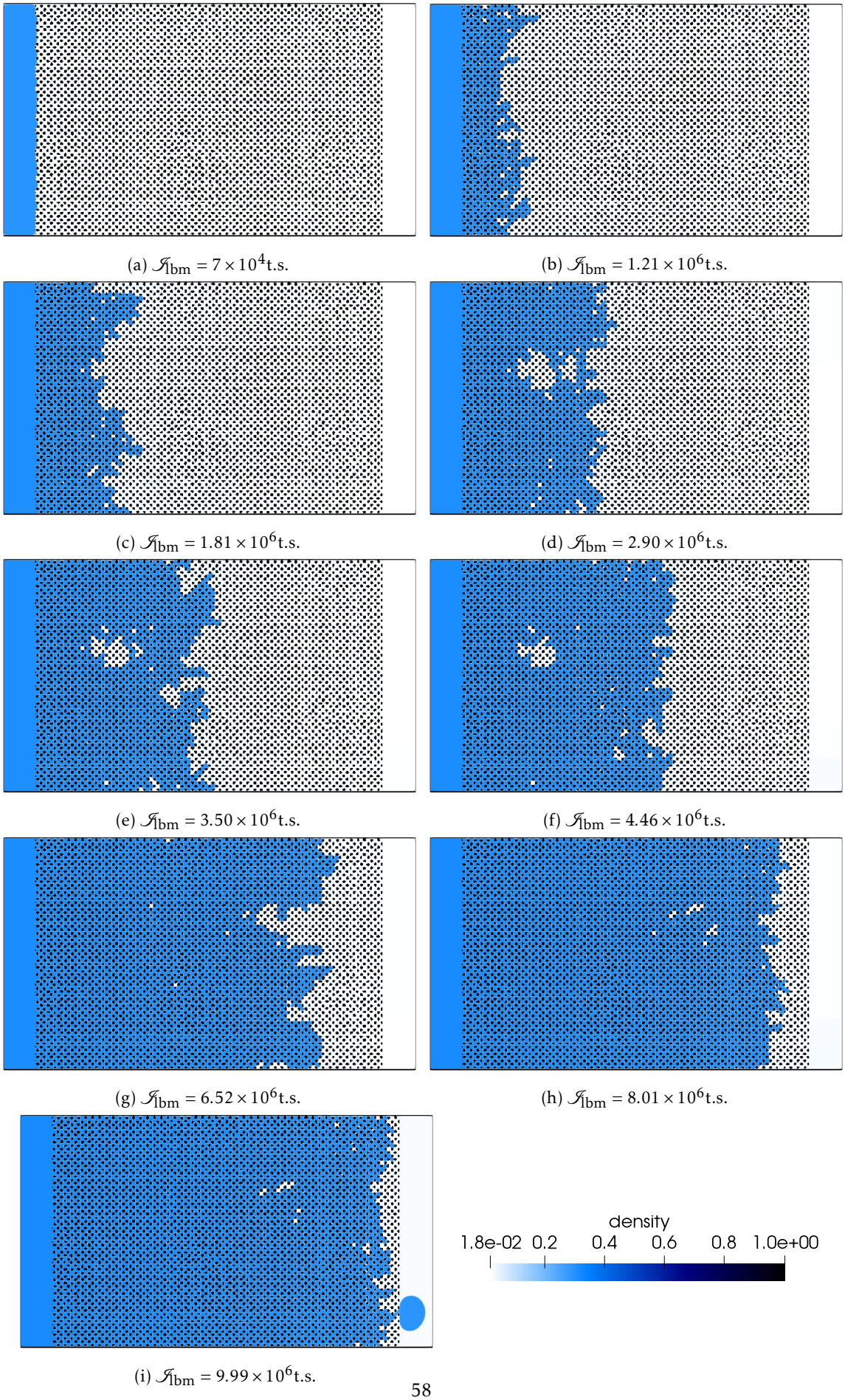

(a) $\mathscr{T}_{\text{lbm}} = 7 \times 10^4$t.s.

(b) $\mathscr{T}_{\text{lbm}} = 1.21 \times 10^6$t.s.

(c) $\mathscr{T}_{\text{lbm}} = 1.81 \times 10^6$t.s.

(d) $\mathscr{T}_{\text{lbm}} = 2.90 \times 10^6$t.s.

(e) $\mathscr{T}_{\text{lbm}} = 3.50 \times 10^6$t.s.

(f) $\mathscr{T}_{\text{lbm}} = 4.46 \times 10^6$t.s.

(g) $\mathscr{T}_{\text{lbm}} = 6.52 \times 10^6$t.s.

(h) $\mathscr{T}_{\text{lbm}} = 8.01 \times 10^6$t.s.

(i) $\mathscr{T}_{\text{lbm}} = 9.99 \times 10^6$t.s.

Figure 2.29: Homogeneous porous media simulation ($\log|\text{Ca}| = -3$, $\log(M) = 0.9$ and $\mathscr{H}_2$)

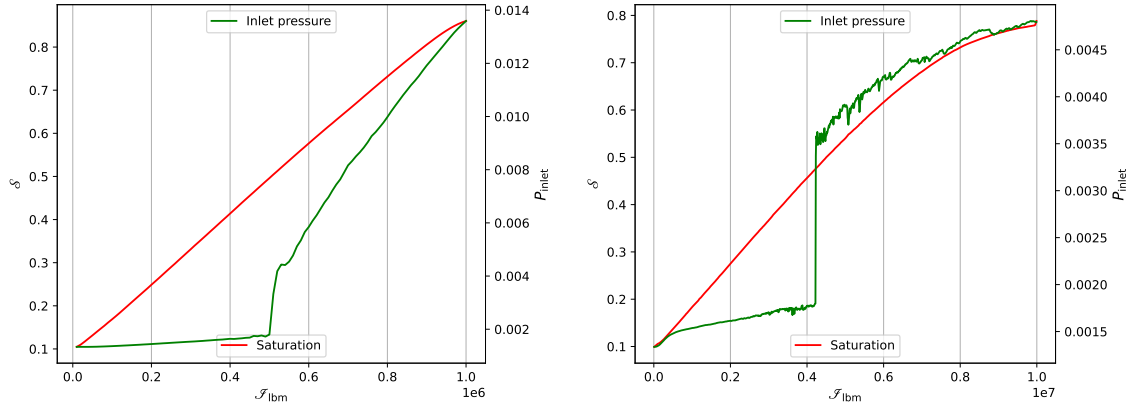

(a) $\log|Ca| = -2.0$ and $\log|M| = 0.9545$

(b) $\log|Ca| = -3.0$ and $\log|M| = 0.9545$

Figure 2.30: Inlet pressure (at the centerline) and the saturation curve ($\mathcal{S}$) for interfacial flow in the homogeneous porous media ($\mathscr{H}_2$, $T/T_c = 0.825$)

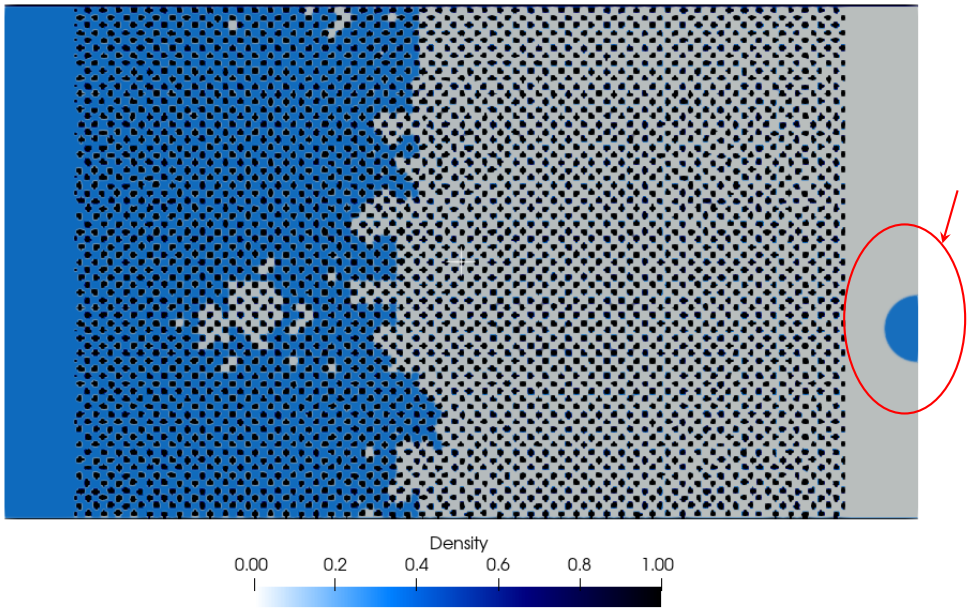

Figure 2.31: Density profile for homogeneous porous media ($\log(|Ca|) = -3.02$ and $\log(M) = 1.077$) ($\mathscr{H}_1$ model)($T/T_c = 0.825$)

filling/collapse of small vapor bubbles/gaps. Similar observations was made in [111], though not discussed in the paper it seems evident from the phase distribution images provided. One possible reason could be the collapse of the vapor bubbles. To illustrate this point a bubble simulation is performed for a bubble radius below a certain threshold radius value. Density and pressure are plotted for a point (approximately at the center of the bubble) versus time as shown in fig. 2.32). As can be observed the density shoots up at a point (in time), as the collapse is completed. This is followed by minor fluctuations after which only a single phase exists.

4. Also, stability could not be achieved for simulations with lower capillary numbers where $u_x = -10^{-4}$ l.u./t.s. for both NBC and CBC-L.

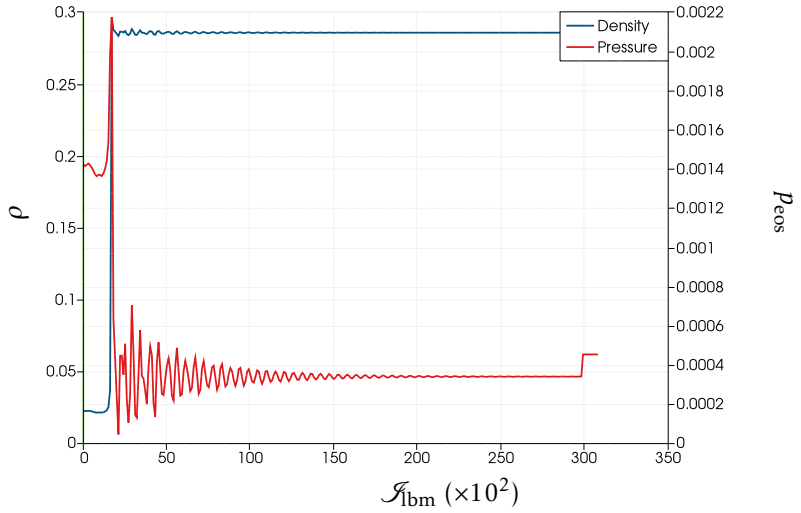

Figure 2.32: Density and pressure fluctuations at the center of the bubble, during the collapse of a vapor bubble

2.8.1. Graded porous simulations

This work has been carried out in collaboration with DHBW, Germany. Also excerpts of the work (carried separately to the thesis) has been presented before at 235^{th} ECS meeting, Dallas, May 2019. The extent of work of the author of this thesis pertains to use of LBM models to model this porous media.

Context: The GDL of the fuel cell could be manufactured by a new process i.e. electro-spinning [112] The given a finer level of control on the pore sizes of the GDL making it possible to have more compact and continuous structure. Here the porous media is made from hydrophobic material ($\theta_{stat} = 130°$), which register better performance for the GDL. To better understand this counter-intuitive behavior both experimental and numerical results were explored. Here the GDL (i.e. a porous media) has two sections. The section of the porous media with smaller pores and smaller fiber diameter is injected with water. The latter section is adjacent to the outlet and has larger pores and larger fiber diameter. The result of the full morphology model predicted a sudden flooding in the GDL when the interface jumps to the latter section. This is a deviation from experimental results which display a continuous and a consistent *thickness of water* as shown in fig. 2.33. In other words, no sudden flooding is observed but rather a consistent saturation in the latter section of porous media allowing for a continuous flow circuit (as the liquid passes through the outlet). This discrepancy (between experimental and numerical results) was due to higher capillary pressure (in the smaller pores section) being applied as the injection pressure at the entry/breakthrough point into the latter section. As the morphology model lacks further analysis, this high pressure liquid saturates the GDL with immediate effect. Thus a transient solver is required for modeling the physics of the fluids in the porous media, this is where LBM comes into the picture. For LBM simulation a 2D plane was extracted form the center of the simulation as shown in fig. 2.34.

As highlighted previously due to different unresolved issues (as of writing this thesis) for simulation regarding model $\mathscr{H}_1$, we refrain from further discussing the results of the SCMP-SC for porous media simulation. The MCMP-SC is a veteran of the porous media simulations. For $\mathscr{H}_5$, the simulation is performed for $\log|\mathrm{Ca}| = -4.25$ and $\log(M) = 0$ on a domain size of $\mathscr{N}_x \times \mathscr{N}_y = 1028 \times 1226$. After the initial *evaporation*, the liquid is gradually injected in the former section (smaller pores with smaller fiber diameters). The liquid forms *finger* like structures as it proceeds along different pathways. As the liquid crosses the entry/breakthrough point (roughly at the center of this plane), minor redistribution of the fluids (i.e. local saturation change) occurs and is predominantly local in nature. In other words, the effect of the pressure gradients due to discovery of larger pores and/or

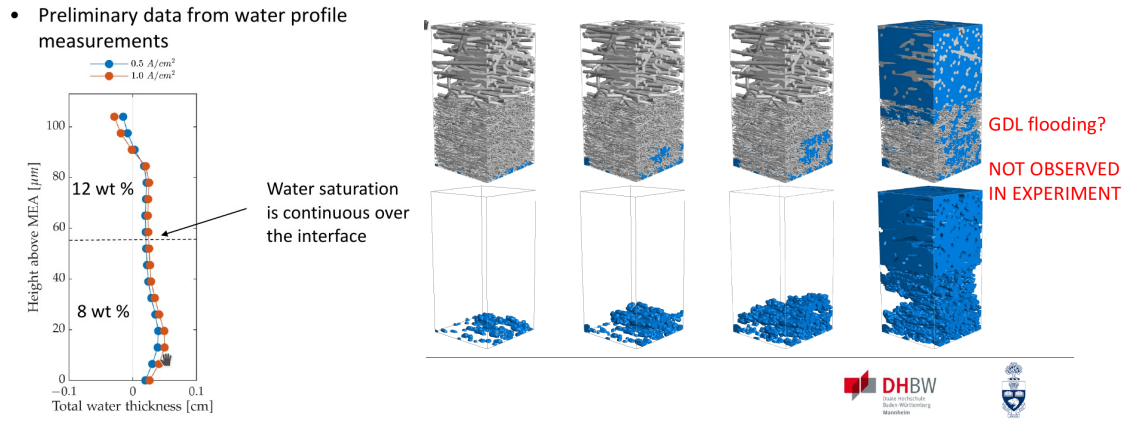

(a) Experimentally measuring the saturation for both sections

(b) Full morphology model results

Figure 2.33: Discrepancy between experimental and numerical results (Results presented at 235^{th} ECS meeting, Dallas, May 2019).

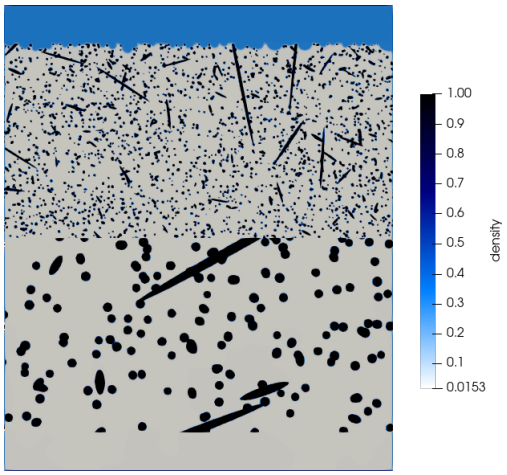

Figure 2.34: 2D slice of the initial 3D geometry for Graded porous media

larger porous media is most evident across the length/shape of the liquid *finger/stream* which passes through the entry point. This is in contrast to our initial expectation of *drying out* i.e. a reduction of saturation of the former section would follow the discovery of the latter section (i.e. larger pores and larger fiber diameters). Saturation profile is linear as excepted with constant velocity inlet. Here the outlet boundary used (pressure boundary: pressure is fixed by fixing liquid density of the flow at the outlet) does not allow for the flow of the liquid (with the *other*/different density) across the outlet, and hence we observe flooding in the porous media. Since we are only interested in the simulation till the first contact with the outlet boundary is established, we ignore the eventual flooding that comes after.

2.9. Conclusion

This chapters explores theoretically different LBM multiphase models and further in the chapter we examine the validity of our model in different circumstances. These results will have implications on the design and setup of our problem when we prepare the optimization tools which is the final goal of this work. The conclusion can be summarized as:

1. In the view of having a robust and light-weight algorithm for modeling the physics for an

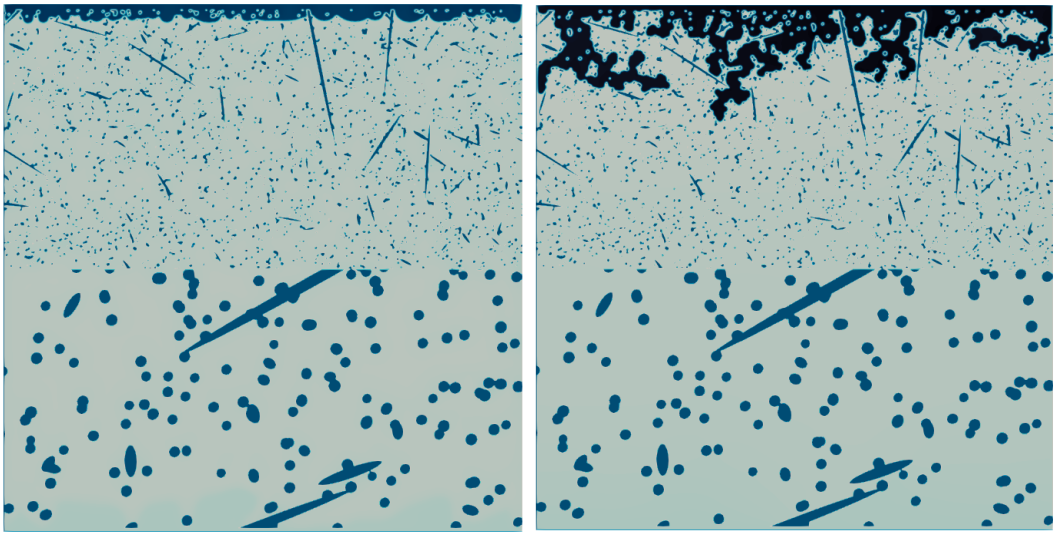

(a) $\mathscr{G}_{\text{lbm}} = 10^5$

(b) $\mathscr{G}_{\text{lbm}} = 5 \times 10^5$

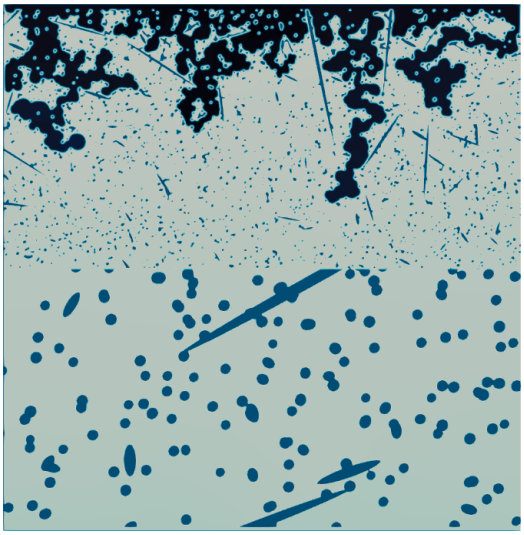

(c) $\mathscr{G}_{\text{lbm}} = 8 \times 10^5$

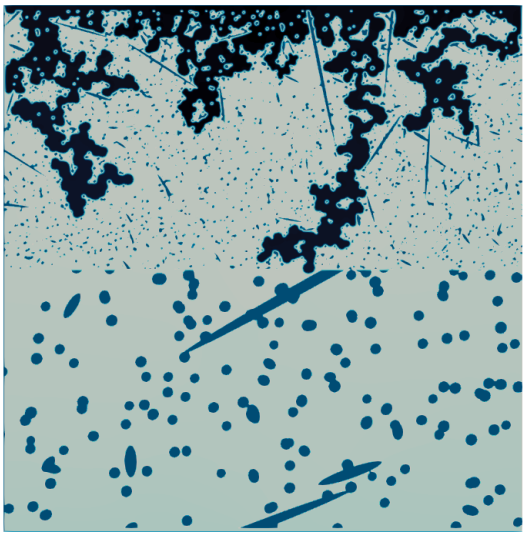

(d) $\mathscr{G}_{\text{lbm}} = 10.5 \times 10^5$

optimizer, we choose SCMP-SC model.

2. The models performs as expected for modeling cases with periodic boundaries and wall boundaries i.e. Laplace law, asymptotic velocity of droplet on plate and washburn simulation.

3. For modeling cases with open boundaries, the simulation model performs decently until such a time when the interface is exposed or arrives at any boundaries. Use of pressure inlet/outlet should be discouraged for SCMP-SC.

4. For modeling flow in porous media using SCMP-SC, cases in conjunction with open boundaries gives fairly unpredictable results (especially for low capillary number ($< 10^{-3}$) flows). Meanwhile, MCMP-SC is up to task for such simulations, as it does not suffer from the same limitations as SCMP-SC.

Hence, for optimization algorithms using SCMP-SC, trustworthy results can be obtained for configurations without open boundaries and also for porous media with higher capillary number flows.

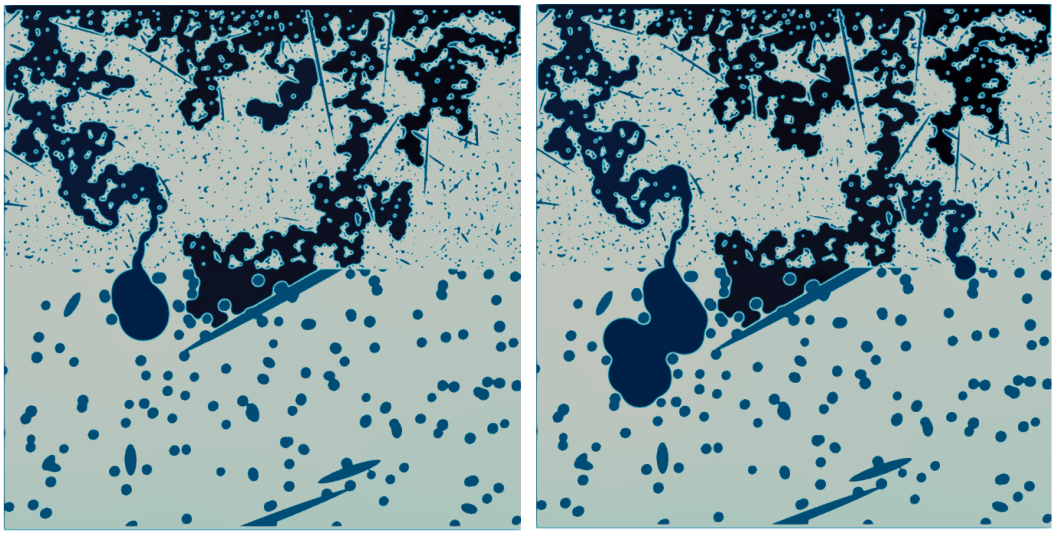

(e) $\mathscr{I}_{\text{lbm}} = 17 \times 10^5$

(f) $\mathscr{I}_{\text{lbm}} = 20 \times 10^5$

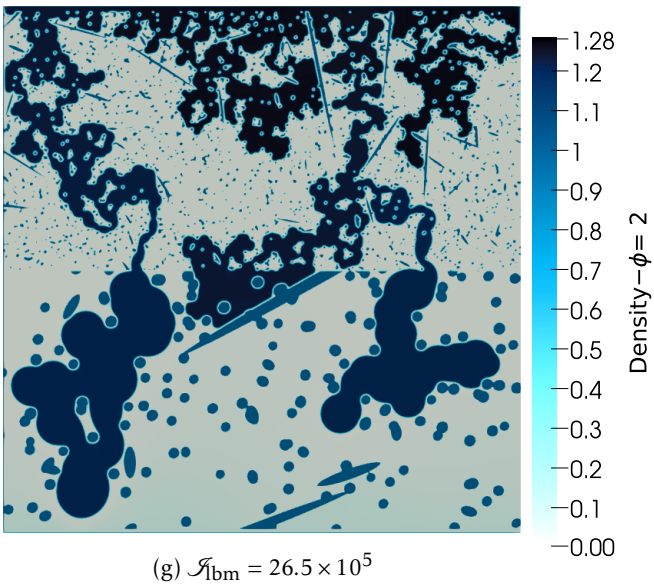

(g) $\mathscr{I}_{\text{lbm}} = 26.5 \times 10^5$

Figure 2.35: Saturation profile for phase (Φ)= 2 in graded porous media when $\log|\text{Ca}| = -4.25$, $\log|M| = 0$ ($\mathscr{H}_5$)

Chapter 3

Topology optimization in monophasic fluids

The origin of topology optimization is generally traced back to ref.[113] who published their work in 1988. Their paper was regarding topology optimization applied to structural design. Starting from the initial set of optimization studies (utilizing the topology optimization algorithm) being applied to mechanical design problems the scope of the studies have now expanded to include [114] problems in the field of: fluid flows [115], acoustics [116], electro-magnetics [117], optics [118] and etc. Presently, topology optimization for structural problems have been made available in commercial computational mechanics software like for e.g. COMSOL, Ansys, Altair. The initial study used the homogenization method [119] where a unit cell is used to represent the shape of the solid domain. Later different methods [114] were developed for the same purpose like density methods (both the rational approximation of material properties i.e. RAMP [120] and the simplified isotropic material with penalization i.e. SIMP [121]), level-set function (LSF) [122], topological derivatives [123, 124] and phase field [125, 126]. Currently the most common methods for material interpolation or representation of the solid domain are SIMP and LSF. Another point of distinction is the nature of the adjoint-state model derivation: continuous [127] or discrete [128, 129]. We utilize the continuous equations (discrete only in the velocity discretization to accommodate for the LBM

boundaries) for derivation of the adjoint-state model and also use the LSF for solid domain representation. For fluid flow problems, the first topology optimization study was conducted in 2003 for the Stokes flow [130] by modeling the Navier-Stokes equations. Later topology optimization studies were carried out for turbulent flows [131], non-Newtonian flows [132], forced and natural convection [133–135], species transport and reactive flows [136, 137], porous media flows [138] among others. For a more rigorous review of topology optimization as applied on fluid flows the readers are directed to ref.[115].

For this chapter we include a simple validation study as this aspect has been thoroughly covered before by the team in LTEN ([40, 136, 139]). We only utilize this chapter to explain different concepts regarding topology optimization. The outline of the chapter is as follows: the following section 3.1 elaborates on different components required for topology optimization, section 3.2 describes the optimization model (which includes the derivation of the adjoint-state problem) and section 3.3 expounds on the result of the numerical simulation. And Section 3.4 finally spells out the conclusions.

3.1. Components of gradient optimization

An optimization process consists of finding a minimum for the objective/cost function for a physical/real state. Before diving into details, we briefly touch upon the algorithm used for optimization. Here the real state of the system is modeled using the single phase lattice Boltzmann model. The fluid modeled here is a compressible fluid. We use the level-set function for describing the structures (i.e. solid wall or obstructions) in the flow (i.e. in the real state). Next important computation step in the optimization algorithm is the adjoint-state. The adjoint-state equations are derived from the real state (using the Lagrange equations) and the computation time required for both these states are the same. Next computational step is the computation of the gradient using the data from the physical state and adjoint-state. The use of the adjoint-state speeds up the computation of the gradient while the only drawback being the complexity it brings to the table. The next computational step is to determine the step size (i.e. the line-search algorithm) to be used while applying a gradient (it is optional but helps in speeding up the process). Finally we apply the gradient (of the cost function) and check for convergence, if convergence is not achieved then we repeat the process. The following algorithm 3 (at page 72) is a topology optimization algorithm used for the computation.

A generic representation of the topology optimization problem is described as:

$$\min\ \mathcal{J}(\Psi,\mathbf{f}) \qquad \text{subject to} \quad \mathcal{F}(\Psi,\mathbf{f}) = 0, \tag{3.1}$$

where $\mathbf{f} = \{f_0, f_1, f_2, f_3, f_4, f_5, f_6, f_7, f_8\}$ as before represents the probability distribution function (for the LBM solver), Ψ represents the design variables or control parameters (more specifically it is the level-set variable), $\mathcal{J}$ is the cost function or the objective function and $\mathcal{F}$ represent the real state (i.e. LBM equations along with their boundary conditions).

3.1.1. Lagrange function

The Lagrange function is the amalgamation of the cost function, real state, adjoint-state and the constraints to form a single equation. This allows for the use of zero constraint optimization algorithms which are less tedious to compute. The general form of the problem now becomes:

$$\mathcal{L}(\Psi,\mathbf{f},\mathring{\mathbf{f}}) = \mathcal{J}(\Psi,\mathbf{f}) + \langle \mathring{\mathbf{f}}, \mathcal{F}(\Psi,\mathbf{f}) \rangle \tag{3.2}$$

where $\mathring{\mathbf{f}}$ is the Lagrange multiplier and it also represents the adjoint-state variables. Also here $\mathring{\mathbf{f}} = \{\mathring{f}_0, \mathring{f}_1, \mathring{f}_2, \mathring{f}_3, \mathring{f}_4, \mathring{f}_5, \mathring{f}_6, \mathring{f}_7, \mathring{f}_8\}$. For optimization we require the minimum of the lagrange function and hence its stationary point. Using directional derivative we can write:

$$\mathcal{L}' = \frac{\partial \mathcal{L}}{\partial \mathring{\mathbf{f}}}\mathring{\mathbf{f}}' + \frac{\partial \mathcal{L}}{\partial \mathbf{f}}\mathbf{f}' + \frac{\partial \mathcal{L}}{\partial \Psi}\Psi' = 0 \tag{3.3}$$

where $\mathcal{L}'$, $\mathring{\mathbf{f}}'$, $\mathbf{f}'$ and Ψ' are arbitrary variations in the directions of $\mathcal{L}$, $\mathring{\mathbf{f}}$, $\mathbf{f}$ and Ψ respectively. Expanding the terms in eq. (3.2):

$$\mathcal{L}(\Psi,\mathbf{f},\mathring{\mathbf{f}}) = \mathcal{J} + \sum_{i=0}^{8}\left\langle \mathcal{R}_i, \mathring{f}_i\right\rangle_{\mathcal{D}\times\mathcal{T}} + \sum_{\beta=\{\text{in,out,bb}\}}\sum_{i=1}^{3}\left\langle \mathcal{P}_{\beta(i)}, \mathring{f}_{\beta(i)}\right\rangle_{\Gamma_\beta\times\mathcal{T}} \tag{3.4}$$

where $\mathcal{R}$ and $\mathcal{P}$ are the residue of LBM equations and their boundary conditions respectively, and $\mathring{f}$ is the corresponding adjoint-state distribution function (similar to the LBM distribution function f). The cost function can be viewed as one acting on the domain ($\mathscr{Y}$) and also on the boundary ($\mathscr{X}$).

Definition 3.1.1. The following L_2 spaces are associated with their corresponding inner products.

$$\int_{t=0}^{t_f}\int_{\mathcal{D}} \mathcal{U}\mathcal{V}\,\mathrm{d}\boldsymbol{r}\,\mathrm{d}t = \langle \mathcal{U},\mathcal{V}\rangle_{\mathcal{D}\times\mathcal{T}} \tag{3.5}$$

$$\int_{\mathcal{D}} \mathcal{U}\mathcal{V}\,\mathrm{d}\boldsymbol{r} = \langle \mathcal{U},\mathcal{V}\rangle_{\mathcal{D}} \tag{3.6}$$

$$\int_{0}^{t_f} \mathcal{U}\mathcal{V}\,\mathrm{d}t = \langle \mathcal{U},\mathcal{V}\rangle_{\mathcal{T}} \tag{3.7}$$

$$\int_{0}^{t_f}\int_{\Gamma_{\text{in}}} \mathcal{U}\mathcal{V}\,\mathrm{d}\boldsymbol{r}\,\mathrm{d}t = \langle \mathcal{U},\mathcal{V}\rangle_{\Gamma_{\text{in}}\times\mathcal{T}} \tag{3.8}$$

$$\int_{\Gamma_{\text{in}}} \mathcal{U}\mathcal{V}\,\mathrm{d}\boldsymbol{r} = \langle \mathcal{U},\mathcal{V}\rangle_{\Gamma_{\text{in}}} \tag{3.9}$$

$$\int_{0}^{t_f}\int_{\Gamma_{\text{out}}} \mathcal{U}\mathcal{V}\,\mathrm{d}\boldsymbol{r}\,\mathrm{d}t = \langle \mathcal{U},\mathcal{V}\rangle_{\Gamma_{\text{out}}\times\mathcal{T}} \tag{3.10}$$

$$\int_{\Gamma_{\text{out}}} \mathcal{U}\mathcal{V}\,\mathrm{d}\boldsymbol{r} = \langle \mathcal{U},\mathcal{V}\rangle_{\Gamma_{\text{out}}} \tag{3.11}$$

$$\int_{0}^{t_f}\int_{\Gamma_{\text{bb}}} \mathcal{U}\mathcal{V}\,\mathrm{d}\boldsymbol{r}\,\mathrm{d}t = \langle \mathcal{U},\mathcal{V}\rangle_{\Gamma_{\text{bb}}\times\mathcal{T}} \tag{3.12}$$

$$\int_{\Gamma_{\text{bb}}} \mathcal{U}\mathcal{V}\,\mathrm{d}\boldsymbol{r} = \langle \mathcal{U},\mathcal{V}\rangle_{\Gamma_{\text{bb}}} \tag{3.13}$$

From the point of view of the physical LBM solver (i.e. forward problem), if we are only interested in the state $\mathcal{F}$ at $t = t_f$ (i.e. if the intermediary transient phenomenon does not play a significant role for the optimization analysis), then the cost function would be required only for the final state. We then apply consistently this cost function throughout adjoint-state time ($\mathring{t}$) for the adjoint-state modeling. The idea of the adjoint-state and its *time* are addressed later in section 3.1.2 and paragraph 3.2.2.a.2 respectively. For our convenience we label this method as TOSFP i.e. topology optimization for steady-state forward problem. Conversely, if the transient phenomenon is of importance then the cost function is required to be determined for all LBM iterations or at least at specific time intervals during the simulations. Also we require to store the LBM simulation data for all or at specific time intervals. In the latter case, while the computational expense is reduced, care should be taken that this time interval is sufficient for capturing the desired phenomenon. Using this stored information the corresponding adjoint-state is then modeled after which the gradient is computed. Similarly we label this method as TOTFP i.e. topology optimization for transient-state forward problem.

For optimization problems which are dependent on the cost function at the final state, i.e. TOSFP. The general form of the cost function is expanded as:

$$\mathcal{J} = \mathcal{J}_{\mathcal{D}} + \mathcal{J}_{\Gamma} = \langle \mathscr{Y}, 1\rangle_{\mathcal{D}}\Big|_{t=t_f} + \sum_{\beta=\{\text{in,out,bb}\}} \langle \mathscr{X}_\beta, 1\rangle_{\Gamma_\beta}\Big|_{t=t_f} \tag{3.14}$$

where $\mathcal{J}_{\mathcal{D}}$ is the cost function applicable on the domain (here $\mathcal{D}$ represents the domain) for e.g. porosity constraint and $\mathcal{J}_{\Gamma}$ is the cost function to be applied on the boundaries (here Γ represents the boundaries) for e.g. pressure and flux constraints. Hence the Lagrange function (for this category of optimization problems) can be further expanded as:

$$\mathcal{L}(\Psi, \mathbf{f}, \mathring{\mathbf{f}}) = \langle \mathscr{Y}, 1 \rangle_{\mathcal{D}} \Big|_{t=t_f} + \sum_{i=0}^{8} \left\langle \mathcal{R}_i, \mathring{f}_i \right\rangle_{\mathcal{D} \times \mathcal{T}} + \sum_{\beta=\{\text{in,out,bb}\}} \left(\sum_{i=1}^{3} \left\langle \mathcal{P}_{\beta(i)}, \mathring{f}_{\beta(i)} \right\rangle_{\Gamma_\beta \times \mathcal{T}} + \langle \mathscr{Z}_\beta, 1 \rangle_{\Gamma_\beta} \right) \tag{3.15}$$

As previously mentioned, optimization requires the stationary point of the Lagrange function, for which directional derivative is used, hence:

$$\mathcal{L}' = \underbrace{\sum_j \frac{\partial \mathcal{L}}{\partial \mathring{f}_j} \mathring{f}_j'}_{\text{aA1}} + \underbrace{\sum_j \frac{\partial \mathcal{L}}{\partial f_j} f_j'}_{\text{aA2}} + \underbrace{\frac{\partial \mathcal{L}}{\partial \Psi} \Psi'}_{\text{aA3}} = 0 \tag{3.16}$$

where $\mathring{f}_j'$, f_j' and Ψ' are arbitrary variations in the directions of $\mathring{f}_j$, f_j and Ψ respectively. Now in eq. (3.16), aA1 = 0 retrieves the forward problem, aA2 = 0 retrieves the equation for the adjoint-state while aA3 = 0 retrieves the gradient for optimization.

3.1.2. Adjoint-state method

The adjoint-state method is considered an efficient manner for computing the sensitivities/gradients and is hence used in different applications for example weather forecast modeling and optimization modeling among others. For explaining why the adjoint-state method is required, we first discuss the crude procedure for obtaining the gradient of the cost function. The procedure being discussed is illustrated using a fluid flow problem which employs a 3×3 optimization mesh as shown in fig. 3.1. We start with an initial condition where we have no solid domain ($\mathcal{D}_s$; i.e. no solid in the domain $\mathcal{D}$), the velocity inlet is at the western boundary and pressure outlet is at the eastern boundary. Thus we obtain a flow as indicated by the streamlines (the flow field is imaginary and used only for purpose of illustration) being modeled by a physical solver (like LBM). In a topology optimization problem the state of each individual node is defined by the value of the level-set function (or by porosity value for the SIMP method) at the corresponding node. Thus the state/nature of each node (α) is registered as an independent variable. For the problem at hand the state/nature of the node can only vary between two states i.e. a fluid node or a solid node. Thus for any cost function we can obtain its gradient by individually varying the state/nature of all the nodes and simultaneous measuring the change in the cost function (as shown in fig. 3.1). This individual changes are used for constructing the total/final gradient of the cost function as:

$$\nabla_\Psi \mathcal{J} = \left[\frac{\mathrm{d}\mathcal{J}}{\mathrm{d}\Psi_1} \quad \frac{\mathrm{d}\mathcal{J}}{\mathrm{d}\Psi_2} \quad \frac{\mathrm{d}\mathcal{J}}{\mathrm{d}\Psi_3} \quad \frac{\mathrm{d}\mathcal{J}}{\mathrm{d}\Psi_4} \quad \frac{\mathrm{d}\mathcal{J}}{\mathrm{d}\Psi_5} \quad \frac{\mathrm{d}\mathcal{J}}{\mathrm{d}\Psi_6} \quad \frac{\mathrm{d}\mathcal{J}}{\mathrm{d}\Psi_7} \quad \frac{\mathrm{d}\mathcal{J}}{\mathrm{d}\Psi_8} \quad \frac{\mathrm{d}\mathcal{J}}{\mathrm{d}\Psi_9} \right]^T \tag{3.17}$$

where for a node η of the cost function (using finite difference for obtaining optimization gradient, LBM solver for modeling the physical state and level-set of defining the solid boundaries) would be obtained as:

$$\frac{\mathrm{d}\mathcal{J}}{\mathrm{d}\Psi_\eta} = \left\langle \nabla \mathcal{J}, \Psi_\eta' \right\rangle_{\mathcal{D}} = \lim_{\epsilon \to 0} \frac{\mathcal{J}(\mathbf{f}, \Psi + \epsilon \Psi_\eta') - \mathcal{J}(\mathbf{f}, \Psi)}{\epsilon} \tag{3.18}$$

where Ψ_η' is the direction of perturbation ϵ. Thus for computing the RHS of eq. (3.18) we need the cost function at the initial state and also later at the perturbed state. Thus for computing the cost function gradient, we would for this case need to solve the forward model 9 additional times. In other words the computational expense of gradient/sensitivity calculation for topology optimization is related to the mesh size. This computational expense is avoided by the use of the adjoint-state method where the computational time is equivalent to the time for solving the forward model, i.e. we effectively solve the forward problem only one additional time irrespective of the mesh size.

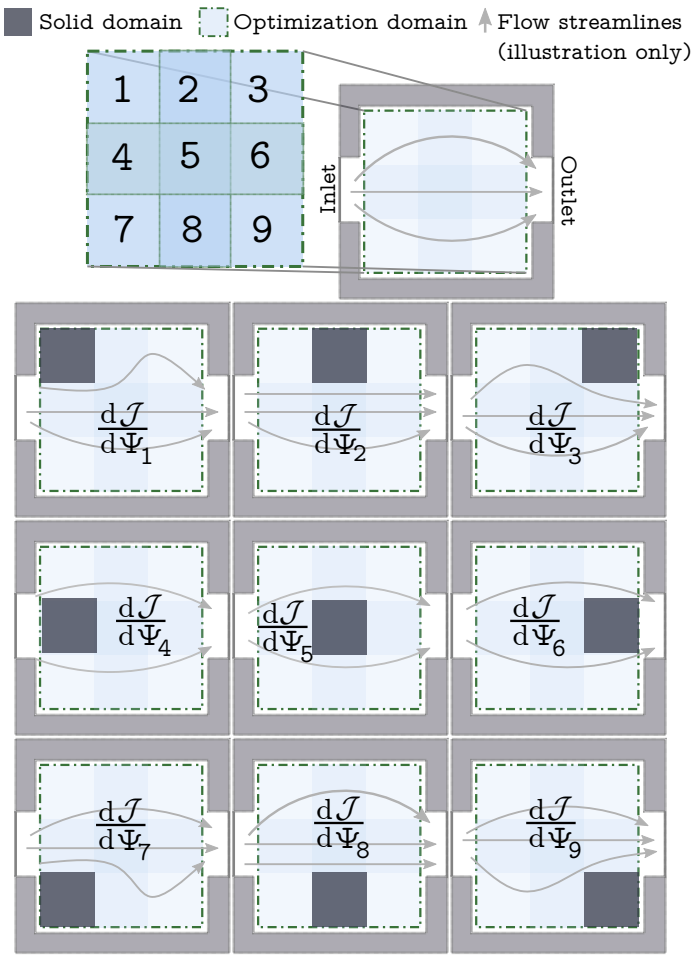

Figure 3.1: 3×3 mesh demonstrating the need for adjoint-state model

Now that we have established the need for the adjoint-state method, we discuss regarding its implementation. If the physical state is defined by the LBM solver and the solid domain is represented by the level-set function, then the cost function now becomes a function of f and Ψ. Thus the change in cost function differentiation w.r.t the control parameter is given as:

$$\frac{\mathrm{d}\mathcal{J}}{\mathrm{d}\Psi} = \frac{\partial \mathcal{J}}{\partial \Psi} + \frac{\partial \mathcal{J}}{\partial \mathbf{f}} \frac{\mathrm{d}\mathbf{f}}{\mathrm{d}\Psi} \tag{3.19}$$

This is similar to eq. (3.17) which represents the gradient in a vector format. Here the derivative $\frac{\mathrm{d}\mathbf{f}}{\mathrm{d}\Psi}$ is computationally expensive (i.e. mesh dependent as mentioned previously). Thus the goal of the adjoint-state method is to circumnavigate the use of this term. This is accomplished by the usage of the Lagrange equation. Using eq. (3.2), we can write:

$$\frac{\mathrm{d}\mathcal{L}}{\mathrm{d}\Psi} = \frac{\partial \mathcal{J}}{\partial \Psi} + \frac{\partial \mathcal{J}}{\partial \mathbf{f}} \frac{\mathrm{d}\mathbf{f}}{\mathrm{d}\Psi} + \left\langle \frac{\partial \mathcal{F}}{\partial \Psi} + \frac{\partial \mathcal{F}}{\partial \mathbf{f}} \frac{\mathrm{d}\mathbf{f}}{\mathrm{d}\Psi}, \mathring{\mathbf{f}} \right\rangle = 0 \tag{3.20}$$

It is to be noted that we utilize ordinary differentiation only for explanation, instead we use directional derivatives–as mentioned before–for the derivation of the adjoint-state model. Thus we could essentially rewrite this equation as:

$$\frac{\mathrm{d}\mathcal{L}}{\mathrm{d}\Psi} = \frac{\partial \mathcal{J}}{\partial \Psi} + \mathring{\mathbf{f}} \frac{\partial \mathcal{F}}{\partial \Psi} + \left(\frac{\partial \mathcal{J}}{\partial \mathbf{f}} + \mathring{\mathbf{f}} \frac{\partial \mathcal{F}}{\partial \mathbf{f}} \right) \frac{\mathrm{d}\mathbf{f}}{\mathrm{d}\Psi} \tag{3.21}$$

Now the adjoint-state problem is to determine/compute $\mathring{\mathbf{f}}$ (i.e. the adjoint-state variable) such that we obtain:

$$\frac{\partial \mathcal{J}}{\partial \mathbf{f}} + \mathring{\mathbf{f}} \frac{\partial \mathcal{F}}{\partial \mathbf{f}} = 0 \tag{3.22}$$

This allows us to neglect the computational expensive derivative thereby increasing the efficiency of the optimization algorithm. Another manner of describing the adjoint-state problem is in terms of sensitivities of the model output w.r.t to the input parameters. Using this terminology we know that the crude manner of obtaining the sensitivity would be to individually vary input parameters and record the corresponding change in the output parameter. Meanwhile, the adjoint-state method allows us to obtain the sensitivity using one set of input parameters and the corresponding set of output parameters.

3.1.3. Level-set function

The level-set function (Ψ) is utilized for topology optimization in two distinct manners as shown in fig. 3.2. The former (which is also the standard usage) method employs an equation for the level-set function (LSF). Here the zero contour of the LSF is tracked as Ψ is advected through out the domain. Here re-initialization of the LSF across the domain is necessary. This is because the performance of the LSF is best in the neighborhood of the optimum curvature/shape. The latter method (which is employed for this thesis) utilizes the zero contour of the level set as a measure for *nature*–solid or fluid–of the node. The *nature* of a node is represented by α–which is the *fluidness/solidness* of the node. Here the LSF is updated at each individual node (by application of the gradient of cost function) which may (or may not) switch the nature of the node. In other words these nodes are independent parameters. Here no re-initialization is necessary for the LSF. From a physical perspective α is discrete and can only hold two values, hence for a node (η) at a location ($\boldsymbol{r}$) the relationship is given as:

$$\alpha_{\text{phy}}(\boldsymbol{r}) = \begin{cases} 0 \text{ if } \Psi(\boldsymbol{r}) < 0 \text{ (solid node) i.e. } \eta \in \mathcal{D}_{\text{s}} \\ 1 \text{ if } \Psi(\boldsymbol{r}) > 0 \text{ (fluid node) i.e. } \eta \in \mathcal{D}_{\text{f}} \end{cases} \tag{3.23}$$

For optimization a pragmatic approach is elected by providing a smooth mapping between α and Ψ:

$$\alpha(\Psi) = \frac{1}{2} + \frac{1}{\pi} \arctan \frac{\Psi}{\epsilon_1} \tag{3.24}$$

The derivative of the continuous function α w.r.t Ψ:

$$\alpha'(\Psi) = \partial_{\Psi}[\alpha] = \frac{\epsilon_1}{\pi(\epsilon_1^2 + \Psi^2)} \tag{3.25}$$

As can been seen from fig. 3.3 the *discrete* nature of α can be reproduced when $\epsilon_1 \to 0$ while still having a finite value for $\alpha'(\Psi)$ (for $\epsilon_1 \neq 0$). The continuous nature of α makes it possible for non-zero (pseudo-)velocity at the solid nodes on the solid-fluid boundary (Γ_{sf}). This is translated into a non-zero gradient for the corresponding solid nodes. This facilitates the removal of solid nodes if the gradient requires so. Previously [40], the LSF was artificially capped such that $\Psi = \{n_1 |\ n_1 \in \mathbb{R} \text{ and } -1 < n_1 < 1\}$. This limit on the LSF have been removed to register the changes/gradients completely. The purpose of capping the LSF value was to allow for use of a smaller gradient step size (ξ) as the LSF value remains in the vicinity of the zero-contour.

3.1.4. Line search algorithm

The line search algorithm determines the step size of the gradient (of the cost function) to be applied while updating the control parameters for the optimization. The methods/algorithm utilized are broadly classified into exact and inexact line search. Examples of the exact line search are the dichotomy method, secant method, quadratic interpolation, Newton-Raphson method and etc. While all these methods aid in reaching close to the minimum of the cost function, some other methods/optimizers (like for example BFGS and LBFGS; optimizers will be explored in the following subsection) could be satisfied by a less precise guess of the step size. This is accomplished by using the inexact line search algorithm. Here instead it would suffice that certain conditions/rules should be satisfied. These rules depend on the method/algorithm in use for e.g. Goldstein rules which

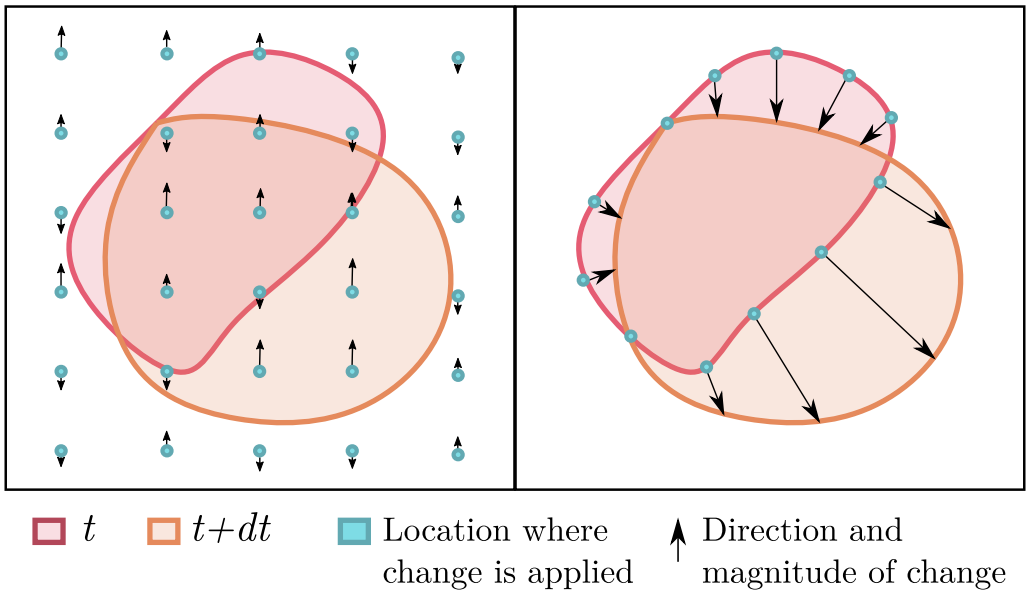

Figure 3.2: The manner of evolution/update in the level-set (LSF): a comparison between the use of LSF for registering optimization change and the standard LSF method (from [40]).

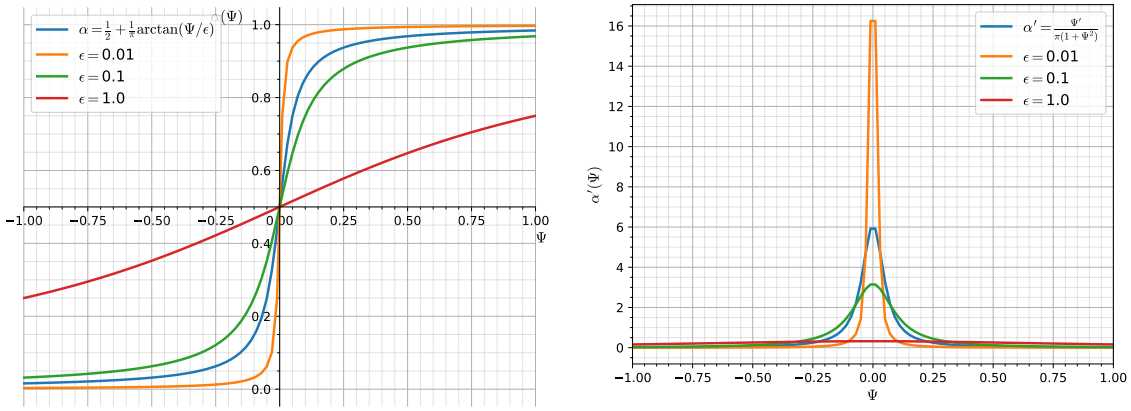

(a) $\alpha(\Psi)$ (b) $\alpha'(\Psi)$

Figure 3.3: Plot of continuous version of α and α'

determines the outermost bounds (i.e. maximum and minimum) for the gradient step size (ξ). In this thesis we use the dichotomy line search also known as the bisection method. Here we halve or double the step size if the application of the gradient of the cost function ($\nabla\mathcal{J}$) on the control parameters results in increasing or decreasing the cost function respectively (please note that for cases where we want to maximize a cost function, we convert it to a minimization problem by multiplying the cost function value by -1). This process is repeated until we determine the step size which breaks the trends of increasing and decreasing of the cost function respectively. This entire process is written in algorithm 2 at page 71.

3.1.5. Optimizers

As is evident, obtaining the (optimization) gradient ($\nabla\mathcal{J}$) is only a part of the optimization process. The next step involves the application of this gradient to the control parameters so as to obtain or arrive at the new (iterative) state. In short, each optimizer represents a strategy to effect change and thus march in the direction of the optimized set of control parameters which for our case is the topol-

Algorithm 2: The bisection/dichotomy algorithm

Input: Physical state: $\mathcal{F}$ & gradient of cost function ($\nabla\mathcal{J}$)
Initialize gradient step size $\xi^{(0)}$
Define the maximum multiple of 2 to be applied on ξ i.e. $k^{\max}$
Calculate the cost function $\mathcal{J}^{(\star)}$ from state $\mathcal{F}^{(\star)}$ provided as the input.
Compute $\mathcal{J}^{(0)}$ from $\mathcal{F}^{(0)}$ obtained from $\Pi^{(0)} = \Pi^{(\star)} - \xi^{(0)}\nabla\mathcal{J}$; where Π = control parameter
if $(\mathcal{J}^{(0)} < \mathcal{J}^{(\star)})$ **then**
  $\xi^{(1)} \leftarrow 2\xi^{(0)}$ (doubling the step size)
  do
    Compute $\mathcal{J}^{(k)}$ from $\mathcal{F}^{(k)}$ obtained from $\Pi^{(k)} = \Pi^{(\star)} - \xi^{(k)}\nabla\mathcal{J}$
    if $(\mathcal{J}^{(k)} < \mathcal{J}^{(k-1)})$ **then**
      $\xi^{(k+1)} \leftarrow 2\xi^{(k)}$
    else
      $\xi^{(k+1)} \leftarrow \xi^{(k)}/2$
    Increment k by 1 i.e. $k \leftarrow k+1$.
  while $(\mathcal{J}^{(k)} < \mathcal{J}^{(k-1)}$ **AND** $k < k^{\max}$ **AND** $|\mathcal{J}^{(k)} - \mathcal{J}^{(k-1)}| > \gamma_c$; *where* γ_c *is a constant.)*;
else
  $\xi^{(1)} \leftarrow \xi^{(0)}/2$ (halving the step size)
  do
    Compute $\mathcal{J}^{(k)}$ from $\mathcal{F}^{(k)}$ obtained from $\Pi^{(k)} = \Pi^{(\star)} - \xi^{(k)}\nabla\mathcal{J}$
    if $(\mathcal{J}^{(k)} < \mathcal{J}^{(\star)})$ **then**
      $\xi^{(k+1)} \leftarrow 2\xi^{(k)}$
    else
      $\xi^{(k+1)} \leftarrow \xi^{(k)}/2$
    $k \leftarrow k+1$.
  while $(\mathcal{J}^{(k)} \leq \mathcal{J}^{(\star)}$ **AND** $k < k^{\max})$;
if $(k == k^{\max}$ **AND** $\mathcal{J}^{(\dagger)} \geq \mathcal{J}^{(\star)})$ **then**
  $\xi^{(\dagger)} = 0$
return *Gradient step size* $(\xi^{(\dagger)})$

ogy ($\mathscr{T}$), i.e. the structure of the wall/solid domain ($\mathcal{D}_s$) or material allocation of the solid nodes in the domain ($\mathcal{D}$). The Newton method is a 2^{nd} order optimizer, which requires the computation of the Hessian ($\nabla^2\mathcal{J}$) for each optimization iteration. Though it uses few optimization iterations, the time taken and computational expense per optimization iteration is huge. If we instead approximate the computation of the Hessian then we would arrive at the quasi-Newton methods like Gauss-Newton, Davidon-Fletcher-Powell (DFP), Broyden-Fletcher-Goldfarb-Shanno (BFGS) and limited BFGS, i.e. LBFGS. These only decrease the computation expense by a margin, further reduction is possible by using first order methods like steepest/gradient descent (GD) and conjugate gradient (CG), amongst others. Though they greatly increase the amount of optimization iteration required these methods are popular due to a lower threshold of required computational resources. In this thesis, we utilize the simplest optimizer which is the gradient descent due to its pragmatic requirements. Hence the new state (i.e. next optimization iteration represented by $k+1$) is obtained by tweaking the control parameters (i.e. the Ψ for the topology optimization) at the current state (i.e. k):

$$\Psi^{(k+1)} = \Psi^{(k)} - \xi^{(k)}\nabla\mathcal{J}^{(k)} \tag{3.26}$$

where ξ is the step size while using gradient descent optimizer.

3.2. Optimization model

Here we are using the adjoint-state model for single phase fluid flow LBM solver that has been previously derived [40]. The only difference is that we derive the adjoint-state model for a com-

Algorithm 3: General flow for a topology optimization algorithm

Input: Initial topology: $\mathscr{T}^{(0)}$ (i.e. the geometry: $\mathcal{D} \in \mathcal{D}_\mathrm{f} \bigcup \mathcal{D}_\mathrm{s}$) obtained from $\Psi^{(0)}$ (which is the control variable), the objective or cost function: $\mathcal{J}$

Initialize Boltzmann variables $f_i^{(0)} = f_i^{\mathrm{eq}}\ \forall\ i$ for the fluid domain ($\mathcal{D}_\mathrm{f}$).

Initialize adjoint-state variables $\mathring{f}_i^{(0)} = 0\ \forall\ i$ for the fluid domain ($\mathcal{D}_\mathrm{f}$).

while *($\|\Psi^{(z)} - \Psi^{(z-1)}\|_1 \geq \gamma_\mathrm{c}$* **AND** *$z \leq z^{\max}$; where γ_c is a constant.)* **do**

- Compute the Boltzmann variables $\boldsymbol{f}^{(z)}$ from which we obtain the physical state $\mathcal{F}^{(k)}$
- Compute the cost function $\mathcal{J}^{(z)}$
- Compute the Adjoint-state variables $\mathring{\boldsymbol{f}}^{(z)}$ i.e. the adjoint-state $\mathring{\mathbf{f}}^{(z)}$
- Calculate the gradient of the cost function ($\nabla_\Psi \mathcal{J}^{(z)}$) using $\mathcal{F}^{(z)}$ and $\mathring{\mathbf{f}}^{(z)}$
- Compute the gradient step size ($\xi^{(z)}$) using a line search algorithm (optional)
- Apply the gradient using an optimizer (in this case, the gradient descent optimizer) to obtain $\Psi^{(z+1)}$ and hence $\mathscr{T}^{(z+1)}$
- Increment z by 1 i.e. $z \leftarrow z + 1$.

return *Optimized topology:* $\mathscr{T}^{(\dagger)} \leftarrow \Psi^{(\dagger)}$

pressible flow. As such the main purpose is to validate our methodology and explain the manner of derivation–This will later aid in the novel derivation of adjoint-state models for the multiphase pseudopotential LBM model.

3.2.1. Forward (LBM) problem

Here we reiterate the major equations used in the LBM solver and present it in the form palatable for the optimization discourse. The semi-discretized set of Boltzmann equations reads:

$$\mathcal{R}_i(\mathbf{f}, \Psi) = \frac{\partial f_i}{\partial t} + \boldsymbol{e}_i \cdot \nabla f_i + \frac{1}{\tau}\left(f_i - f_i^{\mathrm{eq}}\right) = 0 \quad \forall\ i\ \in\ [0,1,2,3,4,5,6,7,8] \tag{3.27}$$

rewriting the equilibrium distribution function as a function of the level-set we obtain:

$$f_i^{\mathrm{eq}}(\mathbf{f}, \Psi) = w_i \rho\left(1 + 3\alpha \boldsymbol{e}_i \cdot \boldsymbol{u} + 4.5\alpha\,(\boldsymbol{e}_i \cdot \boldsymbol{u})^2 - 1.5\alpha \boldsymbol{u}^2\right), \tag{3.28}$$

where $\boldsymbol{u}$ is the velocity defined using eq. (2.4) and eq. (2.5), $\mathbf{f}$ are the Boltzmann variables, while the α is a function of the level-set variable i.e. Ψ. Here for demonstrating the derivation of the adjoint-state boundary equation on all four sides i.e. the north, the east, the west and the south, we fix an inlet at the western boundary and exhibit the outlet boundary at the northern, the eastern and the southern boundaries. In other words, the outlet could be at any boundary or multiple boundaries. The same equations and methodology are applicable for any configuration with an inlet at west and any number of outlets. The partitioned boundary for a configuration with walls, inlet and outlet is denoted by $\Gamma = \Gamma_{\mathrm{in}} \oplus \Gamma_{\mathrm{out}} \oplus \Gamma_{\mathrm{bb}}$. The equation for boundaries are:

1. The inlet: (e.g. on the West boundary)

$$\begin{cases} \mathcal{P}_{\mathrm{in}(1)} = \mathcal{P}_1 = -f_3 + f_1 - \frac{2}{3}\rho u_x \\ \mathcal{P}_{\mathrm{in}(2)} = \mathcal{P}_5 = -f_7 + f_5 - \frac{1}{6}\rho u_x - \frac{1}{2}(f_4 - f_2) \\ \mathcal{P}_{\mathrm{in}(3)} = \mathcal{P}_8 = -f_6 + f_8 - \frac{1}{6}\rho u_x + \frac{1}{2}(f_4 - f_2) \end{cases} \tag{3.29}$$

   where:

$$\rho = \frac{f_0 + f_2 + f_4 + 2(f_3 + f_6 + f_7)}{1 - u_x} \tag{3.30}$$

2. The outlet: For the pressure boundary condition in LBM ρ on the boundary is constant. Now for the eastern boundary.

$$\begin{cases} \mathcal{P}_{\mathrm{out}(1)} = \mathcal{P}_3 = -f_1 + f_3 + \frac{2}{3}\rho u_x \\ \mathcal{P}_{\mathrm{out}(2)} = \mathcal{P}_7 = -f_5 + f_7 + \frac{1}{6}\rho u_x + \frac{1}{2}(f_4 - f_2) \\ \mathcal{P}_{\mathrm{out}(3)} = \mathcal{P}_6 = -f_8 + f_6 + \frac{1}{6}\rho u_x - \frac{1}{2}(f_4 - f_2) \end{cases} \tag{3.31}$$

where:

$$u_x = -1 + \frac{f_0 + f_2 + f_4 + 2(f_1 + f_5 + f_8)}{\rho} \tag{3.32}$$

On the North boundary

$$\begin{cases} \mathcal{P}_{\text{out}(1)} = \mathcal{P}_4 = -f_2 + f_4 + \frac{2}{3}\rho u_y \\ \mathcal{P}_{\text{out}(2)} = \mathcal{P}_7 = -f_5 + f_7 + \frac{1}{6}\rho u_y + \frac{1}{2}(f_3 - f_1) \\ \mathcal{P}_{\text{out}(3)} = \mathcal{P}_8 = -f_6 + f_8 + \frac{1}{6}\rho u_y - \frac{1}{2}(f_3 - f_1) \end{cases} \tag{3.33}$$

where:

$$u_y = -1 + \frac{f_0 + f_1 + f_3 + 2(f_2 + f_5 + f_6)}{\rho} \tag{3.34}$$

On the South boundary

$$\begin{cases} \mathcal{P}_{\text{out}(1)} = \mathcal{P}_2 = -f_4 + f_2 - \frac{2}{3}\rho u_y \\ \mathcal{P}_{\text{out}(2)} = \mathcal{P}_5 = -f_7 + f_5 - \frac{1}{6}\rho u_y - \frac{1}{2}(f_3 - f_1) \\ \mathcal{P}_{\text{out}(3)} = \mathcal{P}_6 = -f_8 + f_6 - \frac{1}{6}\rho u_y + \frac{1}{2}(f_3 - f_1) \end{cases} \tag{3.35}$$

where:

$$u_y = 1 - \frac{f_0 + f_1 + f_3 + 2(f_4 + f_7 + f_8)}{\rho} \tag{3.36}$$

3. The wall (bounce-back) condition: (e.g. on the South boundary)

$$\begin{cases} \mathcal{P}_{\text{bb}(1)} = \mathcal{P}_2 = f_2 - f_4 \\ \mathcal{P}_{\text{bb}(2)} = \mathcal{P}_5 = f_5 - f_7 \\ \mathcal{P}_{\text{bb}(3)} = \mathcal{P}_6 = f_6 - f_8 \end{cases} \tag{3.37}$$

3.2.2. Derivation of the adjoint-state model

From eq. (3.16) we know that the adjoint-state model can be obtained as:

$$\begin{aligned} (\text{aA2}) = 0 = \underbrace{\sum_j \left\langle \frac{\partial \mathscr{Y}}{\partial f_j} f_j', 1 \right\rangle_{\mathcal{D}}\Big|_{t=t_f}}_{\text{A1}} + \underbrace{\sum_i \left\langle \sum_j \frac{\partial \mathcal{R}_i}{\partial f_j} f_j', \mathring{f}_i \right\rangle_{\mathcal{D}\times\mathcal{T}}}_{\text{A2}} \\ + \sum_\beta \left(\underbrace{\sum_{i=1}^{3} \left\langle \sum_j \frac{\partial \mathcal{P}_{\beta(i)}}{\partial f_j} f_j', \mathring{f}_{\beta(i)} \right\rangle_{\Gamma_\beta \times \mathcal{T}}}_{\text{A3}} + \underbrace{\sum_j \left\langle \frac{\partial \mathscr{X}_\beta}{\partial f_j} f_j', 1 \right\rangle_{\Gamma_\beta}\Big|_{t=t_f}}_{\text{A4}} \right) \end{aligned} \tag{3.38}$$

The terms A1 and A4 comes from the derivation of the cost function which is acting in the domain and on the boundaries respectively. The A2 term is related to the lattice Boltzmann equation, which is applicable in the entire domain. The A3 term is derived form the boundary condition equation. Here it is observed that these terms are applicable to (or exist in) different phase spaces and hence for the gradient of Lagrange to be zero, it should be zero for each of these phase spaces.

3.2.2.a. *Adjoint-state equation*

Developing first the A2 term:

$$(\mathrm{A2}) = \sum_i \left\langle \sum_j \frac{\partial \mathcal{R}_i}{\partial f_j} f_j', \mathring{f}_i \right\rangle_{\mathcal{D}\times\mathcal{T}} = \underbrace{\left\langle \sum_i \frac{\partial f_i'}{\partial t}, \mathring{f}_i \right\rangle_{\mathcal{D}\times\mathcal{T}}}_{\mathrm{B1}} + \underbrace{\left\langle \sum_i \boldsymbol{e}_i \cdot \nabla f_i', \mathring{f}_i \right\rangle_{\mathcal{D}\times\mathcal{T}}}_{\mathrm{B2}} + \left\langle \sum_i \tau^{-1} f_i', \mathring{f}_i \right\rangle_{\mathcal{D}\times\mathcal{T}} - \underbrace{\left\langle \sum_i \sum_j \tau^{-1} \frac{\partial f_i^{\mathrm{eq}}}{\partial f_j} f_j', \mathring{f}_i \right\rangle_{\mathcal{D}\times\mathcal{T}}}_{\mathrm{B3}} \tag{3.39}$$

Using the three properties as mentioned before in ref. [139]:

Property 3.2.1. Integration by parts of the temporal operator (for a variable f and its arbitrary variation f'):

$$\left\langle \frac{\partial f'}{\partial t}, \mathring{f} \right\rangle_{\mathcal{T}} = \left\langle -\frac{\partial \mathring{f}}{\partial t}, f' \right\rangle_{\mathcal{T}} + \left[\mathring{f} f' \right]_{t=0}^{t=t_f} \tag{3.40}$$

Property 3.2.2. Green's theorem for the spatial gradient $\forall\ i$:

$$\left\langle \boldsymbol{e}_i \cdot \nabla f_i', \mathring{f}_i \right\rangle_{\mathcal{D}} = \left\langle -\boldsymbol{e}_i \cdot \nabla \mathring{f}_i, f_i' \right\rangle_{\mathcal{D}} + \left\langle \boldsymbol{e}_i \cdot \boldsymbol{n} \mathring{f}_i, f_i' \right\rangle_{\Gamma} \tag{3.41}$$

Property 3.2.3. Permutation of indices:

$$\sum_{i=0}^{8} \sum_{j=0}^{8} \mathring{f}_i \frac{\partial f_i^{\mathrm{eq}}}{\partial f_j} f_j' = \sum_{i=0}^{8} \sum_{j=0}^{8} \mathring{f}_j \frac{\partial f_j^{\mathrm{eq}}}{\partial f_i} f_i' \tag{3.42}$$

Now the term B1 can be further expanded by using integration by parts, while the term B2 can be developed by using Green's theorem. Now the term B3 can be rearranged by permutation of indices. The objective of this expansion of the term A2 is to obtain a final equation where the common factor, i.e. f_i', is segregated from the remainder of the equation. Thus the expanded version:

$$(\mathrm{A2}) = -\left\langle \sum_i \frac{\partial \mathring{f}_i}{\partial t}, f_i' \right\rangle_{\mathcal{D}\times\mathcal{T}} + \underbrace{\left[\sum_i \left\langle \mathring{f}_i, f_i' \right\rangle_{\mathcal{D}} \right]_{t=0}^{t=t_f}}_{\mathrm{C1}} - \sum_i \left\langle \boldsymbol{e}_i \cdot \nabla \mathring{f}_i, f_i' \right\rangle_{\mathcal{D}\times\mathcal{T}} + \underbrace{\sum_\beta \left\langle \sum_i \boldsymbol{e}_i \cdot \boldsymbol{n} \mathring{f}_i, f_i' \right\rangle_{\Gamma_\beta\times\mathcal{T}}}_{\mathrm{C2}} + \left\langle \sum_i \tau^{-1} f_i', \mathring{f}_i \right\rangle_{\mathcal{D}\times\mathcal{T}} - \left\langle \sum_i \sum_j \tau^{-1} \frac{\partial f_j^{\mathrm{eq}}}{\partial f_i} f_i', \mathring{f}_j \right\rangle_{\mathcal{D}\times\mathcal{T}} \tag{3.43}$$

The term C2 is to be applied on all the boundaries, while the term C1 is to be used for setting the initial conditions for adjoint-state problem. The adjoint-state equation is obtained from all terms

existing in the phase space that involve $\mathcal{D}\times\mathcal{T}$, i.e. excluding C1 and C2. Gathering the remaining terms and equating it's sum to zero:

$$\sum_i \left\langle -\frac{\partial \mathring{f}_i}{\partial t} - \boldsymbol{e}_i\cdot\nabla\mathring{f}_i + \tau^{-1}\mathring{f}_i - \tau^{-1}\sum_j \frac{\partial f_j^{\mathrm{eq}}}{\partial f_i}\mathring{f}_j, f_i' \right\rangle_{\mathcal{D}\times\mathcal{T}} = 0 \qquad \forall\ f_i' \tag{3.44}$$

One way to get this equality is to choose:

$$-\frac{\partial \mathring{f}_i}{\partial t} - \boldsymbol{e}_i\cdot\nabla\mathring{f}_i + \tau^{-1}\mathring{f}_i - \tau^{-1}\sum_j \frac{\partial f_j^{\mathrm{eq}}}{\partial f_i}\mathring{f}_j = 0 \qquad \forall\ \boldsymbol{r}\in\mathcal{D},\ \forall\ t\in(0,t_f),\ \forall\ i \tag{3.45}$$

Thus the adjoint-state equation can be rewritten as:

$$-\frac{\partial \mathring{f}_i}{\partial t} - \boldsymbol{e}_i\cdot\nabla\mathring{f}_i + \frac{\mathring{f}_i - \mathring{f}_i^{\mathrm{eq}}}{\tau} = 0 \qquad \forall\ \boldsymbol{r}\in\mathcal{D},\ \forall\ t\in(0,t_f),\ \forall\ i \tag{3.46}$$

3.2.2.a.1. Adjoint-state equilibrium

From eq. (3.46) we can write the adjoint-state equilibrium distribution formulation as:

$$\mathring{f}_i^{\mathrm{eq}} = \sum_j \frac{\partial f_j^{\mathrm{eq}}}{\partial f_i}\mathring{f}_j \tag{3.47}$$

$$\mathring{f}_i^{\mathrm{eq}} = \sum_j \left(w_j\frac{\partial\rho}{\partial f_i} + 3w_j\alpha\frac{\partial\rho\boldsymbol{e}_j\cdot\boldsymbol{u}}{\partial f_i} + 4.5w_j\alpha\frac{\partial\rho\left(\boldsymbol{e}_j\cdot\boldsymbol{u}\right)^2}{\partial f_i} - 1.5w_j\alpha\frac{\partial\rho\boldsymbol{u}^2}{\partial f_i}\right)\mathring{f}_j \tag{3.48}$$

$$\begin{aligned}\mathring{f}_i^{\mathrm{eq}} = \sum_j \Bigg(& w_j\sum_k\frac{\partial f_k}{\partial f_i} + 3w_j\alpha\sum_k\frac{\partial f_k\boldsymbol{e}_j\cdot\boldsymbol{e}_k}{\partial f_i} \\ & +4.5w_j\alpha\frac{\partial}{\partial f_i}\left[\frac{\left(\sum_k f_k\boldsymbol{e}_j\cdot\boldsymbol{e}_k\right)^2}{\sum_k f_k}\right] - 1.5w_j\alpha\frac{\partial}{\partial f_i}\left[\frac{(\sum_k f_k\boldsymbol{e}_k)^2}{\sum_k f_k}\right]\Bigg)\mathring{f}_j\end{aligned} \tag{3.49}$$

$$\begin{aligned}\mathring{f}_i^{\mathrm{eq}} = \sum_j \Bigg(& w_j + 3w_j\alpha\boldsymbol{e}_j\cdot\boldsymbol{e}_{i=k} + 4.5w_j\alpha\left[\frac{2\boldsymbol{e}_j\cdot\boldsymbol{e}_{i=k}(\sum_k f_k\boldsymbol{e}_j\cdot\boldsymbol{e}_k)}{\sum_k f_k} - \frac{(\sum_k f_k\boldsymbol{e}_j\cdot\boldsymbol{e}_k)^2}{(\sum_k f_k)^2}\right] \\ & -1.5w_j\alpha\left[\frac{2\boldsymbol{e}_{i=k}(\sum_k f_k\boldsymbol{e}_k)}{\sum_k f_k} - \frac{(\sum_k f_k\boldsymbol{e}_k)^2}{(\sum_k f_k)^2}\right]\Bigg)\mathring{f}_i\end{aligned} \tag{3.50}$$

Thus we can write:

$$\mathring{f}_i^{\mathrm{eq}} = \sum_j w_j\mathring{f}_j\left(1 + 3\alpha\boldsymbol{e}_j\cdot\boldsymbol{e}_i + 4.5\alpha[2(\boldsymbol{e}_j\cdot\boldsymbol{e}_i)(\boldsymbol{e}_j\cdot\boldsymbol{u}) - (\boldsymbol{e}_j\cdot\boldsymbol{u})^2] - 1.5\alpha[2\boldsymbol{e}_i\boldsymbol{u} - (\boldsymbol{u})^2]\right) \tag{3.51}$$

This provides us with the adjoint-state equilibrium function.

3.2.2.a.2. Going back in time and space

The adjoint-state equation can be written in the same form as eq. (3.27), provided the following changes are made:

$$\mathring{t} = t_f - t \quad \text{and} \quad \mathring{\boldsymbol{e}}_i = -\boldsymbol{e}_i \tag{3.52}$$

In other words, essentially we regress in time and advection (for f) as we iteratively solve for adjoint-state starting form the result at t_f of the forward problem. The discussion of time is of lesser importance as the problem on hand is an optimization problem, where only the final iteration data is important.

Doing so, the adjoint-state eq. (3.46) is rewritten as:

$$\frac{\partial \mathring{f}_i}{\partial \mathring{t}} + \mathring{\boldsymbol{e}}_i \cdot \nabla \mathring{f}_i + \frac{\mathring{f}_i - \mathring{f}_i^{\mathrm{eq}}}{\tau} = 0 \qquad \forall \boldsymbol{r} \in \mathcal{D},\ \forall t \in (t_f, 0),\ \forall i \tag{3.53}$$

and the initial condition (at $\mathring{t} = 0$) is well defined, and the boundary conditions are given for entrant directions $\mathring{\boldsymbol{e}}_i \cdot \boldsymbol{n} < 0$, i.e. for $\boldsymbol{e}_i \cdot \boldsymbol{n} > 0$.

3.2.2.a.3. Adjoint-state initial condition

The initial condition inside the domain is obtained from the terms A1 and C1 and equating the sum of these terms to zero:

$$\begin{aligned}(\mathrm{C1}) + (\mathrm{A1}) = \Bigg[\sum_i \left\langle \mathring{f}_i, f_i' \right\rangle_{\mathcal{D}} \Bigg]_{t=0}^{t=t_f} + \left\langle \sum_j \frac{\partial \mathscr{Y}}{\partial f_j}, f_j' \right\rangle_{\mathcal{D}} \Bigg|_{t=t_f} \\ = \sum_i \left\langle \frac{\partial \mathscr{Y}}{\partial f_i} + \mathring{f}_i, f_i' \right\rangle_{\mathcal{D}} \Bigg|_{t=t_f} - 0 \Big|_{t=0} = 0 \qquad \forall\ f_i'\end{aligned} \tag{3.54}$$

which is satisfied if:

$$\mathring{f}_i(t_f) = -\frac{\partial \mathscr{Y}}{\partial f_i} \qquad \forall\ \boldsymbol{r} \in \mathcal{D},\ \forall\ f_i',\ \forall\ i \tag{3.55}$$

The eq. (3.55) is used for transient-state analysis i.e. TOTFP method. For the current analysis (which uses a TOSFP method), as mentioned previously, we repeatedly apply the cost function differentiation (during the adjoint-state time). In other words, the term A1 is placed on eq. (3.53) where the time integral is ignored as it is no longer of importance. Thus we can rewrite eq. (3.53) as:

$$\frac{\partial \mathring{f}_i}{\partial \mathring{t}} + \mathring{\boldsymbol{e}}_i \cdot \nabla \mathring{f}_i + \frac{\mathring{f}_i - \mathring{f}_i^{\mathrm{eq}}}{\tau} + \sum_j \frac{\partial \mathscr{Y}}{\partial f_j} = 0 \qquad \forall\ \boldsymbol{r} \in \mathcal{D},\ \forall\ f_i',\ \forall\ i \tag{3.56}$$

This is equivalent to applying a constant cost function across the adjoint-state time interval. In other words, the effect of the initial condition is augmented and this term could also be portrayed as a source term rather than an initial condition.

3.2.2.b. Wall (BB) boundary condition

The adjoint-state wall (bounceback) condition can be given by gathering all related terms in A3 and A4 and also the term C2 and equating the sum of all these terms to zero:

$$\underbrace{\sum_{i=1}^{3} \left\langle \sum_j \frac{\partial \mathcal{P}_{\mathrm{bb}(i)}}{\partial f_j} f_j', \mathring{f}_{\mathrm{bb}(i)} \right\rangle_{\Gamma_{\mathrm{bb}} \times \mathcal{T}}}_{\mathrm{D1}} + \underbrace{\sum_i \left\langle \boldsymbol{e}_i \cdot \boldsymbol{n} \mathring{f}_i, f_i' \right\rangle_{\Gamma_{\mathrm{bb}} \times \mathcal{T}}}_{\mathrm{D2}} + \underbrace{\sum_j \left\langle \frac{\partial \mathscr{X}_{\mathrm{bb}}}{\partial f_j}, f_j' \right\rangle_{\Gamma_{\mathrm{bb}}} \Bigg|_{t=t_f}}_{\mathrm{D3}} = 0 \tag{3.57}$$

Hence for BB condition on a wall located in the south given by eq. (3.37). The expansion gives (we take only the integrants within integrals):

$$(\mathrm{D1}) = \langle f_2' - f_4', \mathring{f}_2 \rangle_{\Gamma_{\mathrm{bb}} \times \mathcal{T}} + \langle f_5' - f_7', \mathring{f}_5 \rangle_{\Gamma_{\mathrm{bb}} \times \mathcal{T}} + \langle f_6' - f_8', \mathring{f}_6 \rangle_{\Gamma_{\mathrm{bb}} \times \mathcal{T}} \tag{3.58}$$

$$(\mathrm{D2}) = \langle -f_5' \mathring{f}_5 - f_2' \mathring{f}_2 - f_6' \mathring{f}_6 + f_7' \mathring{f}_7 + f_4' \mathring{f}_4 + f_8' \mathring{f}_8, 1 \rangle_{\Gamma_{\mathrm{bb}} \times \mathcal{T}} \tag{3.59}$$

and

$$(\mathrm{D3}) = \sum_j \left\langle \frac{\partial \mathscr{K}_{\mathrm{bb}}}{\partial f_j}, f_j' \right\rangle_{\Gamma_{\mathrm{bb}}} \Big|_{t=t_f} \tag{3.60}$$

Combining all terms and rearranging equation we get:

$$\begin{aligned}\langle f_2' - f_4' - f_2', \mathring{f}_2\rangle_{\Gamma_{\mathrm{bb}}\times\mathcal{T}} + \langle f_5' - f_7' - f_5', \mathring{f}_5\rangle_{\Gamma_{\mathrm{bb}}\times\mathcal{T}} + \langle f_6' - f_8' - f_6', \mathring{f}_6\rangle_{\Gamma_{\mathrm{bb}}\times\mathcal{T}} \\ + \langle f_7', \mathring{f}_7\rangle_{\Gamma_{\mathrm{bb}}\times\mathcal{T}} + \langle f_4', \mathring{f}_4\rangle_{\Gamma_{\mathrm{bb}}\times\mathcal{T}} + \langle f_8', \mathring{f}_8\rangle_{\Gamma_{\mathrm{bb}}\times\mathcal{T}} \\ + \sum_j \left\langle \frac{\partial \mathscr{K}_{\mathrm{bb}}}{\partial f_j}, f_j' \right\rangle_{\Gamma_{\mathrm{bb}}} = 0\end{aligned} \tag{3.61}$$

$$\begin{aligned}\langle -f_4', \mathring{f}_2\rangle_{\Gamma_{\mathrm{bb}}\times\mathcal{T}} + \langle -f_7', \mathring{f}_5\rangle_{\Gamma_{\mathrm{bb}}\times\mathcal{T}} + \langle -f_8', \mathring{f}_6\rangle_{\Gamma_{\mathrm{bb}}\times\mathcal{T}} + \langle f_7', \mathring{f}_7\rangle_{\Gamma_{\mathrm{bb}}\times\mathcal{T}} \\ + \langle f_4', \mathring{f}_4\rangle_{\Gamma_{\mathrm{bb}}\times\mathcal{T}} + \langle f_8', \mathring{f}_8\rangle_{\Gamma_{\mathrm{bb}}\times\mathcal{T}} + \sum_j \left\langle \frac{\partial \mathscr{K}_{\mathrm{bb}}}{\partial f_j}, f_j' \right\rangle_{\Gamma_{\mathrm{bb}}} = 0\end{aligned} \tag{3.62}$$

rearranging terms and accumulating the remaining irrelevant terms in a dummy function Θ:

$$\langle f_7', \mathring{f}_7 - \mathring{f}_5\rangle_{\Gamma_{\mathrm{bb}}\times\mathcal{T}} + \langle f_4', \mathring{f}_4 - \mathring{f}_2\rangle_{\Gamma_{\mathrm{bb}}\times\mathcal{T}} + \langle f_8', \mathring{f}_8 - \mathring{f}_6\rangle_{\Gamma_{\mathrm{bb}}\times\mathcal{T}} + \left\langle \frac{\partial \mathscr{K}_{\mathrm{bb}}}{\partial f_7} f_7' + \frac{\partial \mathscr{K}_{\mathrm{bb}}}{\partial f_4} f_4' + \frac{\partial \mathscr{K}_{\mathrm{bb}}}{\partial f_8} f_8', 1 \right\rangle_{\Gamma_{\mathrm{bb}}} \Big|_{t=t_f} + \Theta = 0 \tag{3.63}$$

As before, we note that inner product in the phase space Γ_{bb} acts as an initial condition for the wall boundary for a TOTFP problem. For the current state case, we can ignore the temporal aspect and hence write all the terms of eq. (3.63) in the phase space Γ_{bb}. Thus we can write the equation as:

$$\left\langle f_7', \mathring{f}_7 - \mathring{f}_5 + \frac{\partial \mathscr{K}_{\mathrm{bb}}}{\partial f_7} \right\rangle_{\Gamma_{\mathrm{bb}}} + \left\langle f_4', \mathring{f}_4 - \mathring{f}_2 + \frac{\partial \mathscr{K}_{\mathrm{bb}}}{\partial f_4} \right\rangle_{\Gamma_{\mathrm{bb}}} + \left\langle f_8', \mathring{f}_8 - \mathring{f}_6 + \frac{\partial \mathscr{K}_{\mathrm{bb}}}{\partial f_8} \right\rangle_{\Gamma_{\mathrm{bb}}} + \Theta = 0 \tag{3.64}$$

Note here that the three terms gives the three unknowns $\mathring{f}_4, \mathring{f}_7, \mathring{f}_8$ for the adjoint-state problem, so this will give $\mathring{\mathcal{P}}_4$, $\mathring{\mathcal{P}}_7$ and $\mathring{\mathcal{P}}_8$. Since this is to be satisfied $\forall f'$, this gives:

$$\begin{cases} \mathring{\mathcal{P}}_{\mathrm{bb}(1)} = \mathring{\mathcal{P}}_4 = \mathring{f}_2 - \mathring{f}_4 - \dfrac{\partial \mathscr{K}_{\mathrm{bb}}}{\partial f_4} = 0 \\ \mathring{\mathcal{P}}_{\mathrm{bb}(2)} = \mathring{\mathcal{P}}_7 = \mathring{f}_5 - \mathring{f}_7 - \dfrac{\partial \mathscr{K}_{\mathrm{bb}}}{\partial f_7} = 0 \\ \mathring{\mathcal{P}}_{\mathrm{bb}(3)} = \mathring{\mathcal{P}}_8 = \mathring{f}_6 - \mathring{f}_8 - \dfrac{\partial \mathscr{K}_{\mathrm{bb}}}{\partial f_8} = 0 \end{cases} \tag{3.65}$$

3.2.2.c. Inflow adjoint-state

The inflow boundary condition for the adjoint-state is given gathering all relevant inlet boundary terms, and equating this to zero:

$$\underbrace{\sum_j \left\langle \frac{\partial \mathscr{K}_{\mathrm{in}}}{\partial f_j}, f_j' \right\rangle_{\Gamma_{\mathrm{in}}} \Big|_{t=t_f}}_{\mathrm{E1}} + \underbrace{\sum_{i=1}^{3} \left\langle \sum_j \frac{\partial \mathcal{P}_{\mathrm{in}(i)}}{\partial f_j} f_j', \mathring{f}_{\mathrm{in}(i)} \right\rangle_{\Gamma_{\mathrm{in}}\times\mathcal{T}}}_{\mathrm{E2}} + \underbrace{\sum_i \left\langle \boldsymbol{e}_i \cdot \boldsymbol{n} \mathring{f}_i, f_i' \right\rangle_{\Gamma_{\mathrm{in}}}}_{\mathrm{E3}} = 0 \tag{3.66}$$

Hence for inflow condition on a boundary located in west given by eq. (3.29). The expansion gives (again we work only with the integrants):

$$(\mathrm{E1}) = \sum_j \left\langle \frac{\partial \mathscr{K}_{\mathrm{in}}}{\partial f_j}, f_j' \right\rangle_{\Gamma_{\mathrm{in}}} \Big|_{t=t_f} \tag{3.67}$$

$$
\begin{aligned}
(\mathrm{E2}) = &\left\langle -f_3' + f_1' - \frac{2u_x}{3(1-u_x)}(f_0' + f_2' + f_4' + 2(f_3' + f_6' + f_7')), \mathring{f}_1 \right\rangle_{\Gamma_{\text{in}} \times \mathcal{T}} \\
&+ \left\langle -f_7' + f_5' - \frac{f_4' - f_2'}{2} - \frac{u_x}{6(1-u_x)}(f_0' + f_2' + f_4' + 2(f_3' + f_6' + f_7')), \mathring{f}_5 \right\rangle_{\Gamma_{\text{in}} \times \mathcal{T}} \\
&+ \left\langle -f_6' + f_8' + \frac{f_4' - f_2'}{2} - \frac{u_x}{6(1-u_x)}(f_0' + f_2' + f_4' + 2(f_3' + f_6' + f_7')), \mathring{f}_8 \right\rangle_{\Gamma_{\text{in}} \times \mathcal{T}}
\end{aligned} \tag{3.68}
$$

and

$$
(\mathrm{E3}) = \left\langle -f_1' \mathring{f}_1 - f_5' \mathring{f}_5 - f_8' \mathring{f}_8 + f_3' \mathring{f}_3 + f_6' \mathring{f}_6 + f_7' \mathring{f}_7, 1 \right\rangle_{\Gamma_{\text{in}} \times \mathcal{T}} \tag{3.69}
$$

thus E2 becomes:

$$
\begin{aligned}
(\mathrm{E2}) = &\left\langle -\frac{2u_x}{3(1-u_x)} f_0' + f_1' - \frac{2u_x}{3(1-u_x)} f_2' - \left[1 + \frac{4u_x}{3(1-u_x)}\right] f_3' \right. \\
&\left. - \frac{2u_x}{3(1-u_x)} f_4' - \frac{4u_x}{3(1-u_x)} f_6' - \frac{4u_x}{3(1-u_x)} f_7', \mathring{f}_1 \right\rangle_{\Gamma_{\text{in}} \times \mathcal{T}} \\
&+ \left\langle -\frac{u_x}{6(1-u_x)} f_0' - \left[\frac{u_x}{6(1-u_x)} - \frac{1}{2}\right] f_2' - \frac{u_x}{3(1-u_x)} f_3' \right. \\
&\left. - \left[\frac{u_x}{6(1-u_x)} + \frac{1}{2}\right] f_4' + f_5' - \frac{u_x}{3(1-u_x)} f_6' - \left[1 + \frac{u_x}{3(1-u_x)}\right] f_7', \mathring{f}_5 \right\rangle_{\Gamma_{\text{in}} \times \mathcal{T}} \\
&+ \left\langle -\frac{u_x}{6(1-u_x)} f_0' - \left[\frac{u_x}{6(1-u_x)} + \frac{1}{2}\right] f_2' - \frac{u_x}{3(1-u_x)} f_3' - \left[\frac{u_x}{6(1-u_x)} - \frac{1}{2}\right] f_4' \right. \\
&\left. - \left[1 + \frac{u_x}{3(1-u_x)}\right] f_6' - \frac{u_x}{3(1-u_x)} f_7' + f_8', \mathring{f}_8 \right\rangle_{\Gamma_{\text{in}} \times \mathcal{T}}
\end{aligned} \tag{3.70}
$$

Now adding the three terms E1, E2 and E3 and factorizing w.r.t f' we obtain an equation of which we elaborate only the relevant terms. The remainder of terms are accumulated in a dummy function Θ. Thus we write:

$$
\begin{aligned}
(\mathrm{E1}) + (\mathrm{E2}) + (\mathrm{E3}) = &\left\langle f_3', \mathring{f}_3 - \left[1 + \frac{4u_x}{3(1-u_x)}\right] \mathring{f}_1 - \frac{u_x}{3(1-u_x)} \mathring{f}_5 - \frac{u_x}{3(1-u_x)} \mathring{f}_8 \right\rangle_{\Gamma_{\text{in}} \times \mathcal{T}} \\
&+ \left\langle f_6', \mathring{f}_6 - \frac{4u_x}{3(1-u_x)} \mathring{f}_1 - \frac{u_x}{3(1-u_x)} \mathring{f}_5 - \left[1 + \frac{u_x}{3(1-u_x)}\right] \mathring{f}_8 \right\rangle_{\Gamma_{\text{in}} \times \mathcal{T}} \\
&+ \left\langle f_7', \mathring{f}_7 - \frac{4u_x}{3(1-u_x)} \mathring{f}_1 - \left[1 + \frac{u_x}{3(1-u_x)}\right] \mathring{f}_5 - \frac{u_x}{3(1-u_x)} \mathring{f}_8 \right\rangle_{\Gamma_{\text{in}} \times \mathcal{T}} \\
&+ \left\langle f_3', \frac{\partial \mathscr{K}_{\text{in}}}{\partial f_3} \right\rangle_{\Gamma_{\text{in}}} + \left\langle f_6', \frac{\partial \mathscr{K}_{\text{in}}}{\partial f_6} \right\rangle_{\Gamma_{\text{in}}} + \left\langle f_7', \frac{\partial \mathscr{K}_{\text{in}}}{\partial f_7} \right\rangle_{\Gamma_{\text{in}}} + \Theta = 0
\end{aligned} \tag{3.71}
$$

As before, we note that inner product in the phase space Γ_{in} acts as an initial condition for the inlet boundary for a TOTFP problem. For the current state case, we can ignore the temporal aspect and hence write all the terms of eq. (3.71) in the phase space Γ_{in}. Since this is satisfied $\forall f'$, this finally gives us the adjoint-state inflow boundary condition for unknowns $\mathring{f}_3, \mathring{f}_6, \mathring{f}_7$ as:

$$
\begin{cases}
\mathring{\mathcal{P}}_{\text{in}(1)} = \mathring{\mathcal{P}}_3 = \mathring{f}_3 + \dfrac{\partial \mathscr{K}_{\text{in}}}{\partial f_3} - \mathring{f}_1 - \dfrac{u_x}{3(1-u_x)}(4\mathring{f}_1 + \mathring{f}_5 + \mathring{f}_8) \\
\mathring{\mathcal{P}}_{\text{in}(2)} = \mathring{\mathcal{P}}_6 = \mathring{f}_6 + \dfrac{\partial \mathscr{K}_{\text{in}}}{\partial f_6} - \mathring{f}_8 - \dfrac{u_x}{3(1-u_x)}(4\mathring{f}_1 + \mathring{f}_5 + \mathring{f}_8) \\
\mathring{\mathcal{P}}_{\text{in}(3)} = \mathring{\mathcal{P}}_7 = \mathring{f}_7 + \dfrac{\partial \mathscr{K}_{\text{in}}}{\partial f_7} - \mathring{f}_5 - \dfrac{u_x}{3(1-u_x)}(4\mathring{f}_1 + \mathring{f}_5 + \mathring{f}_8)
\end{cases} \tag{3.72}
$$

3.2.2.d. *Outflow adjoint-state*

The outflow boundary condition for the adjoint-state is given gathering all related terms, and zeroing this sum:

$$\sum_{\rho}\left(\underbrace{\sum_{j}\left\langle\frac{\partial\mathscr{K}_{\text{out}}}{\partial f_j},f_j'\right\rangle_{\Gamma_{\text{out}}}\Big|_{t=t_f}}_{\text{F1}}+\underbrace{\sum_{i=1}^{3}\left\langle\sum_{j}\frac{\partial\mathcal{P}_{\text{out}(i)}}{\partial f_j}f_j',\mathring{f}_{\text{out}(i)}\right\rangle_{\Gamma_{\text{out}}\times\mathcal{T}}}_{\text{F2}}+\underbrace{\sum_{i}\left\langle\boldsymbol{e}_i\cdot\boldsymbol{n}\mathring{f}_i,f_i'\right\rangle_{\Gamma_{\text{out}}\times\mathcal{T}}}_{\text{F3}}\right)=0 \tag{3.73}$$

As we see, F1 which comes form A1 is given at t_f only, while the others are for all t. If we were considering the current problem there would be of time. In other words, we can combine all terms in the phase space Γ_{out}. This gives the outflow condition for the adjoint-state at steady state.

1. On the eastern boundary, outflow condition is given by eq. (3.31). The expansion thus is given as (again we work only with the integrants):

$$(\text{F1})_{\text{east}}=\sum_{j}\left\langle f_j',\frac{\partial\mathscr{K}_{\text{out,east}}}{\partial f_j}\right\rangle_{\Gamma_{\text{out,east}}} \tag{3.74}$$

$$(\text{F3})_{\text{east}}=\left\langle\mathring{f}_1f_1'-\mathring{f}_3f_3'+\mathring{f}_5f_5'-\mathring{f}_6f_6'-\mathring{f}_7f_7'+\mathring{f}_8f_8',1\right\rangle_{\Gamma_{\text{out,east}}} \tag{3.75}$$

$$\begin{aligned}(\text{F2})_{\text{east}}=&\left\langle\mathring{f}_3,-f_1'+f_3'+\frac{2\rho}{3}\left[0+\frac{f_0'+f_2'+f_4'+2(f_1'+f_5'+f_8')}{\rho}\right]\right\rangle_{\Gamma_{\text{out,east}}}\\&+\left\langle\mathring{f}_6,-f_8'+f_6'-\frac{f_4'-f_2'}{2}+\frac{\rho}{6}\left[0+\frac{f_0'+f_2'+f_4'+2(f_1'+f_5'+f_8')}{\rho}\right]\right\rangle_{\Gamma_{\text{out,east}}}\\&+\left\langle\mathring{f}_7,-f_5'+f_7'+\frac{f_4'-f_2'}{2}+\frac{\rho}{6}\left[0+\frac{f_0'+f_2'+f_4'+2(f_1'+f_5'+f_8')}{\rho}\right]\right\rangle_{\Gamma_{\text{out,east}}}\end{aligned} \tag{3.76}$$

Now adding the terms F1_{east}, F2_{east} and F3_{east} and factorizing w.r.t f' we obtain an equation of which we elaborate only the relevant terms. The remainder of terms are accumulated in a dummy function Θ. Thus we write:

$$\begin{aligned}(\text{F1})_{\text{east}}+(\text{F2})_{\text{east}}+(\text{F3})_{\text{east}}=&\left\langle f_1',\mathring{f}_1+\frac{\partial\mathscr{K}_{\text{out,east}}}{\partial f_1}-\mathring{f}_3+\frac{1}{3}(4\mathring{f}_3+\mathring{f}_6+\mathring{f}_7)\right\rangle_{\Gamma_{\text{out,east}}}\\&+\left\langle f_5',\mathring{f}_5+\frac{\partial\mathscr{K}_{\text{out,east}}}{\partial f_5}-\mathring{f}_7+\frac{1}{3}(4\mathring{f}_3+\mathring{f}_6+\mathring{f}_7)\right\rangle_{\Gamma_{\text{out,east}}}\\&+\left\langle f_8',\mathring{f}_8+\frac{\partial\mathscr{K}_{\text{out,east}}}{\partial f_8}-\mathring{f}_6+\frac{1}{3}(4\mathring{f}_3+\mathring{f}_6+\mathring{f}_7)\right\rangle_{\Gamma_{\text{out,east}}}+\Theta=0\end{aligned} \tag{3.77}$$

Since this is satisfied $\forall f'$, this finally gives the adjoint-state outflow boundary condition for unknowns $\mathring{f}_1,\mathring{f}_5,\mathring{f}_8$ as:

$$\begin{cases}\mathring{\mathcal{P}}_{\text{out}(1)}=\mathring{\mathcal{P}}_1=\mathring{f}_1+\dfrac{\partial\mathscr{K}_{\text{out,east}}}{\partial f_1}-\mathring{f}_3+\dfrac{1}{3}(4\mathring{f}_3+\mathring{f}_6+\mathring{f}_7)\\ \mathring{\mathcal{P}}_{\text{out}(2)}=\mathring{\mathcal{P}}_5=\mathring{f}_5+\dfrac{\partial\mathscr{K}_{\text{out,east}}}{\partial f_5}-\mathring{f}_7+\dfrac{1}{3}(4\mathring{f}_3+\mathring{f}_6+\mathring{f}_7)\\ \mathring{\mathcal{P}}_{\text{out}(3)}=\mathring{\mathcal{P}}_8=\mathring{f}_8+\dfrac{\partial\mathscr{K}_{\text{out,east}}}{\partial f_8}-\mathring{f}_6+\dfrac{1}{3}(4\mathring{f}_3+\mathring{f}_6+\mathring{f}_7)\end{cases} \tag{3.78}$$

2. On the northern boundary, the outflow condition is given by eq. (3.33). The expansion is given as:

$$(\mathrm{F1})_{\mathrm{north}} = \sum_j \left\langle f_j', \frac{\partial \mathscr{K}_{\mathrm{out,north}}}{\partial f_j} \right\rangle_{\Gamma_{\mathrm{out,north}}} \tag{3.79}$$

$$(\mathrm{F3})_{\mathrm{north}} = \left\langle \mathring{f}_2 f_2' - \mathring{f}_4 f_4' + \mathring{f}_5 f_5' + \mathring{f}_6 f_6' - \mathring{f}_7 f_7' - \mathring{f}_8 f_8', 1 \right\rangle_{\Gamma_{\mathrm{out,north}}} \tag{3.80}$$

$$\begin{aligned}(\mathrm{F2})_{\mathrm{north}} = &\left\langle \mathring{f}_4, -f_2' + f_4' + \frac{2\rho}{3}\left[0 + \frac{f_0' + f_1' + f_3' + 2(f_2' + f_5' + f_6')}{\rho}\right]\right\rangle_{\Gamma_{\mathrm{out,north}}} \\ &+ \left\langle \mathring{f}_7, -f_5' + f_7' + \frac{f_3' - f_1'}{2} + \frac{\rho}{6}\left[0 + \frac{f_0' + f_1' + f_3' + 2(f_2' + f_5' + f_6')}{\rho}\right]\right\rangle_{\Gamma_{\mathrm{out,north}}} \\ &+ \left\langle \mathring{f}_8, -f_6' + f_8' - \frac{f_3' - f_1'}{2} + \frac{\rho}{6}\left[0 + \frac{f_0' + f_1' + f_3' + 2(f_2' + f_5' + f_6')}{\rho}\right]\right\rangle_{\Gamma_{\mathrm{out,north}}}\end{aligned} \tag{3.81}$$

Thus we can similarly obtain the final adjoint-state outflow boundary condition for unknown $\mathring{f}_2$, $\mathring{f}_5$, $\mathring{f}_6$ as:

$$\begin{cases} \mathring{\mathcal{P}}_{\mathrm{out}(1)} = \mathring{\mathcal{P}}_2 = \mathring{f}_2 + \dfrac{\partial \mathscr{K}_{\mathrm{out,north}}}{\partial f_2} - \mathring{f}_4 + \dfrac{1}{3}(4\mathring{f}_4 + \mathring{f}_7 + \mathring{f}_8) \\ \mathring{\mathcal{P}}_{\mathrm{out}(2)} = \mathring{\mathcal{P}}_5 = \mathring{f}_5 + \dfrac{\partial \mathscr{K}_{\mathrm{out,north}}}{\partial f_5} - \mathring{f}_7 + \dfrac{1}{3}(4\mathring{f}_4 + \mathring{f}_7 + \mathring{f}_8) \\ \mathring{\mathcal{P}}_{\mathrm{out}(3)} = \mathring{\mathcal{P}}_6 = \mathring{f}_6 + \dfrac{\partial \mathscr{K}_{\mathrm{out,north}}}{\partial f_6} - \mathring{f}_8 + \dfrac{1}{3}(4\mathring{f}_4 + \mathring{f}_7 + \mathring{f}_8) \end{cases} \tag{3.82}$$

3. On the southern boundary, outflow condition is given by eq. (3.35). The expansion is given as:

$$(\mathrm{F1})_{\mathrm{south}} = \sum_j \left\langle f_j', \frac{\partial \mathscr{K}_{\mathrm{out,south}}}{\partial f_j} \right\rangle_{\Gamma_{\mathrm{out,south}}} \tag{3.83}$$

$$(\mathrm{F3})_{\mathrm{south}} = \left\langle -\mathring{f}_2 f_2' + \mathring{f}_4 f_4' - \mathring{f}_5 f_5' - \mathring{f}_6 f_6' + \mathring{f}_7 f_7' + \mathring{f}_8 f_8', 1 \right\rangle_{\Gamma_{\mathrm{out,south}}} \tag{3.84}$$

$$\begin{aligned}(\mathrm{F2})_{\mathrm{south}} = &\left\langle \mathring{f}_2, -f_4' + f_2' - \frac{2\rho}{3}\left[0 - \frac{f_0' + f_1' + f_3' + 2(f_4' + f_7' + f_8')}{\rho}\right]\right\rangle_{\Gamma_{\mathrm{out,south}}} \\ &+ \left\langle \mathring{f}_5, -f_7' + f_5' - \frac{f_3' - f_1'}{2} - \frac{\rho}{6}\left[0 - \frac{f_0' + f_1' + f_3' + 2(f_4' + f_7' + f_8')}{\rho}\right]\right\rangle_{\Gamma_{\mathrm{out,south}}} \\ &+ \left\langle \mathring{f}_6, -f_8' + f_6' + \frac{f_3' - f_1'}{2} - \frac{\rho}{6}\left[0 - \frac{f_0' + f_1' + f_3' + 2(f_4' + f_7' + f_8')}{\rho}\right]\right\rangle_{\Gamma_{\mathrm{out,south}}}\end{aligned} \tag{3.85}$$

Thus we can similarly obtain the final adjoint-state outflow boundary condition for unknown $\mathring{f}_4$, $\mathring{f}_7$, $\mathring{f}_8$ as:

$$\begin{cases} \mathring{\mathcal{P}}_{\mathrm{out}(1)} = \mathring{\mathcal{P}}_4 = \mathring{f}_4 + \dfrac{\partial \mathscr{K}_{\mathrm{out,south}}}{\partial f_4} - \mathring{f}_2 + \dfrac{1}{3}(4\mathring{f}_2 + \mathring{f}_5 + \mathring{f}_6) \\ \mathring{\mathcal{P}}_{\mathrm{out}(2)} = \mathring{\mathcal{P}}_7 = \mathring{f}_7 + \dfrac{\partial \mathscr{K}_{\mathrm{out,south}}}{\partial f_7} - \mathring{f}_5 + \dfrac{1}{3}(4\mathring{f}_2 + \mathring{f}_5 + \mathring{f}_6) \\ \mathring{\mathcal{P}}_{\mathrm{out}(3)} = \mathring{\mathcal{P}}_8 = \mathring{f}_8 + \dfrac{\partial \mathscr{K}_{\mathrm{out,south}}}{\partial f_8} - \mathring{f}_6 + \dfrac{1}{3}(4\mathring{f}_2 + \mathring{f}_5 + \mathring{f}_6) \end{cases} \tag{3.86}$$

The few sets of equations eq. (3.72), eq. (3.78), eq. (3.82) and eq. (3.86) provides the adjoint-state boundary conditions.

3.2.3. Updating the control parameter i.e. the level-set Ψ

Now the level set function for the next iteration is obtained by eq. (3.26) [136] being defined by the gradient descent algorithm. Here the gradient descent step size (ξ) used is: $\xi = \epsilon_2 \times \xi_s$ where $\epsilon_2 \in \mathbb{Z}_{>0}$ (it is a positive integer), $\xi_s = 10^{-2}$ is a constant. Here 'ϵ_2' refers to an implementation detail, where we incrementally augment (i.e. addition by unity) this quantity until be observe a change in the solid domain. In other words, to ensure that such a change occurs the same gradient is applied sequentially ϵ_2 times. Unlike SIMP, the level-set requires a change such that level-set value crosses the zero-contour. Hence the solid configuration remains unchanged unless the aforementioned change is registered for at least a single node. This becomes important as it is not possible to compute a different gradient for the same configuration. Now that we have discussed regarding other terms in eq. (3.26) the only remaining term to expand upon is the gradient of the cost function ($\nabla\mathcal{J}$). As mentioned previously, the term (aA3) gives us the expression for computing the gradient.

$$\begin{aligned}(\text{aA3}) = \frac{\partial\mathcal{L}}{\partial\Psi}\Psi' = \Psi'\Bigg(\left\langle\frac{\partial\mathscr{Y}}{\partial\Psi}, \partial_\Psi[\alpha]\right\rangle_{\mathcal{D}}\Big|_{t=t_f} + \sum_i\left\langle\frac{\partial\mathcal{R}_i}{\partial\Psi}\partial_\Psi[\alpha], \mathring{f}_i\right\rangle_{\mathcal{D}\times\mathcal{T}}\Bigg) \\ + \sum_\beta\Psi'\Bigg(\sum_{i=1}^{3}\left\langle\frac{\partial\mathcal{P}_{\beta(i)}}{\partial\Psi}\partial_\Psi[\alpha], \mathring{f}_{\beta(i)}\right\rangle_{\Gamma_\beta\times\mathcal{T}} + \left\langle\frac{\partial\mathscr{X}_\beta}{\partial\Psi}, \partial_\Psi[\alpha]\right\rangle_{\Gamma_\beta}\Big|_{t=t_f}\Bigg)\end{aligned} \tag{3.87}$$

For the optimization problem of interest, generally both the cost function at boundary ($\mathscr{X}$) and the boundary residue ($\mathcal{P}$) are explicitly independent of the design variable α. Even in the LBM residue ($\mathcal{R}$) the design variable only appears in the equilibrium distribution function. Thus we obtain:

$$\frac{\partial\mathcal{L}}{\partial\Psi}\Psi' = \langle\nabla_\Psi\mathcal{J}, \Psi'\rangle_{\mathcal{D}\times\mathcal{T}} = -\left\langle\partial_\Psi[\alpha]\Psi', \sum_i w_i\mathring{f}_i\rho\frac{1}{\tau}\left(3\boldsymbol{e}_i\cdot\boldsymbol{u} + \frac{9}{2}(\boldsymbol{e}_i\cdot\boldsymbol{u})^2 - \frac{3}{2}(\boldsymbol{u})^2\right) - \frac{\partial\mathscr{Y}}{\partial\Psi}\Big|_{t=t_f}\right\rangle_{\mathcal{D}\times\mathcal{T}} \tag{3.88}$$

As can be noted in eq. (3.88), the gradient is non-zero only for the fluid nodes. This means that it would not be possible for removal of a solid node once it has been placed by the algorithm even when evolution of the gradient would cause this to be a desirable solution. This can be partially mitigated by application of an interpolation of gradients from the neighboring fluid nodes. This means that the solid can now only be eaten away from its boundary nodes.

From current analysis, we can write eq. (3.88) in the phase space $\mathcal{D}$. Hence we obtain:

$$\langle\nabla_\Psi\mathcal{J}, \Psi'\rangle_{\mathcal{D}} = -\left\langle\Psi', \partial_\Psi[\alpha]\sum_i w_i\mathring{f}_i\rho\frac{1}{\tau}\left(3\boldsymbol{e}_i\cdot\boldsymbol{u} + \frac{9}{2}(\boldsymbol{e}_i\cdot\boldsymbol{u})^2 - \frac{3}{2}(\boldsymbol{u})^2\right) - \frac{\partial\mathscr{Y}}{\partial\Psi}\partial_\Psi[\alpha]\right\rangle_{\mathcal{D}} \tag{3.89}$$

This provides with the equation for the gradient of the cost function ($\nabla\mathcal{J}$) with respect to the level-set Ψ.

3.3. The 90° pipe bend

This is a case of a monophasic compressible flow passing through a hollow component/part/pipe which is connecting two perpendicularly oriented pipes. Here the flow is a laminar flow and hence the regular single phase LBM model and its associated adjoint-state model (as derived in section 3.2) are employed for the optimization algorithm. The objective for this benchmark case is to ensure minimum losses due to pressure drop for 90° pipe bend as the porosity of the component is reduced gradually to the desired minimum value ($\phi_{\min}$). It is to be noted that the problem at hand is a TOSFP.

3.3.1. Setting up parameter values

Initial starting point is the region of interest i.e. the *optimization domain* (as highlighted in the fig. 3.4) having 100% porosity. Now, in the vicinity of both the boundaries (inlet and outlet) we

Algorithm 4: General algorithmic flow of a adjoint-state monophasic LBM for monophasic fluids (TOSFP)

Input: Physical state: $\mathbf{f}$, ρ & $\boldsymbol{u}$, fluid-fluid interface along with geometry: $\mathcal{D} \in \mathcal{D}_{\mathrm{f}} \bigcup \mathcal{D}_{\mathrm{s}}$ and cost function: $\mathcal{J}$

Initialize $\mathring{f}_i^{(0)} = 0 \; \forall \; i$

while *(*$\|\mathring{f}_1^{(z)} - \mathring{f}_1^{(z-1)}\|_1 \geq \gamma_{\mathrm{c}}$ **AND** $k \leq k^{\max}$*; where* γ_{c} *is a constant.)* **do**

  Compute the equilibrium distribution function $\mathring{f}^{\mathrm{eq}}$ and perform adjoint-state collision i.e. to solve eq. (3.53)

  Perform streaming

  Perform adjoint-state bounceback for walls

  Compute for open adjoint-state boundaries and later for ghost nodes.

  if *(*$k \bmod \varsigma = 0$*; where* ς *is an constant.)* **then**

    Writing data to files

    Storing $\mathring{f}_1$ at z i.e. $\rho^{(z)}$

    Increment z by 1 i.e. $z \leftarrow z + 1$.

  $k \leftarrow k + 1$

return *Adjoint-state parameters* $\mathring{\mathbf{f}}^{(\dagger)}$

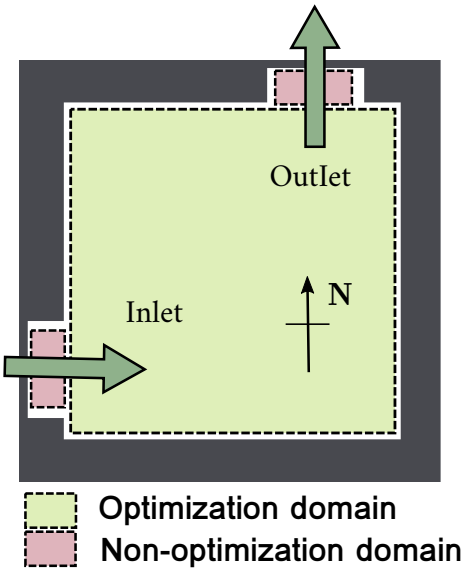

Figure 3.4: Initial solid structure and demarcation of the domain for the 90° pipe bend optimization

have non-optimization zones. This prevents the code from adding solid obstructions in this region, which in turn, avoids sealing/clogging of the boundary and rapid increase in inlet pressure–due to intermediary solid structures in the non-optimization zone. Here the domain size is $\mathscr{N}_x \times \mathscr{N}_y = 150 \times 150$ with the boundaries on the west and the north such that the domain is symmetrical w.r.t the axis passing from the north-west corner to the south-east corner. The inlet boundary lies on the western frontier with a constant velocity initialization across the width of the inlet. The inlet diameter/width is 30 l.u., the inlet velocity $u_y = 10^{-2}$ l.u./t.s. and kinematic viscosity is $\nu = 0.1666$ units, hence the Reynold number is $\mathrm{Re}_{\mathrm{inlet}} = 1.8$, i.e. it is in the Stokes flow regime. The outlet boundary lies on the northern frontier and a constant pressure outlet condition is imposed here. In regards to the optimization algorithm we use a gradient-descent optimizer and (refrain from using a line search algorithm, rather) a constant value is utilized for the optimization step size. The complete algorithm for a topology optimization was specified previously i.e. algorithm 3.

3.3.2. Cost function definition

Two constraints or objective/cost functions are required for achieving our final goal: pressure and porosity constraints. The former (i.e. pressure) constraint keeps a check on the pressure losses as the flow circuit is established through/around different obstacles or solid structures. For our case, it is helpful in keeping the main artery of the flow circuit squeaky clean, as obstacles in the center of flow pathway would raise the frictional/viscous losses. *For the standard LBM model describing a laminar monophasic flow the EOS used is that for ideal gas, which is further simplified (in accordance with the model parameters) such that pressure is defined as a function of density:*

$$p = \rho \frac{RT}{M} = \frac{\rho}{3} \tag{3.90}$$

Previously [40], our local team at LTeN used an exponential function for the pressure constraint, given as:

$$\mathscr{X}_p = \lambda_p \Delta p_{\max} \exp\left(\frac{\Delta p}{\Delta p_{\max}}\right) \tag{3.91}$$

where λ_p is the weight of the pressure constraint, $\Delta p_{\max}$ is the maximum permissible pressure difference. For our case we define the pressure loss as:

$$\Delta p = \left(\frac{1}{3}\int_{\Gamma_{\text{in}}} \sum_i f_i \, \mathrm{d}\boldsymbol{r} - \frac{1}{3}\int_{\Gamma_{\text{out}}} \sum_i f_i \, \mathrm{d}\boldsymbol{r}\right) \tag{3.92}$$

Conversely, the simplest possible cost function is utilized, as this would suffice for our purpose:

$$\mathscr{X}_p = \lambda_p \Delta p \tag{3.93}$$

By the nature of the constraint it could be understood that it is to be applied only at the boundaries. And to be more specific only on the inlet boundary as the outlet pressure and hence by extension the density of fluid at outlet is fixed. This is accomplished for the LBM model using the ZH pressure outlet boundary, where the outlet boundary pressure is fixed by fixing the density. Now as this a TOSFP method, (as mentioned before) we apply the cost function differentiation like a source term. As the pressure constraint is only a function of the Boltzmann variable $\mathbf{f}$, hence its contribution is only in the adjoint-state solver (and at the boundaries). Hence differentiating w.r.t the Boltzmann variables we obtain:

$$\sum_j \frac{\partial \mathscr{X}_{\text{in}}}{\partial f_j} = \sum_j \frac{\partial \mathscr{X}_p}{\partial f_j} = \frac{\lambda_p}{3} \tag{3.94}$$

Meanwhile the latter (porosity) constraint enables us to add material to the domain of interest until the minimum permissible porosity is attained. In absence of the porosity constraint, addition or deduction of material is a slower or not possible. For our case, we require the porosity constraint as no other cost function is present for assisting material allocation i.e. it accelerates the process. This constraint is applied throughout the domain of interest. Previously [40], an exponential function was used to describe the porosity constraint:

$$\mathscr{Y}_\phi = \alpha \lambda_\phi \phi_{\min} \exp\left(\frac{\phi}{\phi_{\min}}\right) \tag{3.95}$$

where ϕ here represents the porosity value varying between 0 and 1, $\phi_{\min}$ is the minimum permissible porosity and λ_ϕ is the weight for the porosity constraint. For our simulation we use a simpler quadratic function given as:

$$\mathscr{Y}_\phi = \alpha \lambda_\phi (\phi - \phi_{\min})^2 \tag{3.96}$$

This constraint is only the function of the level-set function Ψ and hence its contribution is only at the final stage of computing the gradient of the cost function. Here the differentiation w.r.t the level-set variable is given as:

$$\frac{\partial \mathscr{Y}}{\partial \Psi} = \frac{\partial \mathscr{Y}_\phi}{\partial \Psi} = \lambda_\phi (\phi - \phi_{\min})^2 \alpha' \tag{3.97}$$

The weights for pressure and porosity constraints used while optimization are $\lambda_p = 100$ and $\lambda_\phi = 0.1$ respectively.

3.3.3. Result and discussions

The initial condition for the topology optimization algorithm (, as stated previously) is 100% permeability/porosity. With the progression of each iteration the code deposits/allocates materials–solid nodes are depicted using black nodes. The allocation of material is predominately in regions of null or minuscule velocities. In other words, the code begins with depositing material in regions/corners further away from the open boundaries i.e. the north-west and south-east corners. After this the allocation continues more or less along the axis of symmetry. For the current simulation, the magnitude of gradient is influenced significantly by the constraint of porosity. Now as optimization iterations progress (as is evident from the graph) we observe a general decrease in the cost function value. Also the general trend of L_1, L_2 and L_∞ norms of the gradient of the cost function is to decrease till a stable value is reached. Figure 3.5 depicts various stages of material allocation during the optimization process. As internal pathways becomes narrower the flow intensity is dispersed to a lesser extent. The optimization process is halted when the mean gradient value is below i.e. $\frac{\|\nabla_\Psi \mathcal{J}\|_1}{\mathcal{N}_\mathcal{D}} \leq 10^{-7}$ (where $\mathcal{N}_\mathcal{D} = \mathcal{N}_x \times \mathcal{N}_y$). The stopping point coincides with porosity of the component reaching $\phi_{\min} = 50$.

If we compare our result to those in literature,(for e.g. [130, 140])–with the caveat that the minimum porosity threshold for these cases in literature is lower than 50%–then we observe certain similarities. In the first study [130], Stokes flow through the component was modeled using Navier-Stokes equations with finite element discretization with 10^4 nodes. After optimization they obtained (i.e. fig. 3.6b) a straight pathways/walls between gently curved walls (especially the outer wall) near the inlet boundary allowing for the smooth transition in the direction for a Stokes flow. In the second study [140], again utilized finite element discretization of NS equations with 6561 nodes and 12800 triangular elements. After optimization, a more smoother transition with a continuous and gently curved wall resembling a quarter of a torus (i.e. fig. 3.6a) was obtained. Meanwhile, if we extrapolate the behavior of the optimization code, further deposition of material would occur primarily in two regions. The first location would be at the inner wall (referring to fig. 3.6c) where the concave curvature/dip of the pathway/wall allows for the a region of minuscule velocity (referring to fig. 3.5f). The second location would be at the outer wall (again referring to fig. 3.6c) where similar concave dips especially near the boundaries corresponds to region of minuscule velocity.

3.4. Conclusion

Here we discuss regarding different constituent components of the optimization algorithms. For topology representation we utilize the level-set function, to calculate the gradient of cost function we use the adjoint-state model and to register changes/updates using the gradient ($\nabla\mathcal{J}$) we use the gradient-descent algorithm. After we derive the adjoint-state problem using the real world governing equation i.e. the lattice Boltzmann model for compressible flows, we also introduce the concept of the adjoint-state time. We also demonstrate adjoint-state boundary conditions for all four directions i.e. the north, the east, the south and the west. Lastly we conclude the chapter by demonstrating the competence of the adjoint-state based gradient topology optimizer. Here the main observation for the 90° pipe-bend case is that regions of low velocity are ideal regions for material allocation.

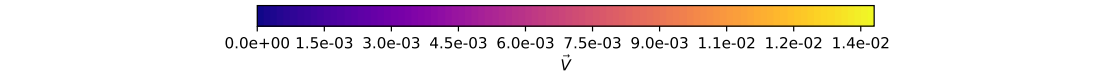

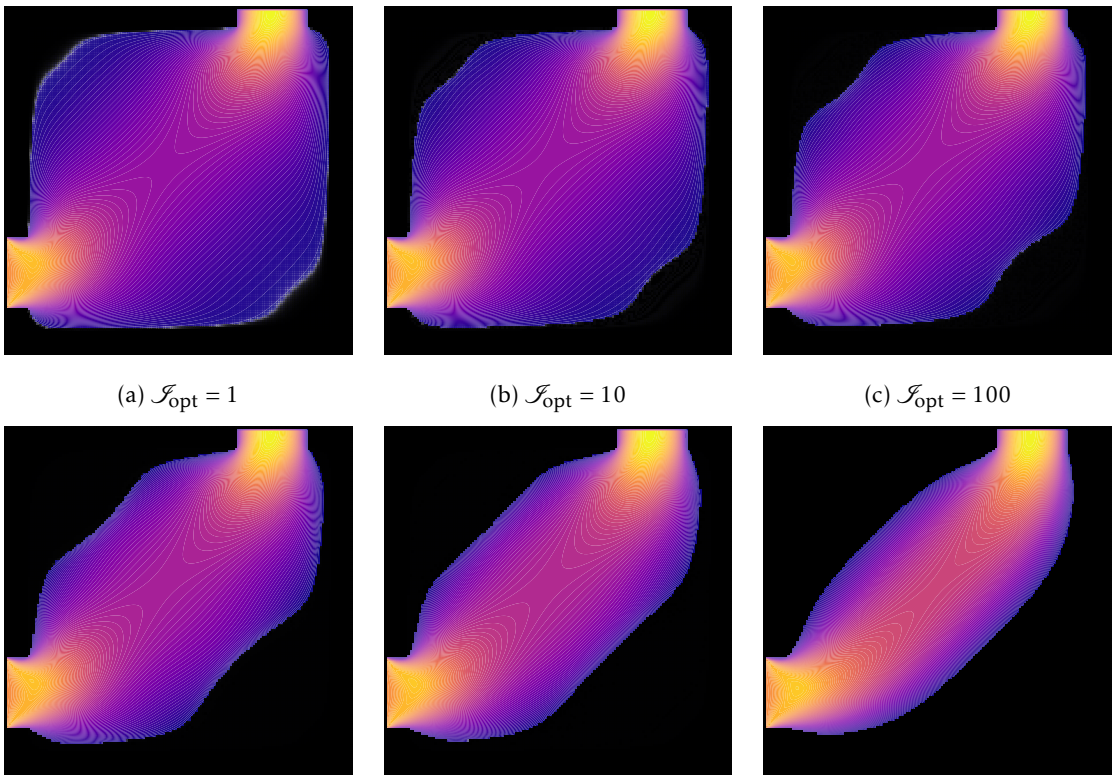

(a) $\mathscr{I}_{\text{opt}} = 1$ (b) $\mathscr{I}_{\text{opt}} = 10$ (c) $\mathscr{I}_{\text{opt}} = 100$

(d) $\mathscr{I}_{\text{opt}} = 1000$ (e) $\mathscr{I}_{\text{opt}} = 2000$ (f) $\mathscr{I}_{\text{opt}} = 3387$

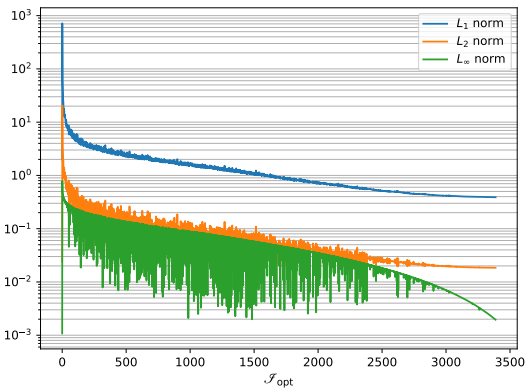

(g) $\|\nabla_\Psi \mathcal{J}\|_1$, $\|\nabla_\Psi \mathcal{J}\|_2$ and $\|\nabla_\Psi \mathcal{J}\|_\infty$

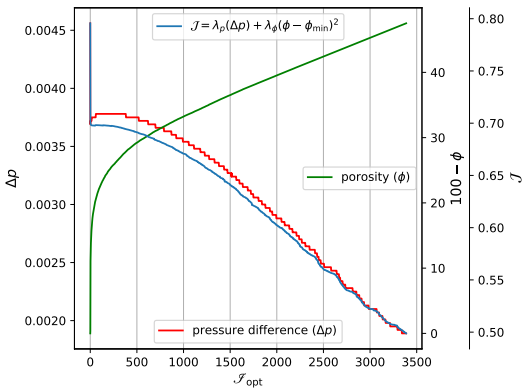

(h) pressure difference and porosity measure

Figure 3.5: (a)-(f) Evolution of the flow domain en-route optimization (solid node depicted by black and gray nodes); (g)-(h) Corresponding norms of the gradient of the cost function and the evolution of the cost function ($\mathcal{J}$), porosity (ϕ) and pressure difference (Δp)

(a) Optimized domain [140] for 90° pipe bend using the shape optimization

(b) Optimized domain [130] for 90° pipe bend–rotated 90° counter-clockwise

(c) Optimized domain (inhouse code result) for 90° pipe bend–rotated 90° counter-clockwise

Figure 3.6: Comparison of the results of a shape optimization algorithm [140] with that of the topology optimization algorithms for monophasic flow in a 90° pipe bend case.

Chapter 4

The droplet race: optimizing a wettability gradient surface (WGS)

In the previous chapter, after discussing the foundational aspects of the adjoint-based optimization solver, we deviate temporarily to using a finite difference optimization solver. As this is the first multiphase optimizer, the results herein are used for later validating the multiphase adjoint-based optimizer. The excerpts from this chapter was published in Physics of fluid [141].

4.1. Introduction

In nature, droplet movement on a still surface occurs mainly due to air currents or gravity (in case of an inclined surface). Recently, unexpected directional motion (without external energy supply) of a liquid droplet on the Araucaria leaf [142] was reported and later this phenomenon has been reproduced numerically [143]. Meanwhile, in a controlled environment, the droplet motion is possible due to either active or passive methods of generating a wettability gradient [144]. Surfaces employed specifically for this purpose are in literature called as wettability gradient surfaces (WGS). Active methods include temperature gradients [145] (first documented in the seminal work of Marangoni [146]), mechanical vibrations [147], electrostatic potential, etc., while passive techniques require surface chemical treatments or alteration of surface topography [148, 149]. A realistic surface is non-ideal as surface roughness due to topographical imperfections is commonplace. Also

a bare surface gathers dirt or residue being exposed to chemical reactions (including corrosion) or deposits due to phenomenon such as evaporation over a period of time. This degrades the performance of WGS with the passage of time as the droplet motion could be inhibited due to pinning defects.

WGS have multiple applications where droplet transport is required. These surfaces could be used for orienting the direction of a moving droplet [150]. It could also function as pump in microscale devices. One major application for a WGS is the lab-on-a-chip (LOC) device which handles fluids even at submicroscopic scale [151]. LOCs have further applications in nano technology, bioengineering, sensors, etc. Liquid transport plays an important role in heat transfer process especially during phase change [152]. In condensation processes, hybrid wettability surfaces improved performances allowing droplet condensation on hydrophobic places whereas droplets are drained toward hydrophilic places and removed due to gravity [153, 154]; the use of a WGS could then prevent the formation of a liquid film. Also these surfaces could be useful for self-cleaning, where the droplet picks up dirt as it is propelled forward; few inclined hydrophobic surfaces have already been used for this purpose [155, 156].

This phenomenon of a wettability gradient initially theoretically studied [101, 157] has been experimentally verified for chemical surface treatments and thermal gradients on an inclined plate [158]. Various theoretical explanations have been put forward providing for different analytical formulations for droplet velocity [159, 160] assuming steady state motion. Numerical simulations have on the other hand been used to investigate situations which are difficult to recreate in an experimental setup. Spatial and temporal fluctuations [161] of the wettability, wettability gradients induced by chemical reactions [162], various wettability distribution profiles [163] and droplet spreading [164] on patterned surfaces, to mention a few studies, have all been explored via numerical modeling to promote/influence droplet motion.

The numerical simulations for a droplet on a surface could be divided into two categories: in the former category the contact angle is prescribed and the fluid behavior (pressure, velocity, etc.) for different configurations are obtained a posteriori. In the latter category the interaction forces are prescribed and both the contact angle and fluid behavior are obtained after numerical solving. While the former category includes macroscopic models, most often coupling Navier-Stokes equations with an interface tracking methods, like Volume of fluid (VOF) [144] or level set (LS), the latter category includes molecular dynamics and mesoscopic methods like Van der Waal model [165] or the lattice Boltzmann model (LBM) [86]. For additional details, regarding selection of solver for physical simulation (in an optimizer), refer to section 2.2. Hereafter physical simulation will also be referred to as the forward problem.

So, even if the motion of a droplet submitted to a wettability gradient is a well documented phenomenon, both experimentally and numerically, the question of the optimization of this displacement remains untreated. Indeed, from the performed bibliography survey, it appears that wettability gradient has always been assumed to be constant, i.e. the wettability distribution is restricted to the linear profile, and the main result is, the steeper the gradient, the greater the mean velocity [1, 101]. Now the wettability cannot vary indefinitely, i.e. this property is bounded, from superhydrophobicity to superhydrophilicity. Consequently, the steeper the gradient, the shorter the displacement length of the droplet. The significance of the study lies in resolving the conflict between the spread of a bounded property (wettability) and the displacement length to achieve highest mean velocity. In other words, for a droplet to seamlessly travel the desired length, the question of the optimal wettability profile seems to have no trivial solutions, and, to the best knowledge of the authors, this has not been addressed yet. Note that, in the field of optimization applied on multiphase flow, an adjoint-state gradient-based shape optimizer demonstrated its competency of propelling a droplet with a variation of surface tension, such an optimizer being based on an approximated two-phase Stokes equations with no solid-fluid interaction [166, 167]. Another shape optimizer has been employed on the surface topography in order to control the droplet shape, without motion [168].

The implication of the current study is that increasing the mean velocity of droplets using spe-

cific WGS would improve, for example, the flow rate of LOC device or the performances of condensers. From an optimization and historical point of view, this problem loosely resembles the brachistochrone problem. The objective of the brachistochrone problem was to find the optimal geometrical path which would be covered by a sliding bead starting from rest at a given location (with gravity and without friction) in order to reach the final location in the shortest time interval [169]. The analytical approaches proposed by five different mathematicians found that a cycloid, rather than a simple constant step is the best shape for the task. So, for a given gravitational potential, i.e. a starting height and a final height, optimization analytical process identified an optimal structure profile. An innovation of this article is the manner of approaching the problem, i.e. similar to the brachistochrone problem, one searches for the best shape or profile of wettability distribution for a WGS. The only difference is that a numerical optimization algorithm is used here rather than an analytical approach (if at all one exists).

In the context of the article the forward problem consists of a droplet resting on a horizontal surface which is a WGS. No pinning effect (i.e. no contact angle hysteresis) on the interface between the droplet and the solid is assumed (i.e. the surface is assumed ideal for the simulation). The optimization process is for finding the optimum wettability distribution profile so that the droplets moves as quickly as possible to a desired location. The simulation is performed in two dimensions of space while the wettability evolves in one dimension. Although three-dimensional (3D) effects are not taken into account in this paper, such a geometric assumption seems not to affect the mean velocity of the droplet, referring to 2D/3D literature comparison [144], whereas it allows for substantial computational benefits.

Section 4.2 describes the methodology of optimization. In this section, we discuss the cost function of the optimization problem, we then elaborate on the forward problem model, we build the parameterization of the control variable, and set-up the optimizer. Section 4.3 gives the performance of several wettability distributions defined by some simple analytical function, and section 4.4 gives some results of optimization. Ultimately, section 4.5 presents the conclusions of this chapter.

4.2. Optimization problem set-up

4.2.1. Cost function definition

The objective of the study is to maximize the droplet velocity on a flat plate by adjusting the distribution of wettability. The mean velocity is computed when the droplet reaches a certain desired location ($\widetilde{\mathcal{C}}_{\text{drop}}$). Here locations and droplet positions are indicated in terms of the droplet center of gravity (denoted as $\mathcal{C}_{\text{drop}}$). The droplet center of gravity is computed as:

$$\mathcal{C}_{\text{drop}}(t) = \frac{\int_{\mathcal{D}_\text{f}} (\rho(\boldsymbol{r},t) - \rho_{\text{vap}}) r_x \, \mathrm{d}\boldsymbol{r}}{\int_{\mathcal{D}_\text{f}} (\rho(\boldsymbol{r},t) - \rho_{\text{vap}}) \, \mathrm{d}\boldsymbol{r}}, \tag{4.1}$$

where, r_x is the x-component of location vector i.e. $\boldsymbol{r}$ for a 2D domain such that the droplet moves along the x-axis on the xy-plane, ρ is the density at $\boldsymbol{r}$ and at time t, ρ_{vap} is the density of the vapor and $\mathcal{D}_\text{f}$ is the fluid domain restriction.

Mathematically, maximization of the mean velocity consists in maximizing the following cost function:

$$\mathcal{J} = \frac{\mathcal{C}_{\text{drop}}|_{t=t_f} - \mathcal{C}_{\text{drop}}|_{t=0}}{t_f}, \tag{4.2}$$

where the final time t_f is the time given a posteriori when $|\mathcal{C}_{\text{drop}} - \widetilde{\mathcal{C}}_{\text{drop}}|$ reaches a very small user-defined value.

4.2.2. Lattice Boltzmann method

The forward problem uses model $\mathscr{H}_1$. Now as mentioned previously in section 2.3.6.b, the formulation of the solid-fluid inter-particular force $\boldsymbol{F}_\text{s}$ enables the quantification of wettability in terms of

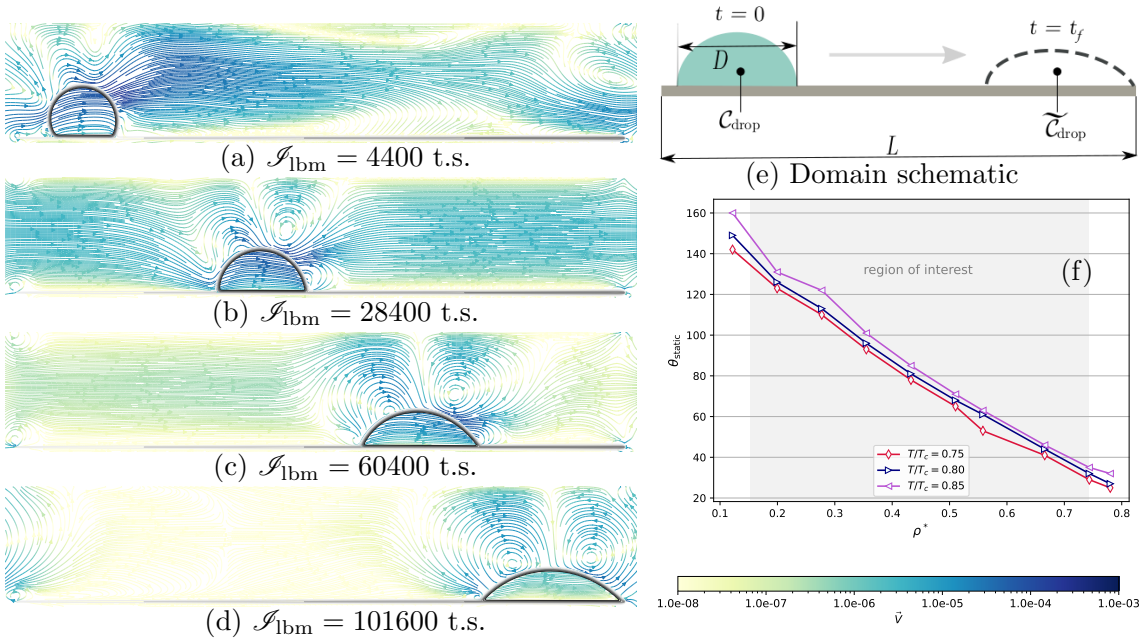

Figure 4.1: (a-d) LBM simulation for droplet motion on a linear wettability profile flat plate at $T/T_c = 0.75$;(model $\mathscr{H}_1$). (e) illustrates the domain schematics; (f) Correlation between static contact angle (θ_{stat}) and pseudo-density of the solid plate

the fictitious density of (adjacent) solid nodes. This density, denoted as ρ_{w}, is referred to as pseudo-density [99]. Varying the pseudo-density from ρ_{liq} to ρ_{vap}, a contact angle between 0° and 180° can be obtained. This mapping allows for a correlation between the static contact angle θ_{stat} and the pseudo-density. Figure 4.1 depicts the correlation between θ_{stat} and the normalized pseudo-density $\left(\rho^*_{\text{w}} = (\rho_{\text{w}} - \rho_{\text{vap}})/(\rho_{\text{liq}} - \rho_{\text{vap}})\right)$. This correlation is consistent across different temperatures T (which is specified relative to the critical point temperature T_c). The static contact angle is unknown a priori and is obtained after the simulation of a droplet resting on a flat horizontal plate with constant wettability. This approach is different from macroscopic methods where contact angle is directly prescribed. As such, LBM is apt for such optimization studies.

The variation of the pseudo-density (wettability) along the length of the plate causes droplet motion which is successfully captured by LBM due to its transient nature. Figure 4.1 illustrates the droplet motion, where $\mathscr{I}_{\text{lbm}}$ is the iteration number i.e. time in the LBM paradigm. Also the fluid streamlines are shaded according to the fluid velocity. The droplet motion occurs for a linear wettability distribution (denoted hereafter as Υ_{lin}), and no pinning effects. Small vortices can be observed in the vicinity of the droplet interface; these are the spurious currents. As the droplet travels forward, a continuous flux of vapor can be observed along with the formation of its boundary layer on the top and the bottom of the flat plate. This vapor flux is an artifact caused by the use of periodic boundary conditions. Both these artifacts have negligible impact on the droplet velocity and shape, hence these are ignored. The forward problem validation for droplet motion on a plate is detailed in section 2.5.1.

4.2.3. Parameterization of control variables

The space-dependent pseudo-density is the control variable which is tweaked to maximize the mean velocity of the droplet. Its physical interpretation was given above in section 4.2.2. This pseudo-density being continuous, a discrete counterpart version is used for the optimization algorithm. As far as this paper is concerned, the discretization is performed using the n linear Lagrange basis functions $\mathscr{L}_m(r_x)$. This originates from the optimization domain having n nodes uniformly spaced one from the other (so using $q = n - 1$ elements, all of equal length). The relationship between the

continuous control variable, $\rho_w(r_x)$, and the discrete one, $\boldsymbol{\rho}_w$ is:

$$\boldsymbol{\rho}_{w,\boldsymbol{m}} = \rho_w(r_{x_m}); \quad \rho_w(r_x) = \sum_{m=1}^{n} \mathscr{L}_m(r_x)\boldsymbol{\rho}_{w,\boldsymbol{m}}. \tag{4.3}$$

4.2.4. Optimizer

Gradient based steepest descent optimizer [170] is used for arriving at an optimum solution. For a given parameterization, the update step is given as:

$$\boldsymbol{\rho}_w{}^{(k+1)} = \boldsymbol{\rho}_w{}^{(k)} - \xi^{(k)}\, \nabla\mathcal{J}(\boldsymbol{\rho}_w{}^{(k)}). \tag{4.4}$$

In eq. (4.4), superscripts denote the iteration count, $\nabla\mathcal{J}$ is the cost function gradient (i.e. it gathers partial derivatives of the cost function with respect to each parameter $\boldsymbol{\rho}_{w,\boldsymbol{m}}$, where $m = 1,\dots,n$); the finite difference method is used to compute the cost function gradient. Eventually, ξ is a positive scalar value that minimizes $\mathcal{J}(\boldsymbol{\rho}_w{}^{(k+1)})$; a dichotomy strategy is used to do so.

From experience it becomes apparent that, performing the optimization with a small number of elements ($q \leq 8$) in the parameterization process inhibits attaining a WGS with high droplet velocities due to lack of resolution of the control variable. On the contrary, beginning the optimization process with a large number of elements ($q \geq 128$) leads the optimizer to quickly reach local minima only, but far away from the global one. Thus we follow the multiscale parameterization described in [171]. The optimization process consists in maximizing the cost function eq. (4.2) for a small number of elements q using the update eq. (4.4), until stabilization of the control variable, then double the number of elements, and repeat the whole process until global stabilization is reached. Algorithm 5 describes schematically this multiscale optimization algorithm. Note that the control variables is allowed to fluctuate within the predetermined limits (further explanation in section 4.2.5).

Algorithm 5: General flow of a multiscale optimization algorithm

Input: Pseudo-density state $\boldsymbol{\rho}_w{}^{(0)} \in \mathcal{D}_s$
Initialize $\boldsymbol{f}$, ρ and $\boldsymbol{u}$ for the fluid domain ($\mathcal{D}_f$).
Choose appropriate initial optimization element number: $q^{(0)}$
while *($q^{(z)} \leq q_{max}$)* **do**
  while *($\|\boldsymbol{\rho}_w{}^{(k)} - \boldsymbol{\rho}_w{}^{(k+1)}\|_1 \geq \gamma_c$; where γ_c is a constant.)* **do**
    Compute the Boltzmann variables $\boldsymbol{f}$ solving eq. (2.3)
    Compute the cost function $\mathcal{J}$ i.e. eq. (4.2)
    Compute the gradient ($\nabla\mathcal{J}$) using finite difference
    Compute the gradient step size (ξ) using dichotomy line search algorithm
    Update the pseudo-density using eq. (4.4)
  Update element number: $q^{(z+1)} = 2q^{(z)}$
return *Optimum wettability distribution* $\boldsymbol{\rho}_w{}^{(\dagger)}$

4.2.5. Forward problem setup

The range of the non-dimensional pseudo-density is limited such that $\rho_w^* \in [0.152, 0.742]$. Thus superhydrophobic and superhydrophilic regions are avoided. The artificial limit is placed to ensure stability of simulation where density ratio is high ($\rho_{liq}/\rho_{vap} > 10$). Table 4.1 describes the geometric parameters like the plate sizes along with the corresponding domain sizes and also the value of the constraints, i.e. $\widetilde{\mathcal{C}}_{drop}$. These parameters have been chosen in order to ensure stability of simulations. Table 4.2 details liquid and vapor densities as well as surface tension, all of these physical properties being obtained for the CS EOS at different temperatures, see eq. (2.82). Periodic boundary conditions are used to ensure domain inter-connectivity. For a temperature value of $T/T_c = 0.75$

the corresponding density ratio is $\rho_{liq}/\rho_{vap} \approx 30$. The Bond number ($Bo = g_{grav} D^2 \Delta\rho/(4\sigma)$, where D is the droplet diameter) of the simulations lies in the range given as $Bo \in [0.001424, 0.02279]$. The corresponding range of mean capillary number ($Ca_{avg} = \nu_{liq}\rho_{liq}\mathcal{J}/\sigma$, where $\mathcal{J}$ is the cost function, i.e. the mean droplet velocity) for simulations lies in the range such that $Ca_{avg} \in [0.0236, 0.0456]$. In the lattice Boltzmann paradigm as the simulation occurs in the mesoscopic scale, the unit system used differs from the real world. Hence the correlation between the two different systems is usually expressed in terms of the relevant non-dimensional numbers.

Many factors influence the motion of the droplet on a surface. The current study proposes a novel manner of attaining the optimum wettability distribution. As such this article lacks an analysis on the complete list of parameters. In the current context, the influence of the size of the droplet (relative to surface area/size) on the optimization results is looked into. In the following sections, results of different simulations are discussed.

Table 4.1: Domain size, plate length and objective used for simulations.

	Plate length (l.u.)	Domain size	$\widetilde{\mathcal{C}}_{drop}$ (l.u.)
small plate	256	277×101	189
medium plate	512	533×101	417
large plate	1024	1045×201	844

Table 4.2: Fluid densities and surface tension(σ) at different temperatures for the LBM model (simulation results)

	ρ_{liq}	ρ_{vap}	σ
$T/T_c = 0.75$	0.333	0.011	0.0090417
$T/T_c = 0.80$	0.306	0.0193	0.0063263
$T/T_c = 0.85$	0.2777	0.03	0.0040333

4.3. Prior to optimization

Three groups of simulations were performed for this research paper. The first group of simulations are only forward LBM simulations, without any optimization algorithm coupled to them. This study, which precedes the optimization studies in section 4.4, and which is the context of this preliminary results section, is done to ascertain values for the optimization constraints, and narrow down the region of search for our optimization study.

Five different wettability profiles corresponding to curves which are monotonous in nature are tested on the medium sized plate, see fig. 4.2a. The equations of these curves can been obtained from the appendix B. The objectives here are twofold: to find a good initial wettability profile for a suitable starting point, and also to find appropriate values for constraints $\widetilde{\mathcal{C}}_{drop}$ and $\mathcal{I}_{lbm}^{max}$ (this latter is a maximum time constraint in the forward LBM simulation). Figure 4.2b provides us with the evolution of the droplet center of gravity as the simulation proceeds. It is apparent that the relative performance of each profile Υ is dependent on $\mathcal{C}^*_{drop} = \mathcal{C}_{drop}/L$. Below in eq. (4.5), the order of performance (in terms of cost function value) is mentioned at three points in the simulation:

$$\text{if} \quad \mathcal{C}^*_{drop} = \begin{cases} 0.3 \text{ then } \mathcal{J}(\Upsilon_{cca}) > \mathcal{J}(\Upsilon_{qca}) > \mathcal{J}(\Upsilon_{lin}) > \mathcal{J}(\Upsilon_{qcv}) > \mathcal{J}(\Upsilon_{ccv}). \\ 0.4 \text{ then } \mathcal{J}(\Upsilon_{qca}) > \mathcal{J}(\Upsilon_{cca}) > \mathcal{J}(\Upsilon_{lin}) > \mathcal{J}(\Upsilon_{qcv}) > \mathcal{J}(\Upsilon_{ccv}). \\ 0.6 \text{ then } \mathcal{J}(\Upsilon_{lin}) > \mathcal{J}(\Upsilon_{qca}) > \mathcal{J}(\Upsilon_{qcv}) > \mathcal{J}(\Upsilon_{cca}) > \mathcal{J}(\Upsilon_{ccv}). \end{cases} \tag{4.5}$$

Moreover, the final center of gravity ($\mathcal{C}_{drop}|_{t=t_f}$) for each droplet is different though the leading edge of all the droplets arrive at the end of the plate. This difference can be explained by the difference in the droplet curvature which in turn is due to the spatial wettability distribution under the belly of the droplet. Now, considering the final center of gravity of the droplet for each individual

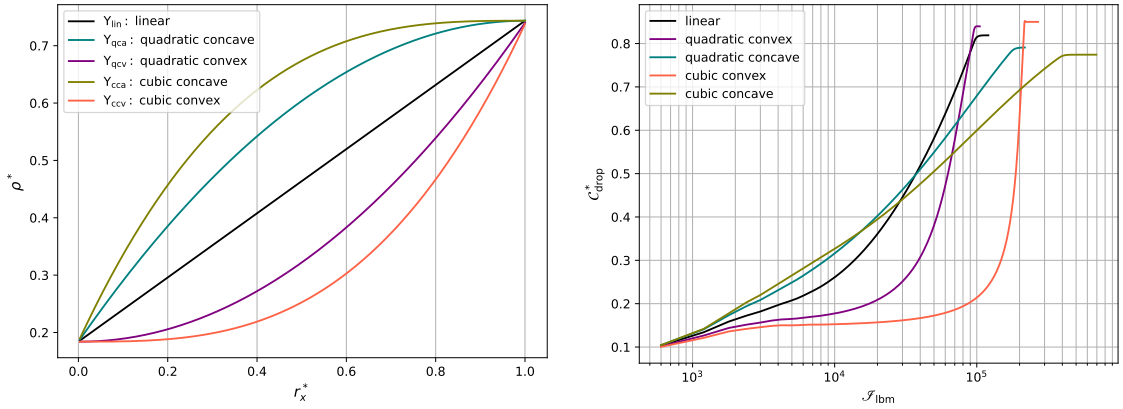

(a) Different initial wettability profiles

(b) Normalized drop center of gravity w.r.t time

Figure 4.2: Prior to optimization study: performance of wettability profiles for a medium sized plate where $L/D = 6.4$ and $T/T_c = 0.75$; (model $\mathscr{H}_1$).

wettability profile, with no time constraint, i.e. $\mathcal{C}^*_{\text{drop}} = \mathcal{C}^*_{\text{drop}}\big|_{t=t_f}$, then the order of performance is:

$$\mathcal{J}(\Upsilon_{\text{qcv}}) > \mathcal{J}(\Upsilon_{\text{lin}}) > \mathcal{J}(\Upsilon_{\text{qca}}) > \mathcal{J}(\Upsilon_{\text{ccv}}) > \mathcal{J}(\Upsilon_{\text{cca}}). \tag{4.6}$$

This means that, for this given objective, the highest mean droplet velocity is for the quadratic convex wettability profile Υ_{qcv}. It appears that even with very simple wettability profiles, the definition of the best one is sensitive to the objective function definition. So, further in the article (for the optimization process) , $\widetilde{\mathcal{C}}_{\text{drop}}$ is chosen such that this objective can be reached with the constant gradient wettability profile Υ_{lin}. The value of the constraint for each plate sizes is given in table 4.1. The maximum iteration number $\mathcal{T}^{\max}_{\text{lbm}}$ is fixed in a similar manner. The linear (Υ_{lin}) and the quadratic convex (Υ_{qcv}) profiles, will be used hereafter as initial guesses.

4.4. Results and discussion

Three sets of optimization simulations are performed to understand how the optimizer behaves in different situations. To begin with, section 4.4.1 presents an optimization test based on the multiscale approach in which the parameterization is progressively refined. As the resolution increases, the route taken by the optimizer to the optimal WGS is examined. Next, section 4.4.2 discusses the study on the dependency of the obtained solutions on the initial wettability profile. Lastly, in section 4.4.3, different plate length to droplet diameter L/D ratio are used for testing the sensitivity of the optimized profiles with respect to both these parameters. Section 4.4.5 then presents the applicability of obtained optimal wettability profiles.

4.4.1. Progressive refinement of the parameterization

For the small plate ($L/D = 3.2$), the route embarked on by the multiscale optimization algorithm is illustrated in fig. 4.3. The successive wettability profiles are obtained after attaining convergence for each respective optimization scale. The initial linear wettability profile, Υ_{lin}, is firstly updated after performing optimization at the first scale, on the 2-elements parameterization, to obtain Υ_{10}. Considering the proximity of Υ_{10} and Υ_{qcv}, relative to Υ_{lin}, it can be said that the optimizer approaches in the direction of Υ_{qcv}. Now, optimization at the next scale (with the 4-elements parameterization) gives Υ_{11}. It is observed that a significant region under the final drop position (FDP) has a constant pseudo-density i.e. no wettability gradient (NWG) region. Also, a reduction of slope is observed for the region under the initial drop position (IDP). This causes a sharper distribution of wettability in the intermediate region (IR) of the plate, which increases the mean droplet velocity. Here the

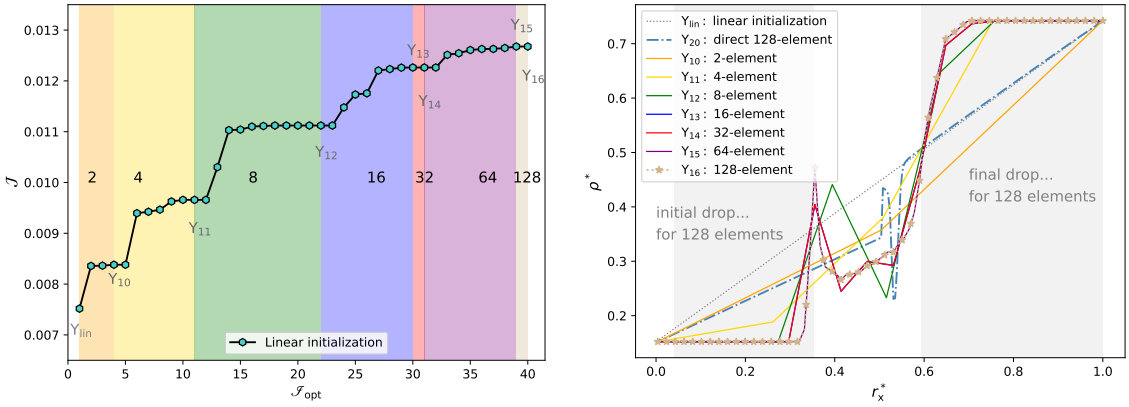

(a) Increase of cost function ($\mathcal{J}$) en-route a multiscale optimization

(b) Intermediate results in a multiscale optimization alongside the direct 128 element optimization

Figure 4.3: Route/path taken by the multiscale optimization algorithm. The small plate is considered ($L/D = 3.2$) with $T/T_c = 0.75$; (model $\mathscr{H}_1$).

optimizer deviates from Υ_{qcv}. Note that both IDP and FDP are defined w.r.t Υ_{16}, these regions being shaded in fig. 4.3b. Optimization on the 8-elements parameterization gives Υ_{12}, where the major change observed is that now, even a fraction of the region under the IDP is a NWG region. Also a bump is observed at the leading edge (LE) of the drop at the IDP, with a peak and valley further along in the IR. Optimization on the 16-elements parameterization gives Υ_{13}, where the major change observed is that the peak is shifted to the LE of the IDP. Also the valley profile is modified in the IR of the plate. Optimization on the 32-elements parameterization converges without any additional major modification. Optimization on the 64-elements parameterization gives Υ_{15}, where the modifications observed were a surge in the peak at the IDP and smoothening of the valley in the IR. The 128-element optimization converges without any additional modification. On the other hand, for an optimization performed directly starting from Υ_{lin} and having a parameterization of 128-elements, the cost function of the resulting profile i.e. Υ_{20} is $\mathcal{J}(\Upsilon_{20}) = 0.009$ l.u./t.s.. Interesting and non obvious features which appear (while using multiscale optimization) are: Firstly, no wettability gradient is required under most of the initial and final location of the droplet to displace the droplet quickly. So, the overall pull-off potential of the WGS is concentrated in the IR having optimal impact on the velocity. Secondly, the optimal (wettability profile) solution is non monotonous, which is counter-intuitive. Although for Υ_{16} the first peak is followed by a deep valley, which ought to cause a local deceleration. This profile is slated to obtain the highest mean droplet velocity. In fact, without this small region defined by the wettability decrease, it would not be possible to reach the performance obtained by the optimizer. Finally, the multiscale feature of the optimization process is very useful, improving the performance by 69 % w.r.t the initial profile i.e. Υ_{lin}. Conversely the performance improvement for optimization only using 128-elements parameterization is 17% w.r.t Υ_{lin}.

4.4.2. Sensitivity to the initial wettability profile

The objective of such a study is to check whether or not a single global minimum is reached. For that purpose, different initial wettability profiles have been tested with the multiscale optimizer, namely Υ_{lin} (with $q^{(0)} = 2$), Υ_{qcv} (with $q^{(0)} = 8$) and Υ_{ccv} (with $q^{(0)} = 8$). These simulation have used the smallest plate, with $L = 256$ l.u. and $L/D = 3.2$. Multiscale optimization results are reported in fig. 4.4. The resulting profiles have the same mean droplet velocity, i.e. $\mathcal{J}(\Upsilon_{16}) = \mathcal{J}(\Upsilon_{21}) = \mathcal{J}(\Upsilon_{22}) \approx 0.0127$ l.u./t.s., but the obtained wettability profiles can be categorized into two groups. The former group is composed of both Υ_{16} and Υ_{21}, where the first peak is observed at the LE of the IDP, followed by a valley in the IR of the plate. Also similar to Υ_{16}, Υ_{21} has no requirement of

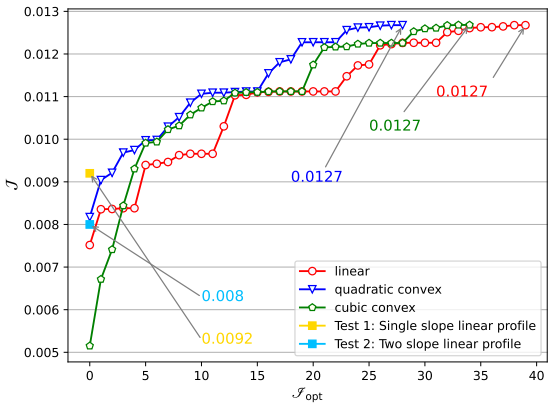

(a) Comparing increase of cost function ($\mathcal{J}$)

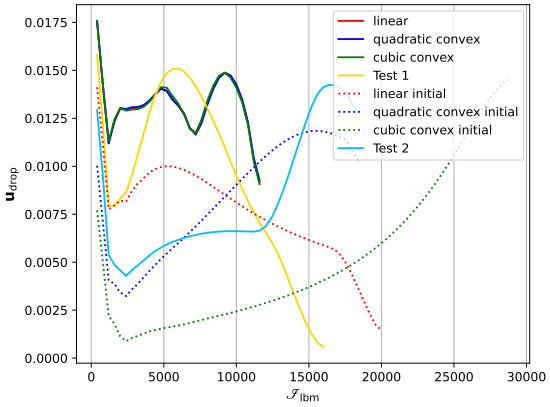

(b) Evolution of droplet velocity ($\boldsymbol{u}_{\text{drop}}$) along the plate in terms of time

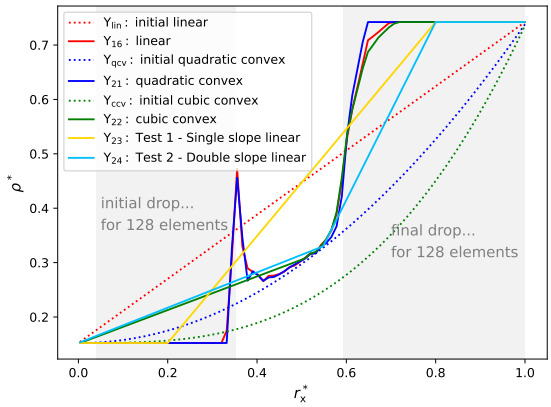

(c) Final and corresponding initialization wettability profiles (along with independent test profiles)

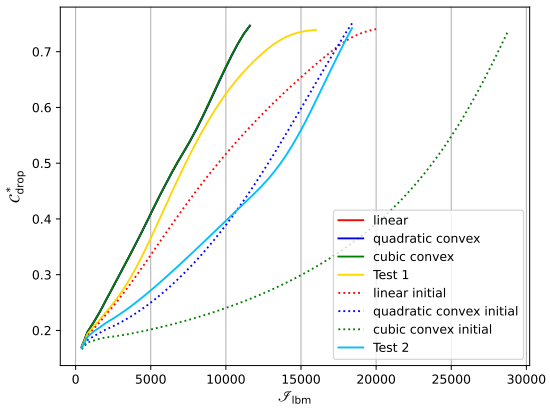

(d) Normalized drop center of gravity($\mathcal{C}^*_{\text{drop}}$) evolution along the plate

Figure 4.4: Comparing final results for different wettability profile initialization for multiscale optimization for small plate with $L/D = 3.2$ and $T/T_c = 0.75$; (model $\mathscr{H}_1$).

wettability distribution for significant regions of IDP and FDP in order to propel the droplet to full displacement. On the contrary, for Υ_{22}, a linear wettability slope starting from the beginning of the plate and including the IDP along with most of the IR of the plate is observed. Though the three obtained profiles are identical at the ending part of the plate (from the latter part of the IR to the FDP), taking all into account, it is observed that optimization result is dependent on the shape of the initial wettability profile. This illustrates the dilemma of the non unicity of solution and also the sensitivity of the solution to the initial guess.

Two additional tests are performed to evaluate the cost function for certain non-trivial curves. As a first example, the curve Υ_{23} uses the maximum wettability distribution in the IR along with a fraction of the IDP and the FDP. The obtained corresponding cost function value is much less than for optimized solutions, since $\mathcal{J}(\Upsilon_{23}) = 0.009$ l.u./t.s.. The decrease in performance is attributed to the absence of the peak at the LE of the IDP. As a second example, the curve Υ_{24} is obtained as Υ_{22} is trimmed to a wettability distribution with two linear slopes. The obtained corresponding cost function value is again much less than for optimized solutions, since $\mathcal{J}(\Upsilon_{24}) = 0.008$ l.u./t.s.. Here, the decrease in performance is attributed to the variation of the slope, as compared to Υ_{22} (especially in the latter part of the IR and also the FDP).

Figure 4.4d depicts the location of the center of gravity with respect to time, transient velocity being simply the local slope of this curve. Analyzing the Υ_{lin} performances, one can recover the classical result: for constant gradient, when the droplet reaches the hydrophilic region, it tends to

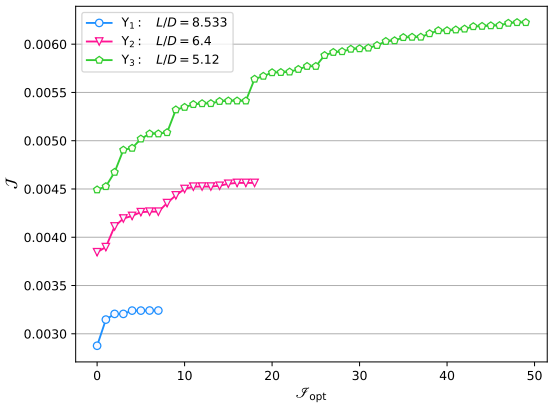

(a) Comparing increase in the cost function ($\mathcal{J}$)

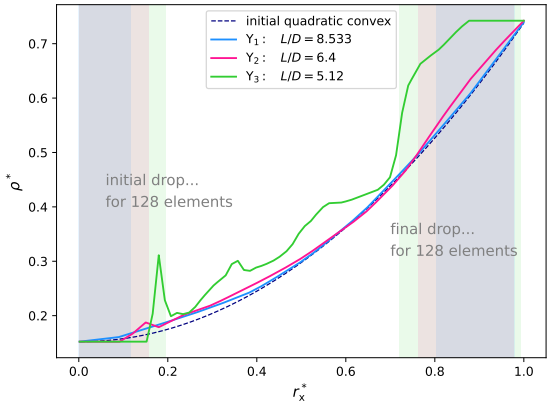

(b) final wettability profile for different droplet diameters (D), for medium plate size

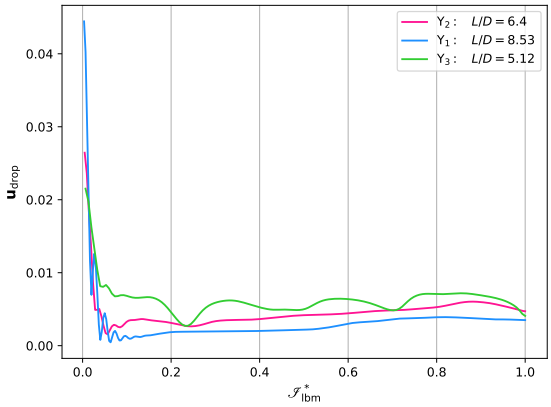

(c) Evolution of droplet velocity ($\boldsymbol{u}_{\text{drop}}$) along the plate

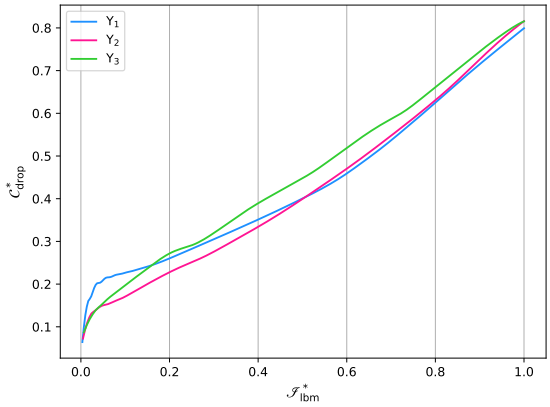

(d) Normalized drop center of gravity ($\mathcal{C}^*_{\text{drop}}$) evolution

Figure 4.5: Comparing final results for different droplet diameters (L/D = 5.12, L/D = 6.4 and L/D = 8.5333) initializations for multiscale optimization with medium plate for T/T_c = 0.75, (model $\mathscr{H}_1$)

spread, increasing the contact surface with the solid, and consequently, slows down. Variable wettability gradient profiles, like all the optimization results succeed in preventing this trend, maintaining a higher final velocity

4.4.3. Sensitivity to relative droplet and plate sizes

Two series of tests are performed, both dealing with dependency of the optimized solutions to different plate and droplet sizes.

The first series of test considers different droplet diameters but with a constant plate size. The medium sized plate has been chosen, and the initial wettability profile is chosen to be the quadratic convex one, Υ_{qcv}. Optimization results are presented in fig. 4.5b. Optimized profiles Υ_1, Υ_2 and Υ_3 correspond to L/D ratio equal to 8.53, 6.4 and 5.12, respectively. It can be observed from Υ_{21}, Υ_1, Υ_2 and Υ_3 that, as the L/D ratio increases, the obtained profile has lesser bumps and gets progressively smoothened, approaching the initial convex quadratic profile Υ_{qcv}. An explanation for this observation could be that, for lower L/D ratio, a large force – due to a steep bump (large wettability gradient) at the LE of the IDP – is necessary to overcome the inertia of a static droplet. Also, bumps of similar magnitude helps to further maintain the momentum of the droplet at the later stage. The decrease in the volume of liquid drop to be transported causes these bumps to be superfluous.

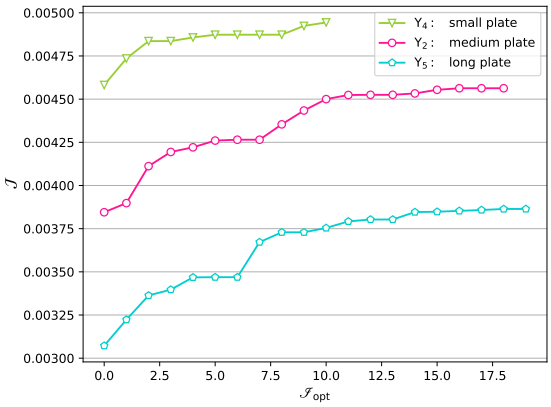

(a) Comparisons of cost function ($\mathcal{J}$) evolution.

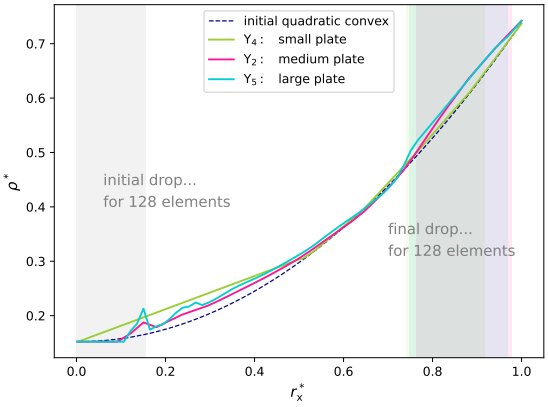

(b) final wettability profile for different plat sizes (L), where $L/D = 6.4$

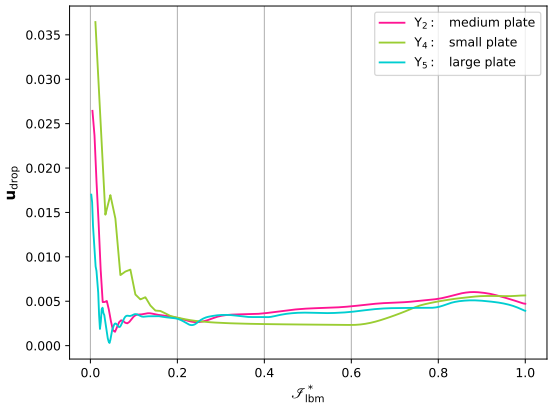

(c) Evolution of drop velocity ($\boldsymbol{u}_{\text{drop}}$) along the plate with respect to time

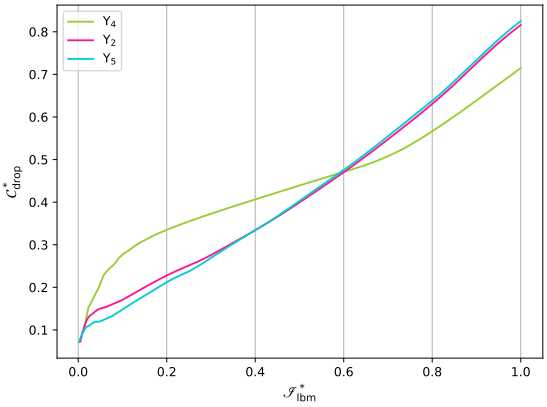

(d) Normalized drop center of gravity ($\mathcal{C}^*_{\text{drop}}$) evolution along the plate

Figure 4.6: Comparing final results for different plate size (small, medium and large) configuration for multiscale optimization with $L/D = 6.4$ parameter for $T/T_c = 0.75$ (model $\mathscr{H}_1$)

The second series of test considers different plate sizes but with a constant ratio $L/D = 6.4$. The initial wettability profile is chosen to be the quadratic convex one, Υ_{qcv}. It is here to be pointed out that for a maximum number of elements $q_{\max} = 128$, the minimum optimization element length is $L/q_{\max} = 2$ l.u., 4 l.u. and 8 l.u. for the small, medium and large plates, respectively. Optimization results are presented in fig. 4.6b, where profiles Υ_4, Υ_2 and Υ_5 correspond to the small, the medium and the large plate sizes respectively. It is observed that, as the plate size increases, more refined features with defined peaks, dips and valleys are obtained. Table 4.4 depicts the results of a post optimization study where the performance of Υ_2, Υ_4 and Υ_5 are evaluated. The performance of Υ_2 and Υ_5 are consistent (it differs slightly for the long plate) and Υ_4 performs the worst overall. Hence, the medium plate is pragmatic choice for computing the optimization gradient ($\nabla\mathcal{J}$) i.e. its resolution is sufficient, while saving in computational expense.

4.4.4. Sensitivity to temperature and viscosity ratios

The third series of test considers the influence of the temperature for a medium plate size and constant ratio $L/D = 6.4$. Again the initial wettability profile is chosen to be the quadratic convex (Υ_{qcv}). One recurring theme which is observed is that as the temperature decrease, the parameters become more sensitive and hence one observes sharper (i.e. of greater amplitude) peaks, valleys and dips. This is further reflected in the post optimization study table 4.5, where the final profile

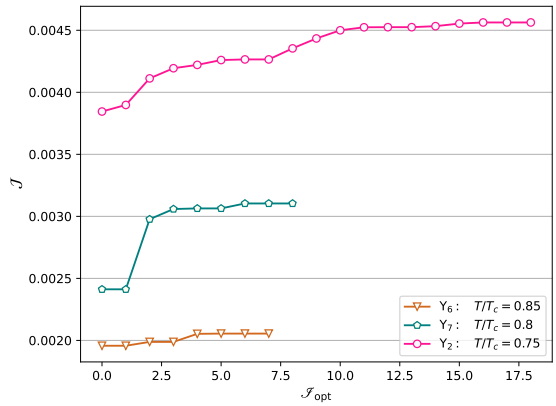

(a) Comparisons of the cost function ($\mathcal{J}$) evolution

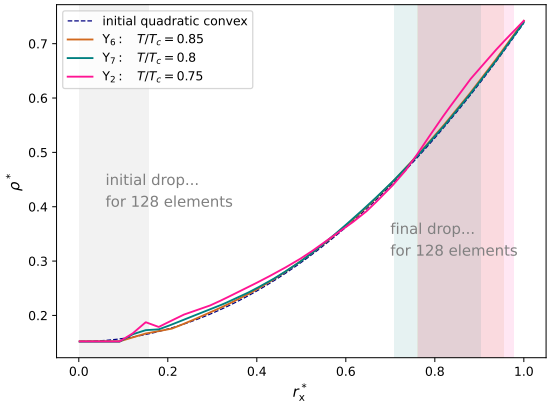

(b) final wettability profiles for different temperatures (T) for a medium sized plate

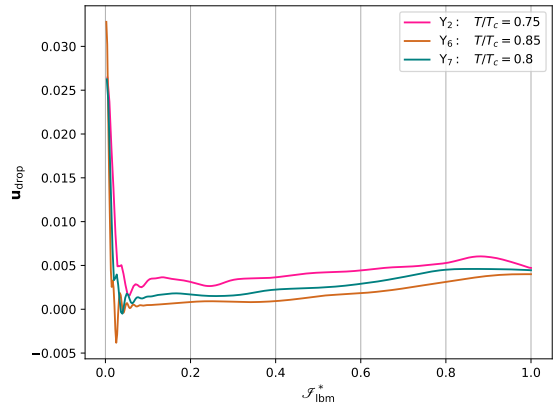

(c) Evolution of droplet velocity $\boldsymbol{u}_{\text{drop}}$ along the plate.

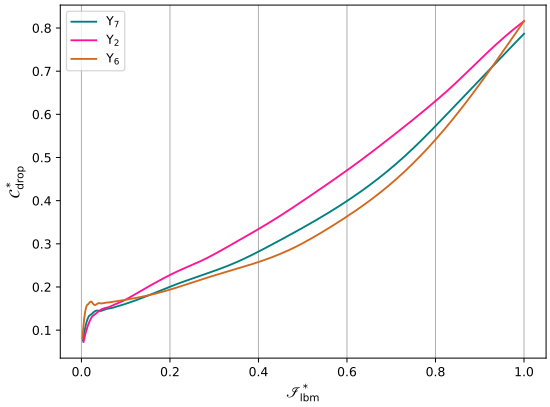

(d) Normalized drop center of gravity($\mathcal{C}^*_{\text{drop}}$) evolution along the plate

Figure 4.7: Comparing final results for different temperature ($T/T_c = 0.75$, $T/T_c = 0.8$ and $T/T_c = 0.85$) initialization configuration for multiscale optimization for a medium sized plate. (model $\mathscr{H}_1$)

obtained at each of the temperatures are cross-checked for robustness. The overall best performance is observed for Υ_2 wettability profile. The only outlier to this phenomenon occurs at $T/T_c = 0.85$ for Υ_6. The increasing sensitivity for decreasing temperature was excepted as due to higher velocity at lower temperature due to lower resistance due to higher density ratio.

The fourth series of test considers the influence of kinematic viscosity relative for each phase for constant temperature ($T/T_c = 0.75$), medium plate and constant ratio ($L/D = 6.4$). Here, the initial wettability profile is chosen to be quadratic convex (Υ_{qcv}). Only minute changes are observed between the wettability profiles and accordingly minor changes are also observed in the performance of the three curves. When the liquid (kinematic) viscosity is lower than the vapor viscosity one observes Υ_9 where the amplitude of features is lower as compared to Υ_2. Also one observes more sensitivity for optimization parameters when the liquid kinematic viscosity is higher. As is evident from the post optimization study table 4.6 the changes in the relative viscosities does not influence majorly the optimization problem.

4.4.5. Applicability of optimization results

The results obtained thus far are for some given prescribed sizes of both a droplet and a plate. The question that arises is how a droplet of a given size behaves when being subject to a profile that has been optimized specifically for a another droplet size. Such a cross-check test somehow

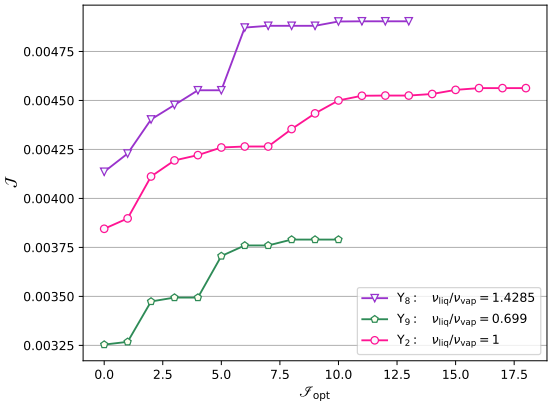

(a) Comparisons of cost function ($\mathcal{J}$) evolution

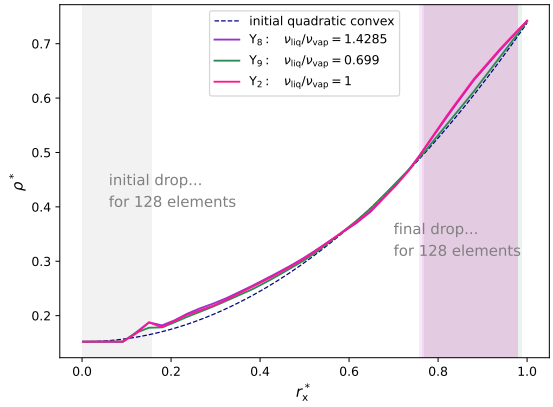

(b) final wettability profiles for different kinematic viscosity ratios (ν_{liq}/ν_{vap}) for a medium sized plate

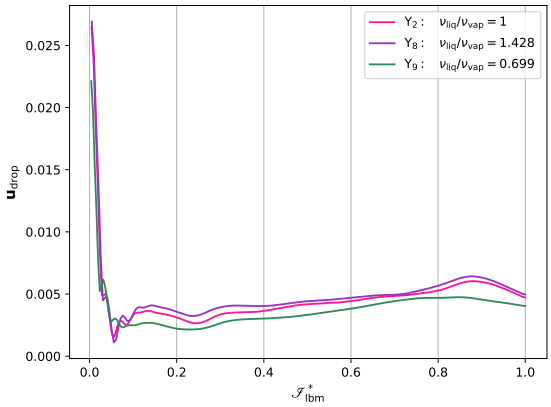

(c) Evolution of droplet velocity ($\boldsymbol{u}_{\text{drop}}$) along the plate

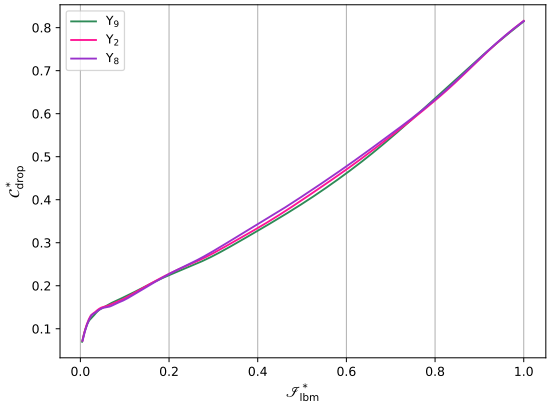

(d) Normalized drop center of gravity($\mathcal{C}^*_{\text{drop}}$) evolution along the plate.

Figure 4.8: Comparing final results for different initialization configuration for multiscale optimization concerning dynamic viscosity ratio (M) parameter for a medium sized plate; ($T/T_c = 0.75$ and model $\mathscr{H}_1$).

evaluates the robustness of obtained optimized wettability profiles. This robustness evaluation is of first importance because, though in some controlled applications, e.g. LOC, the droplet sizes are monodisperse (i.e. the variation around the mean droplet size is very small), in other applications, for example in condensation, the droplet sizes are polydisperse (i.e. the variation around the mean droplet size is high). It has thus to be checked whether an optimal profile that has been obtained for a certain droplet size would be appropriate for another droplet size.

Table 4.3 gives the computed mean velocity for the three optimal profiles Υ_1, Υ_2 and Υ_3 and for the three L/D ratio. Firstly, it is seen that, for a given L/D ratio, the highest mean velocity is the one obtained with the profile obtained specifically for this L/D ratio, which is not a surprise (these results correspond to cells filled in green in this table). Secondly, for a given L/D ratio, the use of other profiles yields either to lower mean velocity (cells filled in orange in the table) or, worse, to a droplet that never reaches the other end of the plate (cells filled in red in this table). The reasons why the droplet does not reach its destination is either that it is stuck in between two wettability peaks, or that the wettability gradient is too low at its IDP, avoiding any motion right from the beginning. From this result, one conclusion is that, for the specific problem of sequential displacement of droplets with size ranging from D_{min} to D_{max} (i.e. assuming no merging of droplets), optimization of the wettability profile must be performed for the smallest one in order to avoid pining of droplets. Now considering merger of droplets, this is a possibility for a droplet diameter (such that)

$D < D_{\min}$. In these cases, the most probable region for smaller droplets to get pinned is where the local wettability gradient is null or the local direction of the wettability gradient is against the direction of the droplet motion. Hence these *regions*, would be hot-spots for droplet merger.

Table 4.3 also gives the computed mean velocity for the quadratic convex wettability profile. It is seen that the droplet reaches its destination in all cases. Moreover, though the gain of use of optimal profile is not much for large L/D ratio (the gain is 7 % when using Υ_1 instead of using Υ_{lin}), this gain is very high for low L/D ratio (the gain is $\approx$ 44 % when using Υ_3 instead of using Υ_{lin}). Note that, comparing the performance of Υ_{qcv} and Υ_{lin} (from table 4.3) for all of the sampled droplet sizes, it is observed that Υ_{qcv} is consistently better for small displacements.

Table 4.3: Post optimization study: cost function ($\mathcal{J}$) for medium sized plate with different L/D at $T/T_c = 0.75$, (fig. 4.5b)

Curves	$L/D = 8.53$	$L/D = 6.4$	$L/D = 5.12$
Υ_{qcv}	0.0029 (+0.2% [1])	0.0038 (+0.3%)	0.0045 (+4%)
Υ_1	0.0032 (+7%)	0.0042	0.0048
Υ_2	×[2]	0.0046 (+21%)	0.0051
Υ_3	×	×	0.0062 (+44%)

[1] : Performance comparison w.r.t Υ_{lin}.
[2] : Droplet does NOT reach the end of plate, hence $\widetilde{C}_{\text{drop}}$ is out of reach.

Table 4.4: Post optimization study: cost function ($\mathcal{J}$) for different sized plate with $L/D = 6.4$ at $T/T_c = 0.75$, (fig. 4.6b)

Curves	$L = 256$	$L = 512$	$L = 1024$
Υ_4	0.0049	0.0042	0.0034
Υ_2	0.0054	0.0046	0.0037
Υ_5	0.0054	0.0047	0.0039

Table 4.5: Post optimization study: cost function ($\mathcal{J}$) for different temperature (T) with $L/D = 6.4$, (fig. 4.7b)

Curves	$T/T_c = 0.75$	$T/T_c = 0.8$	$T/T_c = 0.85$
Υ_6	0.0040	0.0028	0.0021
Υ_2	0.0046	0.0032	0.0020
Υ_7	0.0042	0.0031	0.0019

Table 4.6: Post optimization study: cost function ($\mathcal{J}$) for different kinematic viscosity ratio ($\nu_{\text{liq}}/\nu_{\text{vap}}$) with $L/D = 6.4$, (fig. 4.8b)

Curves	$\nu_{\text{liq}}/\nu_{\text{vap}} = 1.4285$	$\nu_{\text{liq}}/\nu_{\text{vap}} = 1.0$	$\nu_{\text{liq}}/\nu_{\text{vap}} = 0.699$
Υ_8	0.0049	0.0046	0.0039
Υ_2	0.0048	0.0046	0.0038
Υ_9	0.0047	0.0044	0.0038

4.5. Conclusion

Optimization of the wettability gradient surface has been performed in order to increase the mean velocity of a droplet. In order to do so, the pseudo-density (i.e. the control variable) has been tuned; which within the Shan and Chen framework corresponds to locally adjusting the contact angle on the plate (i.e. an ideal surface, without pinning defects or contact angle hysteresis). The major conclusions are summarized as follows:

1. It has been found that the multiscale approach is necessary in order to converge to some optimal robust solutions.

2. For large expected displacements, the proposed quadratic convex wettability profile appears to be a good candidate. On the other hand, for small expected displacements, optimizing the wettability profile is of prime importance as it allows an increase of up to 69 % of the mean velocity when compared to the use of a classical linear wettability profile.

3. Optimization results exhibit some non trivial features. At first, no wettability gradient is needed under most of the initial and the final droplet locations, allowing to focus the potential of the wettability tuning on a smaller area, enhancing its effect. Another interesting feature is the existence of some non monotonous optimal profiles. Indeed, starting with a steep initial profile allows to quickly overcome the inertia, this being followed by an unexpected decrease of the wettability which does not result in a pinning droplet.

4. Multiscale optimization when performed on the medium plate size provides us with results i.e. curves that have sufficient resolution. This curves replicate the performance of the higher resolution (large plate size with same L/D ratio) curves for the most part. Hence a pragmatic trade-off in precision can be made for a reasonable computational effort.

5. The changes to viscosity ratio (between the fluids), causes minor changes to the wettability profile. The prediction of the optimization model improves with the increase in the sensitivity of the system i.e. for low temperatures (or higher density ratio) and for higher liquid viscosity.

Conclusions of this numerical work will be vetted in the future by experimental means, having in mind that many industrial applications could benefit from this, for example lab-on-a-chip. The optimization algorithm could greatly benefit from the development of an adjoint solver, for efficiently solving real world problems. Previously, we introduced an adjoint solver for a single phase problem. In the following chapter, we extend this adjoint solver to address the multiphase problem.

Chapter 5

Multiphase optimization

Now we return back to the topology optimization discourse and intent to demonstrate the derivation of adjoint-state model for the interfacial flows/fluids. As compared to structural and single phase flow topology optimization, applications in this field are nascent. We here discuss some of these interesting optimization studies. The first example of topology optimization for interfacial flows (as far as the author is aware) is recorded in ref.[172] which was published in 2017. Here a diffused interface is modeled using the coupled NS and Cahn-Hillard equations (from commercial tool COMSOL Multiphysics). The solid domain is represented using the level-set method. The optimization algorithm predicts the optimal topology (for different initial conditions) such that maximum capillary force is generated. The next study [173] discusses the distribution of three materials (each with different properties) for maximum and quick absorption of liquid in a diaper like porous structure. To simplify the problem and to avoid the re-meshing of the diaper due to its eventual expansion as it soaks the liquid the assumption is that the diaper is already at its final expanded state. The interfacial flow is modeled using the Richard's equation which is used for describing imbibition. The next study [174] demonstrates topology optimization for transient diphasic problem (i.e. TOTFP) for e.g. dam break problem and Rayleigh-Taylor's instability. The interfacial problems is modeled by the laminar NS equations with LSF being seamlessly integrated using VOF method. Here the flow is controlled by pseudo-rigid domain (this domain is used for implementing topology optimization and) which is assigned by the intensity of the Darcy force. Recently a topological optimization study for diphasic flow boiling [175] was published. Here the mixture model (from the commercial tool ANSYS Fluent) is used for multiphase simulation, while the homogenization method is used for construction of the solid domain/structure (where the rest of the components of the optimization code are implemented in MATLAB). The objective of this study is to optimize heat sinks for diphasic boiling. The results for diphasic boiling are then compared to monophasic flow with heating. For the monophasic heating, (the same implementation of the diphasic boiling is used except that) the vapor phase is absent as the boiling point is set to a unattainably high temperature.

Finally we present some other optimization studies which are related to our field but which do not employ topology optimization. For vapor chambers, there are two published optimization studies for grooved evaporator and condenser wicking structures [176, 177] by the same research team in 2020. While the grooved condenser wick structure design is simplified to an *Area-to-point* (AP) constructal optimization problem, the grooved evaporator wick structure design is simplified to an *Area-to-line* (AL) constructal optimization problem. Later (in 2022), they publish a integrated topology optimization study [178] for vapor chambers working on both evaporator and condenser. The micro-channels or wick structures are build using generative topology optimization with a bifurcation rule. Hierarchical capillary flow channels are produced which minimize global resistance for AP and AL flow problems.

Here we demonstrate first the adjoint-state model (in section 5.1) for changing the porous media structure i.e. topology optimization. Later, we discuss the possibility of another optimization variable/parameter i.e. wettability and develop an adjoint-state model in section 5.2.

5.1. Multiphase topology optimization

For this class of problems in topology optimization, the design variable remains same as previously, i.e., the level-set function (Ψ). Here in topology optimization for interfacial flows, the objective is to generate a porous media/wick structure or network of solid nodes. The solid structure should it be such that minimizes a cost function in the context of the unsaturated/multiphase flow. The preliminary (for this thesis) objective is to increase the capillary force generated by modifying a solid structure (of homogeneous wettability) of the porous media/wick. The Lagrange function is again described by eq. (3.15). Due to unresolved issues regarding the boundary conditions for the interfacial flows, we downscale our problem such that, we in this thesis, utilizes solely the periodic boundary conditions. Hence we neglect the residue of the boundary condition ($\mathcal{P} = 0$) and the cost functions exists exclusively in the domain ($\mathscr{Y}$). The semi-discretized (discretized only in velocity) residue of the LBM governing differential equation for SCMP-SC (model $\mathscr{H}_1$) is given as:

$$\mathcal{R}_i(\mathbf{f},\Psi) = \frac{\partial f_i}{\partial t} + \boldsymbol{e}_i \cdot \nabla_{\boldsymbol{r}} f_i + \boldsymbol{a}_i \cdot \nabla_{\boldsymbol{e}} f_i + \frac{1}{\tau}\left(f_i - f_i^{\mathrm{eq}}\right) = 0 \quad \forall\ i \in [0,\dots,8] \tag{5.1}$$

Using the Exact difference method (EDM) forcing scheme [89] we rewrite the above continuous equation as:

$$\mathcal{R}_i(\mathbf{f},\Psi) = \frac{\partial f_i}{\partial t} + \boldsymbol{e}_i \cdot \nabla_{\boldsymbol{r}} f_i - \mathscr{F}_{\mathrm{edm},i} + \frac{1}{\tau}\left(f_i - f_i^{\mathrm{eq}}\right) = 0 \quad \forall\ i \in [0,\dots,8] \tag{5.2}$$

Now, EDM forcing term (from eq. (2.85)) can be expanded as:

$$\mathscr{F}_{\mathrm{edm,i}} = \widehat{f^{\mathrm{eq},+}}_i - \widehat{f^{\mathrm{eq}}}_i \tag{5.3}$$

where $\widehat{f^{\mathrm{eq}}} = \widehat{f^{\mathrm{eq}}}(\rho,\boldsymbol{u}) = f^{\mathrm{eq}}(\mathbf{f},\Psi)$, $\widehat{f^{\mathrm{eq},+}} = \widehat{f^{\mathrm{eq}}}(\rho,\boldsymbol{u}+\Delta u)$ and $\Delta u = \boldsymbol{F}_{\mathrm{T}}\Delta t/\rho$. For the scope of this thesis (as mentioned previously), the fluid-fluid interparticular force ($\boldsymbol{F}_{\mathrm{p}}$), solid-fluid interparticular force ($\boldsymbol{F}_{\mathrm{s}}$) and gravitational body force ($\boldsymbol{F}_{\mathrm{body}} = \rho g_{\mathrm{grav}}$) constitute the external force ($\boldsymbol{F}_{\mathrm{T}}$).

5.1.1. Derivation of adjoint-state model

Here we describe the process for deriving the adjoint-state model for the SCMP-SC. As explained previously, the (aA2) term in eq. (3.16) gives us the adjoint-state model:

$$(\mathrm{aA2}) = \sum_j \frac{\partial \mathcal{L}}{\partial f_j} f_j' = 0 = \underbrace{\sum_j \left\langle \frac{\partial \mathscr{Y}}{\partial f_j} f_j', 1 \right\rangle_{\mathcal{D}}\Big|_{t=t_f}}_{\mathrm{bB1}} + \underbrace{\sum_i \left\langle \sum_j \frac{\partial \mathcal{R}_i}{\partial f_j} f_j', \mathring{f}_i \right\rangle_{\mathcal{D}\times\mathcal{T}}}_{\mathrm{bB2}} \tag{5.4}$$

Let us first develop the bB2 term:

$$\begin{aligned}(\text{bB2}) = \sum_i \left\langle \sum_j \frac{\partial \mathcal{R}_i}{\partial f_j} f_j', \mathring{f}_i \right\rangle_{\mathcal{D}\times\mathcal{T}} = \\ \underbrace{\left\langle \sum_i \frac{\partial f_i'}{\partial t}, \mathring{f}_i \right\rangle_{\mathcal{D}\times\mathcal{T}}}_{\text{bC1}} + \underbrace{\left\langle \sum_i \boldsymbol{e}_i \cdot \nabla f_i', \mathring{f}_i \right\rangle_{\mathcal{D}\times\mathcal{T}}}_{\text{bC2}} \\ + \left\langle \sum_i \tau^{-1} f_i', \mathring{f}_i \right\rangle_{\mathcal{D}\times\mathcal{T}} - \underbrace{\left\langle \sum_i \sum_j \tau^{-1} \frac{\partial f_i^{\text{eq}}}{\partial f_j} f_j', \mathring{f}_i \right\rangle_{\mathcal{D}\times\mathcal{T}}}_{\text{bC3}} \\ - \underbrace{\left\langle \sum_i \sum_j \frac{\partial \widehat{f^{\text{eq},+}}_i}{\partial f_j} f_j', \mathring{f}_i \right\rangle_{\mathcal{D}\times\mathcal{T}}}_{\text{bC4}} + \underbrace{\left\langle \sum_i \sum_j \frac{\partial \widehat{f^{\text{eq}}}_i}{\partial f_j} f_j', \mathring{f}_i \right\rangle_{\mathcal{D}\times\mathcal{T}}}_{\text{bC5}}\end{aligned} \tag{5.5}$$

The terms bC1 is expanded using integration by parts, while the term bC2 is resolved using the Green's theorem. Now the terms bC3, bC4 and bC5 (can be essentially be treated in the same manner as this are f^{eq} and) can be rearranged by permutation of indices. The objective of this expansion of the term bB2 is to obtain a final equation where the common factor i.e. f_i' is segregated from the remainder of the equation. Thus the expanded version:

$$\begin{aligned}(\text{bB2}) = -\left\langle \sum_i \frac{\partial \mathring{f}_i}{\partial t}, f_i' \right\rangle_{\mathcal{D}\times\mathcal{T}} + \underbrace{\left[\left\langle \sum_i \mathring{f}_i, f_i' \right\rangle_{\mathcal{D}} \right]_{t=0}^{t=t_f}}_{\text{bD1}} \\ - \left\langle \sum_i \boldsymbol{e}_i \cdot \nabla \mathring{f}_i, f_i' \right\rangle_{\mathcal{D}\times\mathcal{T}} + \underbrace{\sum_\beta \left\langle \sum_i \boldsymbol{e}_i \cdot \boldsymbol{n} \mathring{f}_i, f_i' \right\rangle_{\Gamma_\beta\times\mathcal{T}}}_{\text{bD2}} \\ + \left\langle \sum_i \tau^{-1} f_i', \mathring{f}_i \right\rangle_{\mathcal{D}\times\mathcal{T}} - \left\langle \sum_i \sum_j \tau^{-1} \frac{\partial f_j^{\text{eq}}}{\partial f_i} f_i', \mathring{f}_j \right\rangle_{\mathcal{D}\times\mathcal{T}} \\ - \left\langle \sum_i \sum_j \frac{\partial \widehat{f^{\text{eq},+}}_j}{\partial f_i} f_i', \mathring{f}_j \right\rangle_{\mathcal{D}\times\mathcal{T}} + \left\langle \sum_i \sum_j \frac{\partial \widehat{f^{\text{eq}}}_j}{\partial f_i} f_i', \mathring{f}_j \right\rangle_{\mathcal{D}\times\mathcal{T}}\end{aligned} \tag{5.6}$$

As before bD1 = 0 gives us the initial condition, while the term bD2 is applied to all boundary conditions. Gathering all terms existing in the phase space $\mathcal{D}\times\mathcal{T}$, we write:

$$\sum_i \left\langle -\frac{\partial \mathring{f}_i}{\partial t} - \boldsymbol{e}_i \cdot \nabla \mathring{f}_i + \tau^{-1} \mathring{f}_i - \tau^{-1} \sum_j \frac{\partial f_j^{\text{eq}}}{\partial f_i} \mathring{f}_j - \sum_j \frac{\partial \widehat{f^{\text{eq},+}}_j}{\partial f_i} \mathring{f}_j + \sum_j \frac{\partial f_j^{\text{eq}}}{\partial f_i} \mathring{f}_j, f_i' \right\rangle_{\mathcal{D}\times\mathcal{T}} = 0 \qquad \forall f_i' \tag{5.7}$$

One way to get this equality is to choose:

$$-\frac{\partial \mathring{f}_i}{\partial t} - \boldsymbol{e}_i \cdot \nabla \mathring{f}_i + \tau^{-1} \mathring{f}_i - \tau^{-1} \sum_j \frac{\partial f_j^{\text{eq}}}{\partial f_i} \mathring{f}_j - \sum_j \frac{\partial \widehat{f^{\text{eq},+}}_j}{\partial f_i} \mathring{f}_j + \sum_j \frac{\partial f_j^{\text{eq}}}{\partial f_i} \mathring{f}_j = 0 \qquad \forall \boldsymbol{r} \in \mathcal{D},\ \forall t \in (0, t_f),\ \forall i \tag{5.8}$$

This can be rewritten as:

$$\frac{\partial \mathring{f}_i}{\partial \mathring{t}} + \mathring{\boldsymbol{e}}_i \cdot \nabla \mathring{f}_i + \frac{\mathring{f}_i - \mathring{f}_i^{\text{eq}}}{\tau} - \mathring{\mathscr{F}}_{\text{edm},i} = 0 \qquad \forall \boldsymbol{r} \in \mathcal{D},\ \forall t \in (0, t_f),\ \forall i \tag{5.9}$$

This is the adjoint-state equation for the SCMP-SC model (i.e. $\mathscr{H}_1$).

5.1.2. Adjoint EDM forcing

Previously we already defined the adjoint-state equilibrium distribution function (see paragraph 3.2.2.a.1). Thus the only additional part which requires a derivation is the EDM forcing scheme. The EDM forcing for adjoint-state is essentially difference of the two corresponding equilibrium terms differentiated by the Boltzmann variable and given as:

$$\mathring{\mathscr{F}}_{\mathrm{edm},i} = \sum_j \frac{\partial \widehat{f^{\mathrm{eq},+}}_j}{\partial f_i} \mathring{f}_j - \sum_j \frac{\partial f_j^{\mathrm{eq}}}{\partial f_i} \mathring{f}_j \tag{5.10}$$

From eq. (3.51) we can write:

$$\mathring{\mathscr{F}}_{\mathrm{edm},i} = \sum_j \frac{\partial \widehat{f^{\mathrm{eq},+}}_j}{\partial f_i} \mathring{f}_j - \mathring{f}_i^{\mathrm{eq}} \tag{5.11}$$

Recalling that the adjoint equilibrium ($\mathring{f}^{\mathrm{eq}}$) is given as eq. (3.51). We can expand the unresolved term in the R.H.S. as:

$$\mathring{\mathscr{F}}_{\mathrm{edm},i} = -\mathring{f}_i^{\mathrm{eq}} + \sum_j w_j \mathring{f}_j \frac{\partial}{\partial f_i} \left(\rho + 3\alpha\rho \boldsymbol{e}_j \cdot \boldsymbol{u} + 3\alpha \boldsymbol{e}_j \cdot \boldsymbol{F}_{\mathrm{T}} + \frac{4.5\alpha}{\rho} \left[\sum_k f_k \boldsymbol{e}_k \boldsymbol{e}_j + \boldsymbol{e}_j \cdot \boldsymbol{F}_{\mathrm{T}} \right]^2 - \frac{1.5\alpha}{\rho} \left[\sum_k f_k \boldsymbol{e}_k + \boldsymbol{F}_{\mathrm{T}} \right]^2 \right) \tag{5.12}$$

$$\begin{aligned}
\mathring{\mathscr{F}}_{\mathrm{edm},i} = -\mathring{f}_i^{\mathrm{eq}} + \sum_j w_j \mathring{f}_j \Bigg(& \frac{\partial \sum_k f_k}{\partial f_i} + 3\alpha \frac{\partial \boldsymbol{e}_j \cdot \sum_k f_k \boldsymbol{e}_k}{\partial f_i} + 3\alpha \frac{\partial \boldsymbol{e}_j \cdot \boldsymbol{F}_{\mathrm{T}}}{\partial f_i} \\
& + 4.5\alpha \frac{\partial}{\partial f_i} \frac{(\sum_k f_k \boldsymbol{e}_k \cdot \boldsymbol{e}_j)^2}{\sum_k f_k} + 2 \times 4.5\alpha \frac{\partial}{\partial f_i} \frac{(\sum_k f_k \boldsymbol{e}_k \cdot \boldsymbol{e}_j)(\boldsymbol{e}_j \cdot \boldsymbol{F}_{\mathrm{T}})}{\sum_k f_k} + 4.5\alpha \frac{\partial}{\partial f_i} \frac{(\boldsymbol{e}_j \cdot \boldsymbol{F}_{\mathrm{T}})^2}{\sum_k f_k} \\
& - 1.5\alpha \frac{\partial}{\partial f_i} \frac{(\sum_k f_k \boldsymbol{e}_k)^2}{\sum_k f_k} - 2 \times 1.5\alpha \frac{\partial}{\partial f_i} \frac{\sum_k f_k \boldsymbol{e}_k \cdot \boldsymbol{F}_{\mathrm{T}}}{\sum_k f_k} - 1.5\alpha \frac{\partial}{\partial f_i} \frac{(\boldsymbol{F}_{\mathrm{T}})^2}{\sum_k f_k} \Bigg)
\end{aligned} \tag{5.13}$$

$$\begin{aligned}
\mathring{\mathscr{F}}_{\mathrm{edm},i} = -\mathring{f}_i^{\mathrm{eq}} + \sum_j w_j \mathring{f}_j \Bigg(& 1 + 3\alpha \boldsymbol{e}_j \cdot \boldsymbol{e}_i + 3\alpha \boldsymbol{e}_j \cdot \partial_{f_i}[\boldsymbol{F}_{\mathrm{T}}] \\
& + 4.5\alpha [2(\boldsymbol{e}_j \cdot \boldsymbol{e}_i)(\boldsymbol{e}_j \cdot \boldsymbol{u}) - (\boldsymbol{e}_j \cdot \boldsymbol{u})^2] + 2 \times 4.5\alpha \left[\frac{(\sum_k f_k \boldsymbol{e}_k \cdot \boldsymbol{e}_j)(\boldsymbol{e}_j \cdot \partial_{f_i}[\boldsymbol{F}_{\mathrm{T}}])}{\sum_k f_k} + (\boldsymbol{e}_j \cdot \boldsymbol{F}_{\mathrm{T}}) \frac{\partial}{\partial f_i} \frac{(\sum_k f_k \boldsymbol{e}_k \cdot \boldsymbol{e}_j)}{\sum_k f_k} \right] \\
& + 4.5\alpha \left[\frac{2(\boldsymbol{e}_j \cdot \boldsymbol{F}_{\mathrm{T}})(\boldsymbol{e}_j \cdot \partial_{f_i}[\boldsymbol{F}_{\mathrm{T}}])}{\sum_k f_k} - \frac{(\boldsymbol{e}_j \cdot \boldsymbol{F}_{\mathrm{T}})^2}{(\sum_k f_k)^2} \right] \\
& - 1.5\alpha [2\boldsymbol{e}_i \cdot \boldsymbol{u} - (\boldsymbol{u})^2] - 2 \times 1.5\alpha \left[\frac{\sum_k f_k \boldsymbol{e}_k \cdot \partial_{f_i}[\boldsymbol{F}_{\mathrm{T}}]}{\sum_k f_k} + \boldsymbol{F}_{\mathrm{T}} \cdot \frac{\partial}{\partial f_i} \frac{\sum_k f_k \boldsymbol{e}_k}{\sum_k f_k} \right] \\
& - 1.5\alpha \left[\frac{2\boldsymbol{F}_{\mathrm{T}} \partial_{f_i}[\boldsymbol{F}_{\mathrm{T}}]}{\sum_k f_k} - \frac{\boldsymbol{F}_{\mathrm{T}}^2}{(\sum_k f_k)^2} \right] \Bigg)
\end{aligned} \tag{5.14}$$

$$\mathring{\mathscr{F}}_{\mathrm{edm},i} = -\mathring{f}_i^{\mathrm{eq}} + \sum_j w_j \mathring{f}_j \Big(1 + 3\alpha \boldsymbol{e}_j \cdot \boldsymbol{e}_i + 3\alpha \boldsymbol{e}_j \cdot \partial_{f_i}[\boldsymbol{F}_\mathrm{T}]$$
$$+4.5\alpha[2(\boldsymbol{e}_j \cdot \boldsymbol{e}_i)(\boldsymbol{e}_j \cdot \boldsymbol{u}) - (\boldsymbol{e}_j \cdot \boldsymbol{u})^2] + 2\times 4.5\alpha\left[(\boldsymbol{u}\cdot\boldsymbol{e}_j)(\boldsymbol{e}_j \cdot \partial_{f_i}[\boldsymbol{F}_\mathrm{T}]) + (\boldsymbol{e}_j \cdot \boldsymbol{F}_\mathrm{T})\left[\frac{(\boldsymbol{e}_i \cdot \boldsymbol{e}_j)}{\sum_k f_k} - \frac{(\sum_k f_k \boldsymbol{e}_k \cdot \boldsymbol{e}_j)}{(\sum_k f_k)^2}\right]\right]$$
$$+4.5\alpha\left[\frac{2(\boldsymbol{e}_j \cdot \boldsymbol{F}_\mathrm{T})(\boldsymbol{e}_j \cdot \partial_{f_i}[\boldsymbol{F}_\mathrm{T}])}{\rho} - \frac{(\boldsymbol{e}_j \cdot \boldsymbol{F}_\mathrm{T})^2}{\rho^2}\right]$$
$$-1.5\alpha[2\boldsymbol{e}_i \cdot \boldsymbol{u} - (\boldsymbol{u})^2] - 2\times 1.5\alpha\left[\boldsymbol{u}\cdot\partial_{f_i}[\boldsymbol{F}_\mathrm{T}] + \boldsymbol{F}_\mathrm{T}\cdot\left[\frac{\boldsymbol{e}_i}{\sum_k f_k} - \frac{\sum_k f_k \boldsymbol{e}_k}{(\sum_k f_k)^2}\right]\right]$$
$$-1.5\alpha\left[\frac{2\boldsymbol{F}_\mathrm{T}\partial_{f_i}[\boldsymbol{F}_\mathrm{T}]}{\rho} - \frac{\boldsymbol{F}_\mathrm{T}^2}{\rho^2}\right]\Big) \quad (5.15)$$

Thus we can write:

$$\mathring{\mathscr{F}}_{\mathrm{edm},i} = -\mathring{f}_i^{\mathrm{eq}} + \sum_j w_j \mathring{f}_j \Big(1 + 3\alpha \boldsymbol{e}_j \cdot \boldsymbol{e}_i + 3\alpha \boldsymbol{e}_j \cdot \partial_{f_i}[\boldsymbol{F}_\mathrm{T}]$$
$$+4.5\alpha[2(\boldsymbol{e}_j \cdot \boldsymbol{e}_i)(\boldsymbol{e}_j \cdot \boldsymbol{u}) - (\boldsymbol{e}_j \cdot \boldsymbol{u})^2] + 2\times 4.5\alpha\left[(\boldsymbol{u}\cdot\boldsymbol{e}_j)(\boldsymbol{e}_j \cdot \partial_{f_i}[\boldsymbol{F}_\mathrm{T}]) + \frac{\boldsymbol{e}_j \cdot \boldsymbol{F}_\mathrm{T}}{\rho}\left[(\boldsymbol{e}_i \cdot \boldsymbol{e}_j) - (\boldsymbol{u}\cdot\boldsymbol{e}_j)\right]\right]$$
$$+4.5\alpha\left[\frac{2(\boldsymbol{e}_j \cdot \boldsymbol{F}_\mathrm{T})(\boldsymbol{e}_j \cdot \partial_{f_i}[\boldsymbol{F}_\mathrm{T}])}{\rho} - \frac{(\boldsymbol{e}_j \cdot \boldsymbol{F}_\mathrm{T})^2}{\rho^2}\right]$$
$$-1.5\alpha[2\boldsymbol{e}_i \cdot \boldsymbol{u} - (\boldsymbol{u})^2] - 2\times 1.5\alpha\left[\boldsymbol{u}\cdot\partial_{f_i}[\boldsymbol{F}_\mathrm{T}] + \frac{\boldsymbol{F}_\mathrm{T}}{\rho}\cdot[\boldsymbol{e}_i - \boldsymbol{u}]\right]$$
$$-1.5\alpha\left[\frac{2\boldsymbol{F}_\mathrm{T}\partial_{f_i}[\boldsymbol{F}_\mathrm{T}]}{\rho} - \frac{\boldsymbol{F}_\mathrm{T}^2}{\rho^2}\right]\Big) \quad (5.16)$$

Removing common terms form both $\mathring{f}^{\mathrm{eq}}$, we end up with:

$$\mathring{\mathscr{F}}_{\mathrm{edm},i} = \sum_j w_j \mathring{f}_j \Bigg(3\alpha \boldsymbol{e}_j \cdot \partial_{f_i}[\boldsymbol{F}_\mathrm{T}] + 2\times 4.5\alpha\left[(\boldsymbol{u}\cdot\boldsymbol{e}_j)(\boldsymbol{e}_j \cdot \partial_{f_i}[\boldsymbol{F}_\mathrm{T}]) + \frac{\boldsymbol{e}_j \cdot \boldsymbol{F}_\mathrm{T}}{\rho}\left[(\boldsymbol{e}_i \cdot \boldsymbol{e}_j) - (\boldsymbol{u}\cdot\boldsymbol{e}_j)\right]\right]$$
$$+4.5\alpha\left[\frac{2(\boldsymbol{e}_j \cdot \boldsymbol{F}_\mathrm{T})(\boldsymbol{e}_j \cdot \partial_{f_i}[\boldsymbol{F}_\mathrm{T}])}{\rho} - \frac{(\boldsymbol{e}_j \cdot \boldsymbol{F}_\mathrm{T})^2}{\rho^2}\right] - 2\times 1.5\alpha\left[\boldsymbol{u}\cdot\partial_{f_i}[\boldsymbol{F}_\mathrm{T}] + \frac{\boldsymbol{F}_\mathrm{T}}{\rho}\cdot[\boldsymbol{e}_i - \boldsymbol{u}]\right] - 1.5\alpha\left[\frac{2\boldsymbol{F}_\mathrm{T}\partial_{f_i}[\boldsymbol{F}_\mathrm{T}]}{\rho} - \frac{\boldsymbol{F}_\mathrm{T}^2}{\rho^2}\right]\Bigg) \quad (5.17)$$

5.1.2.a. Differentiation of composite force

From eq. (2.65) we can rewrite the continuous form of fluid-fluid force as:

$$\boldsymbol{F}_\mathrm{p} = -\mathscr{G}\nabla\psi^2/2 \quad (5.18)$$

and likewise the continuous form of solid-solid interparticular force

$$\boldsymbol{F}_\mathrm{s} = -\mathscr{G}\psi\nabla\psi_{\mathrm{solid}} \quad (5.19)$$

where $\psi_{\mathrm{solid}} = \psi(\vartheta)\big|_{\vartheta\in\mathcal{D}_\mathrm{s}}$. Also the gravitational body force in this case is given as :

$$\boldsymbol{F}_{\mathrm{body}} = g_{\mathrm{grav}}\rho \quad (5.20)$$

Now as described previously, the total force is expanded as $\boldsymbol{F}_\mathrm{T} = \boldsymbol{F}_\mathrm{p} + \boldsymbol{F}_\mathrm{s} + \boldsymbol{F}_{\mathrm{body}}$. Hence, the differentiation of the source $\boldsymbol{F}_\mathrm{T}$ with respect to the state parameter f_i is given here:

$$\partial_{f_i}[\boldsymbol{F}_\mathrm{T}] = \frac{\partial \boldsymbol{F}_\mathrm{T}}{\partial f_i} = \frac{\partial(\boldsymbol{F}_\mathrm{p} + \boldsymbol{F}_\mathrm{s} + \boldsymbol{F}_{\mathrm{body}})}{\partial f_i} = -\mathscr{G}\nabla\left[\psi\frac{\partial\psi}{\partial f_i}\right] - \mathscr{G}\left[\frac{\partial\psi}{\partial f_i}\right]\nabla\psi_{\mathrm{solid}} + g_{\mathrm{grav}} \quad (5.21)$$

Now, the pseudopotential ψ is given as:

$$\psi = \sqrt{\frac{2(p_{\text{eos}} - \rho e_s^2)}{G e_s^2}} \tag{5.22}$$

Hence the differentiation of the pseudopotential is:

$$\partial_{f_i}[\psi] = \frac{\partial \psi}{\partial f_i} = \left(\frac{2p_{\text{eos}} - 2\rho e_s^2}{G e_s^2}\right)^{-0.5} \left(e_s^{-2} G^{-1} \frac{\partial p_{\text{eos}}}{\partial f_i} - G^{-1}\right) \tag{5.23}$$

where $\mathscr{G}$ is the continuous version of G. Also, where the pressure equation is given as:

$$p_{\text{eos}} = \rho R T \frac{1 + b\rho/4 + (b\rho/4)^2 - (b\rho/4)^3}{(1 - b\rho/4)^3} - a\rho^2 \tag{5.24}$$

Hence its differentiation w.r.t. the state parameter f_i is given as:

$$\frac{\partial p_{\text{eos}}}{\partial f_i} = -2a\rho + RT \frac{1 + 2b\rho/4 + 3(b\rho/4)^2 - 4(b\rho/4)^3}{(1 - b\rho/4)^3} + (3RT) \frac{b\rho/4 + (b\rho/4)^2 + (b\rho/4)^3 - (b\rho/4)^4}{(1 - b\rho/4)^4} \tag{5.25}$$

5.1.3. Gradient calculation

The gradient calculation follows the same pattern as before. As mentioned previously, bA3 gives us the expression for computing the optimization gradient. Both the cost function ($\mathcal{J}$) and the boundary residue ($\mathcal{P}$) are independent of the design variable α. Thus we obtain:

$$\text{(bA3)} = \frac{\partial \mathcal{L}}{\partial \Psi} \Psi' = \langle \nabla_\Psi \mathcal{J}, \Psi' \rangle_{\mathcal{D} \times \mathcal{T}} = \left\langle \Psi', \underbrace{\alpha' \frac{\partial \mathscr{Y}}{\partial \alpha}\bigg|_{t=t_f}}_{\text{bE1}} + \underbrace{\alpha' \sum_i \frac{\partial \mathcal{R}_i}{\partial \alpha} \mathring{f}_i}_{\text{bE2}} \right\rangle_{\mathcal{D} \times \mathcal{T}} \tag{5.26}$$

Now the term bE1 depends on the cost function acting in the domain of interest is a function of the design variable (and this is most likely the case). Likewise in the term bE2 the design variable only appears in the LBM residue ($\mathcal{R}$) where the equilibrium distribution function, i.e. in the collision term and the EDM forcing term. Hence for the SRT model we can expand bE2 for each node as:

$$\text{(bE2)} = \sum_i w_i \mathring{f}_i \rho \left[1 - \frac{1}{\tau}\right] \left(3\boldsymbol{e}_i \cdot \boldsymbol{u} + 4.5(\boldsymbol{e}_i \cdot \boldsymbol{u})^2 - 1.5(\boldsymbol{u})^2\right) - \sum_i w_i \mathring{f}_i \rho \left(3\boldsymbol{e}_i \cdot \left[\boldsymbol{u} + \frac{\boldsymbol{F}_{\text{T}}}{\rho}\right] + 4.5\left(\boldsymbol{e}_i \cdot \left[\boldsymbol{u} + \frac{\boldsymbol{F}_{\text{T}}}{\rho}\right]\right)^2 - 1.5\left[\boldsymbol{u} + \frac{\boldsymbol{F}_{\text{T}}}{\rho}\right]^2\right) \tag{5.27}$$

The gradient is then used for updating the level set function using the eq. (3.26).

5.2. Topology trait optimization – wettability optimization

For this class of problems we propose to utilize the wettability profile of the topology as a control parameter for optimization. To draw a distinction between modifying the topological structure and modifying its properties/traits we label this algorithm as topology trait optimization. While it is the case for some properties to act across the structure, here we are limited to the surface of the structure as wettability is a surface property. As mentioned in chapter 4, SCMP-SC allows us to quantify wettability in terms of the pseudo-density (of the solid nodes). Hence the design variable here is pseudo-density. The objective is to have the best distribution of contact angle or more precisely the

wettability such that it corresponds to the minimum of a cost function. The Lagrange function for this problem is given as:

$$\mathcal{L}(\rho_w, \mathbf{f}, \mathring{\mathbf{f}}) = \mathcal{J} + \sum_{i=0}^{8} \left\langle \mathcal{R}_i, \mathring{f}_i \right\rangle_{\mathcal{D}\times\mathcal{T}} + \sum_{\beta=\{\text{in,out,bb}\}} \left(\sum_{i=1}^{3} \left\langle \mathcal{P}_{\beta(i)}, \mathring{f}_{\beta(i)} \right\rangle_{\Gamma_\beta \times \mathcal{T}} \right) \tag{5.28}$$

Thus the stationary point can be found as:

$$\mathcal{L}' = \underbrace{\sum_j \frac{\partial \mathcal{L}}{\partial \mathring{f}_j} \mathring{f}_j'}_{\text{bF1}} + \underbrace{\sum_j \frac{\partial \mathcal{L}}{\partial f_j} f_j'}_{\text{bF2}} + \underbrace{\frac{\partial \mathcal{L}}{\partial \rho_w} \rho_w'}_{\text{bF3}} = 0 \tag{5.29}$$

5.2.1. Derivation of the adjoint-state model

As the simulation model (described by the LBM residue $\mathcal{R}$) remains the same, the adjoint-state model (described by the term bF2) also remains unchanged. Hence we refrain from repeating the same derivation. The only changes required to obtain the new optimization algorithm is a difference in the calculation of the gradient of the cost function and a difference update step.

5.2.2. Gradient calculation

Here the variable for optimization is different than the previous case. This will change the characteristic of the gradient that will be found. Below are some observations regarding this optimization algorithm:

- Unlike the previous (topology optimization) problems where we would like to see the gradient on all nodes (even on the solid nodes as it could be interesting for removing some solid), in this case we would only be interested to observe the gradient in the solid node. This is because here we deal with a solid property or actually with a perceived attribution of the property to the solid via the pseudo-density.
- Ideally in this case we would want the dynamics of the fluid domain dictating the change in the nature of the solid and hence somehow connecting with the cost function gradient in the fluid. More specifically, we intend to modify only the strength of the fluid-solid interactions between the neighboring fluid-solid node pair. For a fluid node this would be a fraction of its total interparticular force components.
- Thus the only manner of connecting the physical solution for the fluids to the solids would be therefore to consider (from the point of view of the solid node) that the gradient of cost function at a local solid node depends on the contributions/effects of the surrounding fluid nodes. Thus gradient would be non-zero only at Γ_s i.e. only the boundary nodes thus having surface contact angle ($\theta(\rho_w)$) defined.
- For the current case as the variables does not remain the same (i.e. ρ_w instead of α) the meaning of the gradient also changes. In other words if the gradient of the cost function previously decided the solidness, now it decides the strength of the solid-fluid interaction force and hence the contact angle (which is a byproduct).

For the purpose of the derivation of the cost function gradient in this context, let us define:

- $\mathcal{D}_f$ the domain where fluid stands (either in liquid or vapor state);
- $\mathcal{D}_s$ the domain where solid stands;
- $\mathcal{D}$ which is the full domain gathering both fluid and solid domains, ie $\mathcal{D}_f \cup \mathcal{D}_s = \mathcal{D}$ and $\mathcal{D}_f \cap \mathcal{D}_s = \emptyset$;

- $\mathcal{D}_{\mathrm{f}}^{\bigstar}$ is the restriction of $\mathcal{D}_{\mathrm{f}}$ which stands just next to the solid part:

$$\mathcal{D}_{\mathrm{f}}^{\bigstar} = \left\{ \eta \in \mathcal{D}_{\mathrm{f}} \mid \exists\ \vartheta \in \mathcal{D}_{\mathrm{s}} \text{ such that } |\eta - \vartheta| \leq \sqrt{2} \right\}$$

- $\overline{\mathcal{D}_{\mathrm{f}}^{\bigstar}}$ is the complement of $\mathcal{D}_{\mathrm{f}}^{\bigstar}$ in $\mathcal{D}_{\mathrm{f}}$;

- $\mathcal{D}_{\mathrm{s}}^{\bigstar}$ is the restriction of $\mathcal{D}_{\mathrm{s}}$ which stands just next to the fluid part:

$$\mathcal{D}_{\mathrm{s}}^{\bigstar} = \left\{ \eta \in \mathcal{D}_{\mathrm{s}} \mid \exists\ \vartheta \in \mathcal{D}_{\mathrm{f}} \text{ such that } |\eta - \vartheta| \leq \sqrt{2} \right\}$$

- $\overline{\mathcal{D}_{\mathrm{s}}^{\bigstar}}$ is the complement of $\mathcal{D}_{\mathrm{s}}^{\bigstar}$ in $\mathcal{D}_{\mathrm{s}}$;

- $\mathcal{D}^{\bigstar}$ is the domain on the solid-fluid interface: $\mathcal{D}^{\bigstar} = \mathcal{D}_{\mathrm{f}}^{\bigstar} \cup \mathcal{D}_{\mathrm{s}}^{\bigstar}$.

The control variable is the wettability of the solid phase confined next to the fluid phase $\rho_{\mathrm{w}} : \mathcal{D}_{\mathrm{s}}^{\bigstar} \to \mathbb{R}$. There is no much constraint on the regularity of this control variable except that it should be finite. Thus, a *natural* space that can be chosen when *extracting* the cost function gradient is $\mathcal{D}_{\mathrm{s}}^{\bigstar}$ space which is a L_2 space.

Definition 5.2.1. The following L_2 spaces are associated with their corresponding inner products.

$$\int_{\mathcal{D}_{\mathrm{f}}^{\bigstar}} \mathcal{U}\mathcal{V}\, \mathrm{d}\boldsymbol{r} = \langle \mathcal{U}, \mathcal{V} \rangle_{\mathcal{D}_{\mathrm{f}}^{\bigstar}} \tag{5.30}$$

$$\int_{t=0}^{t_f} \int_{\mathcal{D}_{\mathrm{f}}^{\bigstar}} \mathcal{U}\mathcal{V}\, \mathrm{d}\boldsymbol{r}\, \mathrm{d}t = \langle \mathcal{U}, \mathcal{V} \rangle_{\mathcal{D}_{\mathrm{f}}^{\bigstar} \times \mathcal{T}} \tag{5.31}$$

$$\int_{\mathcal{D}_{\mathrm{s}}^{\bigstar}} \mathcal{U}\mathcal{V}\, \mathrm{d}\boldsymbol{r} = \langle \mathcal{U}, \mathcal{V} \rangle_{\mathcal{D}_{\mathrm{s}}^{\bigstar}} \tag{5.32}$$

$$\int_{0}^{t_f} \int_{\mathcal{D}_{\mathrm{s}}^{\bigstar}} \mathcal{U}\mathcal{V}\, \mathrm{d}\boldsymbol{r}\, \mathrm{d}t = \langle \mathcal{U}, \mathcal{V} \rangle_{\mathcal{D}_{\mathrm{s}}^{\bigstar} \times \mathcal{T}} \tag{5.33}$$

The wettability control variable ρ_{w} is involved in the forward model R_i via the force $\boldsymbol{F}_{\mathrm{T}}$ which is in turn involved in the forcing term $\mathring{\mathscr{F}}_{\mathrm{edm},i}$ via $\widehat{f_j^{eq,+}}$. Thus the only source terms that is explicit functions of the wettability:

$$\boldsymbol{F}_{\mathrm{s}} = \boldsymbol{F}_{\mathrm{s}}(\eta \in \mathcal{D}_{\mathrm{f}}^{\bigstar}) = -G\psi(\eta) \sum_{\substack{k \\ \vartheta_k = \eta + \Delta t \boldsymbol{e}_k \in \mathcal{D}_{\mathrm{s}}^{\bigstar} \\ |\vartheta_k - \eta| \leq \sqrt{2}}} w_k \psi(\vartheta_k) \boldsymbol{e}_k \tag{5.34}$$

We use the notation $\boldsymbol{F}_{\mathrm{s}} = \boldsymbol{F}_{\mathrm{s}}(\eta \in \mathcal{D}_{\mathrm{f}}^{\bigstar})$ because the quantity $\boldsymbol{F}_{\mathrm{s}}$ depends on ρ_{w}, which is calculated for all $\eta \in \mathcal{D}_{\mathrm{f}}^{\bigstar}$, also involves locations in the vicinity of η, i.e. for $\vartheta \in \mathcal{D}_{\mathrm{s}}^{\bigstar}$, if the condition $|\vartheta_k - \eta| \leq \sqrt{2}$ is satisfied.

In the process of cost function gradient extraction, we use the following:

$$\frac{\partial \mathcal{L}}{\partial \rho_{\mathrm{w}}} \rho_{\mathrm{w}}' = \langle \nabla_{\rho_{\mathrm{w}}} \mathcal{J}, \rho_{\mathrm{w}}' \rangle_{\mathcal{D}_{\mathrm{s}}^{\bigstar} \times \mathcal{T}} = \sum_i \left\langle \frac{\partial R_i}{\partial \rho_{\mathrm{w}}} \rho_{\mathrm{w}}', \mathring{f}_i^{\dagger} \right\rangle_{\mathcal{D}_{\mathrm{f}}^{\bigstar} \times \mathcal{T}} \quad \forall \rho_{\mathrm{w}} \in \mathcal{D}_{\mathrm{s}}^{\bigstar} \times \mathcal{T} \tag{5.35}$$

The differentiation of $\widehat{f_j^{eq,+}}$ with respect to the control variable ρ_{w} gives:

$$\frac{\partial R_j}{\partial \rho_{\mathrm{w}}} = -\frac{\partial}{\partial \rho_{\mathrm{w}}} \widehat{f_j^{eq,+}} \tag{5.36}$$

Unlike the 1st optimization test case, $\alpha(\Psi)$ is not a variable of optimization and hence we ignore this variable henceforth.

$$\frac{\partial}{\partial\rho_{\mathrm{w}}}\widehat{f_j^{eq,+}} = w_j\Bigg(3\boldsymbol{e}_j\cdot\partial_{\rho_{\mathrm{w}}}[\boldsymbol{F}_{\mathrm{T}}] + \frac{9}{2}\Big((\boldsymbol{e}_j\cdot\boldsymbol{u})\Big(2\boldsymbol{e}_j\cdot\partial_{\rho_{\mathrm{w}}}[\boldsymbol{F}_{\mathrm{T}}]\Big) + 2\bigg(\boldsymbol{e}_j\cdot\frac{\boldsymbol{F}_{\mathrm{T}}}{\rho}\bigg)\Big(\boldsymbol{e}_j\cdot\partial_{\rho_{\mathrm{w}}}[\boldsymbol{F}_{\mathrm{T}}]\Big)\Big) - \frac{3}{2}\bigg(2\boldsymbol{u}\cdot\partial_{\rho_{\mathrm{w}}}[\boldsymbol{F}_{\mathrm{T}}] + 2\frac{\boldsymbol{F}_{\mathrm{T}}}{\rho}\partial_{\rho_{\mathrm{w}}}[\boldsymbol{F}_{\mathrm{T}}]\bigg)\Bigg) \tag{5.37}$$

The differentiation of $\boldsymbol{F}_{\mathrm{T}}$ wrt ρ_{w} is:

$$\partial_{\rho_{\mathrm{w}}}[\boldsymbol{F}_{\mathrm{T}}] = \frac{\partial\boldsymbol{F}_{\mathrm{T}}}{\partial\rho_{\mathrm{w}}}(\eta\in\mathcal{D}_{\mathrm{f}}^{\bigstar}) = -G\psi(\eta)\sum_{\substack{k\\ \vartheta_k=\eta+\Delta t\boldsymbol{e}_k\in\mathcal{D}_{\mathrm{s}}^{\bigstar}\\ |\vartheta_k-\eta|\leq\sqrt{2}}} w_k\partial_{\rho_{\mathrm{w}}}[\psi(\vartheta_k)]\boldsymbol{e}_k \tag{5.38}$$

where only for the force component do we have the ψ depending on the ρ_{w}:

$$\partial_{\rho_{\mathrm{w}}}[\psi] = \frac{\partial\psi}{\partial\rho_{\mathrm{w}}} = \left(\frac{2p_{\mathrm{eos}}-2\rho e_s^2}{Ge_s^2}\right)^{-0.5}\left(e_s^{-2}G^{-1}\frac{\partial p_{\mathrm{eos}}}{\partial\rho_{\mathrm{w}}} - G^{-1}\right) \tag{5.39}$$

where

$$\frac{\partial p_{\mathrm{eos}}}{\partial\rho_{\mathrm{w}}} = -2a\rho_{\mathrm{w}} + RT\frac{1+2b\rho_{\mathrm{w}}/4+3(b\rho_{\mathrm{w}}/4)^2-4(b\rho_{\mathrm{w}}/4)^3}{(1-b\rho_{\mathrm{w}}/4)^3} - 3RT\frac{b\rho_{\mathrm{w}}/4+(b\rho_{\mathrm{w}}/4)^2+(b\rho_{\mathrm{w}}/4)^3-(b\rho_{\mathrm{w}}/4)^4}{(1-b\rho_{\mathrm{w}}/4)^4} \tag{5.40}$$

We replace the discrete summation in forcing terms by its continuous counterpart (the wide tilde over the quantity designs the continuous quantity), in order to perform later on a permutation of integrals for further simplification:

$$\boldsymbol{F}_{\mathrm{s}}\approx\widetilde{\boldsymbol{F}_{\mathrm{s}}} = -G\psi(\eta)\int_{\substack{\vartheta\in\mathcal{D}_{\mathrm{s}}^{\bigstar}\\ |\vartheta-\eta|\leq\sqrt{2}}}\psi(\vartheta)\boldsymbol{e}\ \mathrm{d}\vartheta \tag{5.41}$$

Now total force ($\boldsymbol{F}_{\mathrm{T}}$) consists of body force ($\boldsymbol{F}_{\mathrm{b}}$) and fluid-solid particle force ($\boldsymbol{F}_{\mathrm{s}}$). Now as body force is independent of ρ_{w}, the differentiation leaves with the derivative of the Shan and Chen particular force ($\boldsymbol{F}_{\mathrm{s}}$). Hence we can write:

$$\frac{\partial\boldsymbol{F}_{\mathrm{T}}}{\partial\rho_{\mathrm{w}}}\approx\frac{\widetilde{\partial\boldsymbol{F}_{\mathrm{T}}}}{\partial\rho_{\mathrm{w}}} = -G\psi(\eta)\int_{\substack{\vartheta\in\mathcal{D}_{\mathrm{s}}^{\bigstar}\\ |\vartheta-\eta|\leq\sqrt{2}}}\partial_{\rho_{\mathrm{w}}}[\psi(\vartheta)]\boldsymbol{e}\ \mathrm{d}\vartheta \tag{5.42}$$

Inserting this latter equation (5.42) into the differentiated equation (5.36) involved in (5.35), we have $\forall\rho_{\mathrm{w}}'\in\mathcal{D}_{\mathrm{s}}^{\bigstar}$:

$$\langle\widetilde{\nabla}_{\rho_{\mathrm{w}}}\mathcal{J},\rho_{\mathrm{w}}'\rangle_{\mathcal{D}_{\mathrm{s}}^{\bigstar}} = -\int_{t=0}^{t_f}\sum_j\int_{\eta\in\mathcal{D}^{\bigstar}} w_j\mathring{f}_j\bigg(3\boldsymbol{e}_j+9\boldsymbol{e}_j\bigg(\boldsymbol{e}_j\cdot\boldsymbol{u}+\frac{\boldsymbol{e}_j\cdot\boldsymbol{F}_{\mathrm{T}}}{\rho}\bigg)-3\bigg(\boldsymbol{u}+\frac{\boldsymbol{F}_{\mathrm{T}}}{\rho}\bigg)\bigg)\cdot \frac{\partial\widetilde{\boldsymbol{F}_{\mathrm{T}}}}{\partial\rho_{\mathrm{w}}}\rho_{\mathrm{w}}'\ \mathrm{d}\eta\ \mathrm{d}t \tag{5.43}$$

After developing and factorization of the derivative term, we get:

$$\langle\widetilde{\nabla}_{\rho_{\mathrm{w}}}\mathcal{J},\rho_{\mathrm{w}}'\rangle_{\mathcal{D}_{\mathrm{s}}^{\bigstar}} = -\int_{t=0}^{t_f}\sum_j\int_{\eta\in\mathcal{D}^{\bigstar}} w_j\mathring{f}_j\bigg(3\boldsymbol{e}_j+9\boldsymbol{e}_j\bigg(\boldsymbol{e}_j\cdot\boldsymbol{u}+\frac{\boldsymbol{e}_j\cdot\boldsymbol{F}_{\mathrm{T}}}{\rho}\bigg)-3\bigg(\boldsymbol{u}+\frac{\boldsymbol{F}_{\mathrm{T}}}{\rho}\bigg)\bigg)\cdot \left(-G\psi(\eta)\int_{\substack{\vartheta\in\mathcal{D}_{\mathrm{s}}^{\bigstar}\\ |\vartheta-\eta|\leq\sqrt{2}}}\partial_{\rho_{\mathrm{w}}}[\psi(\vartheta)]\rho_{\mathrm{w}}'\boldsymbol{e}\ \mathrm{d}\vartheta\right)\mathrm{d}\eta\ \mathrm{d}t \tag{5.44}$$

Now the condition on $|\vartheta - \eta|$ is applied on the other integral and we write:

$$\langle \widetilde{\nabla}_{\rho_w} \mathcal{J}, \rho'_w \rangle_{\mathcal{D}_s^\bigstar} = -\int_{t=0}^{t_f} \sum_j \int_{\substack{\eta \in \mathcal{D}^\bigstar \\ |\vartheta-\eta| \le \sqrt{2}}} w_j \mathring{f}_j \left(3\boldsymbol{e}_j + 9\boldsymbol{e}_j \left(\boldsymbol{e}_j \cdot \boldsymbol{u} + \frac{\boldsymbol{e}_j \cdot \boldsymbol{F}_T}{\rho} \right) - 3\left(\boldsymbol{u} + \frac{\boldsymbol{F}_T}{\rho} \right) \right) \cdot \left(-G\psi(\eta) \int_{\vartheta \in \mathcal{D}_s^\bigstar} \partial_{\rho_w}[\psi(\vartheta)] \rho'_w \boldsymbol{e} \ \mathrm{d}\vartheta \right) \mathrm{d}\eta \ \mathrm{d}t \tag{5.45}$$

We further restrict of the integral to the neighboring fluid domain can be applied:

$$\langle \widetilde{\nabla}_{\rho_w} \mathcal{J}, \rho'_w \rangle_{\mathcal{D}_s^\bigstar} = -\int_{t=0}^{t_f} \sum_j \int_{\substack{\eta \in \mathcal{D}_f^\bigstar \\ |\vartheta-\eta| \le \sqrt{2}}} w_j \mathring{f}_j \left(3\boldsymbol{e}_j + 9\boldsymbol{e}_j \left(\boldsymbol{e}_j \cdot \boldsymbol{u} + \frac{\boldsymbol{e}_j \cdot \boldsymbol{F}_T}{\rho} \right) - 3\left(\boldsymbol{u} + \frac{\boldsymbol{F}_T}{\rho} \right) \right) \cdot \left(-G\psi(\eta) \int_{\vartheta \in \mathcal{D}_s^\bigstar} \partial_{\rho_w}[\psi(\vartheta)] \rho'_w \boldsymbol{e} \ \mathrm{d}\vartheta \right) \mathrm{d}\eta \ \mathrm{d}t \tag{5.46}$$

This is possible as only nodes would contribute to the fluid-solid interaction force and hence everywhere else in the domain it (the gradient) is zero. Next we modify the order the integral symbols:

$$\langle \widetilde{\nabla}_{\rho_w} \mathcal{J}, \rho'_w \rangle_{\mathcal{D}_s^\bigstar} = \int_{t=0}^{t_f} \sum_j \int_{\vartheta \in \mathcal{D}_s^\bigstar} G \partial_{\rho_w}[\psi(\vartheta)] \rho'_w \int_{\substack{\eta \in \mathcal{D}_f^\bigstar \\ |\vartheta-\eta| \le \sqrt{2}}} w_j \mathring{f}_j(\eta) \left(3\boldsymbol{e}_j + 9\boldsymbol{e}_j \left(\boldsymbol{e}_j \cdot \boldsymbol{u}(\eta) + \frac{\boldsymbol{e}_j \cdot \boldsymbol{F}_T(\eta)}{\rho(\eta)} \right) - 3\left(\boldsymbol{u}(\eta) + \frac{\boldsymbol{F}_T(\eta)}{\rho(\eta)} \right) \right) \cdot (\psi(\eta)\boldsymbol{e}) \ \mathrm{d}\eta \ \mathrm{d}\vartheta \ \mathrm{d}t \tag{5.47}$$

Finally, we permute of locations (symbols) between η and ϑ.

$$\langle \widetilde{\nabla}_{\rho_w} \mathcal{J}, \rho'_w \rangle_{\mathcal{D}_s^\bigstar} = \int_{t=0}^{t_f} \sum_j \int_{\eta \in \mathcal{D}_s^\bigstar} G \partial_{\rho_w}[\psi(\eta)] \rho'_w \int_{\substack{\vartheta \in \mathcal{D}_f^\bigstar \\ |\vartheta-\eta| \le \sqrt{2}}} w_j \mathring{f}_j(\vartheta) \left(3\boldsymbol{e}_j + 9\boldsymbol{e}_j \left(\boldsymbol{e}_j \cdot \boldsymbol{u}(\vartheta) + \frac{\boldsymbol{e}_j \cdot \boldsymbol{F}_T(\vartheta)}{\rho(\vartheta)} \right) - 3\left(\boldsymbol{u}(\vartheta) + \frac{\boldsymbol{F}_T(\vartheta)}{\rho(\vartheta)} \right) \right) \cdot (\psi(\vartheta)\boldsymbol{e}) \ \mathrm{d}\vartheta \ \mathrm{d}\eta \ \mathrm{d}t \tag{5.48}$$

This gives, for all $\eta \in \mathcal{D}_s^\bigstar$:

$$\widetilde{\nabla}_{\rho_w} \mathcal{J} = \int_{t=0}^{t_f} \sum_j G \partial_{\rho_w}[\psi(\eta)] \int_{\substack{\vartheta \in \mathcal{D}_f^\bigstar \\ |\vartheta-\eta| \le \sqrt{2}}} w_j \mathring{f}_j \left(3\boldsymbol{e}_j + 9\boldsymbol{e}_j \left(\boldsymbol{e}_j \cdot \boldsymbol{u} + \frac{\boldsymbol{e}_j \cdot \boldsymbol{F}_T}{\rho} \right) - 3\left(\boldsymbol{u} + \frac{\boldsymbol{F}_T}{\rho} \right) \right) \cdot (\psi(\vartheta)\boldsymbol{e}) \ \mathrm{d}\vartheta \ \mathrm{d}t \tag{5.49}$$

The discrete version of this gradient is the one we compute:

$$\nabla_{\rho_w} \mathcal{J}\Big|_{\boldsymbol{r}=\eta} = \sum_t G \partial_{\rho_w}[\psi^t(\eta)] \sum_j \sum_{\substack{k \\ \vartheta_k = \eta + \Delta t \boldsymbol{e}_k \in \mathcal{D}_f^\bigstar \\ |\vartheta_k - \eta| \le \sqrt{2}}} w_j \mathring{f}_j^t(\vartheta_k) \left(3\boldsymbol{e}_j + 9\boldsymbol{e}_j \left(\boldsymbol{e}_j \cdot \boldsymbol{u}^t(\vartheta_k) + \frac{\boldsymbol{e}_j \cdot \boldsymbol{F}_T^t(\vartheta_k)}{\rho^t(\vartheta_k)} \right) - 3\left(\boldsymbol{u}^t(\vartheta_k) + \frac{\boldsymbol{F}_T^t(\vartheta_k)}{\rho^t(\vartheta_k)} \right) \right) \cdot \left(\psi^t(\vartheta_k) w_k \boldsymbol{e}_k \right) \tag{5.50}$$

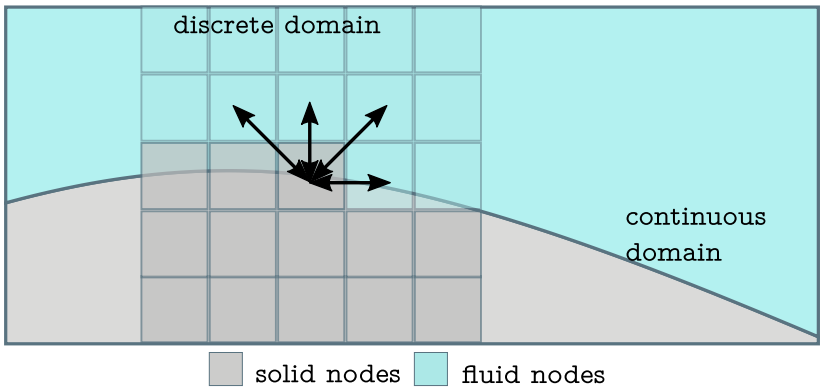

Figure 5.1: Illustration: Contribution of the fluid-solid interaction force to a particular solid node for obtaining the gradient of cost function ($\nabla_{\rho_w}\mathcal{J}$)

$$\nabla_{\rho_w}\mathcal{J}\Big|_{\boldsymbol{r}=\eta} = \sum_t G\partial_{\rho_w}[\psi^t(\eta)] \sum_{\substack{j \\ \boldsymbol{e}_j\cdot\boldsymbol{e}_k=-1 \\ \vartheta_k=\eta+\Delta t\boldsymbol{e}_k\in\mathcal{D}_f^\bigstar \\ |\vartheta_k-\eta|\le\sqrt{2}}} w_j \mathring{f}_j^t(\vartheta_k)\left(3\boldsymbol{e}_j + 9\boldsymbol{e}_j\left(\boldsymbol{e}_j\cdot\boldsymbol{u}^t(\vartheta_k) + \frac{\boldsymbol{e}_j\cdot\boldsymbol{F}_T^t(\vartheta_k)}{\rho^t(\vartheta_k)}\right)\right.$$
$$\left. -3\left(\boldsymbol{u}^t(\vartheta_k) + \frac{\boldsymbol{F}_T^t(\vartheta_k)}{\rho^t(\vartheta_k)}\right)\right)\cdot\left(\psi^t(\vartheta_k)w_k\boldsymbol{e}_k\right) \quad (5.51)$$

Thus we consider for a solid node η the fluid-solid contributions of all its neighboring fluid nodes as shown in fig. 5.1. Finally we utilize this gradient for updating the wettability via the gradient descent optimizer using eq. (4.4).

5.3. Conclusions

Here we demonstrate theoretical novelty by defining the new adjoint-state model for SCMP-SC for topology optimization. We differentiate the interparticular force where the pressure is defined using the realistic Carnahan-Starling equation of state. After we explore the feasibility of developing a wettability optimizer where the gradient is computed using the adjoint-state method for the optimization of wettability profile. One of the novelettes (in wettability optimization) is to obtain the gradient value on solid node due to neighboring fluid nodes. Thereby the change in wettability is coupled to physical changes/ behavior of the surrounding fluids. We spend significant amount of time in the implementation of these adjoint-state models, but our results are currently deemed unsatisfactory (as these could not be verified) at the time of writing this thesis.

Chapter 6

Conclusion & perspectives

The context for the selection of the topic of the thesis was a research interest (of the local team at LTEN, Nantes Université) in proton exchange membrane fuel cell. The fuel cell is deemed as a promising technology though it poses certain challenges for a wider commercial adoption. One such challenge is to achieve a water balance in the gas diffusion layers of the fuel cell. As water released after consummation of H_2 hydrates the membrane (keeping its proton resistivity at the minimum), the efficiency of the cell is maintained high. If the excess water is not channeled out, it would choke out the gas supply (H_2 and O_2) to the catalytic layers, hence shutting down the fuel cell reaction. Thus the initial objective of the thesis was to design/modify the gas diffusion layer (GDL) based on a mathematical tool (i.e. the topology optimization). In other words one is required to build an optimization algorithm or an optimizer which is competent for suggesting designs based on an objective function (i.e. the cost function).

Any optimizer requires a physical model for capturing the relevant phenomenon. The numerical simulation for multiphase/interfacial flows could be divided into two categories: top-to-bottom approach model and bottom-to-top approach model. In the former category we have the macroscopic models often coupling the Navier-Stokes equation and interface tracking methods the most widely used among these models are the Volume of fluid (VOF) and the level set models. In the latter category the interaction forces are prescribed from which we derive macroscopic parameters, common methods are: molecular dynamics and mesoscopic methods like Van der Waal model and the lattice Boltzmann method.

The most extensively used multiphase LBM model i.e. the pseudopotential model exhibits a diffusive interface being devoid of the interface tracking equations. The interface of this model is a result of the interparticular (i.e. mesoscopic) forces. The pseudopotential model is known for its simplicity and efficiency as it does not employ the Poisson pressure equation. Thus the data from the neighboring nodes is only required for calculation of interparticular forces. This allows us to leverage the otherwise highly paralleizable algorithm, running the codes on NVIDIA GPU cards using the `CUDA` interface. Depending upon the problem at hand, one could accelerate the codes upward of 50 times when compared to a `C` program running on a single processor. LBM is as such better suited for GPU styled paralleization i.e. huge amount of threads running concurrently. Though the thesis is silent on the coding aspect, it plays an important role in deciding the appropriate LBM model for optimization. In summary we choose the single component multiphase pseudopotential (SCMP-SC) model for modeling the physics which would later be fed as an input to the optimization algorithm. It is commonplace for an optimizer to require multiple reruns of the physical simulation (i.e. forward problem), which all the more underlines the requirement of a lightweight solver.

Further in chapter 2, various extension or modification to SCMP-SC (like multirange model, forcing schemes, equation of state (EOS), higher order discretization of pseudopotential and etc) are discussed. Here we choose the Carnahan-Starling (CS) EOS and exact difference method forc-

ing scheme (EDM) for greater stability and lower spurious currents. The parameter values fixed both *a priori* and *a posteriori* the physical simulations aid in comparing the performance of different modification/extension. To summarize, the multirange model ($\mathscr{H}_2$) in addition with the CS EOS and EDM forcing scheme performs consistently better having lower spurious currents which reflects in the stability of the forward problem. The results regarding the Laplace law and the correlation between static contact angle (θ_{stat}) and pseudo-density (ρ_{w}) for the wall are consistent across different models. These parameter values are further used for replicating/modeling complex phenomena i.e. setup a simulation. After setting up the parameter values we demonstrate the motion of a droplet on an ideal horizontal wettability gradient surface (WGS). The benchmark simulation for validating the competence of SCMP-SC for modeling droplet motion is to model asymptotic velocity on a low intensity WGS. Here very small hydrophilic wettability gradients we obtain a linear correlation between the migration/asymptotic velocity and the gradient of the cosine of the static contact angle as indicted in eq. (2.100). Also the constant of proportionality $\alpha_v = 0.28$ (in eq. (2.100)) was recovered for hydrophilic wettability distributions against a value of $\alpha_v = 0.33$ obtained in [1].

Next, we validate the rise of the liquid column in the capillary tube by measuring the error (w.r.t a real world air-water capillary height, via dimensionless numbers) after the column attains the Jurin height. Here we observe the compressibility of the vapor phase for the SCMP-SC, which was mitigated by increasing the vapor kinematic viscosity by 40%. Now as the diameter of the capillary tube increases (for a low viscous wetting fluid) then, we observe capillary oscillations in the height of the liquid column. These oscillations (with increasing tube diameter) increases both in amplitude (w.r.t the Jurin height) and frequency and is an indicator for the presence of an inertial component of the initial acceleration of the meniscus when the wetting fluid interface is introduced in the capillary tube. Thus we demonstrate the ability of the SCMP-SC solver/model to capture non-linear or dynamic phenomenon.

After these simulations we started working with the open boundaries for the SCMP-SC model, which were essential for modeling the GDL. The major cases modeled were the normal tube (for drainage and imbibition), the droplet in a channel flow, the stepped tube and the preferred pathway tube. We chose the continuum boundaries (Neumann and convective BCs) for the outlets and used ZH and Ladd's BCs for the velocity inlets. The results obtained for the aforementioned simulations/cases are trustworthy only till the interface makes its way towards the outlet boundary. Unphysical effects (i.e. a plurality of numerical artifacts) were observed mostly as the interface reached in the vicinity of the boundary or crossed the boundary. Apart from this *evaporation* of the liquid phase was observed at the interfacial fronts exposed to the outlets (only in the initial phase of the simulation). Many workarounds were attempted but to no avail. After a significant time and effort, the SCMP-SC provided by OpenLB (i.e. $\mathscr{H}_4$) was employed to recreate these unphysical effects. Now this was partially successful as the pressure ZH caused *evaporation* but an apples to apples comparison was difficult due to lack of the Neumann BC and the instability of the convective BC (both for the in-house and the OpenLB codes). At any rate, at the time of writing this thesis we remain unsuccessful in replicating the results of ref. [2] and ref. [3].

The porous media simulations for SCMP-SC ($\mathscr{H}_1$) has its own challenges, apart from the unphysical effects observed due to the outlet boundaries the porous media simulation turn out to be trustworthy and stable for simple porous media structures and for higher capillary number flows. For these flows we observed linear saturation curve barring phenomena such as the Haines jump. For very low capillary numbers ($\mathrm{Ca} \leq 10^{-3}$), we observe condensation of liquid droplet at the outlet, collapse of the vapor bubbles and instability of the code. Realizing the limitations of the current SCMP-SC algorithm, we repeated the same test case using MCMP-SC (i.e. $\mathscr{H}_5$) for $\log|\mathrm{Ca}| = -4.25$ and finally obtained the desired result similar to the experimental results. These limitations of the SCMP-SC scaled down the initial objective (of the thesis) of the working on the GDL (porous media–with the PEMFC operating in the capillary fingering regime (refer fig. 2.27)–with the open boundary conditions) to working on an application where the open boundaries are not present (periodic boundaries) or are not relevant to the application.

In chapter 3, after a brief introduction, we began by exploring the concepts regarding the topol-

ogy optimization algorithm, i.e. the adjoint-state method, level-set function, line search optimization and the optimizers. Here the only difference as compared to ref. [40] is that we perform the optimization for the compressible flow which remains essential having multiphase simulations in mind. The level-set function (LSF) Ψ is used for representation of the solid domain ($\mathcal{D}_s$), i.e. wall boundaries. Here the LSF is not advected as is common for methods using LSF. But rather it acts as a control variable which registers the cumulative change due to all the cost function gradients calculated by an iterative optimization algorithm. In other words, the final level-set is $\Psi^{(\dagger)} = \Psi^{(0)} - \xi^{(0)}\nabla\mathcal{J}^{(0)} - \cdots - \xi^{(n_{\text{opt}})}\nabla\mathcal{J}^{(n_{\text{opt}})}$; where n_{opt} is the optimization iteration number when convergence is achieved, ξ is the step size used for a gradient of the cost function (i.e. $\nabla\mathcal{J}$). Here the gradient of cost function is calculated using the adjoint-state method. The adjoint-state equations are approximately the mirror image of the governing equations of the model for which it is developed (in our case is the LBE). It enables us to compute the gradient with the computational expense of the forward problem. Though it increases the mathematical complexity, its a worthwhile exercise due to enormous speeding up of the optimization algorithm. Here we derive the adjoint-state method using the Lagrange function. The Lagrange function allows us to accumulate the objective/cost function and the constraints (in our case, the only constraint is that the forward problem should be satisfied) to form a kind of multi-objective zero constraint optimization problem. This simplifies the mathematical treatment required for the optimization problem. The objective function as the name suggests is a mathematical articulation which represents an ideal/optimized system for e.g. minimizing entropy would represent an optimized system/process. Once the gradient of the cost function is obtained we use an optimization strategy, i.e. an optimizer in combination with an optional line-search algorithm which should enable us to approach the desired minimum. The optimization algorithm finally described in algorithm 3.

Next we derive the adjoint-state equations from the LBE. This also includes deriving adjoint-state boundary conditions and initial conditions. As LBM is a naturally transient solver, its adjoint-state model is also transient in nature. We discuss its implications by defining the concept of adjoint-state time and also by delineating between forward problem where a transient phenomenon is of interest (TOTFP) and also when only the final steady-state problem is of interest (TOSFP). The algorithm for a TOSFP is later provided (algorithm 4). Lastly we conclude the chapter by demonstrating the competence of the our optimization algorithm by applying it to a 90° pipe-bend case. This problem is a TOSFP problem, where we apply competing components of the cost function i.e. a pressure constraint (which prevents material allocation if the pressure difference were to increase) at the inlet and a porosity constraint (which attempts to allocate material until the maximum porosity defined is not achieved) all over the domain. We observe that material is allocated to the regions with null or minuscule velocities and the directions of the allocation is along the axis of symmetry.

Now deviating from the discourse about topology optimization, in chapter 4, we make use of the finite-difference based gradient optimization algorithm. The objective of this optimization problem was to maximize the speed of the droplet (being propelled due to wettability gradient) on a flat horizontal plate (i.e. a WGS). Here the strategy used for ensuring the robustness of the result is to progressively refine the optimization mesh (by doubling the optimization elements/parameters) when intermediary check for the convergence (of the results) is satisfied. This is the multiscale parameterization as described in [171], which is different from the usual sense in which the term *multiscale* is used. We also utilize dichotomy method for determining the step size (ξ)–i.e. the line search algorithm–for the optimization gradient ($\nabla\mathcal{J}$). At any rate, we suggest an innovate manner of looking into wettability as a control variable for a mathematical optimization algorithm (and) using it conjointly with multiphase LBM solver. This is possible as the pseudopotential model (SCMP-SC) allows for the quantification of wettability in terms of pseudo-density (i.e. the density of the solid/wall). Here again we utilize the $\mathscr{H}_1$ model for the LBM solver.

The cost function employed for this problem computed the average velocity of the droplet based on the center of gravity (CG) of the droplet. While the droplet CG aids in locating the droplet on the flat plate (due motion only along the x-axis), it brings with it the limitation of not capturing the information of the curvature of the droplet. Meaning that droplets having different curvatures could

have the same CG. One must be cognizant of this while determining the destination CG (i.e. the desired CG, this value ($\widetilde{\mathcal{C}}_{\text{drop}}$) is used for applying the constraint such that the droplet reaches the end of the plate). Likewise a time constraint ($\mathcal{J}_{\text{lbm}}^{\max}$) is also applied to ensure that the simulation does not run perpetually if the droplet is stuck and does not reach the desired CG. The value for these constraints are determined after performing a pre-optimization study. Here the performance of five different monotonous wettability profiles fig. 4.2a are analyzed, which also helps in ascertaining good initial wettability profiles (i.e. starting points for the optimization algorithm). In summary we determine that the linear (Υ_{lin}) and the quadratic convex (Υ_{qcv}) profiles are used for initial guesses. Also the overall best performance (among the five different monotonous curves) is observed for the Υ_{qcv} profile. Hence for the global optimum solution for the monotonous curves lies in the vicinity of Υ_{qcv}.

After the determination of the constraint values we proceed with the optimization studies. For the small plate, we demonstrate the competence of the multiscale parameterization (for $L/D = 6.4$ and density ratio of 30) by improving the average velocity of the droplet by 69%, as compared to 17% when computing gradient directly for the finest optimization mesh (i.e. with the most optimization elements). We also observe that the algorithm introduces no wettability gradient (NWG) zones/regions at the initial droplet position (IDP) and the final droplet position (FDP). This enables to concentrate the pull-off potential of the WGS in the intermediate region (IR). Also a peak/surge in wettability gradient is observed at the leading edge (LE) of the droplet at the IDP (with the local wettability gradient spanning 10-20% into the IDP from the LE), which accelerates the droplet into motion. This is followed by a steep decrease of wettability gradient (i.e. the local wettability gradient direction is contrary to droplet motion) which interestingly does not result in the pinning of the droplet (due to droplet momentum). We also initiate the optimization using the quadratic convex (Υ_{qcv}) and cubic convex (Υ_{ccv}) to obtain similar results. Analyzing the performance of Υ_{lin} one can recover the classical result: for constant gradient, when the droplet reaches the hydrophilic region, it tends to spread, increasing the contact surface with the solid and consequently slowing down; the optimized results succeed in preventing this trend, maintaining a higher final velocity.

Next, we vary the droplet size/diameter (D) for optimization studies with a medium plate such that the L/D ratio of 5.12, 6.24 and 8.533 is obtained. Here we observe that the optimized final curves were progressively smoothening with the increase in the L/D ratio. For the lower L/D ratio we observe a peak at or near the LE when the droplet would be in the IDP i.e. a large force/jerk is required for overcoming the inertia of the large droplet. Also bumps of similar magnitude helps to maintain the momentum for the larger droplets. These results are obtained for individual droplet diameter but in many instances we observe droplets having a range of diameters ($D_{\min}$ to $D_{\max}$). Thus we cross-check the performance of each curve for each droplet size and we observe that when the droplet diameter is lower than the diameter for which the optimization results are obtained, then the droplet does not reach the end of plate and gets stuck on the plate mostly where we have wettability gradient in the direction contrary to the droplet motion or a no wettability gradient (NWG) region. Hence this would also become hot-spots for droplet mergers (until such time when $D > D_{\min}$ is satisfied; where $D_{\min}$ is diameter used for optimization) so as to finally observe motion. Hence one should take care that in such instances when the diameter cannot be fixed, the optimization should be carried out using the $D_{\min}$.

After this we present the results for the optimization with the same L/D ratio of 6.4 but with the variation of the plate size i.e. small, medium and large for $T/T_c = 0.75$. Here it is observed that as the plate size is increased the curve becomes more well defined with sharper bumps (peaks and dips). This is despite the fact that the maximum element number remains same ($q_{\max} = 128$) i.e. minimum element size increase from 2 l.u. to 8 l.u.. We also perform a post-optimization study which supports our previous observations. The performance of Υ_2 and Υ_5 is consistent for small and medium plate sizes, while the Υ_4 has the worst performance overall. Hence we can conclude that multiscale optimization when performed on the medium plate size provides us with results i.e. curves that have sufficient resolution. This curves replicate the performance of the higher resolution (large plate size with same L/D ratio) curves for the most part. Hence a pragmatic trade-off in

precision can be made for a reasonable computational effort.

Next we study the sensitivity of the optimization problem to the temperature and relative kinematic viscosity parameters, for a constant L/D ratio of 6.4 and medium plate. Here we observe that with decreasing temperature T that the velocity of droplet increases due increased density ratio. In other words with decreasing temperature the parameter/model sensitivity increases, which results in better/improved prediction and competence of the optimization algorithm. Also in regards, to the relative kinematic viscosity does not vary (to a large extent) the optimization results. In other words this is not an optimization variable or the problem is invariant/independent w.r.t this variable. This concludes the study, excerpts of which is published in the *Physics of fluids* journal.

In chapter 5, we demonstrate theoretical novelty by defining the new adjoint-state model for SCMP-SC for topology optimization. Here we differentiate the interparticular force where the pressure is defined using the realistic Carnahan-Starling equation of state. Next we explore the feasibility of developing a wettability optimizer where the gradient is computed using the adjoint-state method for the optimization of wettability profile. Another novelty (in the wettability optimization) is that the gradient value on solid node is obtained due to neighboring fluid nodes. Thereby the change in wettability is coupled to physical changes/ behavior of the surrounding fluids. We spend significant amount of time in the implementation of these adjoint-state models, but our results are currently deemed unsatisfactory (as these could not be verified) at the time of writing this thesis. This conclude the summary of the thesis.

Contribution of this thesis

Briefly, the contributions of this thesis are:

1. Using multiscale optimizer for discovering optimized wettability profiles of a horizontal plate (for droplet motion on the plate) i.e. a WGS.
2. Developing wettability optimizer, using adjoint-state model for SCMP-SC.
3. Developing topology optimizer, using adjoint-state model for SCMP-SC.

What's next?

The future research directions based on the results of the current thesis are:

- To validate the adjoint-state model results for both topology and wettability optimization
- To validate experimentally the results of the multiscale optimizer pertaining to the maximization of the velocity of the droplet on a flat horizontal surface.
- To expand the simulation domain to 3D for applying topology optimization in porous media. The current 2D simulations lack an assessment on fluid motion beyond a plane, which is essential especially for optimization. An example of a limiting case would be if two points are connected by the liquid phase in 2D (which would otherwise be modeled as a *finger* in 3D) to form a continuous flow circuit, then, it would naturally be modeled as a barrier for the vapor flow, which may not be the case in the 3D simulation.
- To apply topology optimization for heat exchanges with phase change. Work in this direction has already commenced experimentally and numerically (using the phase-change model [3] derived from the single component multiphase pseudopotential model).
- Working on implementing open boundary conditions for an SCMP-SC model and also including an MCMP-SC model which are better suited for porous media simulations.

Appendix A

LBM boundary conditions

A.1. Zou & He boundary condition

This boundary condition (BC) was originally suggested by [65] in 1996.

A.1.1. Velocity inlet BC

Let us assume a rectangular domain with the inlet at the west, as shown in fig. 2.3. So, we have 3 unknown distribution functions protruding inwards, i.e. f_1, f_5 and f_8. It follows that the density at those locations are unknown. In this case, the knowledge of the velocity at the inlet is required to formulate expressions accordingly and find the unknowns. The first expressions are:

$$\rho = \sum_i f_i \quad \text{and} \quad \boldsymbol{u} = \frac{1}{\rho}\sum_i \boldsymbol{e}_i f_i$$

The other expression is obtained by assuming bounceback is still correct for the non-equilibrium part of the particle distribution, normal to the boundary. Hence, we obtain:

$$f_1 - f_1^{\text{eq}} = f_3 - f_3^{\text{eq}} \tag{A.1}$$

$$f_1 = f_3 - f_3^{\text{eq}} + f_1^{\text{eq}} \tag{A.2}$$

$$\text{Now,} \quad f_i^{\text{eq}} = w_i \rho(r,t)\left(1 + \frac{\boldsymbol{e_i}\cdot\boldsymbol{u}}{e_s^2} + \frac{(\boldsymbol{e_i}\cdot\boldsymbol{u})^2}{2e_s^4} - \frac{(\boldsymbol{u})^2}{2e_s^2}\right) \tag{A.3}$$

$$\text{therefore,} \quad f_1^{\text{eq}} = \frac{\rho}{9}\left(1 + 3u_x + \frac{9}{2}u_x^2 - \frac{3}{2}u_x^2\right) \tag{A.4}$$

$$\text{and} \quad f_3^{\text{eq}} = \frac{\rho}{9}\left(1 - 3u_x + \frac{9}{2}u_x^2 - \frac{3}{2}u_x^2\right) \tag{A.5}$$

Introducing eqs. (A.4) and (A.5) into eq. (A.2), we get:

$$\boxed{f_1 = f_3 + \frac{2}{3}\rho u_x} \tag{A.6}$$

The other equations can be expanded to obtain:

$$\rho = f_0 + f_1 + f_2 + f_3 + f_4 + f_5 + f_6 + f_7 + f_8 \tag{A.7}$$

$$\rho u_x = f_1 - f_3 + f_5 - f_6 - f_7 + f_8 \tag{A.8}$$

$$\rho u_y = f_2 - f_4 + f_5 + f_6 - f_7 - f_8 \tag{A.9}$$

Putting eq. (A.6) into eq. (A.8), we get:

$$\rho u_x = f_3 + \frac{2}{3}\rho u_x - f_3 + f_5 - f_6 - f_7 + f_8$$

Rearranging we get:

$$f_5 + f_8 = \frac{1}{3}\rho u_x + f_6 + f_7 \tag{A.10}$$

Now, introducing eqs. (A.6) and (A.10) into eq. (A.7), we obtain:

$$\rho = f_0 + f_3 + \frac{2}{3}\rho u_x + f_2 + f_3 + f_4 + f_6 + f_7 + \frac{1}{3}\rho u_x + f_6 + f_7$$

Thus,

$$\boxed{\rho = \frac{1}{(1-u_x)}(f_0 + f_2 + f_4 + 2(f_3 + f_6 + f_7))} \tag{A.11}$$

Equation (A.9) can be rewritten as:

$$f_5 - f_8 = \rho u_y - f_2 + f_4 + f_7 - f_6 \tag{A.12}$$

Summing eqs. (A.10) and (A.12) gives us:

$$2f_5 = \rho u_y - f_2 + f_4 + f_7 - f_6 + \frac{1}{3}\rho u_x + f_6 + f_7$$

Hence, rearranging we get:

$$\boxed{f_5 = f_7 - \frac{1}{2}(f_2 - f_4) + \frac{1}{2}\rho u_y + \frac{1}{6}\rho u_x} \tag{A.13}$$

Subtracting eq. (A.12) to eq. (A.10) gives us:

$$2f_8 = \frac{1}{3}\rho u_x + f_6 + f_7 - (\rho u_y - f_2 + f_4 + f_7 - f_6)$$

Hence, rearranging we get:

$$\boxed{f_8 = f_6 + \frac{1}{2}(f_2 - f_4) - \frac{1}{2}\rho u_y + \frac{1}{6}\rho u_x} \tag{A.14}$$

Thus we have found all unknowns using eqs. (A.6), (A.11), (A.13) and (A.14).

A.1.2. Pressure outlet BC

We can mention the inlet/outlet conditions in form of pressure if specific values of velocities at this boundaries are not available. Assuming the pressure outlet boundary condition is applied to the east boundary of the rectangular domain as shown in fig. 2.3. We obtain the density from pressure values, and hence in this case, we have 5 unknowns, i.e. u_x, u_y, f_3, f_6 and f_7. So, we would have to assume a value for any one of the velocity components, and this depends on a case by case basis. For this case, let us assume $u_y = 0$. Equations (A.7) to (A.9) can be reused for deriving the boundary conditions. The fourth and last expression is given in the same way assuming bounce-back for normal distribution function directions. Therefore, we reproduce this equation:

$$f_1 - f_1^{\text{eq}} = f_3 - f_3^{\text{eq}}$$

We finally obtain in the similar fashion:

$$\boxed{f_3 = f_1 - \frac{2}{3}\rho u_x} \tag{A.15}$$

For, an ideal gas case (i.e. not multiphase scenario), the pressure is defined as $p = e_s^2\rho$, and thus we know the density. Equation (A.8) can be rewritten as:

$$f_6 + f_7 = f_1 + f_5 + f_8 - \rho u_x - f_3 \tag{A.16}$$

Introducing eq. (A.15) into this last equation, we get:

$$f_6 + f_7 = \left(f_1 + f_5 + f_8 - \rho u_x - f_1 + \frac{2}{3}\rho u_x\right) \tag{A.17}$$

$$f_6 + f_7 = \left(f_5 + f_8 - \frac{1}{3}\rho u_x\right) \tag{A.18}$$

Substituting eqs. (A.15) and (A.18) into eq. (A.7), we obtain value for u_x, as:

$$\rho = f_0 + f_1 + f_2 + f_1 - \frac{2}{3}\rho u_x + f_4 + f_5 + f_8 + f_5 + f_8 - \frac{1}{3}\rho u_x$$

Rearranging, we obtain:

$$\boxed{u_x = -1 + \frac{f_0 + f_2 + f_4 + 2(f_1 + f_5 + f_8)}{\rho}} \tag{A.19}$$

Since, in our case $u_y = 0$, eq. (A.9) can be rearranged and written as:

$$f_6 - f_7 = -f_2 + f_4 - f_5 + f_8 \tag{A.20}$$

Thus, adding eq. (A.18) to eq. (A.20) gives us:

$$2f_6 = f_5 + f_8 - \frac{1}{3}\rho u_x - f_2 + f_4 - f_5 + f_8 \tag{A.21}$$

Hence, rearranging we get:

$$\boxed{f_6 = f_8 - \frac{1}{2}(f_2 - f_4) - \frac{1}{6}\rho u_x} \tag{A.22}$$

Similarly, subtracting to eq. (A.18) eq. (A.20) gives us:

$$2f_7 = f_5 + f_8 - \frac{1}{3}\rho u_x + f_2 - f_4 + f_5 - f_8 \tag{A.23}$$

Hence, rearranging we get:

$$\boxed{f_7 = f_5 + \frac{1}{2}(f_2 - f_4) - \frac{1}{6}\rho u_x} \tag{A.24}$$

Thus we have found all unknowns using assumption $u_y = 0$, eqs. (A.15), (A.19), (A.22) and (A.24). Now there are some special treatment mentioned for the Zou and He boundary condition at the corner nodes, but this has not been implemented in our codes.

Appendix B

Standard interpolation equations for Υ

The equations described in fig. 4.2. Using the notations $\rho_w^{max} = \rho^+$ at r_x^+, $\rho_w^{min} = \rho^-$ at r_x^-, $\Delta\rho = \rho^+ - \rho^-$ and $\Delta r_x = r_x^+ - r_x^-$ it is possible to write the interpolation equations as:

- Linear evolution (passes by both end points):

$$\rho_w^1(r_x) = \rho^+ - \frac{\Delta\rho}{\Delta r_x}(r_x^+ - r_x)$$

- Quadratic convex (passes by both end points plus null derivative on r_x^- - no linear term):

$$\rho_w^{2,\cup}(r_x) = \rho^- + \frac{\Delta\rho}{\Delta r_x^2}(r_x^- - r_x)^2$$

- Quadratic concave (passes by both end points plus null derivative on r_x^+ - no linear term):

$$\rho_w^{2,\cap}(r_x) = \rho^+ - \frac{\Delta\rho}{\Delta r_x^2}(r_x^+ - r_x)^2$$

- Cubic convex (passes by both end points plus null derivative on r_x^- - no linear and quadratic terms):

$$\rho_w^{3,\cup}(r_x) = \rho^- + \frac{\Delta\rho}{\Delta r_x^3}(r_x^- - r_x)^3$$

- Quadratic concave (passes by both end points plus null derivative on r_x^+ - no linear and quadratic terms):

$$\rho_w^{3,\cap}(r_x) = \rho^+ - \frac{\Delta\rho}{\Delta r_x^3}(r_x^+ - r_x)^3$$

Appendix C

The LBM framework

It is common for macroscopic methods to model the physics at the operational scale of the system. This eliminates the process of (re)scaling the system, which is often the case while building an experimental prototype. It is a general practice to represent (relevant) physical quantities (pertaining to the macroscopic phenomenon) in the framework of the metric system–here the exceptions arise either due to an industrial standard (for e.g. *inches* in the piping industry) or due to regional preference (for e.g. *pounds* in the UK, *gallons* in the USA)–which is carried forward in most macroscopic modeling paradigms.

Conversely, the lattice Boltzmann paradigm provides a mesoscopic description of the physics of the system. This bottom-to-top approach breaks down the conventional manner of defining macroscopic quantities. An example of this is the definition of *density* of the fluid (ρ) which is essentially in the LBM paradigm a sum of the particle/probability distribution function (f) for all the relevant velocity directions (or between relevant neighboring nodes). Though this definition gives us the right sense of the quantity (i.e. density), its difference to the conventional definition i.e. mass per unit volume is apparent. It is along these lines that one must consider that *LBM models physics in a different paradigm as compared to macroscopic models.* This necessitates building a bridge connecting the real and the mesoscopic worlds. This can be accomplished essentially in two ways: the former requires usage of conversion factors and the latter requires usage of the dimensionless parameters. Pragmatic choices for quantities used for conversion are time, length, velocity and density [48]. Once the selection of the primary set of conversion factors is completed, other derived conversion factors are retrieved using the relevant non-dimensional parameter formulations. In some of the cases (as in thesis) we do not require a conversion factor as a direct mapping using relevant non-dimensional parameter formulations is feasible.

Here we borrow from our source [48] an example, utilizing a non-dimensional parameter formulation as a link between the real and the LBM worlds to provide a hands-on example.

Example C.0.1. Liquid glycerol with density $\rho_{\text{liq}} = 1260$ kg/m^3 and kinematic viscosity $\nu_{\text{liq}} = 8.49 \times 10^{-4}$ m^2/s is flowing in a vertical pipe of diameter $d = 0.015$ m in the gravitational field where $g_{\text{gr}} = 9.81$ m/s^2. It is required to simulate an air bubble in the liquid with radius $R_{\text{bub}} = 0.004$ m and large density contrast, $\rho_{\text{liq}}/\rho_{\text{vap}} >> 1$. The Reynolds number is defined according to the flow observed in the absence of the bubble.

$$\text{Re} = \frac{U_{\max} d}{\nu_{\text{liq}}} = \frac{g_{\text{gr}} d^3}{4\nu_{\text{liq}}} = 11.5$$

The surface tension of glycerol in air at 20°C is $\sigma = 6.34{\times}10^{-2}$ N/m resulting in Bo = 6.24. (Note that the *confinement* $x_x := 2R_{\text{bub}}/d = 0.533$ is also a relevant dimensionless parameter which can

Type of units	Description	Nomenclature
Fundamental	Lattice length unit	l.u.
	Lattice mass unit	m.u.
	Lattice time unit	t.s.
Derived	Force, velocity & etc	'units'

Table C.1: Nomenclature for LBM units in literature

be easily mapped to the lattice as it is merely the ratio of two length scales). How should the problem of selection of different simulation parameters should be approached?

We start by setting $d_{\text{lbm}} = 30$ l.u. and $R_{\text{bub, lbm}} = 8$ l.u. obeying the confinement scaling. The Reynolds number $\text{Re} = \text{Re}_{\text{lbm}}$ therefore restricts the ratio of gravity and viscosity:

$$\frac{g_{\text{gr, lbm}}}{\nu^2_{\text{liq, lbm}}} = \frac{4\text{Re}}{d^3_{\text{lbm}}} = 1.7 \times 10^{-3}$$

After, we choose $\Delta\rho_{\text{lbm}} = 1$ and from the Bond number:

$$\frac{\sigma_{\text{lbm}}}{g_{\text{gr, lbm}}} = \frac{2\Delta\rho_{\text{lbm}} R^2_{\text{bub}}}{\text{Bo}_{\text{lbm}}} = 40.5$$

Thus we have one degree of freedom left because the choice of the three parameters $g_{\text{gr, lbm}}$, $\nu_{\text{liq, lbm}}$ and σ_{lbm} are restricted by two conditions. Now we can set the surface tension first: $\sigma_{\text{lbm}} = 0.06$ (*For the model in the thesis we obtain this value* a posteriori *and this value remains fixed*). This gives $g_{\text{gr,lbm}} = 2.93 \times 10^{-3}$ and therefore $\nu_{\text{liq, lbm}} = 1.31$ and $\tau_{\text{lbm}} = 4.44$. Additionally, we find that the maximum velocity $U_{\text{max, lbm}} = 0.50$ units. These parameters are not acceptable and the velocity and viscosity have to be reduced to attain the desired result. Hence we repeat this process iteratively until an acceptable set of values are arrived upon. Different approaches can be utilized to balance the simulation parameters. Here, one only has to keep in mind, the intrinsic limitation of each numerical method which make certain combinations of dimensionless numbers (in this case: Re, Bo, x_x) unfeasible if not impossible to access in a simulation.

Throughout the manuscript we have utilized non-dimensional numbers like Reynolds number (Re), Capillary number (Ca) and Bond number (Bo) for different simulations. Here, as previously mentioned in chapter 2, we use a standard space and time resolution i.e. $\Delta x = \Delta y = 1$ l.u. *and* $\Delta t = 1$ t.s.. *Table C.1 provides us with the notations (for LBM units) used in literature. Here the aim is not to rename all units, but rather we only make mention of the fundamental units and label all other derived units as* 'units'. *Thus in summary, a squared structured mesh with constant time stepping and finite difference discretization along with an explicit solver was used for modeling the physics of the interfacial flows in the LBM paradigm.*

Bibliography

1. Xu, X. & Qian, T. Droplet motion in one-component fluids on solid substrates with wettability gradients. *Physical Review E* **85,** 051601. ISSN: 1539-3755, 1550-2376. https://link.aps.org/doi/10.1103/PhysRevE.85.051601 (2023) (May 2012).
2. Son, S. *Lattice Boltzmann modeling of two-phase flow in macroporous media with application to porous asphalt* (ETH Zurich, 2016).
3. Zhao, W., Liang, J., Sun, M. & Wang, Z. Investigation on the effect of convective outflow boundary condition on the bubbles growth, rising and breakup dynamics of nucleate boiling. *International Journal of Thermal Sciences* **167,** 106877. ISSN: 1290-0729. https://www.sciencedirect.com/science/article/pii/S1290072921000466 (2021).
4. Hashemi, M. R., Ryzhakov, P. B. & Rossi, R. An enriched finite element/level-set method for simulating two-phase incompressible fluid flows with surface tension. *Computer Methods in Applied Mechanics and Engineering* **370,** 113277. ISSN: 0045-7825. https://www.sciencedirect.com/science/article/pii/S004578252030462X (2020).
5. Olsson, E., Kreiss, G. & Zahedi, S. A conservative level set method for two phase flow II. *Journal of Computational Physics* **225,** 785–807. ISSN: 0021-9991. https://www.sciencedirect.com/science/article/pii/S0021999107000046 (2007).
6. Sussman, M., Smereka, P. & Osher, S. A Level Set Approach for Computing Solutions to Incompressible Two-Phase Flow. *Journal of Computational Physics* **114,** 146–159. ISSN: 0021-9991. https://www.sciencedirect.com/science/article/pii/S0021999184711557 (1994).
7. Kinzel, M., Lindau, J. & Kunz, R. in *19th AIAA Computational Fluid Dynamics* (). eprint: https://arc.aiaa.org/doi/pdf/10.2514/6.2009-4152. https://arc.aiaa.org/doi/abs/10.2514/6.2009-4152.
8. Gopala, V. R. & van Wachem, B. G. Volume of fluid methods for immiscible-fluid and free-surface flows. *Chemical Engineering Journal* **141,** 204–221. ISSN: 1385-8947. https://www.sciencedirect.com/science/article/pii/S1385894708000028 (2008).
9. Hirt, C. & Nichols, B. Volume of fluid (VOF) method for the dynamics of free boundaries. *Journal of Computational Physics* **39,** 201–225. ISSN: 0021-9991. https://www.sciencedirect.com/science/article/pii/0021999181901455 (1981).
10. Yu, J., Wang, S., Luo, K. & Fan, J. Discrete Element Simulation of Gas–Solid and Gas–Liquid–Solid Flows. *Industrial & Engineering Chemistry Research* **62,** 17019–17028. eprint: https://doi.org/10.1021/acs.iecr.3c01173. https://doi.org/10.1021/acs.iecr.3c01173 (2023).
11. Swiderski, K., Narayanan, C. & Lakehal, D. Application of N-phase algebraic slip model and direct quadrature method of moments to the simulation of air-water flow in vertical risers and bubble column reactor. *Computers & Chemical Engineering* **90,** 151–160. ISSN: 0098-1354. https://www.sciencedirect.com/science/article/pii/S0098135416301193 (2016).
12. Shynybayeva, A. & Rojas-Solórzano, L. Eulerian-Eulerian Modeling of Multiphase Flow in Horizontal Annuli: Current Limitations and Challenges. *Processes* **8,** 1–24 (1426) (Nov. 2020).

13. Xiong, Q., Baychev, T. G. & Jivkov, A. P. Review of pore network modelling of porous media: Experimental characterisations, network constructions and applications to reactive transport. *Journal of Contaminant Hydrology* **192,** 101–117. ISSN: 0169-7722. https://www.sciencedirect.com/science/article/pii/S016977221630122X (2016).

14. Huang, X., Zhou, W. & Deng, D. Validation of pore network modeling for determination of two-phase transport in fibrous porous media. *Scientific Reports* **10.** ISSN: 2045-2322. https://doi.org/10.1038/s41598-020-74581-0 (2020).

15. Hu, X. & Adams, N. A multi-phase SPH method for macroscopic and mesoscopic flows. *Journal of Computational Physics* **213,** 844–861. ISSN: 0021-9991. https://www.sciencedirect.com/science/article/pii/S0021999105004195 (2006).

16. Zhu, G., Zou, L., Chen, Z., Wang, A. & Liu, M. An improved SPH model for multiphase flows with large density ratios. *International Journal for Numerical Methods in Fluids* **86,** 167–184. eprint: https://onlinelibrary.wiley.com/doi/pdf/10.1002/fld.4412. https://onlinelibrary.wiley.com/doi/abs/10.1002/fld.4412 (2018).

17. Monaghan, J. J. & Rafiee, A. A simple SPH algorithm for multi-fluid flow with high density ratios. *International Journal for Numerical Methods in Fluids* **71,** 537–561. eprint: https://onlinelibrary.wiley.com/doi/pdf/10.1002/fld.3671. https://onlinelibrary.wiley.com/doi/abs/10.1002/fld.3671 (2013).

18. Makaremi, M., Jordan, K. D., Guthrie, G. D. & Myshakin, E. M. Multiphase Monte Carlo and Molecular Dynamics Simulations of Water and CO2 Intercalation in Montmorillonite and Beidellite. *The Journal of Physical Chemistry C* **119,** 15112–15124. eprint: https://doi.org/10.1021/acs.jpcc.5b01754. https://doi.org/10.1021/acs.jpcc.5b01754 (2015).

19. Avalos, J. B. & Mackie, A. D. Dissipative particle dynamics with energy conservation. *Europhysics Letters* **40,** 141. https://dx.doi.org/10.1209/epl/i1997-00436-6 (1997).

20. Bagheri, M., Siavashi, M. & Mousavi, S. An improved three-dimensional lattice Boltzmann-volume of fluid (LB-VOF) method for simulation of laminar liquid jet breakup with high density ratio. *Computers & Fluids* **263,** 105969. ISSN: 0045-7930. https://www.sciencedirect.com/science/article/pii/S0045793023001949 (2023).

21. Janßen, C. F., Grilli, S. T. & Krafczyk, M. On enhanced non-linear free surface flow simulations with a hybrid LBM–VOF model. *Computers & Mathematics with Applications* **65.** Special Issue on Mesoscopic Methods in Engineering and Science (ICMMES-2010, Edmonton, Canada), 211–229. ISSN: 0898-1221. https://www.sciencedirect.com/science/article/pii/S0898122112004026 (2013).

22. Arienti, M. *et al.* Coupled Level-Set/Volume-of-Fluid Method for Simulation of Injector Atomization. *Journal of Propulsion and Power* **29,** 147–157. eprint: https://doi.org/10.2514/1.B34198. https://doi.org/10.2514/1.B34198 (2013).

23. Tong, Z.-X., He, Y.-L. & Tao, W.-Q. A review of current progress in multiscale simulations for fluid flow and heat transfer problems: The frameworks, coupling techniques and future perspectives. *International Journal of Heat and Mass Transfer* **137,** 1263–1289. ISSN: 0017-9310. https://www.sciencedirect.com/science/article/pii/S0017931018349330 (2019).

24. Chaaban, M., Heider, Y. & Markert, B. A multiscale LBM–TPM–PFM approach for modeling of multiphase fluid flow in fractured porous media. *International Journal for Numerical and Analytical Methods in Geomechanics* **46,** 2698–2724. eprint: https://onlinelibrary.wiley.com/doi/pdf/10.1002/nag.3423. https://onlinelibrary.wiley.com/doi/abs/10.1002/nag.3423 (2022).

25. Thomas, Y. R. J., Benayad, A., Schroder, M., Morin, A. & Pauchet, J. New Method for Super Hydrophobic Treatment of Gas Diffusion Layers for Proton Exchange Membrane Fuel Cells Using Electrochemical Reduction of Diazonium Salts. *ACS Applied Materials & Interfaces* **7.** PMID: 26098140, 15068–15077. eprint: https://doi.org/10.1021/acsami.5b04428. https://doi.org/10.1021/acsami.5b04428 (2015).

26. Forner-Cuenca, A. *et al.* Engineered Water Highways in Fuel Cells: Radiation Grafting of Gas Diffusion Layers. *Advanced Materials* **27,** 6317–6322. eprint: https://onlinelibrary.wiley.com/doi/pdf/10.1002/adma.201503557. https://onlinelibrary.wiley.com/doi/abs/10.1002/adma.201503557 (2015).

27. Park, S., Lee, J.-W. & Popov, B. N. A review of gas diffusion layer in PEM fuel cells: Materials and designs. *International Journal of Hydrogen Energy* **37.** XII International Symposium on Polymer Electrolytes: New Materials for Application in Proton Exchange Membrane Fuel Cells, 5850–5865. ISSN: 0360-3199. https://www.sciencedirect.com/science/article/pii/S0360319911028825 (2012).

28. DNP. *A thermal management and miniaturization solution for the latest 5G-compatible electronic devices: Vapor Chamber* Accessed:17/04/2024. https://www.global.dnp/biz/solution/products/detail/10161128_4130.html.

29. Exchange, S. H. *Heat pipes* Accessed:17/04/2024. https://serckglobal.com/products/hvac-climate-control/heat-pipes/.

30. Weibel, J. A. & Garimella, S. V. in (eds Sparrow, E. M., Cho, Y. I., Abraham, J. P. & Gorman, J. M.) 209–301 (Elsevier, 2013). https://www.sciencedirect.com/science/article/pii/B9780124078192000049.

31. Yau, Y. & Ahmadzadehtalatapeh, M. A review on the application of horizontal heat pipe heat exchangers in air conditioning systems in the tropics. *Applied Thermal Engineering* **30,** 77–84. ISSN: 1359-4311. https://www.sciencedirect.com/science/article/pii/S1359431109002294 (2010).

32. Chaudhry, H. N., Hughes, B. R. & Ghani, S. A. A review of heat pipe systems for heat recovery and renewable energy applications. *Renewable and Sustainable Energy Reviews* **16,** 2249–2259. ISSN: 1364-0321. https://www.sciencedirect.com/science/article/pii/S1364032112000391 (2012).

33. Bezerra, M. A. *et al.* Simplex optimization: A tutorial approach and recent applications in analytical chemistry. *Microchemical Journal* **124,** 45–54. ISSN: 0026-265X. https://www.sciencedirect.com/science/article/pii/S0026265X1500168X (2016).

34. Neto, B., Scarminio, I. & Bruns, R. in *Statistical Design – Chemometrics* (eds Bruns, R., Scarminio, I. & de Barros Neto, B.) 365–383 (Elsevier, 2005). https://www.sciencedirect.com/science/article/pii/S0922348705250086.

35. Gad, A. G. Particle Swarm Optimization Algorithm and Its Applications: A Systematic Review. *Archives of Computational Methods in Engineering*. https://doi.org/10.1007/s11831-021-09694-4 (2022).

36. Katoch, S., Chauhan, S. S. & Kumar, V. A review on genetic algorithm: past, present, and future. *Multimedia Tools and Applications*. https://doi.org/10.1007/s11042-020-10139-6 (2021).

37. Li, Y., Roux, S., Castelain, C., Fan, Y. & Luo, L. A genetic algorithm-based topology optimization (GATO) method for convective cooling of a heating surface with multiple heat sources. *International Journal of Heat and Mass Transfer* **224,** 125349. ISSN: 0017-9310. https://www.sciencedirect.com/science/article/pii/S0017931024001807 (2024).

38. Favennec, Y. & Masson, P. L. in *Metti 7 Advanced School: Thermal Measurements and Inverse Techniques* chap. 8 ().

39. Pingen, G. *Optimal design for fluidic systems: Topology and shape optimization with the lattice Boltzmann method* PhD thesis (May 2008). ISBN: 9780549672425.

40. Dugast, F. *Optimisation topologique en convection thermique avec la méthode de Lattice Boltzmann* Thèse de doctorat dirigée par Luo, LingaiFan, Yilin et Josset, Christophe Energétique, thermique, combustion Nantes 2018. PhD thesis (2018). http://www.theses.fr/2018NANT4056.

41. Lou, H. *et al.* Size optimization design of members for shear wall high-rise buildings. *Journal of Building Engineering* **61,** 105292. ISSN: 2352-7102. https://www.sciencedirect.com/science/article/pii/S2352710222012980 (2022).

42. Haslinger, J. & Mäkinen, R. A. E. *Introduction to Shape Optimization* eprint: https://epubs.siam.org/doi/pdf/10.1137/1.9780898718690. https://epubs.siam.org/doi/abs/10.1137/1.9780898718690 (Society for Industrial and Applied Mathematics, 2003).

43. A.J.C., L. & R., V. Lattice-Boltzmann Simulations of Particle-Fluid Suspensions. *Journal of Statistical Physics* **104,** 119–1251 (5-6 September 2001).

44. Montessori, A. *et al.* in *Numerical Methods and Advanced Simulation in Biomechanics and Biological Processes* (eds Cerrolaza, M., Shefelbine, S. J. & Garzón-Alvarado, D.) 357 –370 (Academic Press, 2018). ISBN: 978-0-12-811718-7. http://www.sciencedirect.com/science/article/pii/B9780128117187000204.

45. Maslo, A., Panjan, J. & Žagar, D. Large-scale oil spill simulation using the lattice Boltzmann method, validation on the Lebanon oil spill case. *Marine Pollution Bulletin* **84,** 225 –235. ISSN: 0025-326X. http://www.sciencedirect.com/science/article/pii/S0025326X14002860 (2014).

46. Kang, Q., Lichtner, P. & Janecky, D. Lattice Boltzmann Method for Reacting Flows in Porous Media. **2,** 545–563 (Oct. 2010).

47. Xin, F. *et al.* Simulation of gas exothermic chemical reaction in porous media reactor with lattice Boltzmann method. *Journal of Thermal Science* **22,** 42–47. ISSN: 1993-033X. https://doi.org/10.1007/s11630-013-0590-5 (2013).

48. Krüger, T. *et al. The Lattice Boltzmann Method: Principles and Practice* ISBN: 978-3-319-44647-9 (Springer International Publishing, 2017).

49. McNamara, G. R. & Zanetti, G. Use of the Boltzmann Equation to Simulate Lattice-Gas Automata. *PHYSICAL REVIEW LETTERS* **61** (14 November 1988).

50. Theofanous, T., Joseph, D., Nourgaliev, R. & Dinh, T. The lattice Boltzmann equation method: Theoretical Interpretation, Numerics and Implications. *International Journal of Multiphase Flow*, 117–169 (2003).

51. Bhatnagar, P. L., Gross, E. P. & Krook, M. A Model for Collision Processes in Gases. I. Small Amplitude Processes in Charged and Neutral One-Component Systems. *Phys. Rev.* **94,** 511–525. https://link.aps.org/doi/10.1103/PhysRev.94.511 (3 1954).

52. in. *Rarefied Gas Dynamics: Theory and Simulations* 450–458 (). eprint: https://arc.aiaa.org/doi/pdf/10.2514/5.9781600866319.0450.0458. https://arc.aiaa.org/doi/abs/10.2514/5.9781600866319.0450.0458.

53. Bouzidi, M., d'Humières, D., Lallemand, P. & Luo, L.-S. Lattice Boltzmann Equation on a Two-Dimensional Rectangular Grid. *Journal of Computational Physics* **172,** 704–717. ISSN: 0021-9991. https://www.sciencedirect.com/science/article/pii/S0021999101968500 (2001).

54. Yan, Z., Yang, X., Li, S. & Hilpert, M. Two-relaxation-time lattice Boltzmann method and its application to advective-diffusive-reactive transport. *Advances in Water Resources* **109,** 333–342. ISSN: 0309-1708. https://www.sciencedirect.com/science/article/pii/S0309170816307680 (2017).

55. Hosseini, S., Atif, M., Ansumali, S. & Karlin, I. Entropic lattice Boltzmann methods: A review. *Computers & Fluids* **259,** 105884. ISSN: 0045-7930. https://www.sciencedirect.com/science/article/pii/S0045793023001093 (2023).

56. Shan, X. Pressure tensor calculation in a class of nonideal gas lattice Boltzmann models. *Phys. Rev. E* **77,** 066702. https://link.aps.org/doi/10.1103/PhysRevE.77.066702 (6 2008).

57. McCracken, M. & Abraham, J. Multiple-relaxation-time lattice-Boltzmann model for multiphase flow. *Physical review. E, Statistical, nonlinear, and soft matter physics* **71,** 036701 (Apr. 2005).

58. Lou, Q., Guo, Z. & Shi, B. Evaluation of outflow boundary conditions for two-phase lattice Boltzmann equation. *Phys. Rev. E* **87,** 063301. https://link.aps.org/doi/10.1103/PhysRevE.87.063301 (6 2013).

59. Li, L. & Jia, X. Modified outlet boundary condition schemes for large density ratio lattice Boltzmann models. *Journal of Heat Transfer* **139** (Jan. 2017).

60. Ren, J., Zheng, Q. & Li, Y. Curved boundary condition for lattice Boltzmann modeling of binary gaseous micro-scale flows in the slip regime. *Physica A: Statistical Mechanics and its Applications* **550,** 124181. ISSN: 0378-4371. https://www.sciencedirect.com/science/article/pii/S0378437120300236 (2020).

61. Inamuro, T. Lattice Boltzmann methods for moving boundary flows. *Fluid Dynamics Research* **44,** 024001. https://dx.doi.org/10.1088/0169-5983/44/2/024001 (2012).

62. Silva, D. P. F. *et al.* Lattice Boltzmann simulation of deformable fluid-filled bodies: progress and perspectives. *Soft Matter* **20,** 2419–2441. http://dx.doi.org/10.1039/D3SM01648J (11 2024).

63. Zhou, K. *et al.* An efficient LBM-DEM simulation method for suspensions of deformable preformed particle gels. *Chemical Engineering Science* **167,** 288–296. ISSN: 0009-2509. https://www.sciencedirect.com/science/article/pii/S0009250917302737 (2017).

64. Nash, R. W. *et al.* Choice of boundary condition for lattice-Boltzmann simulation of moderate-Reynolds-number flow in complex domains. *Phys. Rev. E* **89,** 023303. https://link.aps.org/doi/10.1103/PhysRevE.89.023303 (2 2014).

65. Zou, Q. & He, X. On pressure and velocity boundary conditions for the Lattice Boltzmann BGK model. *Physics of Fluids* **9** (Nov. 1996).

66. Li, Q. *et al.* Lattice Boltzmann methods for multiphase flow and phase-change heat transfer. *Progress in Energy and Combustion Science* **52** (Aug. 2015).

67. Schwarzmeier, C. *et al.* Comparison of free-surface and conservative Allen–Cahn phase-field lattice Boltzmann method. *Journal of Computational Physics* **473,** 111753. ISSN: 0021-9991. https://www.sciencedirect.com/science/article/pii/S0021999122008166 (2023).

68. in. *Multiphase Lattice Boltzmann Methods: Theory and Application* 18–70 (John Wiley & Sons, Ltd, 2015). ISBN: 9781118971451. eprint: https://onlinelibrary.wiley.com/doi/pdf/10.1002/9781118971451.ch2. https://onlinelibrary.wiley.com/doi/abs/10.1002/9781118971451.ch2.

69. in. *Multiphase Lattice Boltzmann Methods: Theory and Application* 71–93 (John Wiley & Sons, Ltd, 2015). ISBN: 9781118971451. eprint: https://onlinelibrary.wiley.com/doi/pdf/10.1002/9781118971451.ch3. https://onlinelibrary.wiley.com/doi/abs/10.1002/9781118971451.ch3.

70. in. *Multiphase Lattice Boltzmann Methods: Theory and Application* 94–135 (John Wiley & Sons, Ltd, 2015). ISBN: 9781118971451. eprint: https://onlinelibrary.wiley.com/doi/pdf/10.1002/9781118971451.ch4. https://onlinelibrary.wiley.com/doi/abs/10.1002/9781118971451.ch4.

71. in. *Multiphase Lattice Boltzmann Methods: Theory and Application* 136–166 (John Wiley & Sons, Ltd, 2015). ISBN: 9781118971451. eprint: https://onlinelibrary.wiley.com/doi/pdf/10.1002/9781118971451.ch5. https://onlinelibrary.wiley.com/doi/abs/10.1002/9781118971451.ch5.

72. Rothman, D. H. & Keller, J. M. Immiscible cellular-automaton fluids. *Journal of Statistical Physics* **52.** https://doi.org/10.1007/BF01019743 (3 1988).

73. Gunstensen, A. K., Rothman, D. H., Zaleski, S. & Zanetti, G. Lattice Boltzmann model of immiscible fluids. *Phys. Rev. A* **43,** 4320–4327. https://link.aps.org/doi/10.1103/PhysRevA.43.4320 (8 1991).

74. Grunau, D., Chen, S. & Egger, K. A lattice Boltzmann model for multiphase fluid flows. *Physics of Fluids* **5,** 2557–2562. https://api.semanticscholar.org/CorpusID:118704645 (1993).

75. Reis, T. & Phillips, T. N. Modified lattice Boltzmann model for axisymmetric flows. *Phys. Rev. E* **75,** 056703. https://link.aps.org/doi/10.1103/PhysRevE.75.056703 (5 2007).

76. Wang, H., Yuan, X., Liang, H. & Shi, B. A brief review of the phase-field-based lattice Boltzmann method for multiphase flows. *Capillarity* **2,** 33–52 (Sept. 2019).

77. Fakhari, A., Mitchell, T., Leonardi, C. & Bolster, D. Improved locality of the phase-field lattice-Boltzmann model for immiscible fluids at high density ratios. *Phys. Rev. E* **96,** 053301. https://link.aps.org/doi/10.1103/PhysRevE.96.053301 (5 2017).

78. Shan, X. & Chen, H. Simulation of nonideal gases and liquid-gas phase transitions by the lattice Boltzmann equation. *Phys. Rev. E* **49,** 2941–2948. https://link.aps.org/doi/10.1103/PhysRevE.49.2941 (4 1994).

79. Shan, X. & Chen, H. Lattice Boltzmann model for simulating flows with multiple phases and components. *Phys. Rev. E* **47,** 1815–1819. https://link.aps.org/doi/10.1103/PhysRevE.47.1815 (3 1993).

80. Yuan, P. & Schaefer, L. Equations of state in a lattice Boltzmann model. *Physics of Fluids* **18,** 042101. eprint: https://doi.org/10.1063/1.2187070. https://doi.org/10.1063/1.2187070 (2006).

81. Gong, S. & Cheng, P. Numerical investigation of droplet motion and coalescence by an improved lattice Boltzmann model for phase transitions and multiphase flows. *Computers & Fluids* **53,** 93 –104. ISSN: 0045-7930. http://www.sciencedirect.com/science/article/pii/S0045793011002994 (2012).

82. Zhang, R. & Chen, H. A Lattice Boltzmann method for simulations of liquid-vapor thermal flows. *Physical review. E, Statistical, nonlinear, and soft matter physics* **67,** 066711 (July 2003).

83. Bao, J. & Schaefer, L. Lattice Boltzmann equation model for multi-component multi-phase flow with high density ratios. *Applied Mathematical Modelling* **37,** 1860–1871. ISSN: 0307-904X. http://dx.doi.org/10.1016/j.apm.2012.04.048 (2013).

84. Deng, H., Jiao, K., Hou, Y., Park, J. W. & Du, Q. A lattice Boltzmann model for multi-component two-phase gas-liquid flow with realistic fluid properties. *International Journal of Heat and Mass Transfer* **128,** 536–549. ISSN: 00179310 (2019).

85. Lycett-Brown, D. & Luo, K. H. Improved forcing scheme in pseudopotential lattice Boltzmann methods for multiphase flow at arbitrarily high density ratios. *Phys. Rev. E* **91,** 023305. https://link.aps.org/doi/10.1103/PhysRevE.91.023305 (2 2015).

86. Kang, Q., Zhang, D. & Chen, S. Displacement of a two-dimensional immiscible droplet in a channel. *Physics of Fluids* **14,** 3203–3214. ISSN: 1070-6631, 1089-7666. https://pubs.aip.org/pof/article/14/9/3203/255617/Displacement-of-a-two-dimensional-immiscible (2023) (Sept. 2002).

87. Kuzmin, A. *Multiphase Simulations with Lattice Boltzmann Scheme* (Department of Mechanical and Manufacturing Engineering, University of Calgary, Dec 2009).

88. Sbragaglia, M. *et al.* Generalized lattice Boltzmann method with multirange pseudopotential. *Physical Review E - Statistical, Nonlinear, and Soft Matter Physics* **75,** 1–13. ISSN: 15393755. arXiv: 0611014 [nlin] (2007).

89. Kupershtokh, A., Medvedev, D. & Karpov, D. On equations of state in a lattice Boltzmann method. *Computers & Mathematics with Applications* **58.** Mesoscopic Methods in Engineering and Science, 965 –974. ISSN: 0898-1221. http://www.sciencedirect.com/science/article/pii/S0898122109001011 (2009).

90. Huang, H. & Krafczyk, M. Comment on "Lattice Boltzmann method for simulations of liquid-vapor thermal flows". *Physical review. E, Statistical, nonlinear, and soft matter physics* **84,** 038701; discussion 038702 (Sept. 2011).

91. Huang, H., Krafczyk, M. & Lu, X. Forcing term in single-phase and Shan-Chen-type multiphase lattice Boltzmann models. *Physical review. E, Statistical, nonlinear, and soft matter physics* **84,** 046710 (Oct. 2011).

92. Guo, Z., Zheng, C. & Shi, B. Discrete lattice effects on the forcing term in the lattice Boltzmann method. *Physical review. E, Statistical, nonlinear, and soft matter physics* **65,** 046308 (May 2002).

93. Chen, L., Kang, Q., Mu, Y., He, Y.-L. & Tao, W.-Q. A critical review of the pseudopotential multiphase lattice Boltzmann model: Methods and applications. *International Journal of Heat and Mass Transfer* **76,** 210 –236. ISSN: 0017-9310. http://www.sciencedirect.com/science/article/pii/S0017931014003378 (2014).

94. Kharmiani], S. F., Passandideh-Fard, M. & Niazmand, H. Simulation of a single droplet impact onto a thin liquid film using the lattice Boltzmann method. *Journal of Molecular Liquids* **222,** 1172 –1182. ISSN: 0167-7322. http://www.sciencedirect.com/science/article/pii/S0167732216310650 (2016).

95. Gong, W., Yan, Y. & Chen, S. A study on the unphysical mass transfer of SCMP pseudopotential LBM. *International Journal of Heat and Mass Transfer* **123,** 815–820. ISSN: 0017-9310. https://www.sciencedirect.com/science/article/pii/S0017931017338486 (2018).

96. Falcucci, G., Chibbaro, S., Succi, S., Shan, X. & Chen, H. Lattice Boltzmann spray-like fluids. *Europhysics Letters* **82,** 24005. https://dx.doi.org/10.1209/0295-5075/82/24005 (2008).

97. Peng, C., Tian, S., Li, G. & Sukop, M. C. Simulation of multiple cavitation bubbles interaction with single-component multiphase Lattice Boltzmann method. *International Journal of Heat and Mass Transfer* **137,** 301–317. ISSN: 00179310. https://linkinghub.elsevier.com/retrieve/pii/S001793101835765X (2022) (July 2019).

98. Gong, S. & Cheng, P. A lattice Boltzmann method for simulation of liquid–vapor phase-change heat transfer. *International Journal of Heat and Mass Transfer* **55,** 4923–4927. ISSN: 0017-9310. https://www.sciencedirect.com/science/article/pii/S0017931012002888 (2012).

99. Sukop, M. & Thorne, D. *Lattice Boltzmann Modeling-An Introduction for Geoscientists and Engineers* ISBN: 978-3-540-27982-2 (Springer-Verlag Berlin Heidelberg, 2006).

100. Peng, Y., Mao, Y., Wang, B. & Xie, B. Study on C-S and P-R EOS in pseudo-potential lattice Boltzmann model for two-phase flows. *International Journal of Modern Physics C* **28** (Sept. 2017).

101. Brochard, F. Motions of droplets on solid surfaces induced by chemical or thermal gradients. *Langmuir* **5,** 432–438. ISSN: 0743-7463, 1520-5827. https://pubs.acs.org/doi/abs/10.1021/la00086a025 (2023) (Mar. 1989).

102. Washburn, E. W. The Dynamics of Capillary Flow. *Phys. Rev.* **17,** 273–283. https://link.aps.org/doi/10.1103/PhysRev.17.273 (3 1921).

103. Diotallevi, F. *et al.* Lattice Boltzmann simulations of capillary filling: Finite vapour density effects. *The European Physical Journal Special Topics* **171,** 237–243 (Apr. 2009).

104. Quéré, D. Inertial capillarity. *EPL (Europhysics Letters)* **39,** 533 (Sept. 1997).

105. Krause, M. *et al. OpenLB Release 1.3: Open Source Lattice Boltzmann Code* version 1.3. May 2019. https://doi.org/10.5281/zenodo.3625967.

106. Krause, M. *et al.* OpenLB–Open source lattice Boltzmann code. *Computers & Mathematics with Applications* **81,** 258–288. ISSN: 0898-1221. http://www.sciencedirect.com/science/article/pii/S0898122120301875 (2021).

107. Molaeimanesh, G., Saeidi Googarchin, H. & Qasemian Moqaddam, A. Lattice Boltzmann simulation of proton exchange membrane fuel cells – A review on opportunities and challenges. *International Journal of Hydrogen Energy* **41,** 22221–22245. ISSN: 0360-3199. https://www.sciencedirect.com/science/article/pii/S0360319916329627 (2016).

108. Zacharoudiou, I., Boek, E. S. & Crawshaw, J. The impact of drainage displacement patterns and Haines jumps on CO2 storage efficiency. *Scientific Reports* **8.** ISSN: 1 (2018).

109. Lenormand, R., Touboul, E. & Zarcone, C. Numerical Models and Experiments on Immiscible Displacement in Porous Media. *Journal of Fluid Mechanics* **189,** 165 –187 (Apr. 1988).

110. Liu, H., Zhang, Y.-h. & Valocchi, A. Lattice Boltzmann simulation of immiscible fluid displacement in porous media: Homogeneous versus heterogeneous pore network. *Physics of Fluids* **27,** 052103 (May 2015).

111. Huang, J., Xiao, F. & Yin, X. Lattice Boltzmann simulation of pressure-driven two-phase flows in capillary tube and porous medium. *Computers & Fluids* **155,** 134 (May 2017).

112. Balakrishnan, M. *et al.* Designing Tailored Gas Diffusion Layers with Pore Size Gradients via Electrospinning for Polymer Electrolyte Membrane Fuel Cells. *ACS Applied Energy Materials* **3,** 2695–2707. eprint: https://doi.org/10.1021/acsaem.9b02371. https://doi.org/10.1021/acsaem.9b02371 (2020).

113. Bendsøe, M. P. & Kikuchi, N. Generating optimal topologies in structural design using a homogenization method. *Computer Methods in Applied Mechanics and Engineering* **71,** 197–224. ISSN: 0045-7825. https://www.sciencedirect.com/science/article/pii/0045782588900862 (1988).

114. Sigmund, O. & Maute, K. Topology optimization approaches. *Structural and Multidisciplinary Optimization*. https://doi.org/10.1007/s00158-013-0978-6 (2013).

115. Alexandersen, J. & Andreasen, C. S. A Review of Topology Optimisation for Fluid-Based Problems. *Fluids* **5.** ISSN: 2311-5521. https://www.mdpi.com/2311-5521/5/1/29 (2020).

116. Xu, L., Zhang, W., Liu, Z. & Guo, X. Topology Optimization of Acoustic–Mechanical Structures for Enhancing Sound Quality. *Acta Mechanica Solida Sinica*. https://doi.org/10.1007/s10338-023-00408-w (2023).

117. Lucchini, F., Torchio, R., Cirimele, V., Alotto, P. & Bettini, P. Topology Optimization for Electromagnetics: A Survey. *IEEE Access* **10,** 98593–98611 (2022).

118. Deng, Y. *Adjoint Topology Optimization Theory for Nano-Optics* https://doi.org/10.1007/978-981-16-7969-8 (Springer Singapore, 2023).

119. Hassani, B. & Hinton, E. A review of homogenization and topology optimization I—homogenization theory for media with periodic structure. *Computers & Structures* **69,** 707–717. ISSN: 0045-7949. https://www.sciencedirect.com/science/article/pii/S004579499800131X (1998).

120. Stolpe, M. & Svanberg, K. An alternative interpolation scheme for minimum compliance topology optimization. *Structural and Multidisciplinary Optimization*. https://doi.org/10.1007/s001580100129 (2001).

121. Rozvany, G. in *8th Symposium on Multidisciplinary Analysis and Optimization* (). eprint: https://arc.aiaa.org/doi/pdf/10.2514/6.2000-4738. https://arc.aiaa.org/doi/abs/10.2514/6.2000-4738.

122. Van Dijk, N. P., Maute, K., Langelaar, M. & van Keulen, F. Level-set methods for structural topology optimization: a review. *Structural and Multidisciplinary Optimization*. https://doi.org/10.1007/s00158-013-0912-y (2013).

123. Novotny, A. A., Lopes, C. G. & Santos, R. B. Topological derivative-based topology optimization of structures subject to self-weight loading. *Structural and Multidisciplinary Optimization*. https://doi.org/10.1007/s00158-020-02780-4 (2021).

124. Noda, M., Matsushima, K. & Yamada, T. Orientation optimization via topological derivatives in combination with multi-material topology optimization based on extended level set method. *Computer Methods in Applied Mechanics and Engineering* **418,** 116585. ISSN: 0045-7825. https://www.sciencedirect.com/science/article/pii/S0045782523007090 (2024).

125. Xie, W., Xia, Q., Yu, Q. & Li, Y. An effective phase field method for topology optimization without the curvature effects. *Computers & Mathematics with Applications* **146,** 200–212. ISSN: 0898-1221. https://www.sciencedirect.com/science/article/pii/S0898122123002894 (2023).

126. Gao, J., Song, B. & Mao, Z. Combination of the phase field method and BESO method for topology optimization. *Structural and Multidisciplinary Optimization*. https://doi.org/10.1007/s00158-019-02355-y (2020).

127. Vrionis, P., Samouchos, K. & Giannakoglou, K. Topology optimization in fluid mechanics using continuous adjoint and the cut-cell method. *Computers & Mathematics with Applications* **97,** 286–297. ISSN: 0898-1221. https://www.sciencedirect.com/science/article/pii/S0898122121002406 (2021).

128. Kambampati, S., Chung, H. & Kim, H. A. A discrete adjoint based level set topology optimization method for stress constraints. *Computer Methods in Applied Mechanics and Engineering* **377,** 113563. ISSN: 0045-7825. https://www.sciencedirect.com/science/article/pii/S0045782520307489 (2021).

129. Okubo, C. M., Sá, L. F., Kiyono, C. Y. & Silva, E. C. A discrete adjoint approach based on finite differences applied to topology optimization of flow problems. *Computer Methods in Applied Mechanics and Engineering* **389,** 114406. ISSN: 0045-7825. https://www.sciencedirect.com/science/article/pii/S0045782521006551 (2022).

130. Borrvall, T. & Petersson, J. Topology optimization of fluids in Stokes flow. *International Journal for Numerical Methods in Fluids* **41,** 77–107. eprint: https://onlinelibrary.wiley.com/doi/pdf/10.1002/fld.426. https://onlinelibrary.wiley.com/doi/abs/10.1002/fld.426 (2003).

131. Dilgen, C. B., Dilgen, S. B., Fuhrman, D. R., Sigmund, O. & Lazarov, B. S. Topology optimization of turbulent flows. *Computer Methods in Applied Mechanics and Engineering* **331,** 363–393. ISSN: 0045-7825. https://www.sciencedirect.com/science/article/pii/S0045782517307478 (2018).

132. Dong, X., Yaji, K. & Liu, X. Optimum design of micromixer for a non-Newtonian fluid by topology optimization. *Chemical Engineering Journal* **428,** 131367. ISSN: 1385-8947. https://www.sciencedirect.com/science/article/pii/S138589472102948X (2022).

133. Lee, G., Lee, I. & Kim, S. J. Topology optimization of a heat sink with an axially uniform cross-section cooled by forced convection. *International Journal of Heat and Mass Transfer* **168,** 120732. ISSN: 0017-9310. https://www.sciencedirect.com/science/article/pii/S0017931020336681 (2021).

134. Alexandersen, J., Aage, N., Andreasen, C. S. & Sigmund, O. Topology optimisation for natural convection problems. *International Journal for Numerical Methods in Fluids* **76,** 699–721. eprint: https://onlinelibrary.wiley.com/doi/pdf/10.1002/fld.3954. https://onlinelibrary.wiley.com/doi/abs/10.1002/fld.3954 (2014).

135. Zhang, K., Li, B., Du, F., Liu, H. & Hong, J. Topology optimization of natural convection heat transfer using SEMDOT algorithm based on the reduced-order model. *International Communications in Heat and Mass Transfer* **129,** 105676. ISSN: 0735-1933. https://www.sciencedirect.com/science/article/pii/S0735193321005698 (2021).

136. Dugast, F., Favennec, Y. & Josset, C. Reactive fluid flow topology optimization with the multi-relaxation time lattice Boltzmann method and a level-set function. *Journal of Computational Physics* **409,** 109252 (May 2020).

137. Alizadeh, M., Charoen-amornkitt, P., Suzuki, T. & Tsushima, S. Investigation of transport-reaction dynamics and local/global entropy production in topology optimization of two-species reaction-diffusion systems. *Chemical Engineering Science* **275,** 118739. ISSN: 0009-2509. https://www.sciencedirect.com/science/article/pii/S0009250923002956 (2023).

138. Phatak, T. & Nakshatrala, K. B. Investigation of transport-reaction dynamics and local/global entropy production in topology optimization of two-species reaction-diffusion systems. *Transport in Porous Media*. https://doi.org/10.1007/s11242-021-01616-z (2021).

139. Dugast, F., Favennec, Y., Josset, C., Fan, Y. & Luo, L. Topology optimization of thermal fluid flows with an adjoint Lattice Boltzmann Method. *Journal of Computational Physics* **365,** 376 – 404. ISSN: 0021-9991. http://www.sciencedirect.com/science/article/pii/S0021999118302067 (2018).

140. Abdelwahed, M., Hassine, M. & Masmoudi, M. Optimal shape design for fluid flow using topological perturbation technique. *Journal of Mathematical Analysis and Applications* **356,** 548–563. ISSN: 0022-247X. https://www.sciencedirect.com/science/article/pii/S0022247X09001863 (2009).

141. Koyeerath, G. D., Favennec, Y., Auvity, B. & Josset, C. The droplet race: Optimization of a wettability gradient surface. *Physics of Fluids* **36,** 032120. ISSN: 1070-6631. eprint: https://pubs.aip.org/aip/pof/article-pdf/doi/10.1063/5.0191507/19727500/032120_1_5.0191507.pdf. https://doi.org/10.1063/5.0191507 (Mar. 2024).

142. Feng, S. *et al.* Three-dimensional capillary ratchet-induced liquid directional steering. *Science* **373.** Publisher: American Association for the Advancement of Science, 1344–1348. https://www.science.org/doi/10.1126/science.abg7552 (2023) (Sept. 2021).

143. Shan, F., Chai, Z., Shi, B., Xiao, J. & Wang, C. Directional transport of a droplet on biomimetic ratchet structure. *Physics of Fluids* **35,** 113314. ISSN: 1070-6631. https://doi.org/10.1063/5.0176482 (2023) (Nov. 2023).

144. Baghel, V. & Ranjan, M. Numerical estimation of droplet motion on linear wettability gradient surface in microgravity environment. *Materials Today Communications* **32,** 103916. ISSN: 23524928. https://linkinghub.elsevier.com/retrieve/pii/S2352492822007711 (2023) (Aug. 2022).

145. Sui, Y. Moving towards the cold region or the hot region? Thermocapillary migration of a droplet attached on a horizontal substrate. *Physics of Fluids* **26,** 092102. ISSN: 1070-6631. https://doi.org/10.1063/1.4894077 (2023) (Sept. 2014).

146. Marangoni, C. *Sull'espansione delle goccie d'un liquido galleggianti sulla superfice di altro liquido* 1865. https://scholar.google.com/scholar_lookup?title=Sull%27espamione%20Delle%20Goccie%20di%20on%20Liquids%20Gallegiante%20Sulla%20Superficie%20di%20Altro%20Liquids&author=C.%20G.%20M.%20Marangoni&publication_year=1865&book=Sull%27espamione%20Delle%20Goccie%20di%20on%20Liquids%20Gallegiante%20Sulla%20Superficie%20di%20Altro%20Liquids (2023).

147. Brunet, P., Eggers, J. & Deegan, R. D. Vibration-Induced Climbing of Drops. *Physical Review Letters* **99.** Publisher: American Physical Society, 144501. https://link.aps.org/doi/10.1103/PhysRevLett.99.144501 (2023) (Oct. 2007).

148. Petrie, R. J., Bailey, T., Gorman, C. B. & Genzer, J. Fast Directed Motion of "Fakir" Droplets. *Langmuir* **20,** 9893–9896. ISSN: 0743-7463, 1520-5827. https://pubs.acs.org/doi/10.1021/la048612a (2023) (Nov. 2004).

149. Fang, G., Li, W., Wang, X. & Qiao, G. Droplet Motion on Designed Microtextured Superhydrophobic Surfaces with Tunable Wettability. *Langmuir* **24,** 11651–11660. ISSN: 0743-7463, 1520-5827. https://pubs.acs.org/doi/10.1021/la802033q (2023) (Oct. 2008).

150. Jin, L. & Wang, Y. Control the droplet motion by using chemically stripe-patterned surfaces. *Chemical Physics* **532,** 110678. ISSN: 03010104. https://linkinghub.elsevier.com/retrieve/pii/S0301010419313047 (2023) (Apr. 2020).

151. Maria, M. S., Rakesh, P. E., Chandra, T. S. & Sen, A. K. Capillary flow-driven microfluidic device with wettability gradient and sedimentation effects for blood plasma separation. *Scientific Reports* **7.** Number: 1 Publisher: Nature Publishing Group, 43457. ISSN: 2045-2322. https://www.nature.com/articles/srep43457 (2023) (Mar. 2017).

152. Attinger, D. *et al.* Surface engineering for phase change heat transfer: a review. *MRS Energy & Sustainability* **1.** Number: 1, 4. ISSN: 2329-2229, 2329-2237. http://link.springer.com/10.1557/mre.2014.9 (2021) (2014).

153. Alwazzan, M., Egab, K., Peng, B., Khan, J. & Li, C. Condensation on hybrid-patterned copper tubes (I): Characterization of condensation heat transfer. *International Journal of Heat and Mass Transfer* **112,** 991–1004. ISSN: 00179310. https://linkinghub.elsevier.com/retrieve/pii/S0017931016339394 (2022) (2017).

154. Tang, S., Li, Q., Yu, Y. & Qiu, Y. Enhancing dropwise condensation on downward-facing surfaces through the synergistic effects of surface structure and mixed wettability. *Physics of Fluids* **33.** Number: 8, 083301. ISSN: 1070-6631, 1089-7666. https://aip.scitation.org/doi/10.1063/5.0060443 (2021) (Aug. 2021).

155. Yilbas, B. S. *et al.* Water Droplet Dynamics on a Hydrophobic Surface in Relation to the Self-Cleaning of Environmental Dust. *Scientific Reports* **8,** 2984. ISSN: 2045-2322. https://www.ncbi.nlm.nih.gov/pmc/articles/PMC5813023/ (2023) (Feb. 2018).

156. Yakubu, M., Yilbas, B. S., Abubakr, A. A. & Al-Qahtani, H. Droplet Rolling and Spinning in V-Shaped Hydrophobic Surfaces for Environmental Dust Mitigation. *Molecules* **25,** 3039. ISSN: 1420-3049. https://www.ncbi.nlm.nih.gov/pmc/articles/PMC7412493/ (2023) (July 2020).

157. Greenspan, H. P. On the motion of a small viscous droplet that wets a surface. *Journal of Fluid Mechanics* **84,** 125–143 (1978).

158. Chaudhury, M. K. & Whitesides, G. M. How to Make Water Run Uphill. *Science* **256.** Publisher: American Association for the Advancement of Science, 1539–1541. https://www.science.org/doi/10.1126/science.256.5063.1539 (2023) (June 1992).

159. Subramanian, R. S., Moumen, N. & McLaughlin, J. B. Motion of a Drop on a Solid Surface Due to a Wettability Gradient. *Langmuir* **21.** Publisher: American Chemical Society, 11844–11849. ISSN: 0743-7463. https://doi.org/10.1021/la051943i (2023) (Dec. 2005).

160. Pismen, L. M. & Thiele, U. Asymptotic theory for a moving droplet driven by a wettability gradient. *Physics of Fluids* **18,** 042104. ISSN: 1070-6631, 1089-7666. http://aip.scitation.org/doi/10.1063/1.2191015 (2023) (Apr. 2006).

161. Huang, J., Shu, C. & Chew, Y. Numerical investigation of transporting droplets by spatiotemporally controlling substrate wettability. *Journal of Colloid and Interface Science* **328,** 124–133. ISSN: 00219797. https://linkinghub.elsevier.com/retrieve/pii/S002197970801062X (2023) (Dec. 2008).

162. Thiele, U., John, K. & Bär, M. Dynamical Model for Chemically Driven Running Droplets. *Physical Review Letters* **93,** 027802. ISSN: 0031-9007, 1079-7114. https://link.aps.org/doi/10.1103/PhysRevLett.93.027802 (2023) (July 2004).

163. Chowdhury, I. U., Mahapatra, P. S. & Sen, A. K. Shape evolution of drops on surfaces of different wettability gradients. *Chemical Engineering Science* **229,** 116136. ISSN: 00092509. https://linkinghub.elsevier.com/retrieve/pii/S0009250920306680 (2023) (Jan. 2021).

164. Chang, Q. & Alexander, J. I. D. Analysis of single droplet dynamics on striped surface domains using a lattice Boltzmann method. *Microfluidics and Nanofluidics* **2,** 309–326. ISSN: 1613-4982, 1613-4990. http://link.springer.com/10.1007/s10404-005-0075-2 (2023) (July 2006).

165. Onuki, A. Dynamic van der Waals theory. *Physical Review E* **75,** 036304. ISSN: 1539-3755, 1550-2376. https://link.aps.org/doi/10.1103/PhysRevE.75.036304 (2023) (Mar. 2007).

166. Fikl, A. & Bodony, D. J. Adjoint-based interfacial control of viscous drops. *Journal of Fluid Mechanics* **911,** A39 (2021).

167. Fikl, A. & Bodony, D. J. Adjoint-based control of three dimensional Stokes droplets. *Journal of Computational Physics* **494,** 112532 (2023).

168. Yin, B., Xu, S., Yang, S. & Dong, F. Shape Optimization of a Microhole Surface for Control of Droplet Wettability via the Lattice Boltzmann Method and Response Surface Methodology. *Langmuir* **37** (Mar. 2021).

169. Weisstein, E. W. *Brachistochrone Problem* Publisher: Wolfram Research, Inc. https://mathworld.wolfram.com/.

170. Nocedal, J. & Wright Stephen, J. *Numerical Optimization* ISBN: 978-0-387-30303-1 (Springer New York, NY, 2006).

171. Chavent, G. *Nonlinear least squares for inverse problems: theoretical foundations and step-by-step guide for applications* (Springer Science & Business Media, 2010).

172. Deng, Y., Wu, Y. & Liu, Z. in *Topology Optimization Theory for Laminar Flow: Applications in Inverse Design of Microfluidics* 123–145 (Springer Singapore, Singapore, 2018). ISBN: 978-981-10-4687-2. https://doi.org/10.1007/978-981-10-4687-2_4.

173. Wein, F., Chen, N., Iqbal, N., Stingl, M. & Avila, M. Topology optimization of unsaturated flows in multi-material porous media: Application to a simple diaper model. *Communications in Nonlinear Science and Numerical Simulation* **78,** 104871. ISSN: 1007-5704. https://www.sciencedirect.com/science/article/pii/S1007570419301935 (2019).

174. Yoon, G. H. & Kim, M. K. Topology optimization for transient two-phase fluid systems with continuous behavior. *Finite Elements in Analysis and Design* **225,** 104017. ISSN: 0168-874X. https://www.sciencedirect.com/science/article/pii/S0168874X23001105 (2023).

175. Ozguc, S., Pan, L. & Weibel, J. A. An approach for topology optimization of heat sinks for two-phase flow boiling: Part 1 – Model formulation and numerical implementation. *Applied Thermal Engineering* **249,** 123337. ISSN: 1359-4311. https://www.sciencedirect.com/science/article/pii/S1359431124010056 (2024).

176. Li, B., Xu, J., Wang, Y. & Hong, J. Optimization design of grooved condenser wick structures in a vapor chamber for electronic cooling applications. *Structural and Multidisciplinary Optimization*. https://doi.org/10.1007/s00158-019-02453-x (2020).

177. Li, B., Yin, X., Tang, W. & Zhang, J. Optimization design of grooved evaporator wick structures in vapor chamber heat spreaders. *Applied Thermal Engineering* **166,** 114657. ISSN: 1359-4311. https://www.sciencedirect.com/science/article/pii/S1359431119339791 (2020).

178. Li, B., Chen, H., Xu, J., Yin, X. & Hong, J. Topology optimization of vapor chamber internal structures consisting of evaporator and condenser. *Applied Mathematical Modelling* **107,** 233–255. ISSN: 0307-904X. https://www.sciencedirect.com/science/article/pii/S0307904X22000907 (2022).

179. Zhang, D., Cai, Q. & Gu, S. Three-dimensional lattice-Boltzmann model for liquid water transport and oxygen diffusion in cathode of polymer electrolyte membrane fuel cell with electrochemical reaction. *Electrochimica Acta* **262,** 282 –296. ISSN: 0013-4686. http://www.sciencedirect.com/science/article/pii/S0013468617327639 (2018).

180. Mohamad, A. A. *Lattice Boltzmann Method-Fundamentals and Engineering Applications with Computer Codes* ISBN: 9780857294548 (Springer-Verlag Berlin Heidelberg, 2011).

181. Delbosc, N. *Real - Time Simulation of Indoor Air Flow using the Lattice Boltzmann Method on Graphics Processing Unit* (University of Leeds, September 2015).

182. Viggen, E. M. *The lattice Boltzmann method: Fundamentals and acoustics* (Norwegian University of Science and Technology, February 2014).

183. Liu, H. *et al.* Multiphase lattice Boltzmann simulations for porous media applications. *Computational Geosciences* **20,** 777–805. ISSN: 1573-1499. https://doi.org/10.1007/s10596-015-9542-3 (2016).

184. Breuer, M., Bernsdorf, J., Zeiser, T. & Durst, F. Accurate computations of the laminar flow past a square cylinder based on two different methods: lattice-Boltzmann and finite-volume. *International Journal of Heat and Fluid Flow* **21,** 186 –196. ISSN: 0142-727X. http://www.sciencedirect.com/science/article/pii/S0142727X99000818 (2000).

185. Koosukuntla, N. R. *Towards development of a multiphase simulation model using Lattice Boltzmann Method (LBM)* (The University of Toledo, December 2011).

186. in. *Multiphase Lattice Boltzmann Methods: Theory and Application* 1–17 (John Wiley & Sons, Ltd, 2015). ISBN: 9781118971451. eprint: https://onlinelibrary.wiley.com/doi/pdf/10.1002/9781118971451.ch1. https://onlinelibrary.wiley.com/doi/abs/10.1002/9781118971451.ch1.

187. (eds Kuzmin, A. & Derksen, J.) *Shan-Chen Multiphase Model* Edmonton. University of Alberta (LBM Workshop, August 22,2011). http://lbmworkshop.com/wp-content/uploads/2011/08/shanchen.pdf.

188. Mukherjee, P. P., Wang, C.-Y. & Kang, Q. Mesoscopic modeling of two-phase behavior and flooding phenomena in polymer electrolyte fuel cells. *Electrochimica Acta* **54,** 6861 –6875. ISSN: 0013-4686. http://www.sciencedirect.com/science/article/pii/S0013468609008962 (2009).

189. Kang, Q., Zhang, D. & Chen, S. Displacement of a three-dimensional immiscible droplet in a duct. *Journal of Fluid Mechanics* **545.** Number: -1, 41. ISSN: 0022-1120, 1469-7645. http://www.journals.cambridge.org/abstract_S0022112005006956 (2022) (Dec. 2005).

190. Daniel, S., Sircar, S., Gliem, J. & Chaudhury, M. K. Ratcheting Motion of Liquid Drops on Gradient Surfaces. *Langmuir* **20,** 4085–4092. ISSN: 0743-7463, 1520-5827. https://pubs.acs.org/doi/10.1021/la036221a (2023) (May 2004).

191. Diewald, F. *et al.* Molecular dynamics and phase field simulations of droplets on surfaces with wettability gradient. *Computer Methods in Applied Mechanics and Engineering* **361,** 112773. ISSN: 00457825. https://linkinghub.elsevier.com/retrieve/pii/S0045782519306656 (2023) (Apr. 2020).

192. Qu, J., Yang, X. & Wang, Z. Numerical simulations on the self-motion of droplets in hydrophobic microchannels driven by wettability gradient surfaces. *International Communications in Heat and Mass Transfer* **119,** 104961. ISSN: 07351933. https://linkinghub.elsevier.com/retrieve/pii/S0735193320304899 (2023) (Dec. 2020).

193. Chaudhury, M. K., Chakrabarti, A. & Daniel, S. Generation of Motion of Drops with Interfacial Contact. *Langmuir* **31,** 9266–9281. ISSN: 0743-7463, 1520-5827. https://pubs.acs.org/doi/10.1021/la504925u (2023) (Sept. 2015).

194. Daniel, S. & Chaudhury, M. K. Rectified Motion of Liquid Drops on Gradient Surfaces Induced by Vibration. *Langmuir* **18,** 3404–3407. ISSN: 0743-7463, 1520-5827. https://pubs.acs.org/doi/10.1021/la025505c (2023) (Apr. 2002).

195. Huang, J.-J., Huang, H. & Wang, X. Numerical Study of Drop Motion on a Surface with Wettability Gradient and Contact Angle Hysteresis. *Physics of Fluids* **26.** arXiv:1307.6715 [physics], 062101. ISSN: 1070-6631, 1089-7666. http://arxiv.org/abs/1307.6715 (2023) (June 2014).

196. Schleizer, A. D. & Bonnecaze, R. T. Displacement of a two-dimensional immiscible droplet adhering to a wall in shear and pressure-driven flows. *Journal of Fluid Mechanics* **383,** 29–54. ISSN: 0022-1120, 1469-7645. https://www.cambridge.org/core/product/identifier/S0022112098003462/type/journal_article (2023) (Mar. 1999).

197. Moumen, N., Subramanian, R. S. & McLaughlin, J. B. Experiments on the Motion of Drops on a Horizontal Solid Surface Due to a Wettability Gradient. *Langmuir* **22.** Publisher: American Chemical Society, 2682–2690. ISSN: 0743-7463. https://doi.org/10.1021/la053060x (2023) (Mar. 2006).

198. Ju, Y.-T., Kuo, F.-C., Lin, Y.-T., Huang, T.-C. & Lin, C.-A. Partial wetting boundary conditions on micro-structure surface for Lattice Boltzmann method. *Computers & Fluids* **142,** 37–44. ISSN: 00457930. https://linkinghub.elsevier.com/retrieve/pii/S0045793016300081 (2023) (Jan. 2017).

199. Sinha, P. K. & Wang, C.-Y. Liquid water transport in a mixed-wet gas diffusion layer of a polymer electrolyte fuel cell. *Chemical Engineering Science* **63,** 1081–1091. ISSN: 00092509. https://linkinghub.elsevier.com/retrieve/pii/S0009250907008470 (2023) (Feb. 2008).

200. Randive, P. & Dalal, A. Influence of viscosity ratio and wettability on droplet displacement behavior: A mesoscale analysis. *Computers & Fluids* **102,** 15–31. ISSN: 00457930. https://linkinghub.elsevier.com/retrieve/pii/S0045793014002606 (2023) (Oct. 2014).

201. Russo, A. *et al.* Numerical simulation of droplet impact on wettability-patterned surfaces. *Physical Review Fluids* **5,** 074002. ISSN: 2469-990X. https://link.aps.org/doi/10.1103/PhysRevFluids.5.074002 (2023) (July 2020).

202. Hu, H., Yu, S. & Song, D. No-Loss Transportation of Water Droplets by Patterning a Desired Hydrophobic Path on a Superhydrophobic Surface. *Langmuir* **32,** 7339–7345. ISSN: 0743-7463, 1520-5827. https://pubs.acs.org/doi/10.1021/acs.langmuir.6b01654 (2023) (July 2016).

203. Furtado, K., Pooley, C. M. & Yeomans, J. M. Lattice Boltzmann study of convective drop motion driven by nonlinear chemical kinetics. *Phys. Rev. E* **78,** 046308. https://link.aps.org/doi/10.1103/PhysRevE.78.046308 (4 2008).

Titre : Optimisation topologique en flux interfaciaux avec le modèle pseudopotential

Mots clés : optimisation topologique, écoulements multiphasiques, méthode de lattice Boltzmann, mouvement des gouttelettes, optimisation multi-échelle, modèle pseudopotential.

Résumé : L'optimisation des systèmes et des processus est un exercice qui s'effectue en tenant compte de l'expérience et des connaissances de chacun. Nous explorons ici une approche mathématique pour optimiser les problèmes physiques en utilisant divers algorithmes d'optimisation. Dans cette thèse, l'objectif préliminaire de l'optimiseur est de modifier les caractéristiques d'écoulement du système en ajustant les forces capillaires. Cet objectif peut être atteint en modifiant l'un des deux ensembles de paramètres : (a) en introduisant un matériau solide mouillant (paramètre de niveau) ou (b) en changeant la mouillabilité des surfaces solides existantes (paramètre de mouillabilité).
Nous proposons que le premier ensemble de paramètres soit modifié à l'aide de l'algorithme d'optimisation topologique, où le gradient de la fonction de coût est obtenu en résolvant un modèle d'état adjoint pour le modèle mono-composant multiphase de Shan et Chen (SCMP-SC). De même, nous proposons que ce dernier ensemble de paramètres soit modifié à l'aide de l'algorithme d'optimisation de la mouillabilité, où nous dérivons à nouveau un modèle d'état adjoint pour le modèle SCMP-SC. Enfin, nous utilisons un algorithme d'optimisation multi-échelle, dans lequel nous calculons le gradient de la fonction de coût à l'aide de la différence finie. Nous avons réussi à démontrer la compétence de cet optimiseur pour maximiser la vitesse moyenne d'une gouttelette 2D jusqu'à 69%.

Title : Topology optimization in interfacial flows using the pseudopotential model.

Keywords : topology optimization, multiphase flows, lattice Boltzmann method, droplet motion, multiscale optimization, pseudopotential model.

Abstract : The optimization of systems and processes is an exercise that is carried out taking into account one's experience and knowledge. Here we explore a mathematical approach to optimize physical problems by utilizing various optimization algorithms. In this thesis, the preliminary objective of the optimizer is to modify the flow characteristics of the system by tweaking the capillary forces. This could be accomplished by modifying either of the two sets of parameters: (a) by introducing a wetting solid material i.e. the level-set parameter or (b) by changing the wettability of the existing solid surfaces i.e. the wettability parameter.
We propose that the former set of parameters could be modified using the topology optimization algorithm, where the gradient of the cost function is obtained by solving an adjoint-state state model for the single component multiphase Shan and Chen (SCMP-SC) model. Similarly, we propose that the latter set of parameters are modified using the wettability optimization algorithm where we again derive an adjoint-state model for the SCMP-SC. Lastly, we utilize a multiscale optimization algorithm, where we compute the gradient of the cost function using the finite difference. We have succeeded in demonstrating the competence of this optimizer for maximizing the mean velocity of a 2D droplet by up to 69%.